



HAL
open science

THz radiation confinement using metallic micro-resonators, for spectroscopy and manipulation of single nanometric samples

Théo Hannotte

► **To cite this version:**

Théo Hannotte. THz radiation confinement using metallic micro-resonators, for spectroscopy and manipulation of single nanometric samples. Micro and nanotechnologies/Microelectronics. Université de Lille, 2022. English. NNT : 2022ULILN037 . tel-04129855

HAL Id: tel-04129855

<https://theses.hal.science/tel-04129855>

Submitted on 15 Jun 2023

HAL is a multi-disciplinary open access archive for the deposit and dissemination of scientific research documents, whether they are published or not. The documents may come from teaching and research institutions in France or abroad, or from public or private research centers.

L'archive ouverte pluridisciplinaire **HAL**, est destinée au dépôt et à la diffusion de documents scientifiques de niveau recherche, publiés ou non, émanant des établissements d'enseignement et de recherche français ou étrangers, des laboratoires publics ou privés.

ÉCOLE DOCTORALE SCIENCES POUR L'INGÉNIEUR (SPI-ENGSYS)

UNIVERSITÉ DE LILLE

THÈSE

THz radiation confinement using metallic micro-resonators, for spectroscopy and manipulation of single nanometric samples.

Confinement de rayonnement térahertz par des micro-résonateurs métalliques, pour la spectroscopie et manipulation d'objets nanométriques uniques.

Thèse préparée et soutenue publiquement, pour obtenir le grade de Docteur de l'université de Lille en Électronique et Photonique, par

Théo HANNOTTE

Soutenue le 16 Décembre 2022

Jury:

Yanko TODOROV	<i>Laboratoire de physique de l'ENS</i>	Rapporteur
Oleg MITROFANOV	<i>University College London</i>	Rapporteur
Giacomo SCALARI	<i>ETH Zürich</i>	Examineur
Juliette MANGENEY	<i>Laboratoire de physique de l'ENS</i>	Présidente du jury
Peter Qiang LIU	<i>SUNY at Buffalo</i>	Invité
Jean-François LAMPIN	<i>IEMN</i>	Directeur de Thèse
Romain PERETTI	<i>IEMN</i>	Co-directeur de thèse

Institut d'Electronique, Microélectronique et Nanotechnologie (IEMN)



Abstract

Théo HANNOTTE

THz radiation confinement using metallic micro-resonators, for spectroscopy and manipulation of single nanometric samples.

At the boundary between optics and electronics, the terahertz (THz) frequency range has seen a growing interest in applications going from high data rate telecommunication to non-destructive testing. THz spectroscopy is expected to have a valuable purpose for analyzing biological samples. However, many objects of interest such as living cells, viruses, or proteins are two orders of magnitude smaller than THz wavelengths.

Sub-wavelength resonators have been widely studied as building blocks of metamaterial. Taking advantage of their dispersive properties, one can create an artificial optical medium with exotic dielectric properties such as a negative refractive index. However, the recent progress in THz spectroscopy and near-field optic has opened the path to study individual sub-wavelength resonators and fully take advantage of their near-field properties. This thesis focuses on the case of Split Ring Resonators (SRR), which are small metallic structures behaving as an RLC circuit confining the electric field in an arbitrarily small capacitive area. The electric field confinement provided by SRRs is used to get rid of the Abbe diffraction limit and perform spectroscopy on samples two orders of magnitude smaller than the wavelength of interest.

In this thesis, we develop an analytical model to understand the behavior of an SRR coupled to a sample material and extract information on that material from a spectroscopic measurement of the SRR. Then we design and fabricate an SRR compatible with THz time-domain spectroscopy (THz-TDS) performed on individual resonators. Afterward, we explore scattering scanning near field microscopy as a tool to measure the electric field profile of the fabricated SRR. Next, we perform THz-TDS experiment on single resonators coupled to a nanometric amount of a sample material. Finally, we explore the possibility to generate optical forces from the strong field gradient created by SRRs.

We developed a set of tools that allowed us to be among the first to conduct spectroscopy measurements on single SRRs in the THz range and extract information from them. The analytical models can still be improved, but they already provide a good understanding of the experimental data. We believe this work opens the path to THz spectroscopy at the nano-scale.

Résumé

Théo HANNOTTE

Confinement de rayonnement térahertz par des micro-résonateurs métalliques, pour la spectroscopie et manipulation d'objets nanométriques uniques.

À la frontière entre l'optique et l'électronique, la gamme de fréquence Téraherz (THz) attire un intérêt croissant dans des domaines allant des communications haut-débits au contrôle non destructif. La spectroscopie THz a le potentiel de constituer un outil de choix pour l'analyse d'échantillon biologique. Cependant, beaucoup d'échantillons tels que des cellules vivantes, des virus ou des protéines ont une taille inférieure aux longueurs d'onde THz de deux ordres de grandeur.

Des micro résonateurs, plus petit que leur longueur d'onde de résonance, ont été étudiés et utilisés en tant que composant élémentaire des métamatériaux. En utilisant les propriétés dispersives de ces résonateurs, il est possible de créer des milieux optiques artificiels possédant des propriétés singulières, comme par exemple un indice de réfraction négatif.

Cependant, les progrès récents en spectroscopie THz et en optique de champ proche ont ouvert la voie à l'étude de résonateur unique, et d'utiliser pleinement leurs propriétés en champ proche. Cette thèse se concentre sur le cas des résonateurs métalliques de type RLC, qui permettent de confiner un champ électrique dans un volume arbitrairement petit. Ce champ confiné est utilisé pour contourner la limite de diffraction d'Abbe, et permet la spectroscopie d'objet jusqu'à cent fois plus petit que la longueur d'onde.

Dans cette thèse, nous développons un modèle analytique pour comprendre le comportement d'un résonateur RLC couplé à un matériau, et extraire des informations sur ce matériau via une mesure de spectroscopie sur le résonateur. Après quoi nous concevons et fabriquons des résonateurs mesurables individuellement en spectroscopie THz dans le domaine temporel (THz-TDS). Nous étudions ensuite la microscopie optique en champ proche pour mesurer le profil du champ électrique formé par nos résonateurs. Puis nous procédons à des mesures de THz-TDS sur des résonateurs uniques couplés à un volume nanométrique d'un matériau d'étude.

Nous avons développé un ensemble d'outils qui nous ont permis d'être parmi les premiers à réaliser des mesures spectroscopiques sur des résonateurs RLC uniques dans la gamme THz et en extraire des informations. Les modèles analytiques sont encore améliorables, mais ils offrent déjà une compréhension profonde des données expérimentales. Nous pensons que ces travaux ouvriront la voie à la spectroscopie THz à l'échelle nanoscopique.

Acknowledgements

Je tiens à remercier Romain Peretti pour son excellent encadrement, pour sa confiance, et pour s'être investi autant sur le plan scientifique que pour la suite de ma carrière. Merci aussi pour toutes les digressions sur des sujets variés (souvent café et politique) qui m'ont bien aidé à me changer les idées. Merci à Jean-François Lampin pour les discussions scientifiques et techniques très enrichissantes, et son talent pour dénicher des références inédites, parfois déclassifiées, sur tous les sujets. Et bien sûr merci à Peter Liu de m'avoir accueilli dans son équipe à Buffalo.

Je remercie les membres du jury pour l'évaluation de mon travail et les questions stimulantes lors de la soutenance. Merci à Yanko Todorov et Oleg Mitrofanov pour leurs rapports. Merci à Giacomo Scalari d'avoir accepté d'examiner ma thèse. Merci à Juliette Mangeney d'avoir assumé la présidence du jury.

Je voudrais également remercier Sophie Eliet, Sylvie Lepilliet, Etienne Okada et Vanessa Avramovic pour le soutien technique et moral durant les expériences. Je remercie aussi l'équipe CMNF, en particulier François Vaurette, Yves Deblock et Salih Ouendi pour les multiples écritures et tests, Pascal Tilmant pour ses conseils en lithographie, ainsi qu'à David Guérin pour son aide et ses conseils sur les traitements chimiques. Merci à Louis Thomas et Cristiane Nascimento Santos pour toutes les mesures SNOM. Merci à Jean-Michel Mallet pour toutes les pièces fabriquées sur mesure. Merci à Jean-Michel Droulez pour son aide sur l'utilisation du cluster de calcul. Merci à Kevin Miao et Puspita Paul pour le travail de salle blanche à Buffalo.

Je remercie aussi le personnel de l'IEMN Lionel Buchillot et Thierry Mélin pour leur accueil au laboratoire, Nora et Andy pour leur aide et leur efficacité sur les points administratifs, ainsi que Valérie pour l'organisation des déplacements.

Merci à toute l'équipe THz pour les discussions lors des réunions, et pour les repas qui les suivaient.

Merci à mes compagnons de début de thèse pour tous les cafés partagés, m'avoir encouragé et aidé à reprendre l'escalade, et pour la préservation de notre santé mentale pendant le confinement. Merci à Kathia, présente depuis le début pour affronter la canicule dans la salle des stagiaires. Merci Cybelle pour ta bonne humeur et pour les diagrammes de rayonnements. Merci Mélanie pour ta compagnie dans le bureau, pour m'avoir fait sortir plus qu'à mon habitude, et pour avoir supporté mes bruits pendant 2 ans. Merci Jean-Marc pour toutes les sorties, le rhum banane et la chartreuse. Merci Kévin de m'accompagner dans les conversations de nerds. Merci Arthur pour les pães de queijo que j'essaierais de faire un jour.

Merci à Jeyan et Walter pour l'animation dans le bureau la dernière année, merci Quentin pour toute la nourriture apportée. Merci Adrien, Niels, Alexandre, Elsa, Alexandra pour tous les passages au dernier bar.

Je remercie mes vieux camarades, Samuel et Pierre, toujours présents, jusqu'à superviser personnellement le déroulement de la rédaction dans le Morvan. Merci pour les voyages, et les terrils. Merci à Younes, Mourad pour leur contribution à ma vie sociale cette dernière année. Merci Yvan pour la GameCube. Merci à Anissa Sébou pour ses encouragements pleins d'enthousiasme.

Merci au groupe de grimpeur de Buffalo, grâce à qui je ne suis pas tombé dans l'isolement pendant cette année 2021.

Enfin je remercie mes parents pour leur soutien constant, malgré tout le stress que j'ai pu leur causer. Pour avoir toujours fait le maximum pour moi au long de mes études, qui n'auraient pas pu aboutir de cette façon sans ce soutien; et merci à Sophie, d'avoir toujours volontiers pris ta part de stress dans toutes mes aventures. Merci à toute ma famille pour les nombreux encouragements.

Contents

Abstract	iii
Résumé	v
Acknowledgements	vii
General introduction	1
1 Modelisation of a Split Ring Resonator for sub wavelength characterization of dispersive materials	5
1.1 Split Ring Resonator	5
1.1.1 SRR for light confinement	6
1.1.2 Modelisation of the external coupling in the RLC model	7
1.1.3 RLC resonator	8
1.1.4 Differential equation for the mode amplitude	9
1.2 Reflection and transmission coefficients from the RLC model	9
1.2.1 Transmission and reflection on resonator in a homogeneous lossless medium	10
1.2.2 General conditions on the coupling parameters for a SRR on a substrate	12
1.2.3 Overall transmission of a SRR on a finite substrate	14
1.3 Coupling of the resonator with a material	15
1.3.1 Influence of the refractive index	16
1.3.2 Capacitance fully filled with a dispersive material	16
1.3.3 Interpretation with strong coupling theory	18
1.3.4 Realistic modelisation of the capacitance	19
Capacitance partially filled along the field lines	20
Capacitance partially filled across the field lines	20
Other effective medium models	21
Capacitor model with imperfect contact	22
1.4 Further improvements	25
References	25
2 Design and fabrication	31
2.1 SRR design	31
2.1.1 Coupling with the far-field	31
Magnetic and electric coupling	32
Far-field emission model	33
Model verification with FDTD simulation	34
Overall amplitude of the radiated field	35
Consequences of the resistance variation over the resonance bandwidth	37
Influence of the design on the quality factor in FDTD simulations	38

2.1.2	Quality factor design	41
2.1.3	Field confinement volume	42
2.1.4	Coupling with the sample material	42
	Choice of the substrate material	43
2.1.5	Conformity with the RLC model	43
2.2	Fabrication	44
2.2.1	Main process	44
2.2.2	Optional surface treatment	46
2.3	Limitation of the design and process	47
	References	48
3	Near-field characterization	51
3.1	Near-field	51
3.2	s-SNOM	52
3.2.1	Set-up description	52
3.2.2	Detection scheme	53
3.2.3	Test sample	54
3.2.4	Enhanced probe for THz microscopy	55
3.3	Result	56
3.4	Discussion	61
3.4.1	FDTD simulation including the probe	62
3.4.2	Interpretation	64
3.4.3	s-SNOM with attenuated total internal reflection	67
3.5	Conclusion	68
	References	69
4	Time domain spectroscopy on single SRRs	73
4.1	Time domain spectroscopy	73
4.2	Fitting procedure	75
4.3	Single resonator spectroscopy	77
4.3.1	Single SRR signal compared to the dynamic range	77
4.3.2	Noise analysis and error correction	78
4.3.3	Experimental result on single resonators	83
4.4	Coupling with Glutamic Acid	85
4.4.1	Preliminary characterization of Glutamic Acid	86
4.4.2	Deposition procedure	87
4.4.3	Measurement result	90
4.4.4	About the spectra quality	92
4.4.5	Coupling estimation	94
4.5	Next steps	96
	References	97
5	Optical trapping from the confined field of SRRs and graphene plasmonic resonances.	99
5.1	The Optical Tweezer	99
5.2	Optical forces	101
5.2.1	General case	101
5.2.2	Force on a neutral dielectric Rayleigh particle	103
5.2.3	Optical forces in a Gaussian beam	105
5.3	Terahertz optical tweezer	106
5.3.1	Trapping smaller particle with terahertz radiation	106

5.3.2	Tweezer design	106
5.3.3	Simulation	107
	Numerical force calculation	107
	Simulation result	108
5.3.4	Experiment	109
	Secondary infrared optical tweezers	109
	Force measurement	110
	Terahertz beam path	113
	Microfluidics cell	114
	THz-TDS characterization of the SRR submerged in hexane	116
	Particle sample	116
5.3.5	Protocol and result	117
5.4	Graphene plasmonic tweezer	119
5.4.1	Graphene structure	120
5.4.2	Gate structure	121
5.4.3	Device fabrication	122
5.4.4	Graphene characterization	123
	Conductivity	123
	Mid-IR spectrum	124
5.4.5	Microfluidic sample holder	126
5.4.6	Optical setup	127
5.4.7	Experimental results and next steps	128
	References	131
	Conclusion and perspectives	137
A	Optical torque	141
A.1	Torque calculation in the static approximation	141
A.2	Torque calculation on an ellipsoidal particle	142
A.3	Numerical torque computation	143
	A.3.1 Volumetric technique adaptation	143
	A.3.2 MST technique adaptation	143
	A.3.3 Test of the torque calculation	143
	References	143

List of Figures

1	The terahertz domain in the electromagnetic spectrum.	1
2	Example of microwave metamaterial made of SRRs. Picture taken from "NASA Glenn Research".	2
1.1	Schematic of a simple split ring resonator, and its equivalent RLC circuit.	6
1.2	Equivalent circuit for a SRR coupled to the far field through a voltage source u_e and a radiative resistance R_r	8
1.3	Schematic of the resonator as a two port system.	10
1.4	Illustration of the transmission, reflection and propagation involved in the transmission of a resonator on a substrate of thickness d and refractive index n	14
1.5	Transmission spectra of a resonator with a weak coupling constant	15
1.6	Visualization of the resonance splitting of a SRR coupled with a Lorentz material.	17
1.7	Transmission spectrum of a resonator without substrate coupled with Glutamic Acid, for different inductance values, showing the anti-crossing pattern.	18
1.8	Schematic side view of the electric field lines in a SRR gap coupled with a material flake.	20
1.9	Schematic of a partially filled parallel plate capacitance.	21
1.10	Schematic view of an imperfectly placed sample and equivalent model.	23
1.11	ϵ_{eff} as a function of F_s with $\epsilon_{\text{sample}} = 10$, $\epsilon_{\text{sub}} = 4.1$, $\epsilon_{\text{air}} = 1$ and $F_p = 0.5$	24
1.12	Expected transmission for a SRR coupled with Glutamic acid for different filling factors.	24
2.1	Schematic of a spectroscopic experiment on a resonator on substrate under normal incidence.	32
2.2	Dipole moments in the simple and double SRR.	32
2.3	Schematic of three SRR design and their simplified emission model.	34
2.4	Simulated far-field radiation pattern from different designs and models without substrate.	35
2.5	Normalized polar plot of the scattered intensity in the XZ plane for all the presented designs and from the simplified dipole model of the square design.	36
2.6	Calculated time domain response to an impulsion from a RLC circuit with $R \propto \omega^2$, compared to a damped sinusoidal function.	37
2.7	Two designs for SRR with large capacitance.	38
2.8	Simulated resonance wavelength of square SRRs for different sizes $a = a_x = a_y$ and identical capacitance.	39
2.9	Definition of the main dimension and simulated quality factor for square SRRs in PEC, for different sizes $a = a_x = a_y$ and gap ratio $\frac{A}{C}$	40
2.10	SRRs with identical $\frac{A}{C}$ ratio, but decreasing confinement volume.	42

2.11	(a): Cross section of a SRR gap on substrate ideally coupled to a sample material. (b): Schematic cross section of a gap with an under-etched substrate.	43
2.12	Schematic illustration of the resonator fabrication process.	44
2.13	SEM images of fabricated SRRs. (a), (b) and (c): Examples with different parameters. (d): Close up view on a ~ 28 nm gap.	45
2.14	Schematic illustration of the OTS adsorption on the sample, depending on the initial surface state.	46
2.15	Comparison of the shape of water droplets on quartz with different surface state.	47
3.1	Schematic representation of the s-SNOM setup.	52
3.2	SRR design and its transmission spectra.	55
3.3	Schematic view of the Lprobe, its fabrication process and comparison with the Arrow NCPT probe.	56
3.4	(a): Simulated vertical component of the electric field on a plane above an excited SRR ($a = 19 \mu\text{m}$). (b): Simulated, experimental and topographic cross section for a tuned SRR on Si. The sharp spikes in the experimental S_2 signal are artifacts from the topographic edge (see figure 3.6). (c,d,e,f): Experimental s-SNOM images of 4 SRRs excited at 2.5 THz. (c): Tuned SRR on quartz ($a = 19 \mu\text{m}$). (d): detuned SRR on quartz ($a = 17 \mu\text{m}$). (e): tuned SRR on silicon ($a = 13 \mu\text{m}$). (f) detuned SRR on silicon ($a = 17 \mu\text{m}$). Scale bars are $5 \mu\text{m}$	57
3.5	(a) s-SNOM images of a SRR demodulated at harmonic 1 to 4. (b): Signal cross section along the axis indicated by white triangles in (a), with a $60 \mu\text{V}$ offset. Scale bars are $5 \mu\text{m}$	58
3.6	2 nd harmonic signal, probe oscillation amplitude, and topography measurement on a cross section of a SRR on silicon.	59
3.7	(a): s-SNOM scan on 4 SRRs in a matrix. (b): s-SNOM images of an isolated SRR. All SRRs give identical result. $a = 13 \mu\text{m}$ in both cases.	60
3.8	(a): SRR on Si measured with PHD ($a = 13 \mu\text{m}$). (b): SRR on quartz measured with a shorter AFM probe ($a = 19 \mu\text{m}$).	61
3.9	s-SNOM images of a LSA	62
3.10	Simulated far-field pattern of a SRR and a sSNOM probe at different positions.	63
3.11	Simulated S_2 signal, extracted from the far-field scattering pattern of a SRR coupled with a $70 \mu\text{m}$ long metallic probe, compared with the experimental S_2 profile measured on a SRR on a quartz substrate.	65
3.12	s-SNOM images of SRR differently oriented. The images are rotated to simulate illumination from 8 angles. The four images on the right are rotated versions of the images on the left.	66
3.13	(a) Reconstructed image from the 8 orientations (b): Cross section along the branch axis.	66
3.14	Schematic of a s-SNOM using attenuated total internal reflection.	67
3.15	(a): High resistivity silicon prism mounted in the NeaSNOM microscope. The THz beam is focused in the prism with the parabolic mirror on the left, and collected with the parabolic mirror on the right. (b): First s-SNOM image of a SRR excited through TIR. Only the excitation is done through the prism, the image is still constructed from the scattered field above, hence the remaining asymmetry ($a = 13 \mu\text{m}$).	68

4.1	General schematic of a THz Time Domain Spectroscopy system. The red line represents the infrared path while the blue beam represents the THz pulse path.	74
4.2	THz beam path in our THz-TDS system. Once aligned, the antenna and the parabolic mirror on each side are rigidly attached together to be used as single components. All the components are aligned on a rail.	75
4.3	Example of signal measured in our system without sample, averaged over 10 000 traces.	75
4.4	SEM picture of a complementary SRR. The darker area is an aperture through a gold plane.	78
4.5	(a): Time domain signal detected from a single complementary SRR. (b): Transmission spectrum normalized with the transmission through quartz.	78
4.6	Standard deviation of a THz-TDS signal in time and frequency domain	80
4.7	Effect of the correction in the time domain (top) and frequency domain (bottom). The correction removed most of the correlation between the standard deviation and the signal amplitude. Consequently, the signal to noise ratio between 0.5 THz and 2 THz is improved by almost 20 dB.	81
4.8	Correction effect on the standard deviation for a remarkably large delay drift. The standard deviation is reduced by 28 dB at 1 THz. The spikes in the standard deviation after correction indicate a variation in the water vapor concentration during the acquisition.	82
4.9	Non corrected signal divided by the corrected signal in the frequency domain for the measurement shown in figure 4.7 (blue) and figure 4.8 (red). The strength of the filtering is different for each measurement as it depends on the delay drift during the acquisition. The spikes in the red curve come from variations of water vapor concentration during the acquisition. The fit of the strongest attenuation with equation (4.9) gives $\Delta = 75$ fs. This value gives only an order of magnitude since the delay distribution is not actually uniform (see figure 4.10).	82
4.10	Estimated delay drift during the same two measurements as in figure 4.9. The red curve shows a drift of over 67 fs, which is more than 2 time steps of the THz-TDS.	83
4.11	Transmission spectra of 7 individual SRRs, with sizes ranging from 15.5 μm to 175 μm normalized with the quartz transmission. The lowest resonance is measured at 275 GHz, and the highest at 3 THz. In each spectra from 33 μm to 175 μm , we see a broadband modification of the reflectivity starting at roughly twice the resonance frequency.	84
4.12	Transmission spectrum of a SRR with high quality factor. The decay rates extracted from the fit with the model from chapter 1 give $Q = 29.65$, which is consistent with the ~ 30 GHz bandwidth observed in the spectrum.	85
4.13	Transmission spectrum of a ~ 0.5 mm thick pellet of pure GA normalized with the transmission through the empty holder.	86
4.14	Optical microscope image formed after evaporation of 10 μL of a saturated GA solution.	87

4.15	(a): Deposition attempt of GA on a SRR with hydrophilic quartz surface. (b): Deposition with OTS treatment making the quartz hydrophobic. The SRRs are 21 μm large and indicated by arrows. Both attempts were done with approximately 30 nL of saturated solution. Yet, the droplet on the hydrophilic surface evaporated in a few seconds, while the droplet on the hydrophobic surface lasted several minutes resulting in much better crystals.	88
4.16	(a): Drop with a diameter < 500 μm (b): Drop with a diameter < 250 μm	88
4.17	(a): SRR (indicated by the arrow) covered and surrounded by GA crystals. (b): GA crystals far from any structure, in a quantity similar to the one surrounding the SRRs.	89
4.18	Transmission spectrum of less than 0.25 μg of GA (figure 4.17b) normalized with the substrate transmission. The reflection is broadly modified, with a clear absorption at 2 THz, and no clear feature at 1.2 THz. The sharp spikes are from residual water vapor.	89
4.19	Transmission spectrum without GA, measured on the SRRs specifically designed for coupling with GA. Resonance are distinguishable around 1.3 THz, but the depth of the lines are less than 0.5%, against several percent for the previously measured SRRs (figure 4.11).	90
4.20	Transmission spectrum of SRRs covered with GA, where the resonances either disappeared or are reduced to a small indent in a strong Fabry-Pérot shape.	91
4.21	Transmission spectrum of SRRs slightly out of tune for coupling with the GA resonance. The resonances did shift toward lower frequency, which confirms the presence of a form of coupling with the GA.	91
4.22	Transmission spectrum from one of the SRRs covered with GA. The resonance shift from 1.33 THz (figure 4.19), to 1.24 THz suggests that the coupled with the GA and correctly tuned to interact with its main resonance. Yet the singular and unexplained shape of the spectrum does not allow us to extract information. We were not able to reproduce a similar result.	92
4.23	Transmission spectrum of SRR with the same design and on the same sample, but with a resonance at 1 THz. The resonance is much clearer than for any of the resonances around 1.3 THz (figure 4.19).	93
4.24	Transmission spectrum of the quartz substrate normalized with the transmission in air. The transmission maxima correspond to constructive interference at the interfaces. Oscillations at high frequency are artifacts from the temporal rectangular window.	93
4.25	(a): 23 μm SRR covered with GA crystals used to estimate the coupling strength. (b): Predicted transmission from the RLC model and the experimental coupling strength.	94
4.26	Schematic cross section of a SRR gap and its field line coupled with a crystal. The electric field is polarized out of plane above the metal, but the vertical component is anti-symmetric and has a zero mean value. A mode that couples with a vertically polarized electric field should couple to the SRR, unless the mode is delocalized over a distance larger than the gap.	95
5.1	Ray optics interpretation of optical forces, case of a colimated and focused beam.	101

5.2	General schematic of the tweezers setup.	106
5.3	Example of electric split ring resonator designs with three different gap sizes (0.5 μm , 4 μm and 6 μm), the trapezoidal shape makes the capacitance independent of the gap size.	107
5.4	Pseudo-potential of a diamond particle above a SRR. Value extracted from FDTD simulation with 1 mW input power. The potential well is compared to thermal energy $k_B T$ at $T = 300$ K to estimate the stability of the trap.	109
5.5	Infrared optical tweezer.	110
5.6	Annotated photograph of the modified setup	111
5.7	Shape and positioning of the diode in the quadrant position detector PDQ80A	111
5.8	THz optical setup. (a) : The beam goes through a polarization rotator made of three planar mirrors. It is then enlarged with two confocal parabolic mirrors and directed toward the tweezer optical table. (b) : The beam diameter is reduced with two confocal parabolic mirrors and focused on the sample with another parabolic mirror.	113
5.9	Component used to fill the microfluidics cell.	114
5.10	(a) : Step by step illustration of the microfluidics cell fabrication process. (b) : Complete microfluidic cell mounted in the optical tweezer setup.	115
5.11	THz-TDS transmission spectrum of the same SRR array in a microfluidic cell. As expected, the resonance shifts toward lower frequency when hexane is injected in the cell. The spectra are normalized with the transmission of the cell far from the SRRs (without and with hexane). The large fluctuations are due to the multiple reflection inside the three layers of the microfluidic cell.	116
5.12	SEM images of the diamond particles with two different size distributions. The shapes are far from spherical, which can be an issue for the gaussian beam OT, but does not matter as much for the near-field OT.	117
5.13	Photograph of diamond microparticles (sizes ranging from 0.5 μm to 1 μm) in hexane. Left : Without surface treatment. Right : With OTS surface treatment. Both solutions were agitated a few seconds before the photograph was taken.	118
5.14	(a) : Schematic of the simulated structure. The GNR is excited with a plane wave horizontally polarized. We use periodic boundary condition in the plane of the GNR. (b) : Field profile above a GNR with a non-uniform Fermi energy as represented in (a).	121
5.15	Gate structure subdivided to provide movable trapping position. In this picture, the polarization of the mid-IR beam must be horizontal to excite the GNR, hence this gate structure is opaque to the excitation beam.	122
5.16	Field profile of a GNR above a nano-slot.	123
5.17	Schematic of the gate structure for the optical conveyor belt and for the proof of concept experiment.	124
5.18	(a) : Top view schematic of the fabricated device. The gate is isolated from the other component with a HfO_2 layer. The drain and source contact serves for graphene characterization. (b) : Step by step schematic of the fabrication process.	125

5.19	Source-Drain current as a function of the gate voltage with a constant source-drain voltage $V_{sd} = 0.1$ V, measured in air and in hexane. The presence of hexane increases the graphene conductivity but does not disturb its tunability.	126
5.20	(a) : Photograph of the fabricated device through the optical microscope. The clear rectangle is an image of the aperture through which the FTIR spectrum is measured. The aperture covers 4 slots aligned along 1 GNR. (b) : Simulated reflection spectrum of the device for different graphene chemical potential. The simulation predicts a strong coupling regime between the slot and GNR resonances.	127
5.21	FTIR reflection spectrum of the area represented in figure 5.20a. The area covers 4 slots along a graphene ribbon. We were not able to detect any change in the spectrum when applying a gate voltage.	128
5.22	Schematic cross section and photographs of the sample holder	129
5.23	Schematic of the optical setup, including the illumination, observation, mid-IR excitation, and fluorescence excitation.	130
5.24	Two optical images of the same spot in a cell without reflective device. (a) : With only white light illumination. Only a reflective gold particle is visible. (b) : With white light and UV illumination. We see the fluorescence from CdSe quantum dots.	131

Acronyms

- a-SNOM** aperture Scanning Near-field Optical Microscopy. 47
- AFM** Atomic Force Microscope. xii, 48, 49, 52, 56, 57
- ATIR** Attenuated Total Internal Reflection. 62–64
- BFI** Back Focal plane Interference. 105
- CNP** charge neutrality point. 120
- CVD** Chemical Vapor Deposition. 119, 120
- EMM** Effective Medium Model. 17
- FDTD** Finite Difference Time Domain. xv, 30, 51, 53, 54, 58, 78, 99, 103, 104, 118, 121
- FIB** Focused Ion Beam. 43
- FTIR** Fourier-Transform Infrared. xvi, 121, 122, 125
- GA** Glutamic Acid. viii, xiv, 81–91
- GNR** Graphene Nano-ribbon. xv, xvi, 115–122, 124, 125
- HD** homodyne detection. 49, 50
- InGaAs** indium gallium arsenide. 70
- LSA** Log Spiral Antenna. 56, 61
- MST** Maxwell’s Stress Tensor. 98, 104, 105, 132
- NP** nanoparticles. 95, 115, 126
- OT** Optical Trapping. xv, 95, 103, 111–114, 124–126
- OTS** Octadecyltrichlorosilane. xii, xiv, xv, 42, 43, 83, 112, 113, 124, 125
- PEC** Perfect Electrical Conductor. xi, 35, 37, 104
- PHD** pseudo-heterodyne detection. xii, 50, 57
- PSD** Power Spectrum Density. 106
- s-SNOM** scattering Scanning Near-field Optical Microscopy. viii, xii, xiii, 48–64, 69, 125

SNOM Scanning Near-field Optical Microscopy. 1, 30

SRR Split Ring Resonator. viii, ix, xi–xv, 2, 3, 5, 7, 9–12, 15, 20, 21, 27–43, 47, 49–51, 53–64, 69, 73–75, 77–81, 83–91, 95, 103–105, 110–114

TDCMT Time Domain Coupled Mode Theory. 2, 5, 7, 8

TFSF Total-Field Scattered-Field. 30, 58

THz-TDS THz Time Domain Spectroscopy. ix, xiii, xv, 1, 10, 15, 20, 27, 30, 36, 39, 51, 64, 69–71, 73–75, 79, 81, 91, 111, 112

TIR Total Internal Reflection. xiii, 63, 64

UB State University of New York at Buffalo. 95

General introduction

At the boundaries between optics and electronics, the THz frequency range is commonly defined as the range between 100 GHz to 10 THz. For decades, the lack of sources and detectors caused this part of the electromagnetic spectrum to remain mostly unexplored, and referred to as the “terahertz gap”. But the rapid progress in optics and electronics in the past 30 years have made it an increasingly attractive area of research. This range of frequency stays largely unknown from the general public, yet it is key to massively important outbreaks in domains such as astronomy. For example, the cosmic microwave background, electromagnetic radiation that is remnant of an early stage of the universe, when it became transparent, has a frequency around 180 GHz. More recently, the first images of black holes were recorded in 2019 and 2022 by the Event Horizon Telescope. This telescope array, consisting of a global network of radio telescopes, operates between 230 and 450 GHz. Those massive scientific advances are closely tied to the development of THz technology.

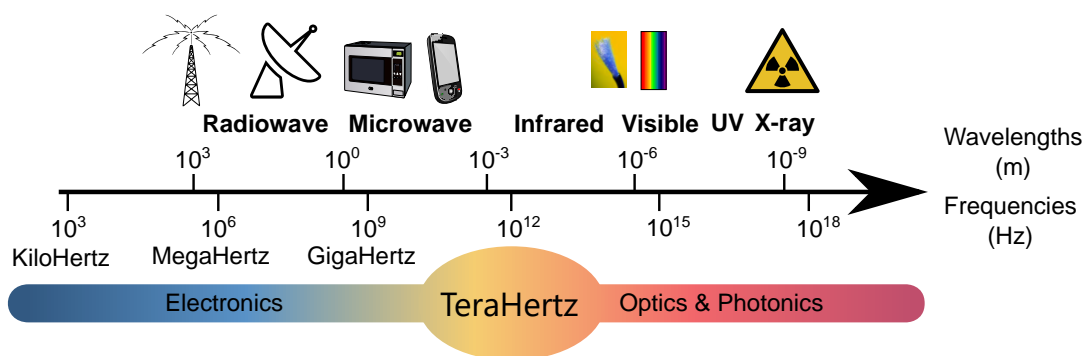


Figure 1: The terahertz domain in the electromagnetic spectrum.

Outside of astronomy, the THz range found applications in a wide variety of domains such as non destructive control, explosive detection, high data rate telecommunication and biology. More specifically, the advent of powerful short pulsed lasers in the 1980s, along with nonlinear optics, brought the possibility to generate broadband THz pulses. Hence setting the path to the spring of THz spectroscopy.

While mid-infrared spectroscopy probes the vibration of inter-atomic bound, Vibrational spectroscopy probes inter-molecular vibration, rotational mode, or vibration of large molecules. The vibrational mode of large molecules such as proteins, or other biological objects such as DNA and viruses lie in the THz range. One of the main difficulties for THz spectroscopy of such objects is their small sizes, several orders of magnitudes smaller than THz wavelengths, which strongly limit their interaction with propagating THz radiation.

This thesis explores a resonant approach to circumvent the diffraction limit and confine THz radiation in an arbitrary small volume, leading to massive enhancement of light-matter interaction with objects as small as a few nanometers. This

approach is based on Split Ring Resonators (SRRs). SRRs originate from the microwave domain where they were first introduced for their tunable dispersive properties, as a building block for meta-materials. In this context, a large assembly of sub-wavelength resonators is treated as an homogeneous effective material, with potentially exotic electromagnetic properties.

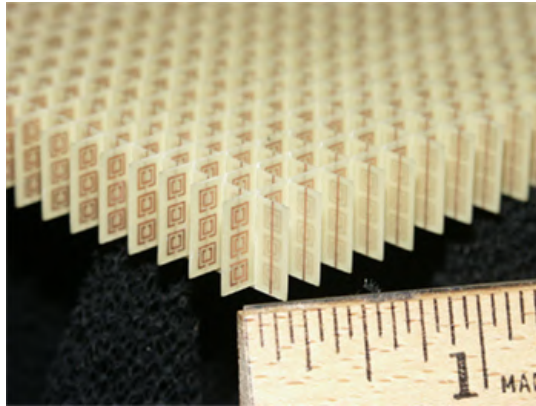


Figure 2: Example of microwave metamaterial made of SRRs. Picture taken from “NASA Glenn Research”.

With the progress made in THz sources and detectors, it is now possible to interact with individual resonators, and take advantage of their near-field properties. SRRs behave as RLC circuits and, as such, they confine electric fields in their capacitor, which can be made arbitrarily small, down to the nanometer scale. Although SRRs have already been used in the past for light matter enhancement and analysis of small objects, it is usually done with a large quantity of resonators, and only rarely on individual ones. This effectively increases the volume where the field is confined. Furthermore, unless each resonator is coupled to the sample in the exact same way, such spectroscopy experiments can only lead to *detection* of low volume samples rather than *measurement*.

We mostly focused on spectroscopy, but tight radiation confinement is key for numerous applications, including (but not limited to) microscopy, nonlinear optics and optical trapping. Using SRRs for any of these applications requires an accurate understanding of the resonators properties, how it couples to the near-field and far-field, both theoretically and experimentally.

Firstly, we focus our attention on the SRR itself. We study its behavior and what a spectroscopy measurement can tell us about the material we put in its capacitor. We see how it can be designed according to the needs of each application. We use near-field THz microscopy to characterize the electric profile of the resonators.

Secondly, we will put the field confinement provided by a SRR to the test for two applications where it is required: THz spectroscopy on nanometric samples with single SRRs, and optical trapping with THz radiation.

The outline of this thesis is organized as follow:

- In chapter 1, we develop a model to describe and predict the behavior of a SRR probed with THz Time Domain Spectroscopy (THz-TDS) in transmission or reflection. In particular, we study how its transmission spectrum is affected by the presence of a dispersive material in its capacitor. We will see how small differences in the way the material is coupled to the SRR significantly affects the transmission, motivating the need for experiment on single SRRs.

- Chapter 2 focuses on the design and fabrication of the SRRs. Using FDTD simulations, we will see how we can control the resonance frequency, quality factor, and coupling directivity of a SRR.
- In chapter 3, we use a near field microscopy technique called scattering Scanning Near-field Optical Microscopy (s-SNOM) to experimentally characterize the near-field profile of our SRR. This chapter is as much about s-SNOM itself as it is about SRR. Indeed, we will address the issue related to near-field imaging of structures with antenna-like properties.
- Chapter 4 starts the second part of this thesis, focusing on *using* the field confinement provided by a SRR. In this chapter, we demonstrate THz-TDS on single resonators, in a configuration that allows us to physically access the capacitor. We identify a major source of error in THz-TDS and a solution to correct it, which proved to be essential for long acquisitions. Using Glutamic Acid (GA) as a test sample, we detect its presence in the capacitor of a single SRR. However, we were not able to extract quantitative information from it.
- Finally, chapter 5 focuses on a second application of extreme field confinement: the generation of optical forces. We show that the strong field gradient generated by a SRR, as predicted by FDTD simulation and validated with near-field microscopy, should induce optical forces on micro and nano-particles strong enough to form a stable optical trap at room temperature. Similarly, we will see that the plasmonic resonance of Graphene Nano-ribbon (GNR) should provide similar trapping capability in the mid-IR, with increased flexibility. To avoid the strong absorption of water in these frequency ranges, we develop a microfluidic device fully compatible with non polar solvent. Yet, the unexpected behavior of micro-particles in non-polar solvent prevents us from reaching conclusive results at this time.

Chapter 1

Modelisation of a Split Ring Resonator for sub wavelength characterization of dispersive materials

1.1 Split Ring Resonator

THz spectroscopy is expected to have a valuable purpose for analyzing biological samples. Because far-field spectroscopy techniques such as THz Time Domain Spectroscopy (THz-TDS) are subject to the diffraction limits, those samples are often in the form of pressed powder pellets[1] or diluted in liquid[2]. Indeed a THz beam with a wavelength between 0.1 and 1 mm cannot be focused on a spot smaller than about 50 μm [3], which is two orders of magnitude larger than biological objects such as bacteria, cells, proteins or viruses[4]. The powder pellet approach has several issues. Firstly, some of the objects of interest such as viruses simply cannot be produced in quantities large enough to produce a pellet. Secondly, it has been shown that vibrational signatures of protein crystals in the THz range are often the result of delocalized vibration in the crystal structure[5], meaning that a measurement on a large quantity of crystals will be blurred by the random orientations and sizes of each crystal.

There is a clear interest in analyzing small volume samples beyond the diffraction limit, which requires a way to enhance light matter interaction. According to Purcell's theory[6], strong light matter interaction can be achieved through tight radiation confinement. THz radiation confinement has been widely experimented with three different approaches:

- Guided approach[7–13]: taking advantage of the low losses of metal in the THz range, a metallic waveguide can be optimized to confine a propagating beam of light in a sub-wavelength volume without introducing much losses and dispersion. This approach is broadband and can confine light in one or two dimensions.
- Near-field microscopy approach[14–19]: using near-field microscopy techniques such as Scanning Near-field Optical Microscopy (SNOM) which can image a sample with a nanometric resolution. This method provides the best spatial resolution, but the interpretation of the result is far from straight-forward, and although it is possible to use a broadband source on those systems, the powers required are difficult to achieve and measurements are most often done on a single frequency.

- Resonant approach[20–25]: Using a resonator to confine THz radiation in three dimensions, and to increase the interaction time by recycling light. This approach intrinsically has a smaller bandwidth than the guided approach, but shows better field confinement and is easily tunable during the resonators fabrication.

In this thesis, we will mainly focus on the third approach, and more specifically on radiation confinement using Split Ring Resonators (SRRs). This chapter aims at defining a theoretical framework to use SRRs as a tool for spectroscopy of microscopic sample. This framework will allow us to correctly interpret the results from the measurements in chapter 4.

1.1.1 SRR for light confinement

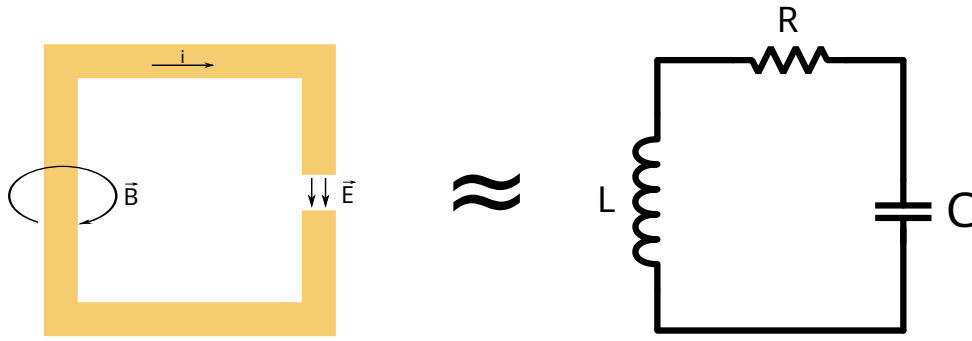


Figure 1.1: Schematic of a simple split ring resonator, and its equivalent RLC circuit.

SRRs were originally invented for microwave applications, where they served mainly as building blocks for metamaterials. Applications include dielectric function engineering[26], optical cloaking[27, 28] and negative refraction[29].

A SRR is a metallic structure with capacitive and inductive areas. The simplest design is a single metallic loop with a gap. The loop itself acts as an inductor while the gap acts as a capacitor, as illustrated in figure 1.1. The SRR thus behaves as a RLC circuit in the frequency range where the quasi-static approximation is valid, i.e. the length of the loop is much smaller than the wavelength. When excited near its natural frequency $\omega_n = \frac{1}{\sqrt{LC}}$, a RLC circuit stores energy in the form of an electric field in the capacitor, and a magnetic field in the inductance. This makes the SRR highly suitable for radiation confinement since the size of the capacitor and inductor can be designed arbitrarily small. We will mainly focus on SRR optimized for interaction through an electric field, allowing to probe the dielectric permittivity ϵ of a material, but all the reasoning are also applicable for magnetic field confinement around the inductance if one needs to probe the magnetic permeability μ of a material.

A RLC circuit is a single-mode resonator that can be coupled with farfield radiation. One of the most efficient ways to treat such a system is the Time Domain Coupled Mode Theory (TDCMT) [30]. TDCMT uses the complex amplitude of the mode a defined such that the squared magnitude of a is the energy in the resonator. This approach allows one to simplify the problem by considering only the resonance at positive frequency. Indeed the temporal evolution of the mode amplitude is described by a complex first order differential equation:

$$\frac{da}{dt} = \left(j\omega_0 - \frac{1}{\tau} \right) a + \kappa_1 s_{+1}, \quad (1.1)$$

where ω_0 is the resonance frequency, $\frac{1}{\tau}$ is the decay rate of the mode, κ_1 is the coupling coefficient with an input port, and s_{+1} is the amplitude of the wave from the port (defined such that $|s_{+1}|^2$ is the power of the incident wave). Although this approach is very convenient to extract results such as transmission and reflection coefficient, it is only valid when the line width of the mode is small compared to the resonant frequency, i.e. $\frac{1}{\tau} \ll \omega_0$. However, this assumption is often not valid for SRR which have non negligible ohmic and radiative losses. We will check the necessity of this assumption in section 1.1.4. To properly interpret the spectroscopic response of SRRs, we derive the transmission and reflection coefficient from the RLC model, using only variables derived from the parameters of the SRR.

1.1.2 Modelisation of the external coupling in the RLC model

The inductive loop of current and the charge accumulation in the capacitance lead to oscillating magnetic and electric dipole moments. Those oscillating dipoles radiate energy in the far field, which is a source of losses adding up to the ohmic losses of a regular RLC circuit. In antenna theory, the concept of radiative resistance is used to model the radiative loss in an antenna. It is defined as $R_r = \frac{W}{I^2}$, where W is the total radiated power and I is the current injected in the antenna. For example, the radiative resistance of a loop antenna with a uniform current is given by[31]:

$$R_r = \frac{Z_0}{2} C_\lambda \int_0^{2C_\lambda} J_2(y) dy, \quad (1.2)$$

where Z_0 is the free space impedance, C_λ is the circumference of the loop in wavelengths, and J_2 is the second order Bessel function. This expression can be simplified when the loop is much smaller or much larger than the wavelength. Hence the radiative resistance scales with ω^4 for a sub-wavelength loop, and with ω for a large loop. Hence the radiative resistance does not behave as a regular resistance since its value is strongly frequency dependent. The behavior of the SRR will deviate from a strict RLC circuit when the radiative resistance variations are not negligible across the resonance bandwidth.

Note that using the definition of radiative resistance from antenna theory implies that the circuit loses energy when the current in the loops is high. Nonetheless, an antenna usually emits radiation proportional to the *derivative* of the current[32]. This could be modeled with a resistor in *parallel* with the inductance. However, the formulas of radiative resistances do not apply in this configuration, and finding a meaningful definition of this alternative resistance would require further investigation in antenna theory.

Inversely, electric and magnetic dipoles are excited when placed in a variable external electric or magnetic field. In the case of magnetic excitation, the variable magnetic field through a metallic loop creates an electromotive force following Faraday's law of induction:

$$u_{em}(t) = -\frac{d\Phi(t)}{dt}, \quad (1.3)$$

where $\Phi(t)$ is the magnetic flux across the circuit. A SRR can be designed to optimize coupling with the electric field or magnetic field, that is why the precise nature of the coupling will be discussed in chapter 2. For the moment, we model it with a radiative resistance and a voltage source as illustrated in figure 1.2, while keeping in mind that the value of R_r may be complex and frequency dependent.

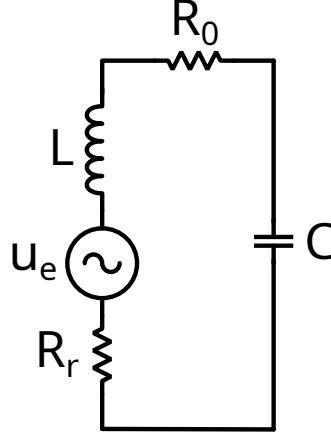


Figure 1.2: Equivalent circuit for a SRR coupled to the far field through a voltage source u_e and a radiative resistance R_r .

Finally, we end up with a RLC circuit with $R = R_0 + R_r$, where R_0 represents the ohmic loss, and R_r represents the radiative loss, with a voltage source arising from the external electromagnetic field.

1.1.3 RLC resonator

Under the quasi-static approximation, we consider a simple RLC series circuit with a voltage input u_e , defined by

$$u_r = Ri, \quad (1.4)$$

$$u_l = L \frac{di}{dt}, \quad (1.5)$$

$$i = C \frac{du_c}{dt}, \quad (1.6)$$

$$\text{and } u_r + u_l + u_c = u_e. \quad (1.7)$$

By expressing every term as a function of the current i , we get the following differential equation:

$$\frac{d^2i}{dt^2} + \frac{R}{L} \frac{di}{dt} + \frac{1}{LC} i = \frac{1}{L} \frac{du_e}{dt}. \quad (1.8)$$

Which can be written in harmonic notation as:

$$\frac{i}{u_e} = \frac{\frac{1}{L} j\omega}{-\omega^2 + \frac{R}{L} j\omega + \frac{1}{LC}}. \quad (1.9)$$

To simplify and generalize further notation, we define the decay time of the resonator and its resonant angular frequency as:

$$\frac{1}{\tau} = \frac{R}{2L}, \quad (1.10)$$

$$\text{and } \omega_0 = \sqrt{\frac{1}{LC} - \frac{R^2}{4L^2}}. \quad (1.11)$$

The resonance frequency ω_0 is not to be confused with the *natural* frequency of a resonator $\omega_n = \frac{1}{\sqrt{LC}}$ which is the resonance frequency of the undamped oscillator.

1.1.4 Differential equation for the mode amplitude

To compare our result with TDCMT, we can define the mode amplitude a for a RLC resonator. Indeed the energy in such a resonator is stored in the capacitance and in the inductor, and the total stored energy is:

$$E = \frac{1}{2}Cu_c^2 + \frac{1}{2}Li^2. \quad (1.12)$$

Therefore, we can write the mode amplitude as

$$a = \sqrt{\frac{C}{2}}u_c - j\sqrt{\frac{L}{2}}i. \quad (1.13)$$

Without assumption on the quality factor of the mode, the differential equation in terms of mode amplitude of a RLC resonator is

$$\frac{d^2a}{dt^2} + \frac{R}{L} \frac{da}{dt} + \frac{1}{LC}a = \frac{j}{\sqrt{2L}} \left(\frac{du_e}{dt} + j\frac{1}{\sqrt{LC}}u_e \right). \quad (1.14)$$

This differential equation shows very little resemblance with equation (1.1). However, it can be expressed in the frequency domain as:

$$\frac{a}{u_e} = \frac{j(\omega + \frac{1}{\sqrt{LC}})}{-\omega^2 + j\omega\frac{R}{L} + \frac{1}{LC}} \frac{j}{\sqrt{2L}}. \quad (1.15)$$

Which can be rewritten as:

$$\frac{a}{u_e} = \frac{j(\omega + \omega_n)}{(j(\omega - \omega_0) + \frac{1}{\tau})(j(\omega + \omega_0) + \frac{1}{\tau})} \kappa', \quad (1.16)$$

Where $\kappa' = \frac{j}{\sqrt{2L}}$. In this expression we can check the consistency of our model with TDCMT. Indeed, if we assume a large quality factor, i.e. $\frac{1}{\tau} \ll \omega_0$, and that we only look around the resonance frequency, then $\omega_n \simeq \omega_0$ and $(j(\omega + \omega_0) + \frac{1}{\tau}) \simeq j(\omega + \omega_0)$. In that case, the expression for a becomes

$$\frac{a}{u_e} = \frac{\kappa'}{j(\omega - \omega_0) + \frac{1}{\tau}'}, \quad (1.17)$$

which is the harmonic notation of equation (1.1) from TDCMT. Hence we confirmed that our approach is consistent with the widely used TDCMT[30, 33, 34].

1.2 Reflection and transmission coefficients from the RLC model

In the case of a SRR in the THz domain, we do not have access to the current and voltage inside the circuit. To link the transfer function (1.9) to the result of a spectroscopy experiment, we need to derive the transmission and reflection coefficient.

We consider the resonator as a two port system, where s_{1+} is the amplitude of the incident wave, s_{1-} is the reflected wave, and s_{2-} is the transmitted wave (see figure 1.3). We assume that the resonator is illuminated from one side only, hence $s_{2+} = 0$. All the amplitudes are normalized such that their squared modulus is equal

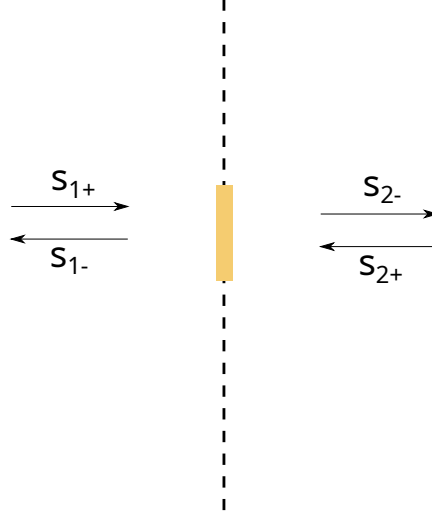


Figure 1.3: Schematic of the resonator as a two port system. The resonator is approximated as a planar structure, hence all the coefficients and their phases are expressed from a single reference plane (dashed line).

to the wave power. Equation (1.8) gives us the current in the loops i as a function of the input voltage u_e . To derive the reflection and transmission formula, we must link those two variables to the amplitudes of the external propagating waves. The coupling between the SRR and the far-field is represented by the radiative resistance R_r . By definition of R_r , the total radiated power from the SRR is $W_{\text{out}} = R_r i^2$, but we need to distinguish between the power emitted forward and backward. Let R_1 and R_2 be the radiative resistances representing respectively the backward and forward emission¹, such that $R_r = \frac{1}{2}(R_1 + R_2)$. The amplitudes of the backward and forward propagating waves emitted from the resonator are:

$$s_{1\text{out}} = i\sqrt{R_1}e^{j\theta_1}, \quad (1.18)$$

$$s_{2\text{out}} = i\sqrt{R_2}e^{j\theta_2}, \quad (1.19)$$

Where θ_1 and θ_2 are the phase differences between the current and the outgoing waves.

1.2.1 Transmission and reflection on resonator in a homogeneous lossless medium

When the resonator is embedded in a homogeneous lossless medium, there is no reflection or absorption outside of the resonance. We have

$$s_{1-} = i\sqrt{R_1}e^{j\theta_1}, \quad (1.20)$$

$$s_{2-} = s_{1+} + i\sqrt{R_2}e^{j\theta_2}. \quad (1.21)$$

Since the transmitted power cannot be larger than the incident power, we see from (1.21) that the value θ_2 is not arbitrary. The conditions on the coupling parameters will be discussed in the next subsection.

¹The definition of R_1 and R_2 is chosen to fulfill the relation (1.29), for consistency with TDCMT[30, 34]

Symmetrically, the power injected in the resonator from the incident wave is also proportional to the radiative resistance, hence the voltage induced by the incident wave s_{1+} is

$$u_e = s_{1+} \sqrt{R_1} e^{j\theta_1}. \quad (1.22)$$

We can thus express the transmission and reflection coefficients by combining (1.9), (1.20), (1.21) and (1.22)[30]:

$$t = \frac{s_{2-}}{s_{1+}} = 1 + \frac{\frac{1}{L}j\omega}{-\omega^2 + \frac{R_0+R_r}{L}j\omega + \frac{1}{LC}} \sqrt{R_1 R_2} e^{j(\theta_2+\theta_1)}, \quad (1.23)$$

$$r = \frac{s_{1-}}{s_{1+}} = \frac{\frac{1}{L}j\omega}{-\omega^2 + \frac{R_0+R_r}{L}j\omega + \frac{1}{LC}} R_1 e^{2j\theta_1} \quad (1.24)$$

To express those coefficients with more generic quantities, we define the decay rates of the resonator as:

$$\frac{1}{\tau_0} = \frac{R_0}{2L'} \quad (1.25)$$

$$\frac{1}{\tau_e} = \frac{R_r}{2L'} \quad (1.26)$$

$$\frac{1}{\tau_1} = \frac{R_1}{2L'} \quad (1.27)$$

$$\frac{1}{\tau_2} = \frac{R_2}{2L'}. \quad (1.28)$$

By definition of R_1 and R_2 , we have the relation

$$\frac{2}{\tau_e} = \frac{1}{\tau_1} + \frac{1}{\tau_2}. \quad (1.29)$$

Thus

$$t = 1 + \frac{2j\omega}{\left(j(\omega - \omega_0) + \frac{1}{\tau_0} + \frac{1}{\tau_e}\right) \left(j(\omega + \omega_0) + \frac{1}{\tau_0} + \frac{1}{\tau_e}\right)} \frac{1}{\sqrt{\tau_1 \tau_2}} e^{j(\theta_1+\theta_2)}, \quad (1.30)$$

$$r = \frac{2j\omega}{\left(j(\omega - \omega_0) + \frac{1}{\tau_0} + \frac{1}{\tau_e}\right) \left(j(\omega + \omega_0) + \frac{1}{\tau_0} + \frac{1}{\tau_e}\right)} \frac{1}{\tau_1} e^{2j\theta_1}. \quad (1.31)$$

To simplify the notation in the following calculations, let us set

$$H(j\omega) = \frac{2j\omega}{\left(j(\omega - \omega_0) + \frac{1}{\tau_0} + \frac{1}{\tau_e}\right) \left(j(\omega + \omega_0) + \frac{1}{\tau_0} + \frac{1}{\tau_e}\right)}. \quad (1.32)$$

When the resonator is a planar structure embedded in a homogeneous lossless medium, the system is fully symmetrical. Thus we have $\tau_1 = \tau_2 = \tau_e$, $\theta_1 = \theta_2 = \theta$ and

$$t = 1 + H(j\omega) \frac{1}{\tau_e} e^{2j\theta}, \quad (1.33)$$

$$r = H(j\omega) \frac{1}{\tau_e} e^{2j\theta}. \quad (1.34)$$

1.2.2 General conditions on the coupling parameters for a SRR on a substrate

We have considered the special case where the resonator is floating in a medium with a homogeneous index. However, SRR in the THz range are almost always fabricated on a substrate, and are therefore located right at the interface between two media. This interface has its own reflection and transmission coefficients. Fan et al. showed in the case of TDCMT how the direct pathway between the ports affects the coupling parameter of the resonator [34]. The conditions on the coupling parameters arise from energy conservation and time reversal symmetry. We already took into account the energy conservation in equation (1.22) by using the same coupling constant for the energy injected in the resonator as for the energy emitted from the resonator. Although we are not exactly in the conditions of TDCMT, the reasoning used in [34] only requires that, without external excitation, the mode of the resonator decays exponentially into the ports, which remains true in our case.

We define the scattering matrix S of the system as

$$\begin{pmatrix} s_{1-} \\ s_{2-} \end{pmatrix} \equiv S \begin{pmatrix} s_{1+} \\ s_{2+} \end{pmatrix}. \quad (1.35)$$

Hence the coefficients of this matrix are the reflection and transmission coefficients for the forward and backward propagating waves. This scattering matrix can be expressed as:

$$S = C_d + H(j\omega) \begin{pmatrix} \frac{1}{\tau_1} e^{2j\theta_1} & \frac{1}{\sqrt{\tau_1 \tau_2}} e^{j(\theta_1 + \theta_2)} \\ \frac{1}{\sqrt{\tau_1 \tau_2}} e^{j(\theta_1 + \theta_2)} & \frac{1}{\tau_2} e^{2j\theta_2} \end{pmatrix}, \quad (1.36)$$

where C_d is the scattering matrix of the direct pathway between the ports. Time reversal symmetry of the system imposes that the matrix C_d and the coupling constants fulfill the following conditions[34]:

$$C_d \begin{pmatrix} \frac{1}{\sqrt{\tau_1}} e^{-j\theta_1} \\ \frac{1}{\sqrt{\tau_2}} e^{-j\theta_2} \end{pmatrix} = - \begin{pmatrix} \frac{1}{\sqrt{\tau_1}} e^{j\theta_1} \\ \frac{1}{\sqrt{\tau_2}} e^{j\theta_2} \end{pmatrix}. \quad (1.37)$$

In the case of the interface between two lossless media with different refractive indices, the matrix C_d is explicitly known from Fresnel equations. For the reflection and transmission coefficient involving a lossy medium, using Fresnel equations with the complex refractive indices does *not* give physically correct coefficients and break the conservation of energy[35–37]. Adapting our models to work with lossy substrate will be the subject of a future work.

At normal incidence, we have the reflection and transmission coefficient

$$r_d = \frac{n_1 - n_2}{n_1 + n_2}, \quad (1.38)$$

$$\text{and } t_d = \frac{2\sqrt{n_1 n_2}}{n_1 + n_2}, \quad (1.39)$$

where n_1 and n_2 are the respective refractive indices of the media. Here the variable s_{1+} and s_{2-} are defined such that their modulus squared are the power of the incident and transmitted beam, hence why the expression for t_d is different from the

Fresnel transmission usually written for the electric field amplitude. Thus

$$C_d = \begin{pmatrix} r_d & t_d \\ t_d & -r_d \end{pmatrix}, \quad (1.40)$$

with $r_d^2 + t_d^2 = 1$. For a planar structure like a SRR, the continuity of the transverse electric field imposes that the phase of the field radiated on each side of the interface are in phase in the plane of the interface, thus

$$\theta_1 = \theta_2 \equiv \theta. \quad (1.41)$$

Solving (1.37) with (1.40) and (1.41), we get the conditions on the coupling parameters:

$$\frac{\tau_1}{\tau_2} = \left(\frac{1 - r_d}{t_d} \right)^2 = \frac{n_2}{n_1}, \quad (1.42)$$

$$e^{2j\theta} = -1. \quad (1.43)$$

Combining (1.42) and (1.29) we can express the forward and backward radiative decay rate as a function of the total radiative decay rate and the refractive indices:

$$\frac{1}{\tau_1} = \frac{2n_1}{n_1 + n_2} \frac{1}{\tau_e}, \quad (1.44)$$

$$\frac{1}{\tau_2} = \frac{2n_2}{n_1 + n_2} \frac{1}{\tau_e}. \quad (1.45)$$

Finally, injecting (1.40), (1.43), (1.44) and (1.45) in (1.36), we get the formula for the reflection and transmission coefficient of a single mode resonator on an interface:

$$r = \frac{n_1 - n_2}{n_1 + n_2} - \frac{\frac{1}{\tau_e} 2j\omega}{\left(j(\omega - \omega_0) + \frac{1}{\tau_0} + \frac{1}{\tau_e} \right) \left(j(\omega + \omega_0) + \frac{1}{\tau_0} + \frac{1}{\tau_e} \right)} \frac{2n_1}{n_1 + n_2}, \quad (1.46)$$

$$t = \frac{2\sqrt{n_1 n_2}}{n_1 + n_2} \left(1 - \frac{\frac{1}{\tau_e} 2j\omega}{\left(j(\omega - \omega_0) + \frac{1}{\tau_0} + \frac{1}{\tau_e} \right) \left(j(\omega + \omega_0) + \frac{1}{\tau_0} + \frac{1}{\tau_e} \right)} \right). \quad (1.47)$$

For applications, it is also useful to write the coefficients for the electric field amplitude, in that case, the transmission coefficient of the interface alone is $t_{df} = \frac{2n_1}{n_1 + n_2}$ while the reflection coefficient stays the same ($r_{df} = r_d$), therefore

$$r_f = r_d - \frac{\frac{1}{\tau_e} 2j\omega}{\left(j(\omega - \omega_0) + \frac{1}{\tau_0} + \frac{1}{\tau_e} \right) \left(j(\omega + \omega_0) + \frac{1}{\tau_0} + \frac{1}{\tau_e} \right)} t_{df}, \quad (1.48)$$

$$t_f = t_{df} \left(1 - \frac{\frac{1}{\tau_e} 2j\omega}{\left(j(\omega - \omega_0) + \frac{1}{\tau_0} + \frac{1}{\tau_e} \right) \left(j(\omega + \omega_0) + \frac{1}{\tau_0} + \frac{1}{\tau_e} \right)} \right). \quad (1.49)$$

We notice in this formulation that the separate decay rates $\frac{1}{\tau_1}$ and $\frac{1}{\tau_2}$ are replaced by a single coupling factor $\frac{1}{\tau_e} t_{df}$. This result, derived with the general method of Fan et al.[34] is consistent with the continuity of the transverse electric field at an interface.

1.2.3 Overall transmission of a SRR on a finite substrate

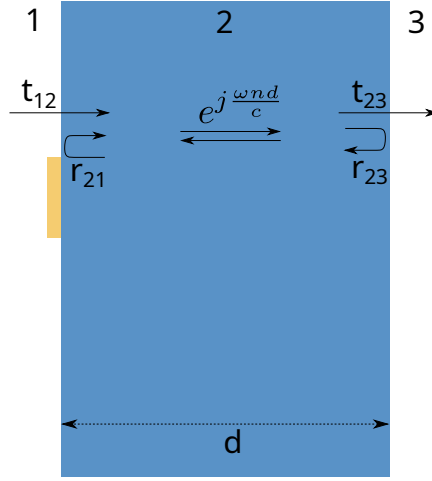


Figure 1.4: Illustration of the transmission, reflection and propagation involved in the transmission of a resonator on a substrate of thickness d and refractive index n .

We have calculated the transmission and reflection coefficient for a SRR at the interface between two media. To compare the model with the experiment, we need to calculate the overall transmission on a substrate with a finite thickness, as illustrated in figure 1.4. The two partially reflective sides of a substrate creates a Fabry-Pérot cavity that affects the transmission. The total transmitted field is the sum of the infinitely many possible paths inside the substrate. The propagation inside the substrate induces a delay represented in the frequency domain by the coefficient $e^{j\frac{\omega nd}{c}}$, where $n = \sqrt{\epsilon}$ is the refractive index of the substrate, and d is the thickness of the substrate. The sum of all possible transmission paths is written as

$$t_{\text{total}} = t_{12}t_{23}e^{j\frac{\omega nd}{c}} \sum_{k=0}^{\infty} \left(r_{23}r_{21}e^{2j\frac{\omega nd}{c}} \right)^k = \frac{t_{12}t_{23}e^{j\frac{\omega nd}{c}}}{1 - r_{23}r_{21}e^{2j\frac{\omega nd}{c}}}, \quad (1.50)$$

where t_{ij} (respectively r_{ij}) is the transmission (reflection) coefficient from medium i to j (see figure 1.4). Using the coefficients from equation (1.46) and (1.47) for t_{12} and r_{21} , and the Fresnel coefficients for t_{23} and r_{23} , we calculate the overall transmission coefficient expected from the THz-TDS measurement. Figure 1.5 shows the calculated transmission coefficient for a resonator without substrate, the transmission from the same resonator on a 150 μm thick quartz substrate, and the same transmission normalized with the transmission of the bare quartz substrate. The coupling constant used for this example is $\frac{1}{\tau_c} = 4.6 \times 10^9 \text{ s}^{-1}$. This value is deliberately low and corresponds to what we can expect from a single SRR as opposed to an array of resonators as seen in chapter 4. With such a low coupling constant, the resonance is almost invisible in comparison with the Fabry-Pérot interference from the substrate. One can recover the resonance spectrum by dividing the spectrum by the transmission coefficient of the bare substrate. Figure 1.5 shows that the amplitude of the resonance is unaffected, but the line takes an asymmetric shape.

Starting from the RLC model, we derived the transmission and reflection coefficients expected from a SRR fabricated on a dielectric substrate. Our model does not require prior assumption on the quality factor of the mode, and takes into account the multiple reflections in the substrate. In chapter 4, we will use this model

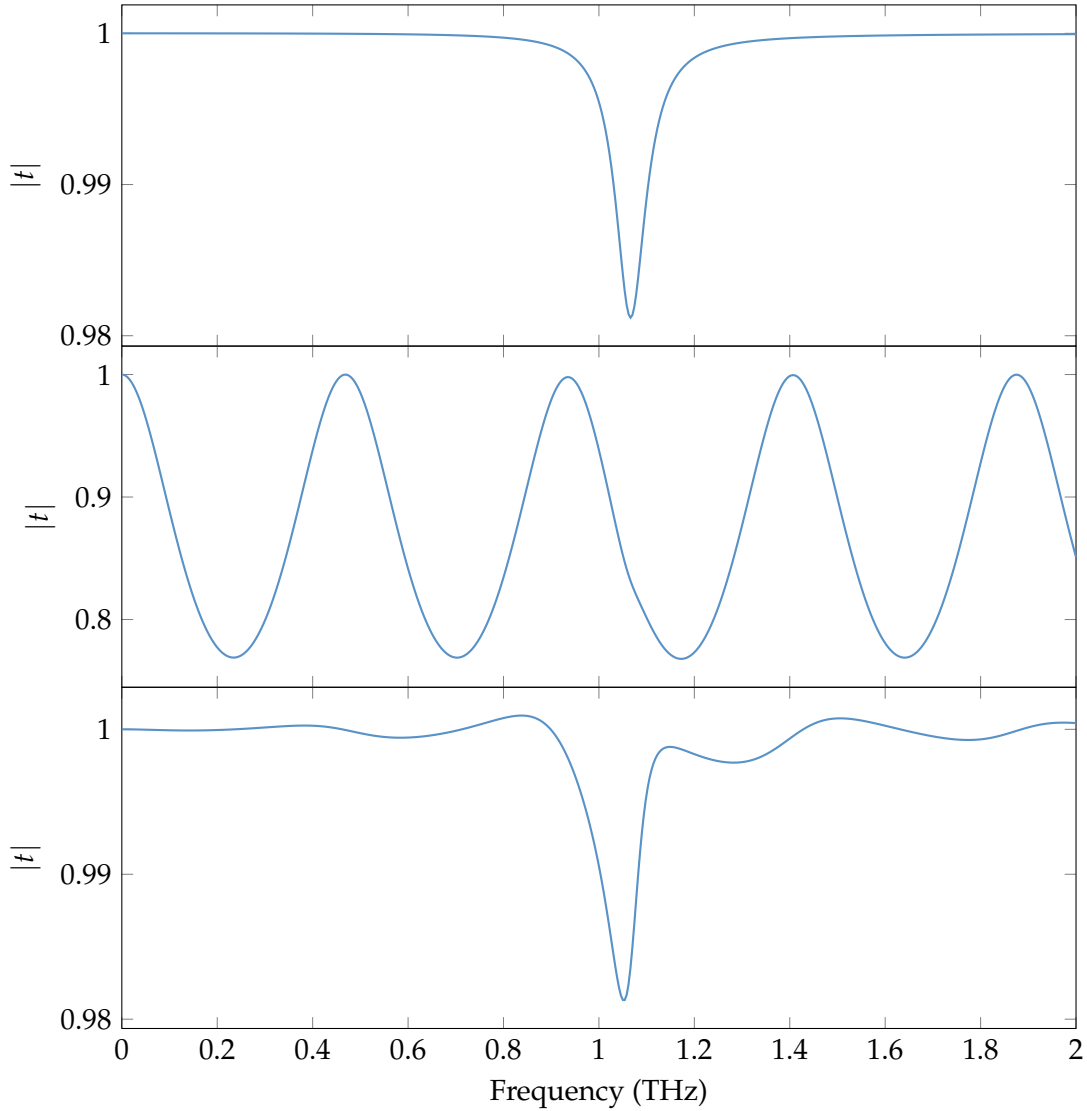


Figure 1.5: Transmission spectra of a resonator with a weak coupling constant $\frac{1}{\tau_e} = 4.6 \cdot 10^9$. **Top:** Transmission coefficient without substrate. **Middle:** Transmission coefficient for the same resonator on a 150 μm thick quartz substrate. **Bottom:** Transmission on substrate normalized with the transmission of the substrate without resonators. The frequency shift caused by the substrate higher refractive index is not taken into account in this figure and will be discussed in [1.3.4](#)

to fit the experimental transmission spectrum measured with THz-TDS to evaluate its validity and extract the parameter of our SRRs.

1.3 Coupling of the resonator with a material

Until now, we have presented analytical tools to predict and characterize the behavior of a SRR. Our motivation is to use the strong field confinement provided by a SRR to extract information about a material placed in its gap.

1.3.1 Influence of the refractive index

SRRs and more generally resonant metasurfaces have been used to detect changes in the medium refractive index[20, 23–25, 38].

In the previous sections, we defined the resonator parameters as

$$\frac{1}{\tau_i} = \frac{R_i}{2L'}, \quad (1.51)$$

$$\text{and } \omega_0 = \sqrt{\frac{1}{LC} - \frac{R^2}{4L^2}}. \quad (1.52)$$

where C is the capacitance of the gap. The value of this capacitance depends on the geometry of the gap and on the permittivity of the surrounding material. For example in the case of a parallel plate capacitance, we have: $C = \frac{A}{d}\epsilon\epsilon_0$ where A is the area of the plates, d is the distance between them, ϵ is the relative permittivity of the material between the plates and ϵ_0 is the vacuum permittivity. More generally, the capacitance of any capacitor is expressed as $C = \alpha_G\epsilon\epsilon_0$ where α_G depend on the geometry of the capacitor.

For a RLC resonator with a high quality factor, such that $\omega_0 = \omega_n = \frac{1}{\sqrt{LC}}$, we have

$$\omega_0 = \frac{1}{n} \frac{1}{\sqrt{L\alpha_G\epsilon_0}}, \quad (1.53)$$

where $n = \sqrt{\epsilon}$ is the refractive index of the medium. Hence the rate of change of the resonance frequency in regard to the medium refractive index is

$$\frac{d\omega_0}{dn} = -\frac{1}{n^2} \frac{1}{\sqrt{L\alpha_G\epsilon_0}} = -\frac{\omega_0}{n}. \quad (1.54)$$

This means that the variation in the resonance frequency is independent from the resonator geometry, as long as the capacitance is entirely submerged in the material of interest. However, this last condition is usually not fulfilled, which requires using an effective permittivity which is itself dependent on the geometry. This point is discussed in section 1.3.4.

1.3.2 Capacitance fully filled with a dispersive material

Beside refractive index measurements, one of the main goals of THz spectroscopy is to detect and identify resonance mode in a material. Such resonances are characterized by dispersion in the material permittivity.

In this section, we study how the presence of a dispersive material inside the capacitance of a SRR affects the transmission and reflection coefficient.

In that case, if we consider a dispersive material, i.e. with ϵ complex and frequency dependent, the capacitance C becomes itself complex and frequency dependent, but the harmonic notation of equation (1.6) ($i = jC\omega u_c$) still holds true, and so does the subsequent formulas for the reflection and transmission. Typically, if the permittivity of the material in the gap follow a Lorentz model, we have

$$\epsilon_l = \epsilon_\infty + \frac{\Delta\epsilon\omega_l^2}{\omega_l^2 + j\gamma\omega - \omega^2}, \quad (1.55)$$

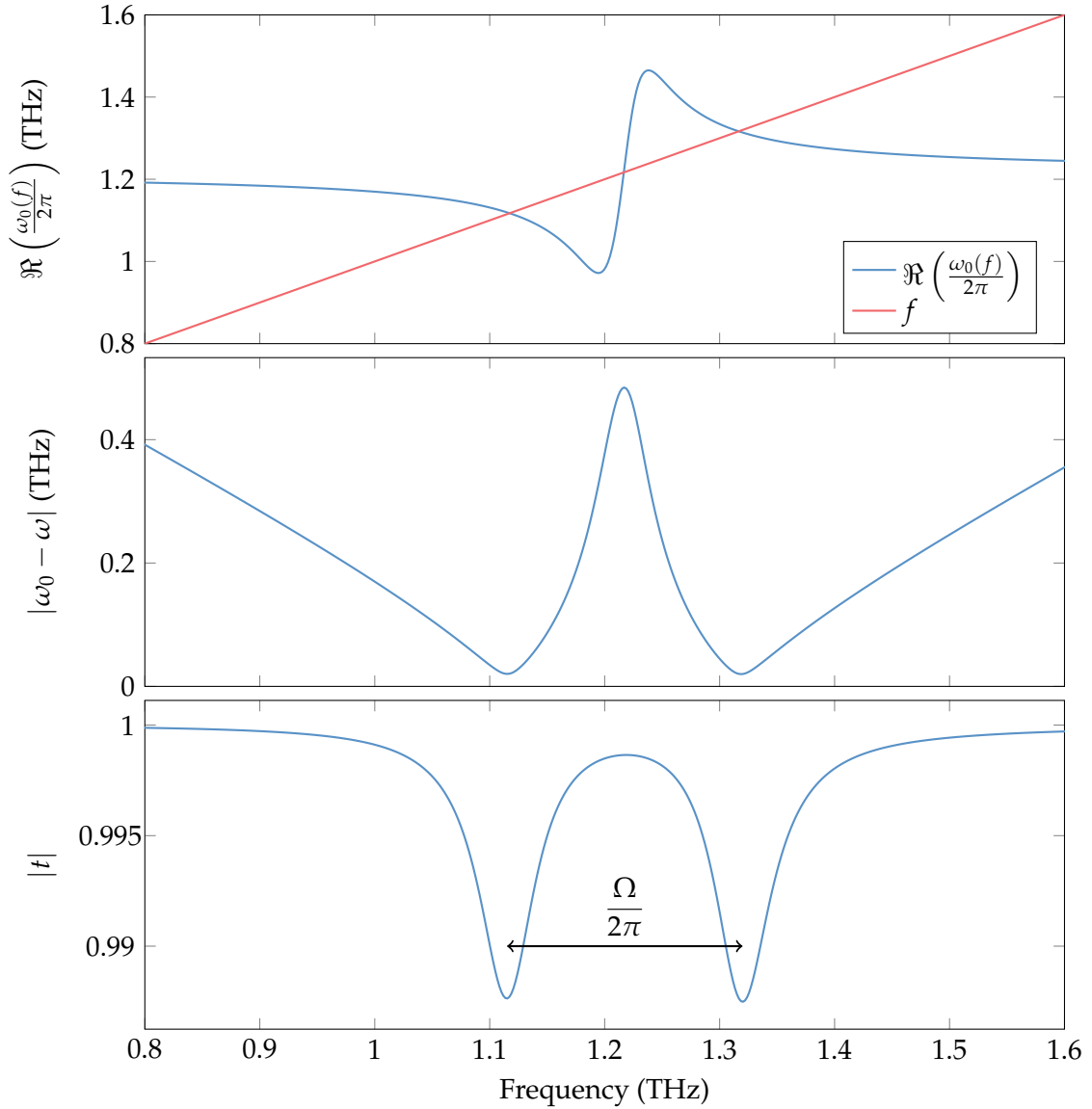


Figure 1.6: **Top:** Predicted resonance frequency from equation (1.11) for a RLC resonator with a capacity entirely filled with Glutamic Acid versus frequency. Despite the real part of the frequency crossing three times, $|\omega_0 - \omega|$ only has two minima (**middle**), which are coincident with the resonances seen in the transmission without substrate (**bottom**).

where ε_∞ is the permittivity at high frequency, $\Delta\varepsilon$ is the Lorentz oscillator strength, ω_l is the resonant frequency of the oscillator, and γ is the linewidth of the mode. In that case H becomes a fourth order transfer function, meaning that the resonator can have up to two resonance modes. For a regular single mode resonator, the resonance angular frequency is ω_0 . In the case of the coupled resonator, ω_0 as defined in (1.11) is not a constant, but instead a frequency dependent variable. Nonetheless, it is still possible to predict the resonant frequencies by looking at the solutions of the equation

$$\omega = \omega_0(\omega). \quad (1.56)$$

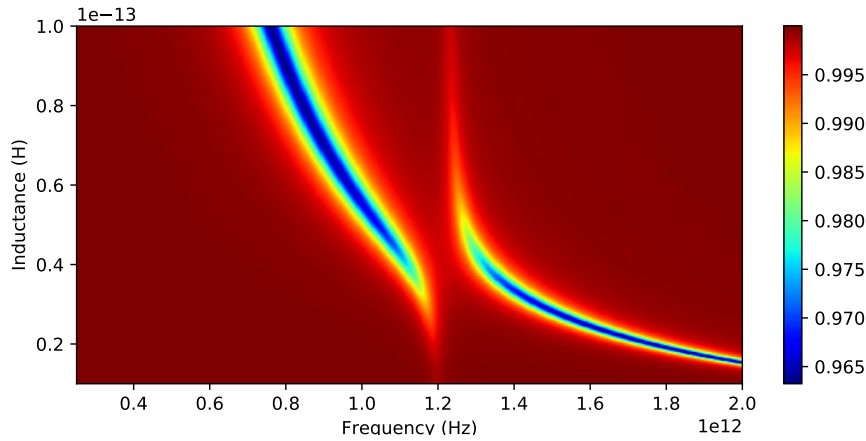


Figure 1.7: Transmission spectrum of a resonator without substrate coupled with Glutamic Acid, for different inductance values, showing the anti-crossing pattern.

If the lorentzian resonance is infinitely thin, i.e. the permittivity is a step function, then when $\omega < \omega_1$ (respectively $\omega > \omega_1$) the resonator behaves as a single mode RLC resonator with a resonance frequency $\omega_1 = \omega_0(\varepsilon = \varepsilon_\infty + \Delta\varepsilon)$ ($\omega_2 = \omega_0(\varepsilon = \varepsilon_\infty)$). Which means there are two distinct resonances under the following condition: $\omega_1 < \omega_1 < \omega_2$. With a more realistic material, equation (1.56) does not have any exact real solution since ω_0 is a complex number. Nonetheless looking at the real part of $\omega_0 - \omega$ still gives an intuitive idea of the resonances. Figure 1.6 shows an example with Lorentz parameter extracted from measurement on Glutamic Acid (see section 4.4.1). In this example, one can see that the real part of ω_0 crosses ω three times, but only two crossing correspond to actual minima of $|\omega - \omega_0|$ due to the high dielectric losses. Figure 1.6 shows that the two minima of $|\omega - \omega_0|$ are coincident with minima in the transmission coefficient of the resonator. It is easy to see with the graph of $\omega_0(\omega)$ that the system has two resonances only when the resonance frequency of the RLC with a fixed capacitor is close to the Lorentz resonance of the material. This behavior is consistent with what is expected from two strongly coupled oscillators, here being a RLC and the vibration in the material. The anticrossing behavior of the coupled system is better illustrated in figure 1.7, with the transmission spectrum calculated for multiple inductance values.

1.3.3 Interpretation with strong coupling theory

In the previous subsection, we used the RLC model to describe a single mode resonator coupled with a Lorentz resonator, and predicted a splitting of its fundamental mode. Such a system is commonly described in the literature as light matter strong coupling[39, 40]. Two oscillators are considered strongly coupled when the energy exchange rate between them is higher than the energy dissipation rate of the system[41]. This coupling regime is recognizable when both oscillators are tuned at the same frequency by the existence of two hybrid modes separated by the Rabi splitting frequency Ω . Since the coupled system in our model is described by a fourth order transfer function, it is technically possible to extract analytical value for its roots and poles, and consequently for the resonance frequency. However, this approach does not lead to any usable result without strong approximations. We can nonetheless extract numerically the exchange rate between the resonators directly

from the transmission coefficient. In the example shown in figure 1.6, based on glutamic acid, we have $\frac{\Omega}{2\pi} \simeq 205$ GHz. And the normalized Rabi frequency is $\frac{\Omega}{\omega_l} \simeq 0.17$ which means the system is actually in the ultra-strong coupling regime[42], usually defined by the criteria $\frac{\Omega}{\omega_l} > 0.1$.

In this regime, the coupled oscillator model predicts that the Rabi splitting frequency is given by [1, 43–47]:

$$\Omega = 2\sqrt{\left(\frac{V}{\hbar}\right)^2 - \frac{1}{16}\left(\gamma - \frac{2}{\tau}\right)^2}, \quad (1.57)$$

where V is the interaction energy between the electric field in the resonator and dipole moment of the material, and γ and $\frac{2}{\tau}$ are the respective linewidth of the Lorentz resonance and SRR resonance. The interaction energy V is given by:

$$V = d\sqrt{\frac{\hbar\omega_l N}{2\varepsilon_0\varepsilon_\infty v}} \quad (1.58)$$

where d is the transition dipole of each molecule, v is the volume of the mode, and N is the number of molecules coupled with the SRR mode. When the capacitor of the SRR is fully filled, the ratio $\frac{N}{v}$ is simply the molecular density of the material, in the case of glutamic acid, $\frac{N}{v} = 5.976 \times 10^{27} \text{ m}^{-3}$. As mentioned before, the THz resonances from organic crystals such as Glutamic acid are delocalized vibrations and thus cannot be described from the vibration mode of each individual molecule[5, 48]. It is still possible to extract an effective transition dipole from the absorption of the material[49, 50]:

$$d^2 = \frac{\varepsilon_0 \hbar c n_\infty}{4\pi\omega_l} \gamma \sigma, \quad (1.59)$$

where ε_0 is the vacuum permittivity, c is the speed of light in vacuum, $n_\infty = \sqrt{\varepsilon_\infty}$ and σ is the maximum absorption cross section of one molecule at resonance. We can express the cross section as a function of the absorption coefficient α as $\sigma = \frac{\alpha}{n}$, and from Beer-Lambert law, $\alpha = \frac{4\pi\kappa\omega_l}{c}$, where κ is the imaginary part of the refractive index at resonance, extracted from the Lorentz model. Using the parameters extracted from THz-TDS measurement of glutamic acid pellets (as in figure 1.6), the coupled oscillator model predicts the Rabi frequency:

$$\frac{\Omega}{2\pi} = 195 \text{ GHz}, \quad (1.60)$$

which is in good agreement with the result of the RLC model.

By using a purely linear dispersion model, we are neglecting any saturation effect. In other words, we assume that the number of photons is much smaller than the number of Lorentz oscillators in the fundamental state. The Rabi splitting in that case corresponds to the case where there is no photon in the cavity, and is called *vacuum* Rabi splitting[40].

1.3.4 Realistic modelisation of the capacitance

We have discussed the coupling between a RLC circuit and a dispersive material when the capacitance is entirely filled with the material. However, this configuration is very difficult to achieve experimentally on a SRR. Figure 1.8 shows a more

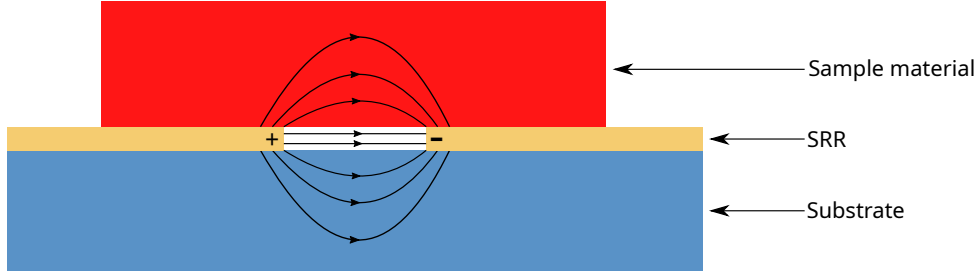


Figure 1.8: Schematic side view of the electric field lines in a SRR gap coupled with a material flake. In this configuration, each field line goes through a single material, and the gap can be modeled as three capacitors in parallel.

realistic example of what the capacitor of the SRR looks like during an experiment for measurement on a microscopic flake of dispersive material. The sample is laid on top of the SRR gap. Thus the capacitance is only partially filled with the sample material, and partially filled with air and the substrate material. Hence the value of the capacitance is a function of the permittivity of all three materials. Most importantly, the relation between the permittivities and the capacitance is strongly dependent on the geometry and position of the sample material.

Capacitance partially filled along the field lines

To study the different ways inhomogeneous permittivity can affect a capacitor, we come back to the simple case of the parallel plate capacitor. We begin with the case illustrated in figure 1.9a, where the permittivity is homogeneous along the direction of the electric field, but not along the direction orthogonal to the electric field. In that case, the part of the capacitor filled with the material of permittivity ϵ_1 and the part filled with the material of permittivity ϵ_2 are subject to the same potential difference, they can be treated as two capacitors in parallel with respective capacitance

$$C_1 = \epsilon_0 \epsilon_1 \frac{(1-F)A}{d}, \quad (1.61)$$

$$C_2 = \epsilon_0 \epsilon_2 \frac{FA}{d}, \quad (1.62)$$

where F is the filling factor of the material 2. Hence the total capacitance is given by

$$C = \epsilon_0 ((1-F)\epsilon_1 + F\epsilon_2) \frac{A}{d}. \quad (1.63)$$

This expression can be interpreted by defining the effective relative permittivity of the mixed medium as

$$\epsilon_{\text{eff,p}} = (1-F)\epsilon_1 + F\epsilon_2. \quad (1.64)$$

Capacitance partially filled across the field lines

Next we consider the case illustrated in figure 1.9b where the permittivity is inhomogeneous in the direction of the electric field, but homogeneous in the orthogonal direction. Let Q be the charge of the capacitor. The potential difference between the capacitor plates is found by integrating the electric field along a straight line between

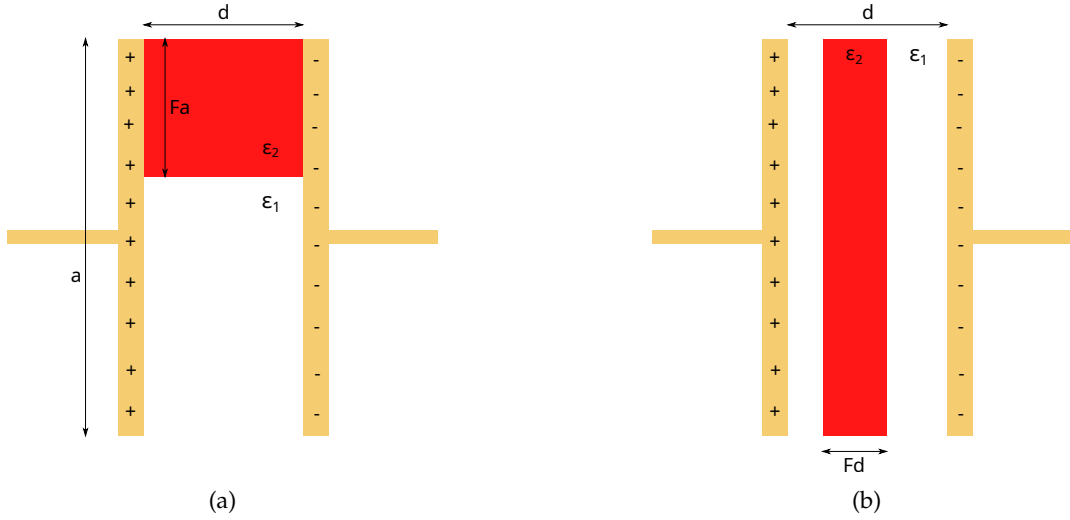


Figure 1.9: Schematic of a parallel plate capacitance partially filled with a material of relative permittivity ϵ_2 with a filling factor F . **(a)**: Inhomogeneity orthogonal to the electric field. **(b)**: Inhomogeneity along the electric field.

the two capacitor plates.

$$\Delta V = \int_0^d E(x) dx \quad (1.65)$$

We found from Gauss law that the displacement field D in a parallel plate capacitor is given by $D = \frac{Q}{A}$, and $D = \epsilon E$. Thus the electric field is uniform inside each material, and

$$\Delta V = (1 - F) \frac{dQ}{\epsilon_0 \epsilon_1 A} + F \frac{dQ}{\epsilon_0 \epsilon_2 A}. \quad (1.66)$$

We can then express the inverse of the capacitance:

$$\frac{1}{C} = \frac{\Delta V}{Q} = (1 - F) \frac{d}{\epsilon_0 \epsilon_1 A} + F \frac{d}{\epsilon_0 \epsilon_2 A}. \quad (1.67)$$

This is equivalent to two capacitors connected in series. Here the effective relative permittivity of the mixed medium is given by

$$\frac{1}{\epsilon_{\text{eff},s}} = \frac{1 - F}{\epsilon_1} + \frac{F}{\epsilon_2}, \quad (1.68)$$

$$\Rightarrow \epsilon_{\text{eff},s} = \frac{\epsilon_1 \epsilon_2}{(1 - F) \epsilon_2 + F \epsilon_1}. \quad (1.69)$$

By comparing equations (1.64) and (1.69), one can see that different ways to fill the capacitor change the nature of the relation between the effective permittivity and the properties of each material in the capacitor.

Other effective medium models

Effective Medium Models (EMMs) are designed to estimate the electromagnetic properties of a mixture of materials by defining its effective permittivity[51]. Those

models can be used to estimate the capacitance of SRR if the mixture can be approximated as homogeneous at the scale of the gap, for example when coupling the SRR with a fine powder.

A common EMM is the Maxwell-Garnett model [52, 53]. This model assumes spherical inclusions of permittivity ε_2 inside a matrix of permittivity ε_1 , and that the quantity of inclusion is small compared to the quantity of matrix material. This model is adapted to analyze a small quantity of fine powder diluted in a pellet, or aerosol particle in air. In that case, the effective permittivity of the medium is given by solving

$$\frac{\varepsilon_{\text{eff}} - \varepsilon_1}{\varepsilon_{\text{eff}} + 2\varepsilon_1} = F \frac{\varepsilon_2 - \varepsilon_1}{\varepsilon_2 + 2\varepsilon_1}, \quad (1.70)$$

where F is the volumetric filling factor of the inclusion.

To get rid of the low filling factor hypothesis, Bruggeman [53, 54] developed a model where both materials are considered as inclusion inside a matrix with permittivity ε_{eff} . The effective permittivity in this model is found for any filling factor by solving

$$(1 - F) \frac{\varepsilon_1 - \varepsilon_{\text{eff}}}{\varepsilon_1 + 2\varepsilon_{\text{eff}}} + F \frac{\varepsilon_2 - \varepsilon_{\text{eff}}}{\varepsilon_2 + 2\varepsilon_{\text{eff}}} = 0. \quad (1.71)$$

This model is however still limited to spherical inclusions, or inclusions much smaller than the electric field spatial variation, which is a strong assumption when working on a microscopic capacitor.

If the spherical assumption cannot be made, Lichtenecker and Rother [55–58] developed a more abstract model taking into account the shapes of the inclusions through a power $k \in [-1, 1]$. The effective permittivity in this model is given by

$$\varepsilon_{\text{eff}}^k = (1 - F)\varepsilon_1^k + F\varepsilon_2^k. \quad (1.72)$$

The special cases $k = 1$ and $k = -1$ are used to describe composite material made of parallel layers, and are indeed consistent with equations (1.64) and (1.69) from the parallel plate capacitor model.

Capacitor model with imperfect contact

We have presented a few models for a capacitor partially filled with a sample material. We now need to choose which one is more suitable for the geometry of our experiment. Figure 1.8 shows the ideal configuration for the experiment, where a flake of the sample material is in direct contact with the metal. If the thickness of the flake is much larger than the electric field extension, then each electric field line only goes through one material. Under this condition we treat the capacitor as three capacitors in parallel, one filled with the sample material, a second filled with air, and a third filled with the substrate material. We can therefore express the effective relative permittivity with equation (1.64), except the filling factor F is not a straightforward volume ratio, since the electric field is non uniform.

In a real experiment, where a sample flake is placed on top of the SRR with a low degree of control, the contact between the SRR and the flake is likely to be imperfect. Figure 1.10a shows a schematic view of the imperfect contact. The permittivity is no longer uniform along each field line. We model this imperfection by using two distinct filling factors F_p and F_s representing respectively the filling factor along the direction of the field lines, and the orthogonal the field lines. The meaning of F_p and F_s

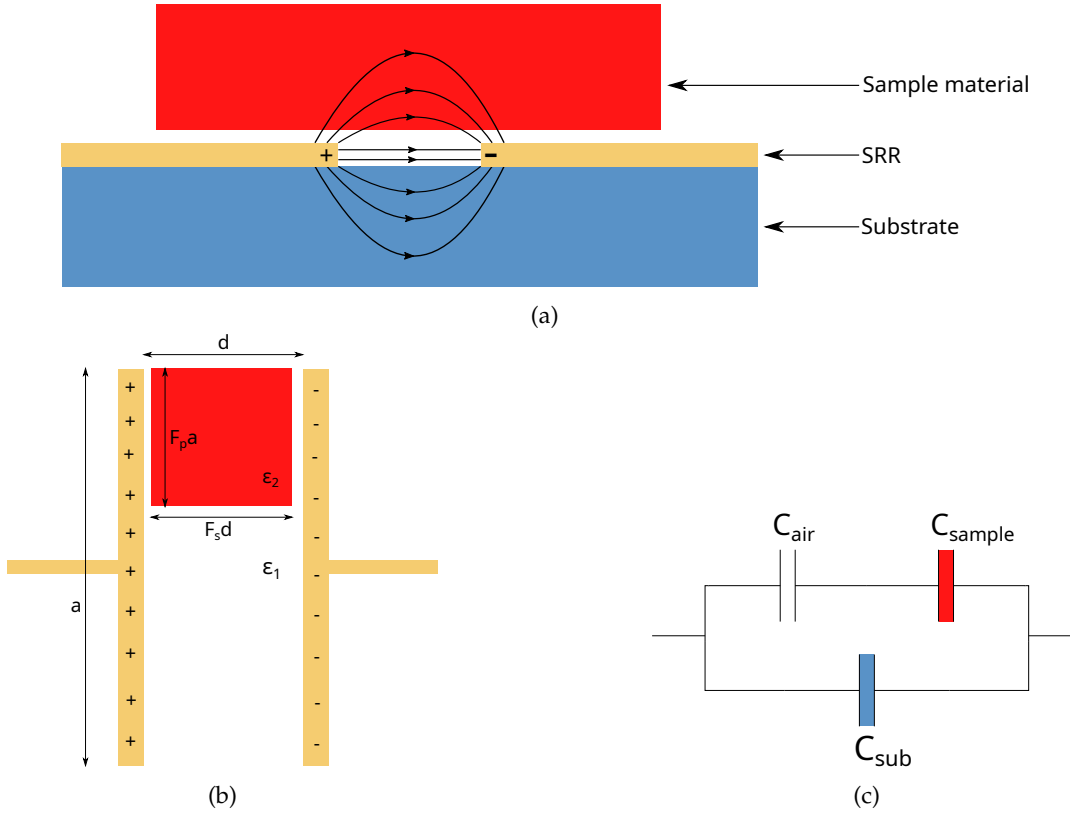


Figure 1.10: **(a)**: Schematic view of an imperfectly placed sample. **(b)**: Parallel plate capacitor model with the geometrical definition of F_p and F_s . **(c)**: Equivalent circuit with three capacitors representing the sample, the air gap and the substrate.

for a parallel plate capacitor is illustrated in figure 1.10b. Neglecting fringing fields, figure 1.10b is equivalent to three capacitors connected as shown in figure 1.10c.

The equivalent capacitance of figure 1.10c is

$$C_{\text{eff}} = C_{\text{sub}} + \frac{C_{\text{air}} C_{\text{sample}}}{C_{\text{air}} + C_{\text{sample}}}. \quad (1.73)$$

The equivalent relative permittivity is given by

$$\epsilon_{\text{eff}} = (1 - F_p) \epsilon_{\text{sub}} + F_p \frac{\epsilon_{\text{air}} \epsilon_{\text{sample}}}{(1 - F_s) \epsilon_{\text{sample}} + F_s \epsilon_{\text{air}}}. \quad (1.74)$$

Figure 1.11 shows ϵ_{eff} versus F_s for a fixed value of $F_p = 0.5$, with a sample permittivity $\epsilon_{\text{sample}} = 10$ and a quartz substrate with permittivity $\epsilon_{\text{sub}} = 4.1$. The graph shows a steep slope when F_s is almost 1. This means that even a small air gap greatly reduces the coupling between the resonator and the flake.

Figure 1.12 shows the expected transmission spectra for different values of F_s and F_p . The case $F_s = F_p = 1$ correspond to a capacitor entirely filled with the sample material, identical to figure 1.6. The two cases with $F_p = 0.5$ both correspond to realistic configurations, since the substrate takes about half of the capacitance, while F_s can take a large range of values depending on how the sample material happens to land on the SRR. Finally, the case $F_s = F_p = 0.3$ corresponds to a weak coupling configuration where the splitting disappears and is replaced by a single slightly distorted line. As expected from strong coupling theory, the Rabi splitting

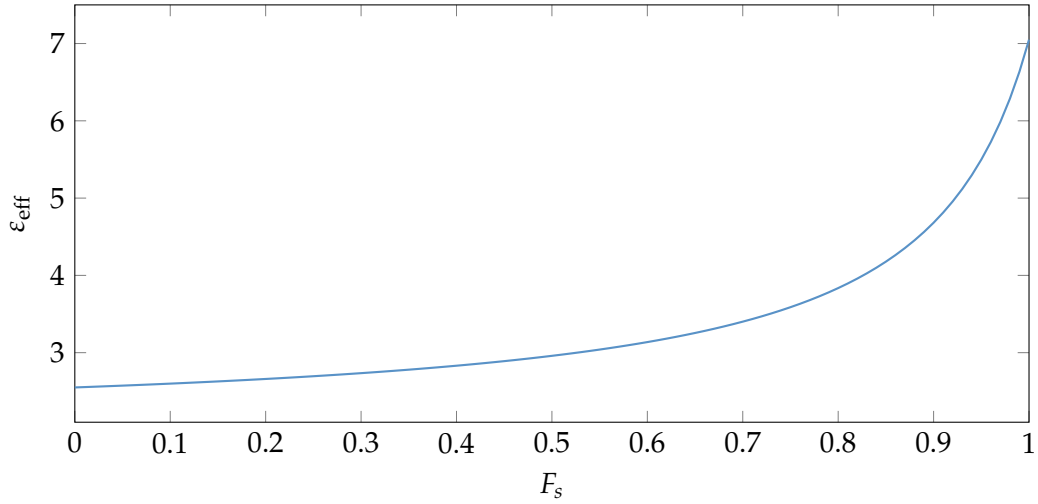


Figure 1.11: ϵ_{eff} as a function of F_s with $\epsilon_{\text{sample}} = 10$, $\epsilon_{\text{sub}} = 4.1$, $\epsilon_{\text{air}} = 1$ and $F_p = 0.5$.

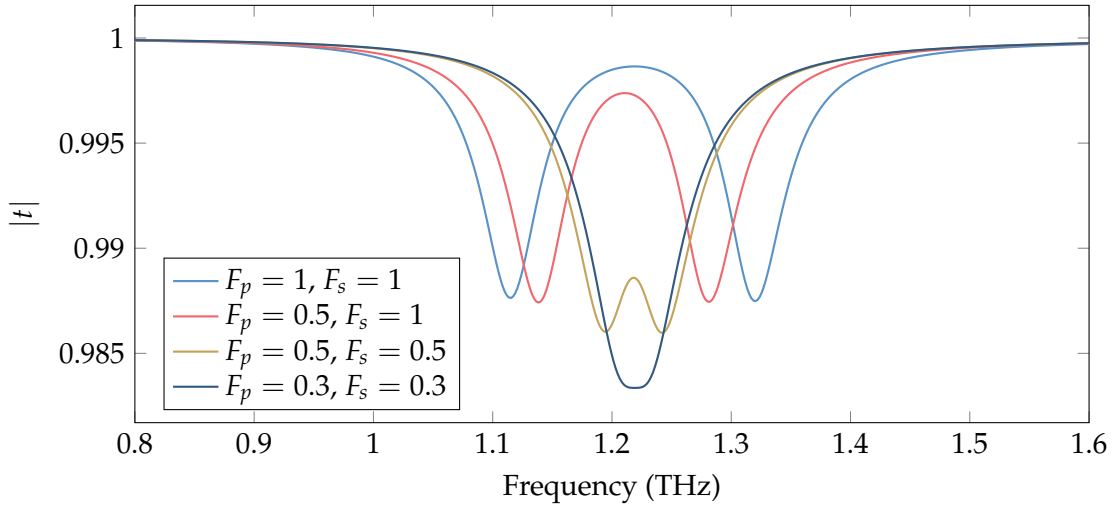


Figure 1.12: Expected transmission for a SRR coupled with Glutamic acid for different filling factors. The inductance of the SRR is adjusted to keep the SRR in tune with the Lorentz resonance.

frequency Ω decreases as the filling factors decrease. The main takeaway from this figure 1.12 is the fact that the shape of the spectrum varies significantly for different values of F_s , which means that an experimental measurement on a large array of SRRs coupled with a sample material will result in a blurry average between spectra with all kind of different F_s value, unless one of the following conditions is met:

- The coupling with the sample material is perfectly identical for each SRR. This condition is met for example if the sample material is the substrate itself, or the surrounding medium.
- The measurement is done on a single resonator instead of an array.

Since our goal is the measurement of microscopic amounts of sample material, the first condition is virtually impossible to fulfill. Far-field measurements on single

SRRs in the THz domain are rare in the literature, but Rajabali et al. recently demonstrated the feasibility of such an experiment with THz-TDS[59]. Hence why we will perform all our coupling experiments on single SRRs.

1.4 Further improvements

We have gathered a set of tools to interpret as accurately as possible the data from TDS measurement on a resonator coupled with a dispersive material. We focused mainly on the coupling with a material following a Lorentz dispersion, but the model is usable with any dispersion model, or even tabulated data. We discussed how small differences in the sample material position can strongly affect the final measurement, and the subsequent necessity of measuring single resonators if the positioning of the sample is not perfectly reproducible.

Because the model is entirely expressed in physically meaningful variables, more accurate descriptions of those values can be implemented to make the model more accurate. Indeed we briefly mentioned in 1.1.2 that some of the physical values that were implicitly considered as constant could actually be frequency dependent. This is the case of the radiative resistance R_r which is well known for being highly frequency dependent in antenna theory[31]. This is also true for the ohmic resistance R_0 which is more accurately described in terms of the complex conductivity predicted by the Drude model: $R_0 = R_{DC}(1 - j\omega\tau_D)$, where τ_D is the mean free time between ionic collisions in the conductive material, and R_{DC} is the DC resistance. Additionally, we mainly focus on the study of material permittivity through the capacitance of the SRR, but the model can be adapted to the study of magnetic permeability, by implementing a dispersive μ in the inductance model. However, this model cannot predict the higher order mode of the SRR that exists at frequencies for which the quasi-static approximation is not valid anymore. The perimeter of the SRR designed for the THz range is typically in the order of 100 μm , which means the frequency range of a THz-TDS system reaches beyond the quasi-static approximation. Therefore, we need to be extremely careful in our interpretation of the SRR response at high frequency. We can also conclude that for a given resonance frequency, a smaller SRR will follow our model more accurately.

The model and its requirements gives us all the elements needed to design and characterize SRR, and use them for THz spectroscopy on microscopic samples.

References

- [1] Ran Damari et al. "Strong coupling of collective intermolecular vibrations in organic materials at terahertz frequencies". In: *Nature Communications* 10.1 (July 2019). DOI: [10.1038/s41467-019-11130-y](https://doi.org/10.1038/s41467-019-11130-y) (cit. on pp. 5, 19).
- [2] Gerhard Schwaab, Federico Sebastiani, and Martina Havenith. "Ion Hydration and Ion Pairing as Probed by THz Spectroscopy". In: *Angewandte Chemie International Edition* 58.10 (Mar. 2019), pp. 3000–3013. DOI: [10.1002/anie.201805261](https://doi.org/10.1002/anie.201805261) (cit. on p. 5).
- [3] Max Born and Emil Wolf. *Principles of Optics*. Cambridge University Press, June 1980. 836 pp. ISBN: 9781483103204. URL: https://www.ebook.de/de/product/26502522/max_born_emil_wolf_principles_of_optics.html (cit. on p. 5).

- [4] A Ashkin and J. Dziedzic. “Optical trapping and manipulation of viruses and bacteria”. In: *Science* 235.4795 (Mar. 1987), pp. 1517–1520. DOI: [10.1126/science.3547653](https://doi.org/10.1126/science.3547653) (cit. on p. 5).
- [5] Sergey Mitryukovskiy et al. “On the influence of water on THz vibrational spectral features of molecular crystals”. In: *Physical Chemistry Chemical Physics* 24.10 (2022), pp. 6107–6125. DOI: [10.1039/d1cp03261e](https://doi.org/10.1039/d1cp03261e) (cit. on pp. 5, 19).
- [6] E. M. Purcell. “Spontaneous Emission Probabilities at Radio Frequencies”. In: *Confined Electrons and Photons*. Springer US, 1995, pp. 839–839. DOI: [10.1007/978-1-4615-1963-8_40](https://doi.org/10.1007/978-1-4615-1963-8_40) (cit. on p. 5).
- [7] Romain Peretti et al. “Broadband Terahertz Light-Matter Interaction Enhancement for Precise Spectroscopy of Thin Films and Micro-Samples”. In: *Photonics* 5.2 (May 2018), p. 11. DOI: [10.3390/photonics5020011](https://doi.org/10.3390/photonics5020011) (cit. on p. 5).
- [8] Sergey Mitryukovskiy et al. “Device for Broadband THz Spectroscopy of 1-nL-Volume Samples”. In: *2019 44th International Conference on Infrared, Millimeter, and Terahertz Waves (IRMMW-THz)*. IEEE, Sept. 2019. DOI: [10.1109/irmmw-thz.2019.8874026](https://doi.org/10.1109/irmmw-thz.2019.8874026) (cit. on p. 5).
- [9] Melanie Lavancier. “Heuristic approach to take up the challenge of terahertz time-domain spectroscopy for biology”. Theses. Université de Lille, Oct. 2021. URL: <https://tel.archives-ouvertes.fr/tel-03539445> (cit. on p. 5).
- [10] Markus Walther, Mark R. Freeman, and Frank A. Hegmann. “Metal-wire terahertz time-domain spectroscopy”. In: *Applied Physics Letters* 87.26 (Dec. 2005), p. 261107. DOI: [10.1063/1.2158025](https://doi.org/10.1063/1.2158025) (cit. on p. 5).
- [11] R. Mendis and D. Grischkowsky. “Undistorted guided-wave propagation of subpicosecond terahertz pulses”. In: *Optics Letters* 26.11 (June 2001), p. 846. DOI: [10.1364/ol.26.000846](https://doi.org/10.1364/ol.26.000846) (cit. on p. 5).
- [12] N. Laman et al. “High-Resolution Waveguide THz Spectroscopy of Biological Molecules”. In: *Biophysical Journal* 94.3 (Feb. 2008), pp. 1010–1020. DOI: [10.1529/biophysj.107.113647](https://doi.org/10.1529/biophysj.107.113647) (cit. on p. 5).
- [13] Alisha J. Shutler and D. Grischkowsky. “Gap independent coupling into parallel plate terahertz waveguides using cylindrical horn antennas”. In: *Journal of Applied Physics* 112.7 (Oct. 2012), p. 073102. DOI: [10.1063/1.4754846](https://doi.org/10.1063/1.4754846) (cit. on p. 5).
- [14] Théo Hannotte et al. “Imaging of THz Photonic Modes by Scattering Scanning Near-Field Optical Microscopy”. In: *ACS Applied Materials & Interfaces* 14.28 (July 2022), pp. 32608–32617. DOI: [10.1021/acsmi.2c01871](https://doi.org/10.1021/acsmi.2c01871) (cit. on p. 5).
- [15] Curdin Maissen et al. “Probes for Ultrasensitive THz Nanoscopy”. In: *ACS Photonics* 6.5 (Apr. 2019), pp. 1279–1288. DOI: [10.1021/acsp Photonics.9b00324](https://doi.org/10.1021/acsp Photonics.9b00324) (cit. on p. 5).
- [16] Hou-Tong Chen, Roland Kersting, and Gyu Cheon Cho. “Terahertz imaging with nanometer resolution”. In: *Applied Physics Letters* 83.15 (Oct. 2003), pp. 3009–3011. DOI: [10.1063/1.1616668](https://doi.org/10.1063/1.1616668) (cit. on p. 5).
- [17] Xinzhong Chen et al. “Modern Scattering-Type Scanning Near-Field Optical Microscopy for Advanced Material Research”. In: *Advanced Materials* (Apr. 2019), p. 1804774. DOI: [10.1002/adma.201804774](https://doi.org/10.1002/adma.201804774) (cit. on p. 5).
- [18] T. Hannotte et al. “Consequences of antenna effects on s-SNOM imaging of a photonic mode”. In: *Conference on Lasers and Electro-Optics*. OSA, 2021. DOI: [10.1364/cleo_si.2021.sw2k.5](https://doi.org/10.1364/cleo_si.2021.sw2k.5) (cit. on p. 5).

- [19] Xinzhong Chen et al. "THz Near-Field Imaging of Extreme Subwavelength Metal Structures". In: *ACS Photonics* 7.3 (Jan. 2020), pp. 687–694. DOI: [10.1021/acsp Photonics.9b01534](https://doi.org/10.1021/acsp Photonics.9b01534) (cit. on p. 5).
- [20] Tao Chen, Suyan Li, and Hui Sun. "Metamaterials Application in Sensing". In: *Sensors* 12.3 (Feb. 2012), pp. 2742–2765. DOI: [10.3390/s120302742](https://doi.org/10.3390/s120302742) (cit. on pp. 6, 16).
- [21] Audrey Berrier et al. "Selective detection of bacterial layers with terahertz plasmonic antennas". In: *Biomedical Optics Express* 3.11 (Oct. 2012), p. 2937. DOI: [10.1364/boe.3.002937](https://doi.org/10.1364/boe.3.002937) (cit. on p. 6).
- [22] Curdin Maissen et al. "Ultrastrong coupling in the near field of complementary split-ring resonators". In: *Physical Review B* 90.20 (Nov. 2014). DOI: [10.1103/physrevb.90.205309](https://doi.org/10.1103/physrevb.90.205309) (cit. on p. 6).
- [23] S. J. Park et al. "Detection of microorganisms using terahertz metamaterials". In: *Scientific Reports* 4.1 (May 2014). DOI: [10.1038/srep04988](https://doi.org/10.1038/srep04988) (cit. on pp. 6, 16).
- [24] Dong-Kyu Lee et al. "Highly sensitive and selective sugar detection by terahertz nano-antennas". In: *Scientific Reports* 5.1 (Oct. 2015). DOI: [10.1038/srep15459](https://doi.org/10.1038/srep15459) (cit. on pp. 6, 16).
- [25] Xin Hu et al. "Metamaterial absorber integrated microfluidic terahertz sensors". In: *Laser & Photonics Reviews* 10.6 (Oct. 2016), pp. 962–969. DOI: [10.1002/lpor.201600064](https://doi.org/10.1002/lpor.201600064) (cit. on pp. 6, 16).
- [26] D. R. Smith, J. B. Pendry, and M. C. K. Wiltshire. "Metamaterials and Negative Refractive Index". In: *Science* 305.5685 (Aug. 2004), pp. 788–792. DOI: [10.1126/science.1096796](https://doi.org/10.1126/science.1096796) (cit. on p. 6).
- [27] J. B. Pendry. "Controlling Electromagnetic Fields". In: *Science* 312.5781 (June 2006), pp. 1780–1782. DOI: [10.1126/science.1125907](https://doi.org/10.1126/science.1125907) (cit. on p. 6).
- [28] Wenshan Cai et al. "Optical cloaking with metamaterials". In: *Nature Photonics* 1.4 (Apr. 2007), pp. 224–227. DOI: [10.1038/nphoton.2007.28](https://doi.org/10.1038/nphoton.2007.28) (cit. on p. 6).
- [29] Elena Mavrona et al. "Terahertz refractive index matching solution". In: *Optics Express* 27.10 (May 2019), p. 14536. DOI: [10.1364/oe.27.014536](https://doi.org/10.1364/oe.27.014536) (cit. on p. 6).
- [30] C. Manolatou et al. "Coupling of modes analysis of resonant channel add-drop filters". In: *IEEE Journal of Quantum Electronics* 35.9 (1999), pp. 1322–1331. DOI: [10.1109/3.784592](https://doi.org/10.1109/3.784592) (cit. on pp. 6, 9–11).
- [31] Donald Foster. "Loop Antennas with Uniform Current". In: *Proceedings of the IRE* 32.10 (Oct. 1944), pp. 603–607. DOI: [10.1109/jrproc.1944.233062](https://doi.org/10.1109/jrproc.1944.233062) (cit. on pp. 7, 25).
- [32] Yun-Shik Lee. *Principles of Terahertz Science and Technology*. Springer-Verlag GmbH, Mar. 2009. 340 pp. ISBN: 9780387095400. URL: https://www.ebook.de/de/product/12469854/yun_shik_lee_principles_of_terahertz_science_and_technology.html (cit. on p. 7).
- [33] Lieven Verslegers et al. "Temporal coupled-mode theory for resonant apertures". In: *Journal of the Optical Society of America B* 27.10 (Sept. 2010), p. 1947. DOI: [10.1364/josab.27.001947](https://doi.org/10.1364/josab.27.001947) (cit. on p. 9).
- [34] Shanhui Fan, Wonjoo Suh, and J. D. Joannopoulos. "Temporal coupled-mode theory for the Fano resonance in optical resonators". In: *Journal of the Optical Society of America A* 20.3 (Mar. 2003), p. 569. DOI: [10.1364/josaa.20.000569](https://doi.org/10.1364/josaa.20.000569) (cit. on pp. 9, 10, 12, 13).

- [35] M. A. Dupertuis, B. Acklin, and M. Proctor. "Generalization of complex Snell–Descartes and Fresnel laws". In: *Journal of the Optical Society of America A* 11.3 (Mar. 1994), p. 1159. DOI: [10.1364/josaa.11.001159](https://doi.org/10.1364/josaa.11.001159) (cit. on p. 12).
- [36] M. A. Dupertuis, B. Acklin, and M. Proctor. "Generalized energy balance and reciprocity relations for thin-film optics". In: *Journal of the Optical Society of America A* 11.3 (Mar. 1994), p. 1167. DOI: [10.1364/josaa.11.001167](https://doi.org/10.1364/josaa.11.001167) (cit. on p. 12).
- [37] Shangyu Zhang, Linhua Liu, and Yuanbin Liu. "Generalized laws of Snell, Fresnel and energy balance for a charged planar interface between lossy media". In: *Journal of Quantitative Spectroscopy and Radiative Transfer* 245 (Apr. 2020), p. 106903. DOI: [10.1016/j.jqsrt.2020.106903](https://doi.org/10.1016/j.jqsrt.2020.106903) (cit. on p. 12).
- [38] Yun-Tzu Chang et al. "A multi-functional plasmonic biosensor". In: *Optics Express* 18.9 (Apr. 2010), p. 9561. DOI: [10.1364/oe.18.009561](https://doi.org/10.1364/oe.18.009561) (cit. on p. 16).
- [39] G. S. Agarwal. "Vacuum-Field Rabi Splittings in Microwave Absorption by Rydberg Atoms in a Cavity". In: *Physical Review Letters* 53.18 (Oct. 1984), pp. 1732–1734. DOI: [10.1103/physrevlett.53.1732](https://doi.org/10.1103/physrevlett.53.1732) (cit. on p. 18).
- [40] Yifu Zhu et al. "Vacuum Rabi splitting as a feature of linear-dispersion theory: Analysis and experimental observations". In: *Physical Review Letters* 64.21 (May 1990), pp. 2499–2502. DOI: [10.1103/physrevlett.64.2499](https://doi.org/10.1103/physrevlett.64.2499) (cit. on pp. 18, 19).
- [41] Said Rahimzadeh-Kalaleh Rodriguez. "Classical and quantum distinctions between weak and strong coupling". In: *European Journal of Physics* 37.2 (Jan. 2016), p. 025802. DOI: [10.1088/0143-0807/37/2/025802](https://doi.org/10.1088/0143-0807/37/2/025802) (cit. on p. 18).
- [42] Anton Frisk Kockum et al. "Ultrastrong coupling between light and matter". In: *Nature Reviews Physics* 1.1 (Jan. 2019), pp. 19–40. DOI: [10.1038/s42254-018-0006-2](https://doi.org/10.1038/s42254-018-0006-2) (cit. on p. 19).
- [43] V. Savona et al. "Quantum well excitons in semiconductor microcavities: Unified treatment of weak and strong coupling regimes". In: *Solid State Communications* 93.9 (Mar. 1995), pp. 733–739. DOI: [10.1016/0038-1098\(94\)00865-5](https://doi.org/10.1016/0038-1098(94)00865-5) (cit. on p. 19).
- [44] Thomas W. Ebbesen. "Hybrid Light-Matter States in a Molecular and Material Science Perspective". In: *Accounts of Chemical Research* 49.11 (Oct. 2016), pp. 2403–2412. DOI: [10.1021/acs.accounts.6b00295](https://doi.org/10.1021/acs.accounts.6b00295) (cit. on p. 19).
- [45] J. M. Raimond, M. Brune, and S. Haroche. "Manipulating quantum entanglement with atoms and photons in a cavity". In: *Reviews of Modern Physics* 73.3 (Aug. 2001), pp. 565–582. DOI: [10.1103/revmodphys.73.565](https://doi.org/10.1103/revmodphys.73.565) (cit. on p. 19).
- [46] R. Houdré, R. P. Stanley, and M. Ilegems. "Vacuum-field Rabi splitting in the presence of inhomogeneous broadening: Resolution of a homogeneous linewidth in an inhomogeneously broadened system". In: *Physical Review A* 53.4 (Apr. 1996), pp. 2711–2715. DOI: [10.1103/physreva.53.2711](https://doi.org/10.1103/physreva.53.2711) (cit. on p. 19).
- [47] P Törmä and W L Barnes. "Strong coupling between surface plasmon polaritons and emitters: a review". In: *Reports on Progress in Physics* 78.1 (Dec. 2014), p. 013901. DOI: [10.1088/0034-4885/78/1/013901](https://doi.org/10.1088/0034-4885/78/1/013901) (cit. on p. 19).
- [48] Jino George et al. "Multiple Rabi Splittings under Ultrastrong Vibrational Coupling". In: *Physical Review Letters* 117.15 (Oct. 2016), p. 153601. DOI: [10.1103/physrevlett.117.153601](https://doi.org/10.1103/physrevlett.117.153601) (cit. on p. 19).

- [49] Emmanuel Rosencher and Borge Vinter. *Optoelectronics*. Cambridge University Press, 2002, p. 112. ISBN: 9780521771290 (cit. on p. 19).
- [50] Rosencher and Vinter. *Optoélectronique. Cours et exercices corrigés, 2e édition*. Dunod, 2002. ISBN: 9782100065547 (cit. on p. 19).
- [51] Cyril Guers. “Optimisation des matériaux cellulose pour des applications en radiofréquences et térahertz”. Theses. Université Grenoble Alpes, June 2019. URL: <https://tel.archives-ouvertes.fr/tel-02520923> (cit. on p. 21).
- [52] J. C. Maxwell Garnett. “XII. Colours in metal glasses and in metallic films”. In: *Philosophical Transactions of the Royal Society of London. Series A, Containing Papers of a Mathematical or Physical Character* 203.359-371 (Jan. 1904), pp. 385–420. DOI: [10.1098/rsta.1904.0024](https://doi.org/10.1098/rsta.1904.0024) (cit. on p. 22).
- [53] M. H. Boyle. “The electrical properties of heterogeneous mixtures containing an oriented spheroidal dispersed phase”. In: *Colloid and Polymer Science* 263.1 (Jan. 1985), pp. 51–57. DOI: [10.1007/bf01411248](https://doi.org/10.1007/bf01411248) (cit. on p. 22).
- [54] D. A. G. Bruggeman. “Berechnung verschiedener physikalischer Konstanten von heterogenen Substanzen. I. Dielektrizitätskonstanten und Leitfähigkeiten der Mischkörper aus isotropen Substanzen”. In: *Annalen der Physik* 416.7 (1935), pp. 636–664. DOI: [10.1002/andp.19354160705](https://doi.org/10.1002/andp.19354160705) (cit. on p. 22).
- [55] Karl Lichtenecker. “Die Ableitung der logarithmischen Mischungsregel aus dem Maxwell-Rayleighschen Schrankenwertverfahren”. In: *Kolloidchemische Beihefte* 23.1-9 (Aug. 1926), pp. 285–291. DOI: [10.1007/bf02557784](https://doi.org/10.1007/bf02557784) (cit. on p. 22).
- [56] Tarik Zakri, Jean-Paul Laurent, and Michel Vauclin. “Theoretical evidence for ‘Lichtenecker’s mixture formulae’ based on the effective medium theory”. In: *Journal of Physics D: Applied Physics* 31.13 (July 1998), pp. 1589–1594. DOI: [10.1088/0022-3727/31/13/013](https://doi.org/10.1088/0022-3727/31/13/013) (cit. on p. 22).
- [57] A.V. Goncharenko, V.Z. Lozovski, and E.F. Venger. “Lichtenecker’s equation: applicability and limitations”. In: *Optics Communications* 174.1-4 (Jan. 2000), pp. 19–32. DOI: [10.1016/S0030-4018\(99\)00695-1](https://doi.org/10.1016/S0030-4018(99)00695-1) (cit. on p. 22).
- [58] Artur Büchner. “Das Mischkörperproblem in der Kondensatorentechnik”. In: *Wissenschaftliche Veröffentlichungen aus den Siemens-Werken*. Springer Berlin Heidelberg, 1939, pp. 204–216. DOI: [10.1007/978-3-642-99673-3_15](https://doi.org/10.1007/978-3-642-99673-3_15) (cit. on p. 22).
- [59] Shima Rajabali et al. “An ultrastrongly coupled single terahertz meta-atom”. In: *Nature Communications* 13.1 (May 2022). DOI: [10.1038/s41467-022-29974-2](https://doi.org/10.1038/s41467-022-29974-2) (cit. on p. 25).

Chapter 2

Design and fabrication

2.1 SRR design

We have defined in chapter 1 all the parameters of a Split Ring Resonator (SRR) as a RLC circuit: the ohmic resistance R_0 , the radiative resistance R_r , the inductance L and the capacitance C . We described how those parameters relate to the resonance mode properties: the internal decay time τ_0 , the external decay time τ_e , and the resonance frequency ω_0 . We showed that we can take advantage of the relationship between the capacitance and the permittivity of the surrounding medium to probe the properties of a dispersive material at an arbitrarily small scale, through a transmission measurement. We now proceed to discuss how to optimize the design of SRR for the purpose of studying light matter coupling through far-field spectroscopy methods such as THz Time Domain Spectroscopy (THz-TDS). The following parameters need to be taken into account:

Coupling with the far-field: The coupling of a single sub-wavelength object with the far-field is by nature very weak, therefore it is critical to optimize this parameter to maximize the signal measurable in far-field spectroscopy.

Quality factor: These parameters define the bandwidth that can be probed with a SRR, it needs to be adjusted to the material we want to study.

Field confinement volume: The confinement volume in a RLC resonator can theoretically be arbitrarily small. We need control over this parameter in our design to take advantage of this property.

Coupling with the sample material: The design needs to be optimized to maximize the impact of a sample material on the capacitance.

Conformity with the model: In order to extract quantitative information from a transmission measurement, we need to make sure our design fulfills all the hypotheses of the model derived in chapter 1.

2.1.1 Coupling with the far-field

As mentioned before, our SRR are made to be probed with THz-TDS in transmission. In chapter 1, we divided the losses in two terms: The internal (or Ohmic) losses, modeled by a resistance R_0 , and the external (or radiative) losses, modeled by a resistance R_r . In the two port model used in chapter 1, this strict distinction implies that all the energy radiated from the SRR ends up in one of the two ports s_{1-} or s_{2-} . However, in a real spectroscopy experiment with finite numerical aperture, some of the radiated energy is lost because it never reaches the detector as illustrated in figure 2.1. This kind of loss is still external loss, but it does not contribute to the

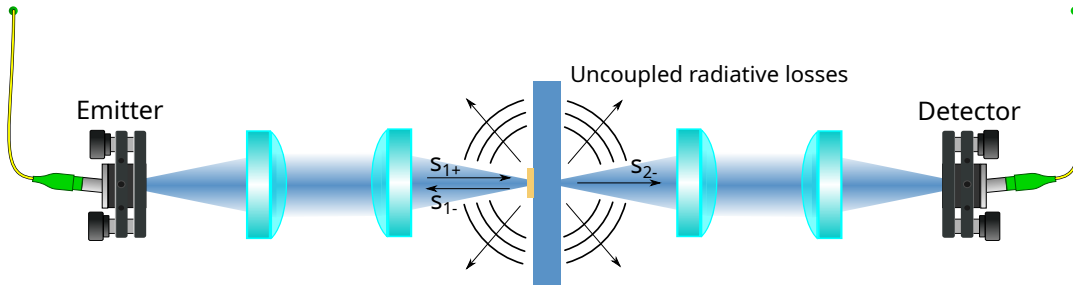


Figure 2.1: Schematic of a spectroscopic experiment on a resonator on substrate under normal incidence. All the energy radiated outside of the blue beam is lost and do not contribute to the coupling with the detector and receptor.

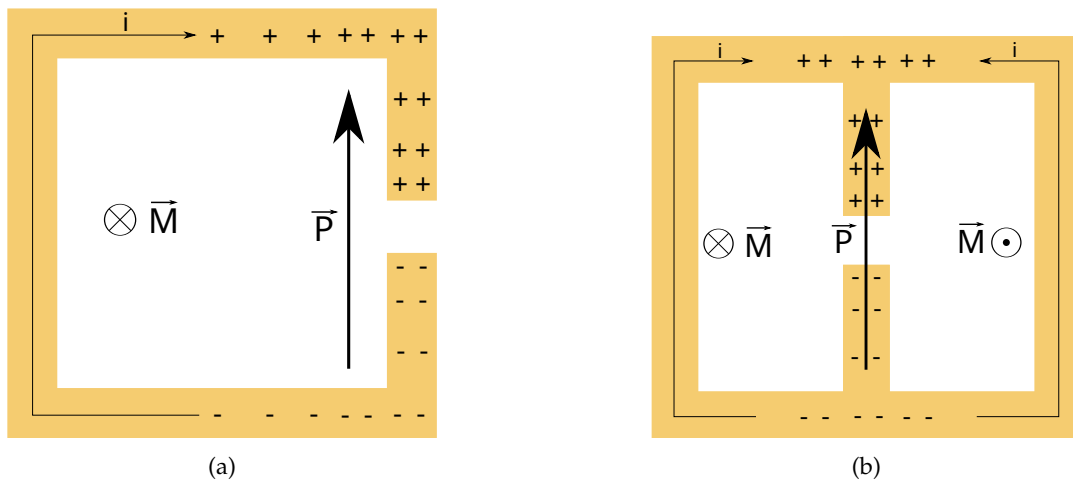


Figure 2.2: **(a)**: Schematic of the dipole moments in the single loop SRR. The current along the loop induces an out of plane magnetic dipole moment \vec{M} , while the charges accumulating on each side of the SRR induce an in plane electric dipole moment \vec{P} . **(b)**: Schematic of the dipole moments in the double SRR. The magnetic dipole moments from both loops are in opposite directions such that the net moments for the SRR is 0.

coupling with the emitter and detector and is therefore indistinguishable from the internal loss in our model. Thus the uncoupled radiative loss adds up to the term R_0 rather than R_r in the RLC model, despite being fundamentally different from ohmic loss. Consequently, the coupling with the far-field includes two distinct parameters:

- The total amount of radiative losses, which affects the quality factor of the resonator.
- The directivity of the radiated field. We want to increase as much as possible the proportion of radiated energy that couples with the detector and emitter. For the latter, one needs to pay attention to the far-field pattern.

Magnetic and electric coupling

To tackle both of the mentioned problems of far-field coupling, we need to understand the mechanisms involved in this coupling. A SRR couples to the far-field through magnetic coupling, when an oscillating magnetic field goes through a conductive loop, leading to an electromotive force[1], and through electric coupling,

when an oscillating electric field creates an electric dipole moment inside the metallic structure[2]. Both mechanisms play a significant role in the single loop resonator as illustrated in figure 2.2a. When a SRR is fabricated on a planar substrate, every loop of current is necessarily in the plane of the substrate, therefore the magnetic dipole moment is orthogonal to the substrate. This property is useful when coupling the SRR with a waveguide, a transmission line[3], a near-field magnetic coupler[4, 5], or when used in a 3D metamaterial[6]. But since we want to probe our SRR in normal incidence, the magnetic field of a collimated incident beam has no component orthogonal to the substrate, and a very weak one for a focused beam.

In contrast, the electric dipole moment induced by any charge distribution inside a plane has to be contained in this plane, which is ideal for coupling with a beam in normal incidence which has an electric field parallel to the substrate plane[7].

Thus the first modification to reduce the uncoupled radiative losses is to suppress the magnetic dipole moment of the SRR while keeping the electric dipole moment. This is classically done by adding a second loop symmetrical to the first one such that the current distribution is always symmetrical, and the dipole moment of each loop cancels each other[8, 9], as illustrated in figure 2.2b.

Far-field emission model

We now have a wavelength structure with an electric dipole moment in the direction of the gap, which can couple with a beam at normal incidence. If the resonator was designed to be used in a periodic array, we would not need to investigate the far-field coupling further, since the periodic arrangement guarantees a high degree of directivity, regardless of the radiation pattern of the individual resonators. Indeed if the resonators are excited in phase with each other, the emissions that are not orthogonal to the array plane will interfere destructively. For a single resonator however, we cannot count on this effect and it becomes relevant to investigate how to shape the far-field radiation pattern of a SRR. It is important to note that diffraction prevents any sub-wavelengths source from being highly directional, but it can still be better than a point dipole source. With the vast majority of SRR experiments being done on metasurface, the question of the far-field pattern of SRRs is only rarely mentioned in the literature[10].

Since the structure only has an electric dipole moment, it is comparable to a short electric dipole antenna. A short dipole antenna is essentially a sub-wavelength linear wire fed with an oscillating current. The back and forth acceleration of charges along the wire creates a propagating electromagnetic wave following a radiation pattern almost identical to a point source dipole[11]. In the double SRR presented in figure 2.2b, charges are linearly accelerated in both side branches. Therefore we model the far-field radiation pattern of a double split ring resonator as the radiation pattern of two point source dipoles located at the position of the side branches, and oscillating with the same phase (see figure 2.3a). In this model, the emissions from the dipole sources in the normal direction are perfectly in phase, but the in-plane emissions, orthogonal to the branches, are phase shifted and thus attenuated by a factor

$$\alpha(\lambda) = \frac{1}{2} + \frac{1}{2} \cos\left(2\pi \frac{a_x}{\lambda}\right), \text{ or } \alpha(\omega) = \frac{1}{2} + \frac{1}{2} \cos\left(\frac{\omega a_x}{c}\right), \quad (2.1)$$

where a_x is the width of the SRR, and λ is the wavelength. It appears from equation (2.1) that the side emission from a double SRR can be reduced by increasing the ratio $\frac{a_x}{\lambda}$. The inductance of a metallic loop is proportional to its surface area. Thus, by

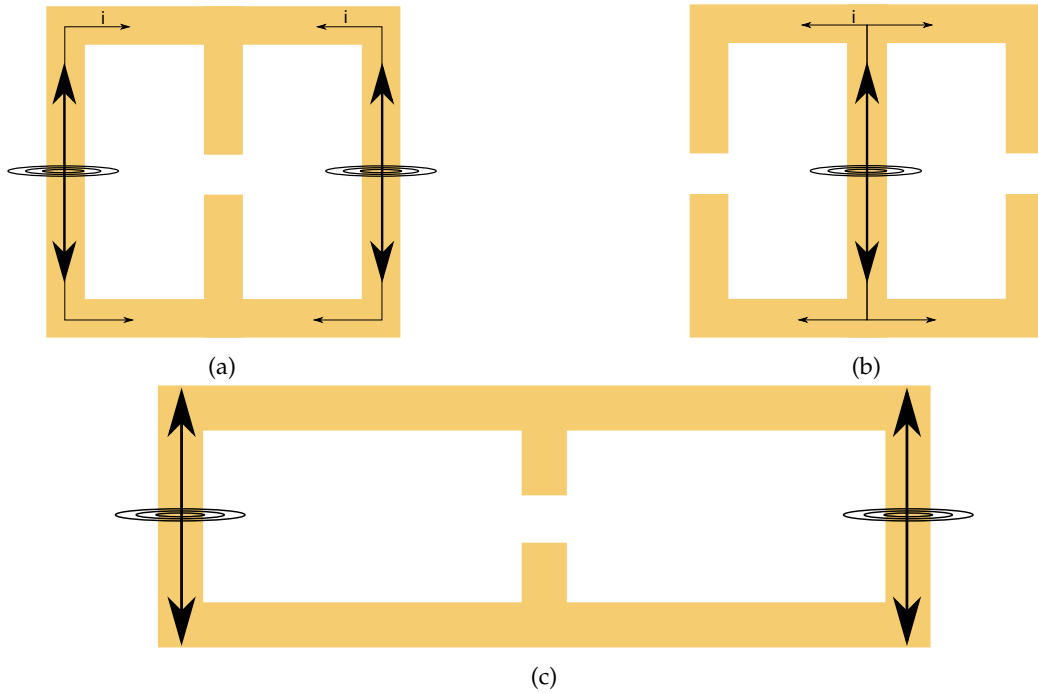


Figure 2.3: Schematic of three design and their simplified emission model. **(a)**: Square design. **(b)**: Lateral gap design, expected to behave as a single electric dipole. **(c)**: Wide design, expected to be more directional than the square design.

using loops with the same surface area but a wider aspect ratio, one can increase the distance between the branches without changing the resonance frequency. Hence we expect the design illustrated in figure 2.3c is expected to be more directional than the square design.

On the other hand, the design illustrated in figure 2.3b features only one branch where charges are accelerated. This SRR is expected to have a radiation pattern similar to a single short dipole antenna.

Model verification with FDTD simulation

To check the validity of the proposed far-field emission model, we simulate the presented designs without substrate with Finite Difference Time Domain (FDTD) from Lumerical. The SRR is excited with a Total-Field Scattered-Field (TFSF) source, which simulates a plane wave inside a closed box containing the SRR, and suppresses the plane wave outside the box, leaving only the scattered field. The far-field radiation pattern is projected from the field measured on a closed box containing the TFSF box. We will see in chapter 4 and 3 that the FDTD simulations are consistent with THz-TDS and Scanning Near-field Optical Microscopy (SNOM) measurements. Figure 2.4a shows the simulated pattern for a square SRR with $a_x = 30 \mu\text{m}$ and a branch width $w = 2 \mu\text{m}$. For comparison, figure 2.4b shows the simulated radiation pattern from a single dipole sources and from two dipole source laterally spaced by $28 \mu\text{m}$. Differences between figure 2.4a and 2.4b is likely due to the emission from the remaining magnetic quadrupole, and oscillating current outside of the main branches, which are neglected in this model. Nonetheless, the radiation pattern from the SRR shows a good agreement with the simplified emission model with two dipoles. Even the square design proves to be significantly more directional than

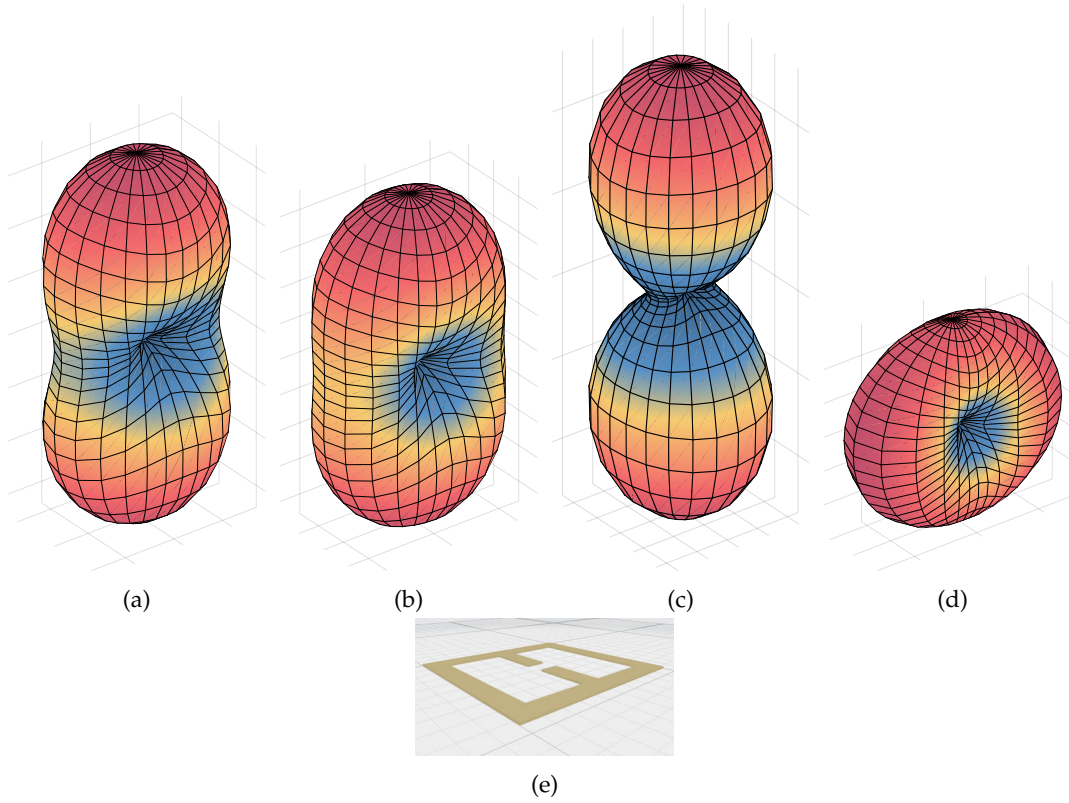


Figure 2.4: Simulated far-field radiation pattern from different designs and models without substrate. **(a)**: Square SRR design (figure 2.3a). **(b)**: 2 point dipole sources spaced like the branches of the square design. **(c)**: Wide SRR design (figure 2.3c). **(d)**: Lateral gap design (figure 2.3b). All the patterns are oriented as the SRR in **(e)**.

a single point source dipole. The far-field pattern from the wide SRR (figure 2.4c) and from the SRR with lateral gap (figure 2.4d) further confirms the predictive efficiency of our simplified model. Cross sections of the far-fields in the XZ plane are shown in figure 2.5, where we can see that the square SRR is actually slightly better than the prediction from the simplified model, while the lateral gap SRR is slightly worse. Figure 2.5 confirms that the wide design is indeed the best one by far on the directivity criteria.

However, one has to keep in mind that increasing the ratio $\frac{a_x}{\lambda}$ this way also increases the perimeters of the loops, which decreases the validity of the quasi-static approximation and thus makes the SRR less reliable for extracting information using the model presented in chapter 1. Hence why we will keep the square shape illustrated in figure 2.2b since it minimizes the length of the loops while still having a narrower far-field radiation pattern than a single dipole.

Overall amplitude of the radiated field

We identified the oscillating currents in the continuous branches along \vec{y} as the main source of radiative emission (see figure 2.5 for axis definition). We saw that approximating those branches with short dipole antennas is valid to predict the shape of the radiation pattern. We will now check the validity of this approximation to predict the overall intensity of the radiated field.

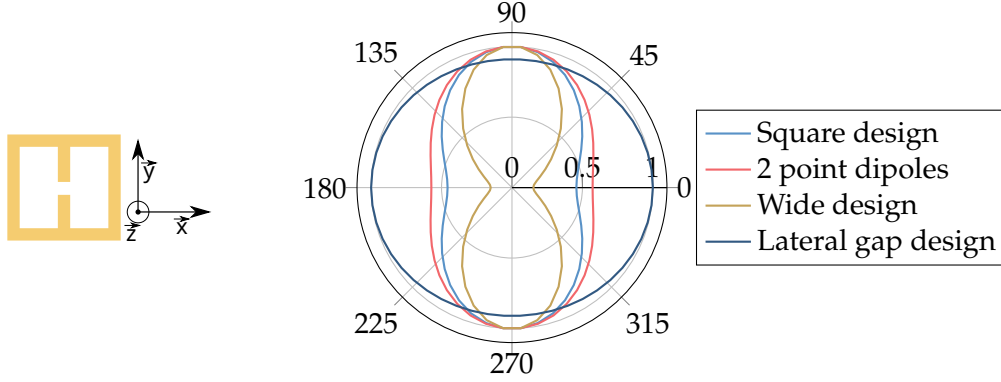


Figure 2.5: Normalized polar plot of the scattered intensity in the XZ plane for all the presented designs and from the simplified dipole model of the square design. Axis are defined in the left picture. 0° correspond to the \vec{x} direction.

As mentioned in chapter 1, the concept of radiative resistance is commonly used to model the radiative losses of an antenna. It is defined as $R_r = \frac{W}{I^2}$, where W is the total radiated power and I is the current injected in the antenna. For a short dipole antenna with a central feed-point, the radiative resistance is given by [12]:

$$R_r = \frac{\pi}{6} Z_0 \left(\frac{a_y}{\lambda} \right)^2 = \frac{Z_0}{24\pi c^2} (a_y \omega)^2, \quad (2.2)$$

where a_y is the length of the antenna (see figure 2.9a lengths definitions), and $Z_0 \simeq 377 \Omega$ is the impedance of free space. Equation (2.2) is derived using a effective current equal to the average current over the antenna. The average current in a regular short dipole antenna is half of the maximum current, since the current distribution linearly drops to zero toward the extremities. This is however not the case for a SRR. We expect the real resistance to differ from (2.2) by a multiplicative constant. It is possible to reduce the radiative resistance of the SRR by reducing the length a_y . However, it does not necessarily mean that the radiative losses would decrease. Indeed, the decay rate of the resonator is given by

$$\frac{1}{\tau} = \frac{R}{2L}. \quad (2.3)$$

Let us consider a square SRRs design, where we only change the parameters $a = a_x = a_y$ and $\frac{A}{G}$, while keeping the thickness constant. The inductance L is proportional to the area of the loops. We can define the constant β such that $L = \beta a_y^2$, we have

$$\frac{1}{\tau} = \frac{\pi Z_0}{12\beta c^2} \omega^2, \quad (2.4)$$

$$\text{or } Q = \frac{6\beta c^2 \omega_0}{\pi Z_0 \omega^2}. \quad (2.5)$$

Here we see that the short dipole model predicts that for a given resonance frequency (kept constant by changing C), the decay rate is *independent* from the size of the resonator. Because of R_r being frequency dependent, Q and τ as defined from equation (2.3) also become frequency dependent. Although it does not pose any fundamental problem to use those expression in the context of the RLC model

in chapter 1, they do not match the regular definition of quality factor and decay rate. Indeed those values simply describe how quickly a damped oscillator loses its energy. Thus a resonant mode only has one single value for its quality factor and decay rate. If we assume that the radiative resistance variation are negligible over the bandwidth of the resonances ($\frac{2}{\tau} \frac{dR_r}{d\omega} \ll R_r$), the real quality factor of the mode is given by evaluating (2.5) for $\omega = \omega_0$:

$$Q = \frac{6\beta c^2}{\pi Z_0 \omega_0}. \quad (2.6)$$

Thus the short dipole model also predicts the quality factor of low frequency resonators to be higher than the high frequency ones. We will see in section 2.1.1 and chapter 4 that this statement is in contradiction with the FDTD simulations and THz-TDS experiments.

Consequences of the resistance variation over the resonance bandwidth

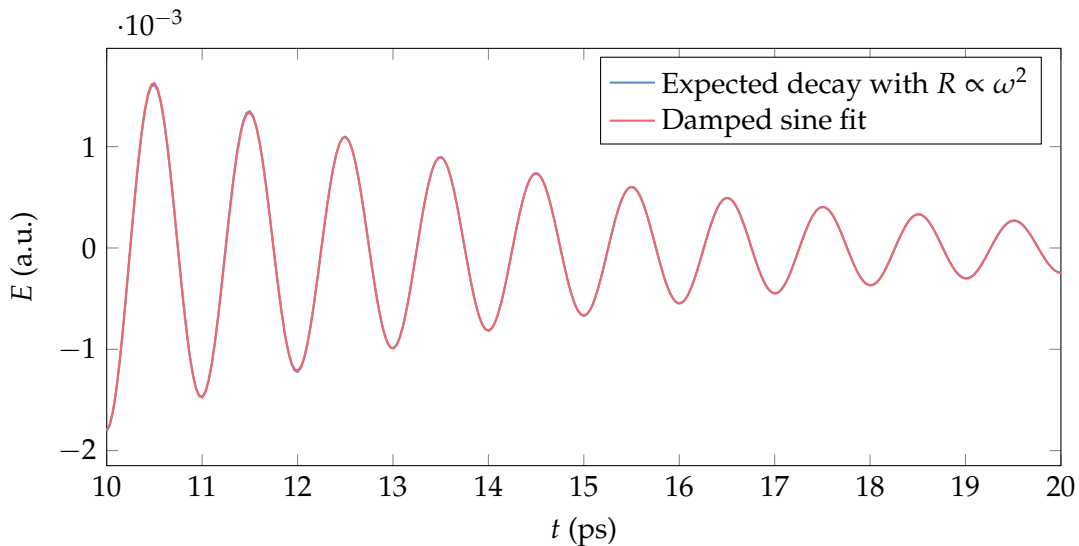


Figure 2.6: Calculated time domain response to an impulsion from a RLC circuit with $R \propto \omega^2$, compared to a damped sinusoidal function. The normalized error is $\chi^2 = 4 \times 10^{-11}$.

Since SRRs do not necessarily have extremely high quality factors, we shall evaluate how the variation of radiative resistance affects the estimation of the quality factor. More specifically, we want to check that the concept of quality factor is valid for an oscillator with a frequency dependent damping factor, and how good is the approximation (2.6).

To do so, we numerically calculate the time domain response of a RLC circuit from the transfer function derived in chapter 1, with the radiative resistance of a short dipole antenna, with parameters chosen such that $Q(\omega = \omega_0) = 5$. The time response of the circuit to a pulse excitation is the inverse Fourier transform of its transfer function. We then fit the damped oscillation with an exponentially decaying sinusoidal function to extract the actual decay time and quality factor of the mode.

Figure 2.6 shows that the response of a RLC circuit with a frequency dependent $R \propto \omega^2$ still matches a damped sine function (normalized error 4×10^{-11}). Thus it still makes full sense to talk about decay rates and quality factor for this type

Antenna type	Radiative resistance	Type of scaling
Short dipole[12]	$\frac{\pi}{6} Z_0 \left(\frac{a_y}{\lambda}\right)^2$	$\propto \omega^2$
Loop of circumference $C \ll \lambda$ [12]	$20\pi^2 \left(\frac{C^2}{\lambda^2}\right)^2$	$\propto \omega^4$
Loop of any circumference C [1]	$\frac{Z_0 C}{2\lambda} \int_0^{2\frac{C}{\lambda}} J_2(y) dy$	$\propto \omega^4$ for $C \ll \lambda$, $\propto \omega$ for $C \gg \lambda$

Table 2.1: Radiative resistances of common antenna.

of system. The extracted quality factor of this damped oscillation is $Q_{\text{fit5}} = 5.038$. Doing the same numerical experiment with $Q(\omega = \omega_0) = 20$, we get $Q_{\text{fit20}} = 20.155$. In both cases, the quality factor obtained from evaluating the decay rate from the definition in a RLC circuit (2.3) with $\omega = \omega_0$ slightly underestimates the real quality factor by about 0.76%.

We mentioned in chapter 1, the radiation resistance and its dependence to the frequency is different from one model to another. The radiative resistance formulas of a few types of antenna are summarized in table 2.1. In a circuit involving a small loop antenna, the radiative resistance scales with the fourth power of the frequency. In that case, the same numerical experiment gives fitted quality factors $Q_{\text{fit5}} = 5.11$ and $Q_{\text{fit20}} = 20.2$. Which correspond respectively to 1.02% and 1.01% errors.

Even with a resistance scaling with the fourth power of the frequency, the temporal response of the circuit is still an exponentially decaying oscillation, hence the concept of quality factor stays valid. Furthermore, the evaluation of Q at $\omega = \omega_0$ stays a good approximation even with stronger variation of R .

Influence of the design on the quality factor in FDTD simulations



Figure 2.7: Two designs for SRR with large capacitance.

Despite being quite effective to predict the shape of far-field patterns, the short dipole model is likely to be too simplistic to quantitatively predict the decay rate of a real resonator. We will check the validity of the model, and especially equation (2.4), by looking at the variation of the quality factor of a SRR in the following scenarios:

- Square SRRs with same resonance frequency, but different $\frac{C}{L}$ ratio.
- Constant inductance, varying capacitance.
- Constant capacitance, varying inductance.

All the simulations are done with Perfect Electrical Conductor (PEC), so that the quality factor is entirely defined by the radiative losses. The decay rates are extracted from the time domain response of a SRR to a pulse excitation. The capacitance can be tuned using one of the two designs illustrated in figure 2.7. For this test, we chose the design from figure 2.7b, as it has a lesser impact on the inductance. However for experiments involving real metal instead of PEC, the design from figure 2.7a shall be considered for its lower ohmic losses.

Before we can judge the validity of the short dipole model, we first need to make sure that our expression of the inductance as $L = \beta a_y^2$ is coherent with the simulations. Since $\omega_0 \simeq \frac{1}{\sqrt{LC}}$, λ_0 is directly proportional to \sqrt{L} when C is a constant. Figure 2.8 shows the simulated resonant wavelength $\lambda_0 = \frac{2\pi c}{\omega_0}$ for different sizes $a = a_x = a_y$ and identical capacitors. The simulations confirms the linear relationship $\lambda_0 \propto a$, and thus $L \propto a^2$. Hence the validity of equation (2.6) relies only on the validity of the short dipole approximation.

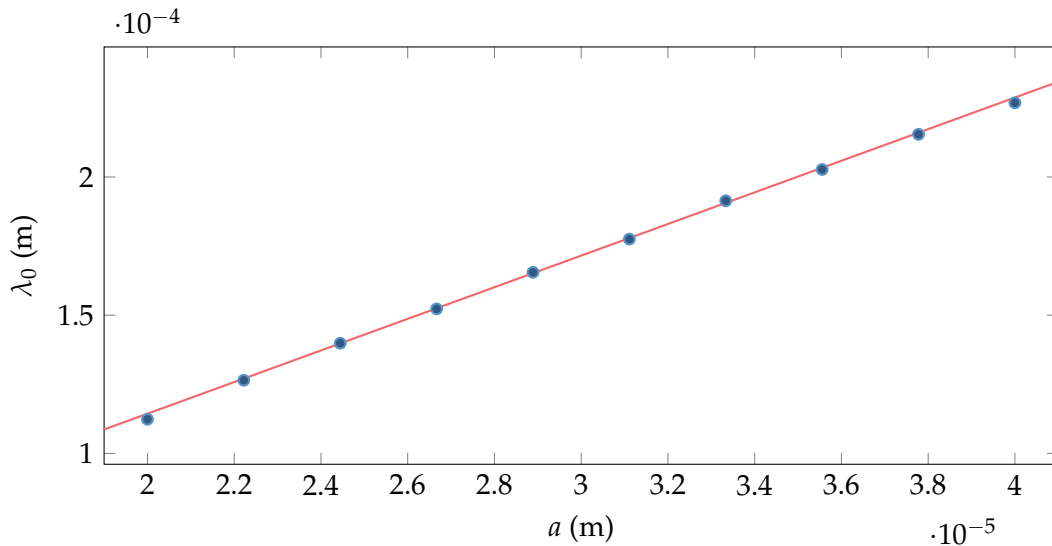


Figure 2.8: Simulated resonance wavelength of square SRRs for different sizes $a = a_x = a_y$ and identical capacitance. The continuous line is the linear regression with $r^2 = 0.99948$, and a slope $\frac{\lambda_0}{a} = 5.71$

Figure 2.9b shows the quality factor of 6 resonators with sizes ranging from $24 \mu\text{m}$ to $38 \mu\text{m}$, and a gap ratio $\frac{A}{C}$ (see figure 2.9a) adapted to keep the resonance frequency at 1.8 THz. The simulated evolution of the quality factor at constant resonance frequency is in clear contradiction with the short dipole model, and in particular with equation (2.6), which predicted a quality factor independent from the size parameter a . On the other hand, the simulation shows very little variation of the quality factor when changing only the size a (see figure 2.9c), while equation (2.6) predict a linear growth. At last figure 2.9d shows the variation of the quality factor as function of the wavelength of the mode, for SRRs with identical size and capacitance ratio $\frac{A}{C}$ ranging from 0 to 30. Here equation (2.6) also predicts a linear growth, while the simulation shows a much faster growth.

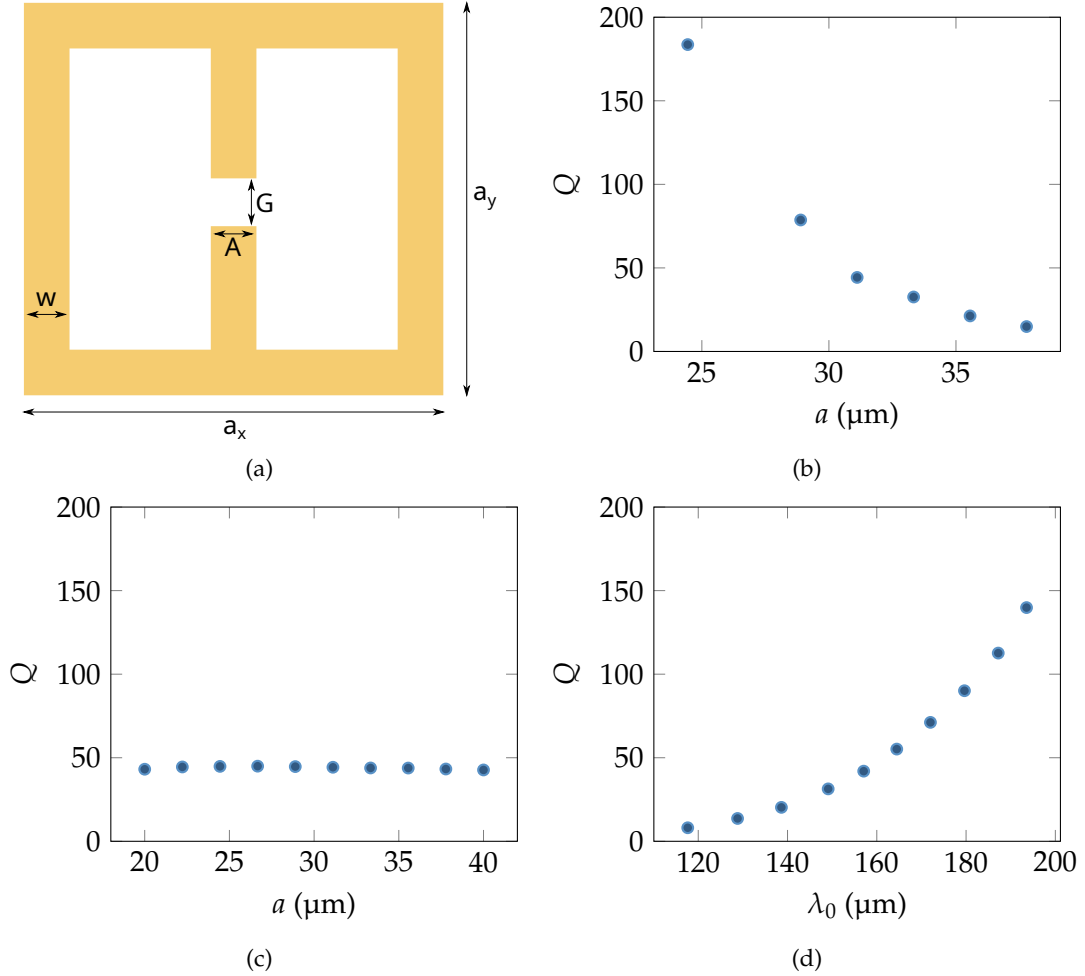


Figure 2.9: **(a)**: Main dimension of a SRR. **(b)**, **(c)** and **(d)**: Simulated quality factor for square SRRs in PEC, for different sizes $a = a_x = a_y$ and gap ratio $\frac{A}{G}$. **(b)**: Varying size a , with a gap ratio adapted to keep the resonance at 1.8 THz. **(c)**: Varying size a , identical capacitance. **(d)**: Varying gap ratio, identical size a , represented as a function of the resonance wavelength λ_0 . All those graphs are in complete *disagreement* with the short dipole model.

Figure 2.9b, 2.9c and 2.9d show that the quality factor for a square resonator mostly depends on the ratio $\frac{a}{\lambda_0}$ and that the short dipole approximation widely underestimate the influence of the frequency on the quality factor. Assuming the quality factor takes the form $Q = \alpha \left(\frac{a}{\lambda_0}\right)^p$, a linear regression on $\log(Q) = f\left(\log\left(\frac{a}{\lambda_0}\right)\right)$ gives a power $p \simeq -5.7$.

In conclusion, although the far-field analysis showed that a symmetrical SRR mostly radiates from its continuous branches along the \vec{y} axis with a radiation pattern similar to a short dipole antenna, it is clear that the expression of the radiative resistance (2.2) for a short dipole antenna of length a_y is not valid in our design. This discrepancy likely comes from one or several of the following assumptions:

- In figure 2.8, we have established that \sqrt{LC} scales with a , and therefore L scale with a^2 . This relies on the assumption that C does not change with a .
- The current distribution in the branch of a SRR is different from the current distribution in a real short dipole antenna. For a given SRR shape, this induces

a deviation from equation (2.2) by a multiplicative factor. We assumed that this factor is not strongly dependent on the size a . Having this factor proportional to a would explain the result from figure 2.9c.

- The radiative resistance does not take into account the possible interaction between both dipoles. For example, we have neglected the radiative resistance induced by the magnetic dipoles because their far-field radiation mostly cancels each other. This type of interference effect is absent from the radiative resistance formula. We know from figure 2.5 that the interference between the dipoles does exist and attenuate the radiation in some direction[13]. However, we assumed that this effect would have a negligible impact on the total radiated power.
- We mentioned in the previous chapter (section 1.1.2) that the radiative losses of a SRR could possibly be more accurately described with a resistance in parallel with the inductance, instead of in series. In that case, the decay rate of the circuit would not scale with $\frac{R}{L}$, but with $\frac{1}{RC}$. Hence the quality factor of a parallel RLC circuit grows with the capacitance, which is closer to what we observe.

Finding out the precise nature of the inconsistency requires further investigations which are out of the scope of this thesis. Indeed, from a design point of view, the main takeaway of this section is that the quality factor from a square SRR *without ohmic losses* grows quickly with $\frac{\lambda_0}{a}$. Since $\frac{\lambda_0}{a}$ grows with the capacitance, we have identified a straightforward way to tune the radiative coupling of a SRR.

2.1.2 Quality factor design

The quality factor of a resonance mode is defined by the losses of the mode. This includes the ohmic losses as well as the radiative losses, already discussed above. The desired quality factor depends on the application. Indeed a high quality factor means the resonator will be very sensitive, but on a narrow bandwidth, while a low quality factor allows one to probe a sample material on a broader range of frequency. Furthermore, for the specific purpose of achieving the strong coupling regime, the quality factor of the SRR should be as close as possible to the quality factor of the resonance of the sample material[14, 15]. This means our goal is not necessarily to have the highest quality factor possible. In case we need to purposefully decrease the quality factor of a SRR, it is highly preferable to do so by increasing the radiative losses rather than the internal ones, since they also improve the coupling with the THz-TDS system. Thus we want to decrease as much as possible the internal losses, and use the radiative losses to tune the quality factor.

To keep the ohmic losses as low as possible:

1. We use gold for the fabrication, as it is a good conductor in the THz range, and does not oxidize.
2. We chose a thickness of 500 nm, larger than the skin depth of Gold in the THz.
3. We use relatively large branches and scale their width with their length, such that the large SRRs designed for low frequency do not have more ohmic resistance than the one designed for higher frequency. ($\frac{w}{a_x} = 0.1$)

We performed FDTD simulation for such a SRR, using tabulated gold permittivity in the THz[16]. This design reaches quality factors up to 40. For comparison, the

Lorentz resonance of Glutamic Acid at 1.2 THz has a quality factor $Q_{GA} \simeq 29.3$. Therefore our design is perfectly suitable to reach the criteria $Q_{SRR} = Q_{GA}$, leading to the highest possible Rabi splitting frequency[15].

2.1.3 Field confinement volume



Figure 2.10: SRRs with identical $\frac{A}{C}$ ratio, but decreasing confinement volume.

Our main goal is to use the highly confined electric field provided by a SRR to probe the properties of a sample material at scales ranging from a few tens of nanometers, to several micrometers. For this purpose, we need to be able to control the field confinement volume without changing too much the other properties of the resonator.

The electric field confinement volume is defined by the shape of the capacitor. In any capacitance model, the value of C is roughly proportional to the surface area available for charge accumulation, and inversely proportional to the distance between the two conductors forming the capacitor. Unless the distance G (see figure 2.9a for definition of the SRR dimensions) is much smaller than the thickness of the SRR, we cannot define an accurate value for the surface area as in the parallel plates capacitor model. To design our resonator, we approximate the surface area as being directly proportional to A . Under this approximation, we can change the confinement volume without changing the capacitance as long as we keep a constant ratio $\frac{A}{C}$. To avoid extremely thin branches that would cause high ohmic losses, we adopt a trapezoidal design for the capacitor branches. Figure 2.10 shows three SRRs designed to have the same capacitance but widely different field confinement volume.

2.1.4 Coupling with the sample material

When coupling the capacitor of the SRR with a sample material, the best coupling possible would be similar to the cross section represented in figure 2.11a. As discussed in chapter 1, a significant part of the electric field is actually confined in the substrate. The only way to prevent this would be to chemically under-etch the substrate (See figure 2.11b). However, this solution would greatly complexify the experiment as one would need to fill the irregularly shaped cavity formed under the gap.

Leaving the under-etching solution aside, it is still possible to optimize the coupling efficiency with the choice of the substrate material. Indeed the energy stored in a capacitor is given by

$$E = \frac{1}{2}Cu^2. \quad (2.7)$$

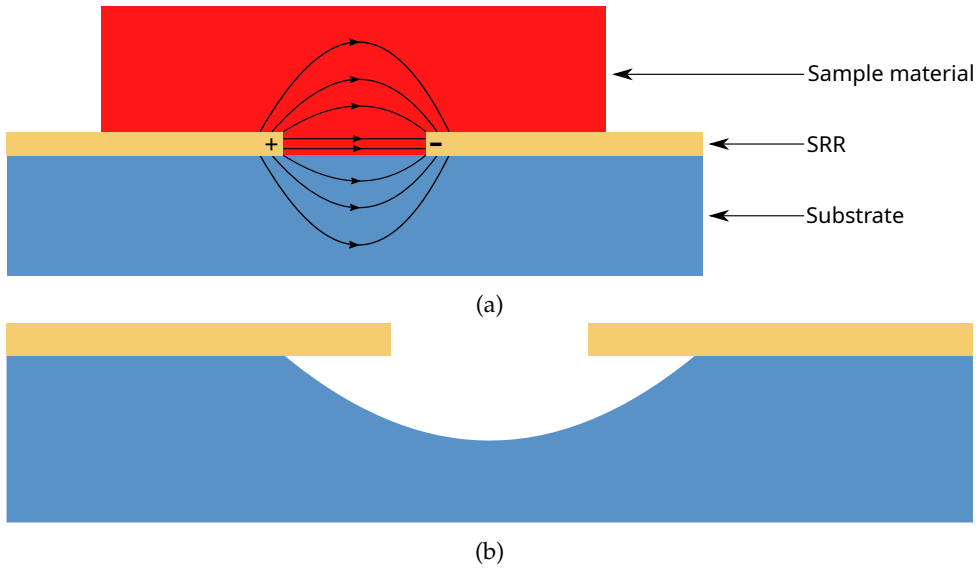


Figure 2.11: **(a)**: Cross section of a SRR gap on substrate ideally coupled to a sample material. **(b)**: Schematic cross section of a gap with an under-etched substrate. This technique can technically improve the coupling, under the condition that one can efficiently fill the cavity formed under the gold.

We have seen in chapter 1 that the capacitor is equivalent to two capacitors in parallel, one being filled with the substrate material while the other one is filled either with the sample material, or a mix of air and sample material. Since the capacitance is directly proportional to the permittivity of the filling medium, one can decrease the proportion of the resonator energy interacting with the substrate rather than the sample by choosing a substrate with a low permittivity.

Choice of the substrate material

Since we are probing our SRRs with THz-TDS in transmission, the main requirements for the substrate material are:

1. Very transparent in the TDS bandwidth, i.e. from 200 GHz to 6 THz.
2. Compatible with a lithography process
3. Low refractive index

The first two point leave us with the following main candidates: Silicon, Germanium, quartz and diamond. Quartz is more suitable for our application as it has the lowest permittivity $\epsilon_{\text{SiO}_2} = 4.41$. There exist material with even lower permittivity, such as organic material like Kapton or PTFE[17], or even exotic material like silica based aerogel[18]. But fabrication processes on those materials are not nearly as mature as processes on SiO_2 , and developing them is out of the scope of this thesis.

2.1.5 Conformity with the RLC model

Our last criteria for the SRR is the validity of all the hypotheses of the RLC model developed in chapter 1. The most critical hypothesis is the quasi-static approximation. The simulated resonance frequency of a resonator with dimensions $a_x = a_y = 30 \mu\text{m}$ and gap ratio $\frac{A}{C} = 1$ is $f_0 = 1.5 \text{ THz}$, which correspond to a wavelength $\lambda = 200 \mu\text{m}$.

The perimeter of each loop of such a resonator is $l = 90 \mu\text{m}$ which is only slightly less than half the resonant wavelength. Such SRR is very close to the limit of validity of the model. Note that going away from the model is not a bad thing on its own, but it makes the interpretation of the result more difficult, hence why we choose to stay as close as possible to the model conditions. Reducing the length of the loops also reduces the inductance, which has to be compensated with higher capacitance value. Therefore it is preferable to use SRR with higher $\frac{A}{G}$ ratio like the ones represented in figure 2.7a and 2.7b whenever it is compatible with the desired confinement volume.

Another hypothesis made for the RLC model is the absence of losses in the substrate. This criteria was already checked in the previous subsection.

2.2 Fabrication

2.2.1 Main process

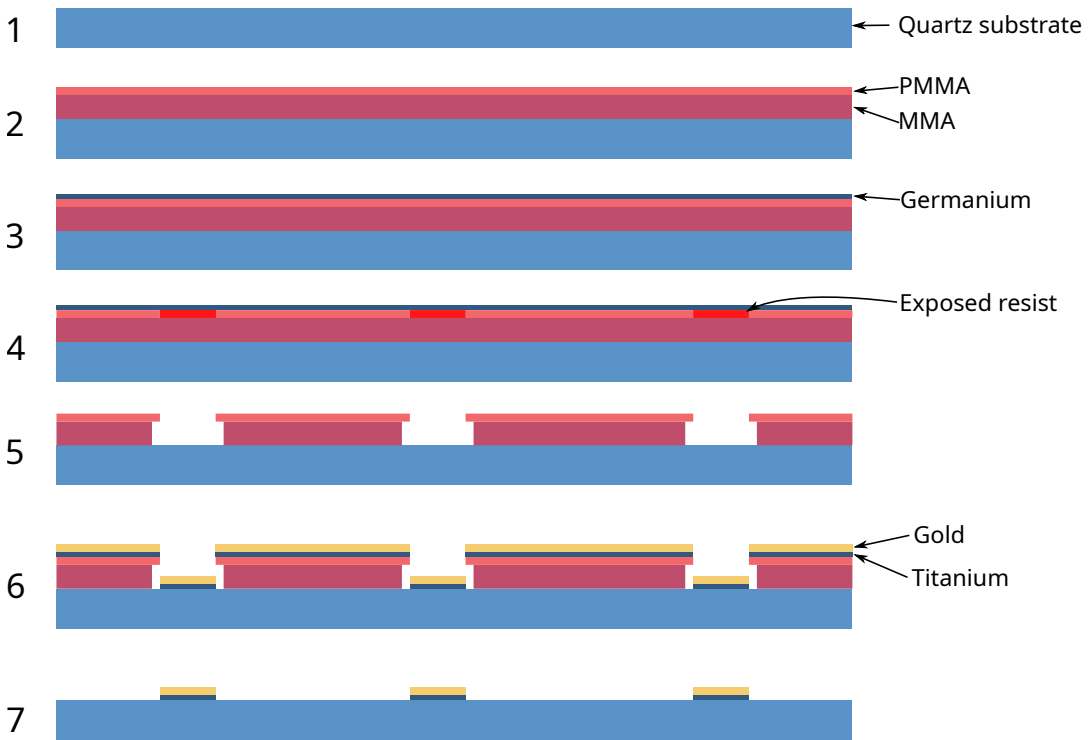


Figure 2.12: Schematic illustration of the resonator fabrication process.

We have defined all the main characteristics of our SRR design. In particular, we decided that they would be 500 nm thick gold structures fabricated on a Quartz substrate. We fabricate them with an electron beam lithography process. The main step of the process, illustrated in figure 2.12, are:

1. Cleaning of a bare quartz substrate using piranha solution (2 part sulfuric acid for 1 part hydrogen peroxide). In addition to the cleaning, the highly oxidizing piranha makes the surface hydrophilic by introducing $-\text{OH}$ termination (hydroxylation). This ensures a good and reproducible adhesion of the resist coating.

2. Spin-coating of a double positive resist layer (MMA/PMMA). The bottom layer is 800 nm thick, the top layer is $\simeq 20$ nm thick.
3. Deposition of 10 nm Ge layer by electron-beam evaporation. Because the substrate is insulating, this step is necessary to make the substrate the sample conductive and avoid charge accumulation during the e-beam writing step.
4. Electron beam writing of the SRR shape. The exposure makes the top resist layer locally soluble in the developer.
5. Ge removal using hydrogen peroxide and resist development. The different dissolution rate of the two layers creates the undercut profile necessary for the lift-off.
6. Deposition of a 20 nm thick layer of titanium for the adhesion and 500 nm of gold.
7. Stripping of the remaining resist to remove everything but the SRRs (Lift-off).

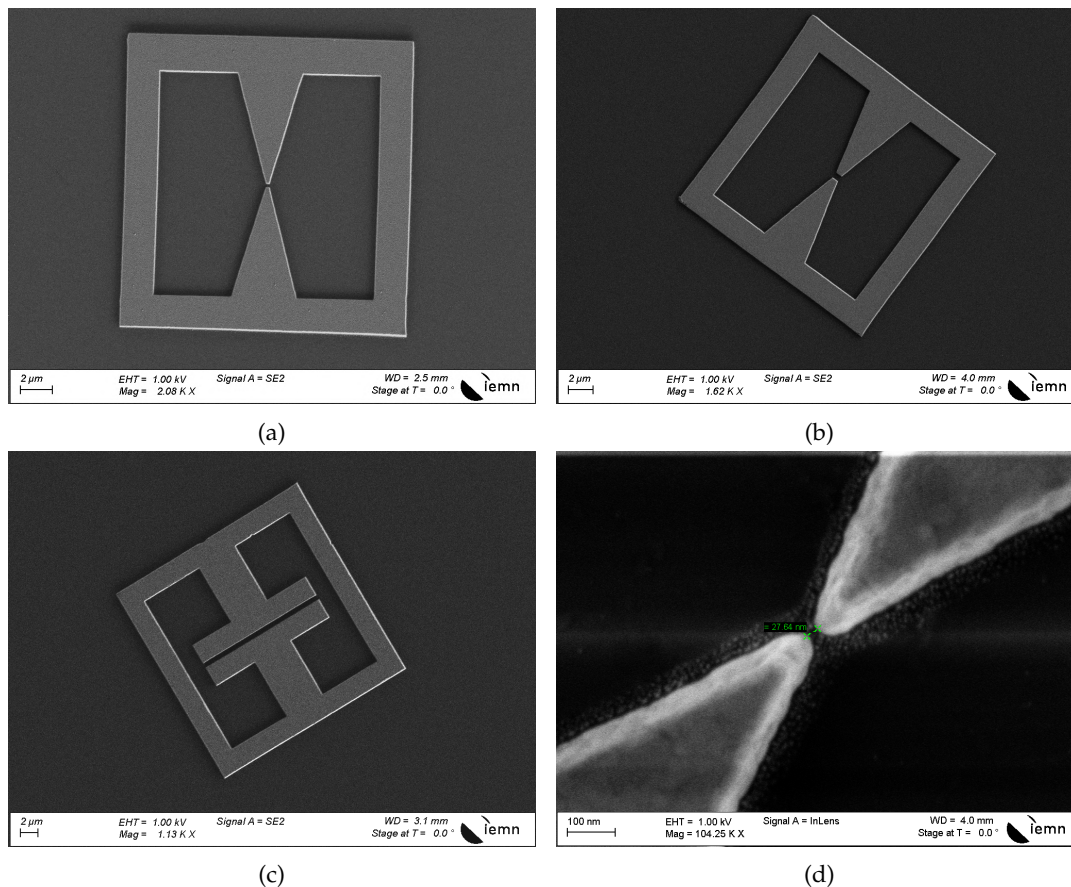


Figure 2.13: SEM images of fabricated SRRs. (a), (b) and (c): Examples with different parameters. (d): Close up view on a ~ 28 nm gap.

Figure 2.13 shows SEM images of SRRs fabricated according to this process. We observe an excellent conformity with the desired shapes. We were able to achieve gap sizes less than 30 nm on a thinner SRR (200 nm), as shown in figure 2.13d. For a

SRR with a resonance at $\lambda_0 = 100 \mu\text{m}$, this correspond to a confinement volume

$$V \simeq 30 \text{ nm} \times 30 \text{ nm} \times 200 \text{ nm} = \left(\frac{\lambda_0}{1770} \right)^3. \quad (2.8)$$

2.2.2 Optional surface treatment

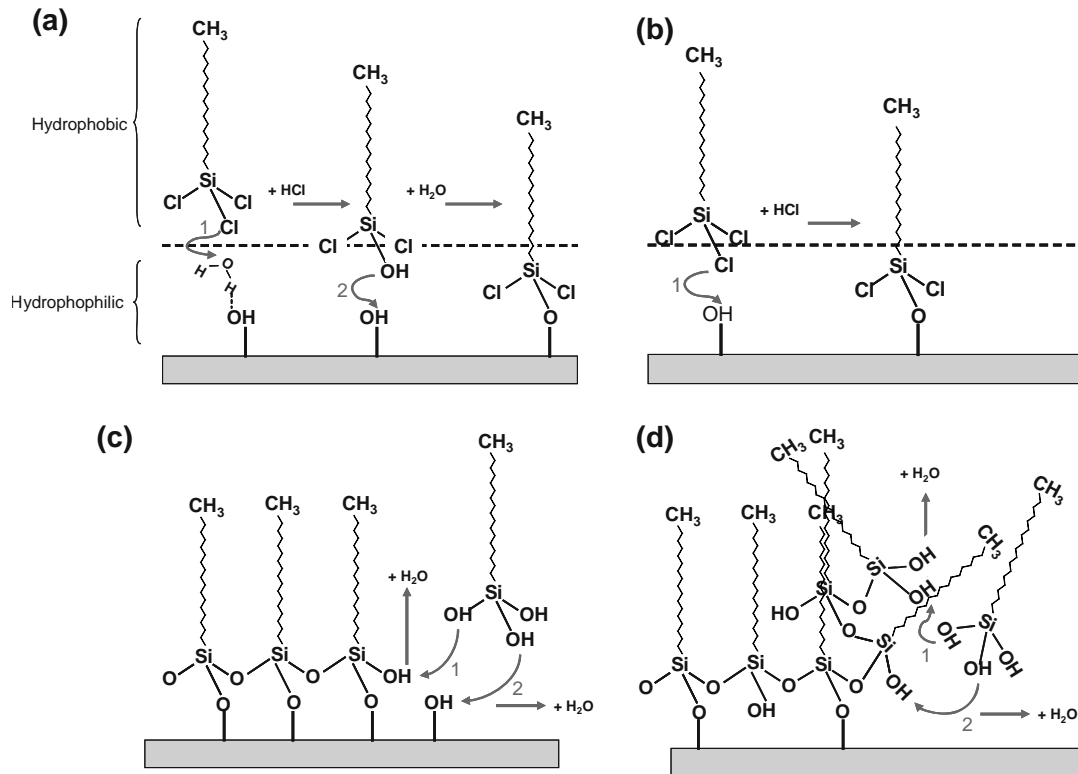


Figure 2.14: Schematic illustration of the OTS adsorption on the sample, depending on the initial surface state. **(a)** and **(b)**: Two possible adsorption mechanisms (ligand exchange and direct hydrolysis). **(c)** Ideal situation where the initial surface state presents a high density of hydroxyls, and the OTS forms a hydrophobic monolayer. **(d)**: disorganized adsorption resulting from a low density of hydroxyls. The initial treatment of the quartz substrate with piranha solution should ensure an ideal hydroxyl density. Figure reproduced from [19].

To couple the SRRs with a material such as amino acid crystals, some method involve the deposition of a droplet of saturated solution on a SRR, for the material to crystallize directly on the SRR (see chapter 4). To improve the chances of a crystal actually forming on the SRR and not somewhere around, the droplet should be as small as possible. At the end of the previously described process, we are left with a highly hydrophilic sample. This causes the droplets to spread out on a large surface, which not only reduces the chances of getting a crystal on the SRR, but also speeds up the evaporation, and thus reduces the quality of the crystals. To improve the viability of this deposition method, we use surface functionalization with Octadecyltrichlorosilane (OTS). the OTS molecules form a hydrophobic self-assembled monolayer on a surface densely populated with hydroxyl groups –OH as illustrated on figure 2.14[19]. The surface of quartz previously treated with piranha solution is ideal for this surface functionalization[20].

We start by cleaning the surface with UV/Ozone for 15 minutes to remove potential contaminants[21]. Then we let the sample react in a solution of 20 μ L OTS diluted in enough Hexane to cover the sample for another 15 minutes. The sample is then rinsed several times with clean Hexane to remove the excess OTS. Because OTS is highly reactive with water, the reaction and first rinse are done under a dry nitrogen atmosphere. Figure 2.15 shows the comparison of a water droplet on the sample after OTS treatment, compared to a water droplet on an untreated quartz substrate. We successfully made the sample hydrophobic with a contact angle greater than 90° .

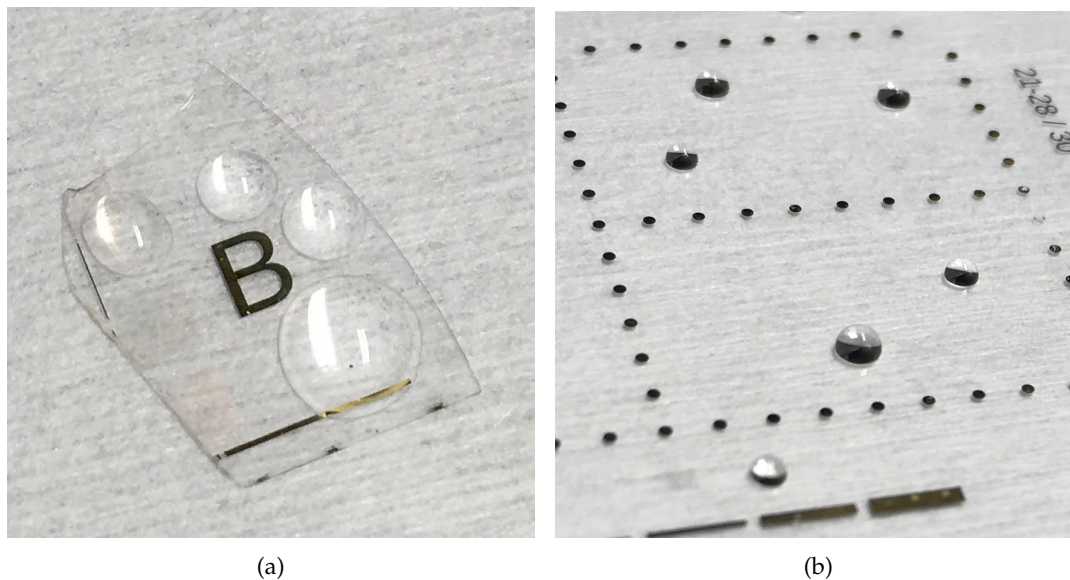


Figure 2.15: Comparison of the shape of water droplets on quartz with different surface states. **(a)**: Quartz substrate after cleaning in piranha solution. **(b)**: Sample after OTS surface functionalization.

2.3 Limitation of the design and process

We studied in detail how to design a SRR optimized for far-field measurement and capacitive coupling, with a wide control over its directivity, its quality factor and over the electric field confinement, even though the precise nature of the relation between the radiative decay rate and the SRR shape are still to be clarified. Although it is possible to design SRRs with strong directivity, it requires larger structure, incompatible with the quasi-static approximation. We demonstrated the viability of the e-beam lithography process to fabricate SRRs with gap sizes down to a few tens of nanometers. In an experiment on a SRR array, all the SRRs need to be virtually identical, which requires a fabrication process with an excellent yield. Since we are aiming at experiments on single resonators, any yield above 10% would be viable. Hence we can afford to aim at gap sizes at the edge of the possibilities offered by e-beam lithography. Alternatively, we can reach even smaller dimensions with a two step process for thinner gold close to the center of the SRR, and directly cutting a gap with Focused Ion Beam (FIB), then the limit is not the fabrication process, but quantum effects such as electrons tunneling through the gap for gap sizes smaller than a few nanometers[22]. Such effects would drastically change the nature of the resonator. This kind of SRRs would open the way to spectroscopy and optical trapping of single proteins.

In the next chapters, we will characterize the near-field and far-field properties of the fabricated SRRs, in order to check the viability of the analytical model, and proceed to the coupling experiment with dispersive material.

References

- [1] Donald Foster. “Loop Antennas with Uniform Current”. In: *Proceedings of the IRE* 32.10 (Oct. 1944), pp. 603–607. DOI: [10.1109/jrproc.1944.233062](https://doi.org/10.1109/jrproc.1944.233062) (cit. on pp. 32, 38).
- [2] Jordi Naqui, Miguel Duran-Sindreu, and Ferran Martin. “Modeling Split-Ring Resonator (SRR) and Complementary Split-Ring Resonator (CSRR) Loaded Transmission Lines Exhibiting Cross-Polarization Effects”. In: *IEEE Antennas and Wireless Propagation Letters* 12 (2013), pp. 178–181. DOI: [10.1109/lawp.2013.2245095](https://doi.org/10.1109/lawp.2013.2245095) (cit. on p. 33).
- [3] J.D. Baena et al. “Equivalent-circuit models for split-ring resonators and complementary split-ring resonators coupled to planar transmission lines”. In: *IEEE Transactions on Microwave Theory and Techniques* 53.4 (Apr. 2005), pp. 1451–1461. DOI: [10.1109/tmtt.2005.845211](https://doi.org/10.1109/tmtt.2005.845211) (cit. on p. 33).
- [4] W. N. Hardy and L. A. Whitehead. “Split-ring resonator for use in magnetic resonance from 200-2000 MHz”. In: *Review of Scientific Instruments* 52.2 (Feb. 1981), pp. 213–216. DOI: [10.1063/1.1136574](https://doi.org/10.1063/1.1136574) (cit. on p. 33).
- [5] W Froncisz and James S Hyde. “The loop-gap resonator: a new microwave lumped circuit ESR sample structure”. In: *Journal of Magnetic Resonance* (1969) 47.3 (May 1982), pp. 515–521. DOI: [10.1016/0022-2364\(82\)90221-9](https://doi.org/10.1016/0022-2364(82)90221-9) (cit. on p. 33).
- [6] R. A. Shelby. “Experimental Verification of a Negative Index of Refraction”. In: *Science* 292.5514 (Apr. 2001), pp. 77–79. DOI: [10.1126/science.1058847](https://doi.org/10.1126/science.1058847) (cit. on p. 33).
- [7] N. Katsarakis et al. “Electric coupling to the magnetic resonance of split ring resonators”. In: *Applied Physics Letters* 84.15 (Apr. 2004), pp. 2943–2945. DOI: [10.1063/1.1695439](https://doi.org/10.1063/1.1695439) (cit. on p. 33).
- [8] Fusheng Ma et al. “Tunable multiband terahertz metamaterials using a reconfigurable electric split-ring resonator array”. In: *Light: Science & Applications* 3.5 (May 2014), e171–e171. DOI: [10.1038/lsa.2014.52](https://doi.org/10.1038/lsa.2014.52) (cit. on p. 33).
- [9] Tao Xu, Ruijia Xu, and Yu-Sheng Lin. “Tunable terahertz metamaterial using electrostatically electric split-ring resonator”. In: *Results in Physics* 19 (Dec. 2020), p. 103638. DOI: [10.1016/j.rinp.2020.103638](https://doi.org/10.1016/j.rinp.2020.103638) (cit. on p. 33).
- [10] Mingkai Liu et al. “Tunable Meta-Liquid Crystals”. In: *Advanced Materials* 28.8 (Dec. 2015), pp. 1553–1558. DOI: [10.1002/adma.201504924](https://doi.org/10.1002/adma.201504924) (cit. on p. 33).
- [11] Gerald Cooray and Vernon Cooray. “ELECTROMAGNETIC FIELDS OF A SHORT ELECTRIC DIPOLE IN FREE SPACE – REVISITED”. In: *Progress In Electromagnetics Research* 131 (2012), pp. 357–373. DOI: [10.2528/pier12071601](https://doi.org/10.2528/pier12071601) (cit. on p. 33).
- [12] John D. Kraus. *Antennas*. McGraw-Hill, 1950 (cit. on pp. 36, 38).
- [13] A.A. Pistolkors. “The Radiation Resistance of Beam Antennas”. In: *Proceedings of the IRE* 17.3 (Mar. 1929), pp. 562–579. DOI: [10.1109/jrproc.1929.221705](https://doi.org/10.1109/jrproc.1929.221705) (cit. on p. 41).

- [14] Ran Damari et al. "Strong coupling of collective intermolecular vibrations in organic materials at terahertz frequencies". In: *Nature Communications* 10.1 (July 2019). DOI: [10.1038/s41467-019-11130-y](https://doi.org/10.1038/s41467-019-11130-y) (cit. on p. 41).
- [15] Thomas W. Ebbesen. "Hybrid Light-Matter States in a Molecular and Material Science Perspective". In: *Accounts of Chemical Research* 49.11 (Oct. 2016), pp. 2403–2412. DOI: [10.1021/acs.accounts.6b00295](https://doi.org/10.1021/acs.accounts.6b00295) (cit. on pp. 41, 42).
- [16] Mark A. Ordal et al. "Optical properties of Au, Ni, and Pb at submillimeter wavelengths". In: *Applied Optics* 26.4 (Feb. 1987), p. 744. DOI: [10.1364/ao.26.000744](https://doi.org/10.1364/ao.26.000744) (cit. on p. 41).
- [17] Paul D. Cunningham et al. "Broadband terahertz characterization of the refractive index and absorption of some important polymeric and organic electro-optic materials". In: *Journal of Applied Physics* 109.4 (Feb. 2011), pp. 043505–043505–5. DOI: [10.1063/1.3549120](https://doi.org/10.1063/1.3549120) (cit. on p. 43).
- [18] Jiangquan Zhang and D. Grischkowsky. "Terahertz Time-Domain Spectroscopy Study of Silica Aerogels and Adsorbed Molecular Vapors". In: *The Journal of Physical Chemistry B* 108.48 (Nov. 2004), pp. 18590–18600. DOI: [10.1021/jp046869b](https://doi.org/10.1021/jp046869b) (cit. on p. 43).
- [19] Elnaz Ajami and Kondo-Francois Aguey-Zinsou. "Formation of OTS self-assembled monolayers at chemically treated titanium surfaces". In: *Journal of Materials Science: Materials in Medicine* 22.8 (June 2011), pp. 1813–1824. DOI: [10.1007/s10856-011-4356-x](https://doi.org/10.1007/s10856-011-4356-x) (cit. on p. 46).
- [20] Ran Zhang et al. "Investigating the Role of Glass and Quartz Substrates on the Formation of Interfacial Droplets". In: *The Journal of Physical Chemistry C* 123.2 (Dec. 2018), pp. 1151–1159. DOI: [10.1021/acs.jpcc.8b08492](https://doi.org/10.1021/acs.jpcc.8b08492) (cit. on p. 46).
- [21] John R. Vig. "UV/ozone cleaning of surfaces". In: *Journal of Vacuum Science & Technology A: Vacuum, Surfaces, and Films* 3.3 (May 1985), pp. 1027–1034. DOI: [10.1116/1.573115](https://doi.org/10.1116/1.573115) (cit. on p. 47).
- [22] Li Mao et al. "Effects of quantum tunneling in metal nanogap on surface-enhanced Raman scattering". In: *Applied Physics Letters* 94.24 (June 2009), p. 243102. DOI: [10.1063/1.3155157](https://doi.org/10.1063/1.3155157) (cit. on p. 47).

Chapter 3

Near-field characterization

Most of the results presented in this chapter were published in ACS Applied Materials & Interfaces[1].

3.1 Near-field

In the previous chapters, we designed and fabricated Split Ring Resonators (SRRs) theoretically optimized to provide strong electric field enhancement in their capacitive gaps. Furthermore, working with single resonators allows us to push our fabrication process to its limit, with gap sizes down to 30 nm. In a context where the field confinement is the main feature of our design, and is likely to deviate from the simulation due to fluctuations in the fabrication process, characterization of the field profile is necessary. The gap size of a SRR, typically between a few tens of nanometers and a few micrometers, is far below the diffraction limit in the THz range. Thus the characterization of the field profile is only possible through near-field microscopy.

The idea of using near-field microscopy for imaging beyond the diffraction limit is not specific to THz. The concept of near-field microscopy was first mentioned by Syngé in 1928 in an article entitled “*A suggested method for extending microscopic resolution into the ultra-microscopic region*”[2]. He suggested using an intensely illuminated 10 nm aperture in an opaque plate to scan a sample and construct an image with a resolution that only depends on the diameter of the aperture. The described method corresponds to the main principles of modern aperture Scanning Near-field Optical Microscopy (a-SNOM)[3]. The first experimental demonstration of this method was performed in the microwave range by Ash et al., who achieved a resolution of $\lambda/60$ [4]. With the progress made to accurately control displacements at the nano-scale, near-field microscopy was then brought up to the visible range[5–7].

In the THz range, microscopy techniques have been developed, relying on the detection of the evanescent near-field[1]. Typically, these schemes detect the interactions between THz radiation, the sample and a raster-scanning sub- λ probe [8]. Different imaging apparatus and near-field probes have been explored to reach sub- λ resolution: In THz emission microscopy, the probe is a focused femtosecond laser beam of shorter wavelength interacting with the sample, or the substrate beneath, to emit THz radiation [9, 10]. Additionally, solid probes illuminated by THz radiation such as photoconductive (PC) detectors [11–13], electro-optic sensors [14], waveguides [15] or tips with [16] or without aperture [17] have demonstrated the ability to detect the near-field. It is also worth mentioning that out of scanning microscopy schemes, real-time THz microscopy has been demonstrated, but requires objects to be placed on electro-optic crystals [18].

3.2 s-SNOM

Scattering Scanning Near-field Optical Microscopy (s-SNOM) is an aperture-less near-field imaging method. It uses the probe of an Atomic Force Microscope (AFM) operating in intermittent tapping mode to scan a sample under external illumination. The sharp probe couples to the electric field at the surface of the sample, and scatters it in the far-field.

In the simplest model, the probe is reduced to its apex, approximated as a sub-wavelength polarizable sphere[3] (see 5.2 on page 101 for more detail on polarizability), and the scattered field is estimated with the point electric dipole model. With this model, the scattered intensity is proportional to the local field intensity, in accordance with Rayleigh scattering[19], and to the squared modulus of the tip polarizability, which itself depends on the properties of the surrounding materials. However, the validity of this model is quite limited, especially in the THz range where the probe giving the best results are long metallic (or metal coated) tips, with a length in the order of magnitude of the wavelength. Such probes are more accurately described as antennas, rather than point dipoles.

By measuring the scattered field, a s-SNOM produces images with resolution much finer than the wavelength. The highest resolution recorded to date in the THz is less than 15 nm[20].

3.2.1 Set-up description

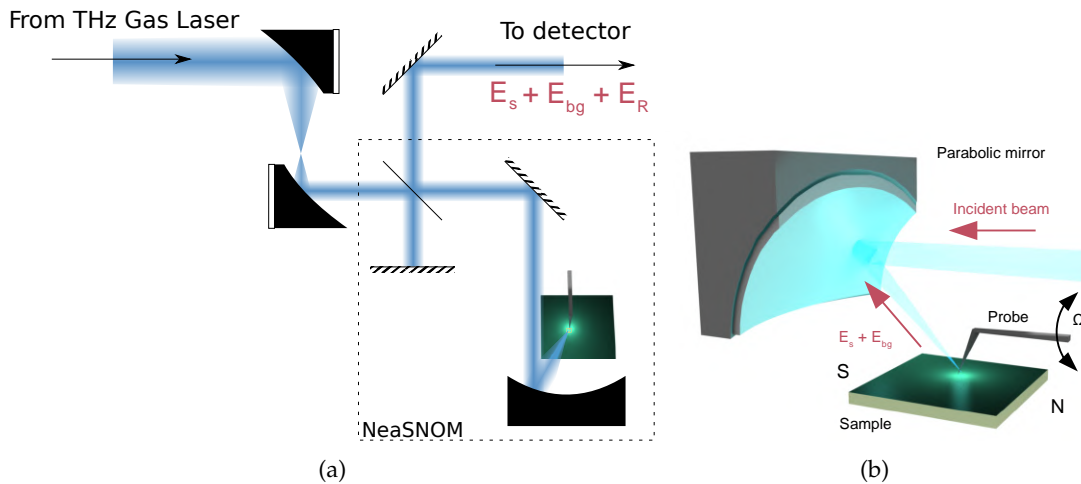


Figure 3.1: Schematic representation of the s-SNOM setup (not to scale). **(a)**: The beam of a CO₂-pumped methanol gas laser enters the interferometer of the microscope and is focused by a parabolic mirror on the tip in intermittent contact with the sample. The parabolic mirror also collects the scattered near-field and the background. Optical signals are combined with the reference arm of the interferometer and detected by an InSb hot electrons bolometer. We use a mylar beam-splitter for the interferometer. **(b)**: Side view of the parabolic mirror, the probe and the sample. The NS axis is defined as the direction orthogonal to the parabolic mirror[1].

We employ a s-SNOM apparatus based on the NeaSNOM microscope from NeaSpec¹. The THz source is a CO₂ pumped methanol gas laser (FIRL-100, Edinburgh

¹https://www.qd-latam.com/_libs/dwns/668.pdf

Instruments²) emitting at 2.522 THz (continuous wave). To adapt the beam size to the dimension of the internal optics of the neaSNOM, the beam size is reduced with a set of two confocal parabolic mirrors. In addition, this set of mirrors also allows to compensate for the non negligible diffraction of the THz beam along the one meter long path between the laser and the microscope. At the entrance of the integrated interferometer of the microscope, we measured typical constant optical power during a scan between 20 and 40 mW.

The incident beam is polarized in the plane of incidence (p-polarized), consequently, there is an incident vertical component that is parallel to the tip and efficiently coupled with its long metal-coated shaft (see 3.2.4). This configuration was selected through trial and error since attempts of s-SNOM imaging with an incident s-polarized beam exhibited poor signal-to-noise ratios and electric field concentrations were indistinguishable for SRRs oriented with $\psi = 0$ or 90° (not shown), with ψ defined as the angle between the SRR and the NS axis (axis defined in figure 3.1). It can be explained by the fact that, with s-polarization, the coupling of the incident radiation with the tip is very low. The resulting coupling between the weakly concentrated light and the SRR is lower compared to the p-polarization where light is efficiently coupled to the tip. For $\psi = 90^\circ$ and with s-polarization, the incident electric field is ideally polarized to couple directly to the SRR. The poor signal to noise ratio in this configuration suggests that the tip does not efficiently perturbs the field distribution due to its small coupling with the SRR.

Inside the microscope is a Michelson interferometer with a plane mirror for the reference arm. On the other arm, the beam is focused on the AFM stage with another parabolic mirror. The scattered field is collected with the same parabolic mirror, combined with the reference beam and sent to the detector. The interferometer increases the sensitivity of the microscope by converting phase modulations to amplitude modulations.

The detector is a pulse-tube-cooled InSb hot electron bolometer (QMC Instruments). This detector is polarization independent. However the phase modulation is detected by interference with a polarized reference beam, thus the detection *scheme* is polarization dependent.

3.2.2 Detection scheme

To discriminate the near-field signal from the so-called background signal (i.e. any light reflected independently from the near-field interaction), we use homodyne detection (HD)[21]: the AFM probe oscillates at a frequency Ω close to its eigenfrequency and the signal is demodulated at the higher order harmonics of the probe driving frequency $n\Omega$, where n is an integer. Hence the parts of the signal that are independent or linearly dependent on the probe vertical position are eliminated. Going to higher harmonics, we decrease the proportion of background signal, but we also decrease the overall signal intensity and thus the signal to noise ratio. Unless specified otherwise, all the images shown in this chapter are demodulated at the second harmonic ($n = 2$), as it is most often the best compromise between noise and background reduction.

In the HD scheme, the intensity received by the detector and demodulated at $n\Omega$ can be expressed as:

$$I_n = [|E_s|^2]_n + 2 [|E_s||E_{bg}| \cos(\phi_s - \phi_{bg})]_n + 2 [|E_s||E_R| \cos(\phi_s - \phi_R)]_n, \quad (3.1)$$

²<https://www.edinst.com/products/firl-100-pumped-fir-system/>

where $[x]_n$ is the variable x demodulated at the harmonic $n\Omega$, and ϕ_s , ϕ_{bg} and ϕ_R are the respective phases of the scattered near-field, the background and the reference beam. Equation (3.1) can be approximated as equation (3.2), provided that $|E_R| \gg |E_{bg}|$:

$$I_n \approx [|E_s|^2]_n + 2 [|E_s| |E_R| \cos(\phi_s - \phi_R)]_n. \quad (3.2)$$

The HD scheme in pair with the interferometer detects a product of the amplitude and phase modulation. The phase and amplitude information cannot be separated with HD only. If we assume that the scattered field is only modulated in amplitude, then $|E_s|^2$ is more strongly modulated than $|E_s|$, and the demodulated signal is approximated as $I_n \approx [|E_s|^2]_n$. In that case, the reference arm can be completely removed. This configuration gives good results in the mid-IR range. However, when we do this experiment in the THz, the demodulated signal is much lower and we are not able to form an image. Hence we conclude that the phase modulation is a significant part of the signal in our image. Furthermore, since we experimentally demonstrated that the term $[|E_s|^2]_n$ is a negligible part of the demodulated signal, we approximate the intensity as:

$$I_n \approx [|E_s| |E_R| \cos(\phi_s - \phi_R)]_n. \quad (3.3)$$

To isolate the phase from the amplitude information, we use the pseudo-heterodyne detection (PHD) scheme, where we modulate the reference phase ϕ_R . In PHD scheme[22], the length of the reference arm of the interferometer is modulated by vibrating its mirror with a piezoelectric element at a frequency f . The phase modulation of the reference beam generates sidebands spaced by f in the $n\Omega$ -demodulated output signal of the detector. With the proper modulation depth, from these sidebands, amplitude free of multiplicative background and phase can be recovered. We used this method with $f = 305$ Hz and a modulation depth of a few tens of μm . Unfortunately, we were not able to produce a usable phase image with this method. We attribute this problem to the modulation amplitude of the mirror, which should ideally be of the same order of magnitude as the wavelength. The modulation offered by the neaSNOM microscope is perfectly suited for the mid-IR rather than the THz. Hence all the images presented in this chapter are measured in HD unless specified otherwise.

3.2.3 Test sample

Since s-SNOM imaging is an indirect method, it is not trivial to correctly interpret the measured images. We will develop in more detail the question of the image interpretation in section 3.4. To simplify as much as possible the interpretation, we select our SRR dimensions such that all the features are

- larger than the probe apex, to make sure we are not limited by the microscope resolution.
- larger than the SRR thickness, to keep the structure mostly planar even at the scale of the single SRR.
- much larger than the potential defects from the fabrication process, such that the fabricated SRR shape conforms to the design and we can reasonably trust the simulations.

To satisfy those conditions, we choose the simplified design illustrated in figure 3.2a, with rectangular branches, a gap size $G = 2 \mu\text{m}$ and a gold thickness $e = 200 \text{ nm}$.

Since the working frequency is imposed by the laser frequency, we need to find the right SRR dimensions for a resonance at 2.5 THz. We start with Finite Difference Time Domain (FDTD) simulation to get a rough estimation of the desired size. Then, we fabricate several arrays of resonators (period $50 \mu\text{m}$) with sizes around the FDTD estimation. Using THz Time Domain Spectroscopy (THz-TDS), we identify the SRRs whose resonance most closely matches the laser frequency. Figure 3.2b shows the measured transmission spectrum for SRR arrays on quartz substrate, with sizes ranging from $17 \mu\text{m}$ to $19 \mu\text{m}$. The transmission spectrum shows that the best suited dimension is $a = 19 \mu\text{m}$.

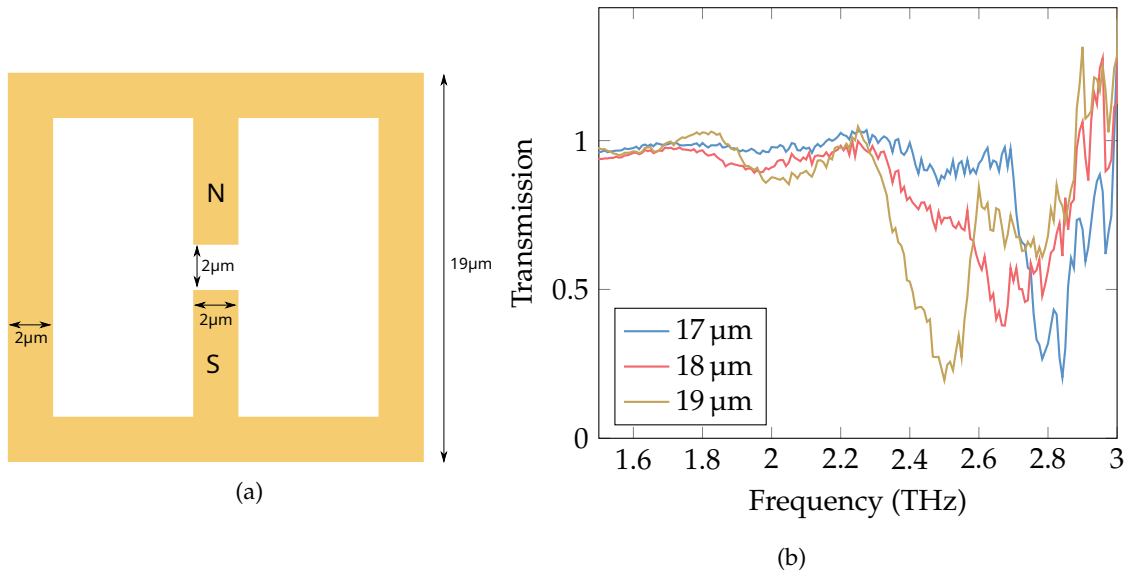


Figure 3.2: **(a)**: SRR design chosen for the s-SNOM experiment, and definition of the N arm and S arm. **(b)**: THz-TDS transmission measurements of arrays of resonators with different sizes on quartz. The spectra are normalized with the transmission through a bare quartz substrate. Those measurements are older than the one presented in chapter 4.

We claimed in chapter 2 that a SRR fabricated on a substrate with a low refractive index provides a better field enhancement than one on a substrate with a high refractive index, because a lower proportion of the energy ends up confined *in* the substrate. To test this claim, we also fabricate SRR on high resistivity silicon, which has a much higher refractive index in the THz ($n = 3.43$ as opposed to $n = 2.1$ for quartz). We expect a lower contrast from s-SNOM images on the silicon substrate. Using the same method as for the quartz substrate, we find that the best size for a resonance at 2.5 THz on a silicon substrate is $a = 13 \mu\text{m}$.

3.2.4 Enhanced probe for THz microscopy

The s-SNOM tip used for all the experiments was a Lprobe model “CT”. This probe was designed and fabricated by Vmicro[25] in collaboration with our research group. This probe is especially designed for THz s-SNOM experiments. Indeed, Maissen et al. demonstrated that the imaging resolution can be greatly increased by using long and ultrasharp s-SNOM tips, and achieved resolution down to 15 nm [20]. Additionally, a metal coated s-SNOM tip can be modeled as a dipole antenna excited

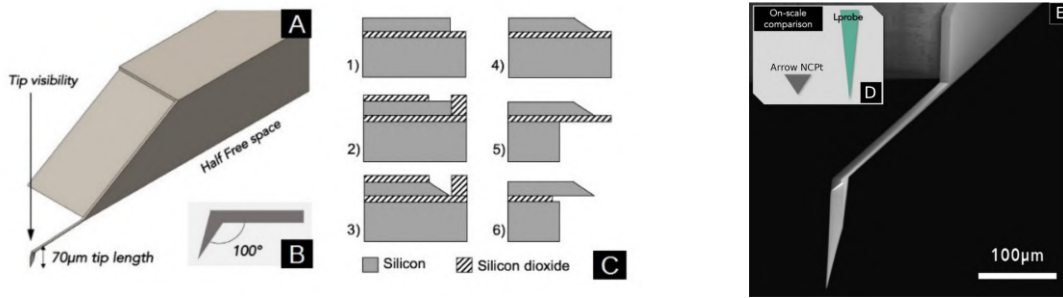


Figure 3.3: **A:** Schematic view of the Lprobe cantilever and its holder. **B:** The angle between the tip and the cantilever let an optical path to see the tip end from the top. **C:** Process flow for Lprobe micro-fabrication. See main text for detailed steps. **D:** On-scale comparison of tip aspect ratio between the Arrow NCPT probe (pyramidal shape, commonly used in AFM and s-SNOM[23]) and the Lprobe tip. **E:** SEM image of the Lprobe cantilever and tip[24].

by the near-field concentration on the sample[23]; hence, a longer tip (close to the excitation wavelength) will have a better scattering efficiency despite the small apex. The Lprobe aims at coping with these issues.

The fabrication process of such probes differs from all other commercially available cantilevers. The Lprobes are fabricated on a SOI (Silicon On Insulator) wafer. The cantilever and the tip are fabricated in the wafer plane, in the Device Layer (DL) which is the top silicon layer of the SOI wafer. The fabrication process gives access to a wide range of cantilever parameters regarding the resonant frequencies and stiffnesses as well as tip geometry. In this work, the angle between the tip and the cantilever is 100° and the tip length is $70\ \mu\text{m}$ (figure 3.3A-B). In figure 3.3C, we present the simplified process flow implemented by Vmicro :

1. Initial cantilever patterning with photolithography and plasma etching.
2. Oxide hard mask deposition.
3. Anisotropic chemical etching of the silicon using a KOH solution. The chemical etching stops on the $\langle 111 \rangle$ plane.
4. Oxide hard mask removal using an HF acid solution.
5. Back side plasma etching defines the AFM chip.
6. Final HF etching of the buried silicon.
7. Platinum coating

On figure 3.3E, we present the fabricated cantilever with up to $70\ \mu\text{m}$ long tips. Getting back to the probe properties described by Maissen et al. for nanoscopic resolution[20], the schematic on figure 3.3D is an on-scale comparison with an Arrow NCPT tip showing an aspect ratio improved by a factor 2.

3.3 Result

The long metallic AFM behaves as a dipole antenna polarized by the electric field at its apex. The polarizability of the probe is much higher along its length, thus we

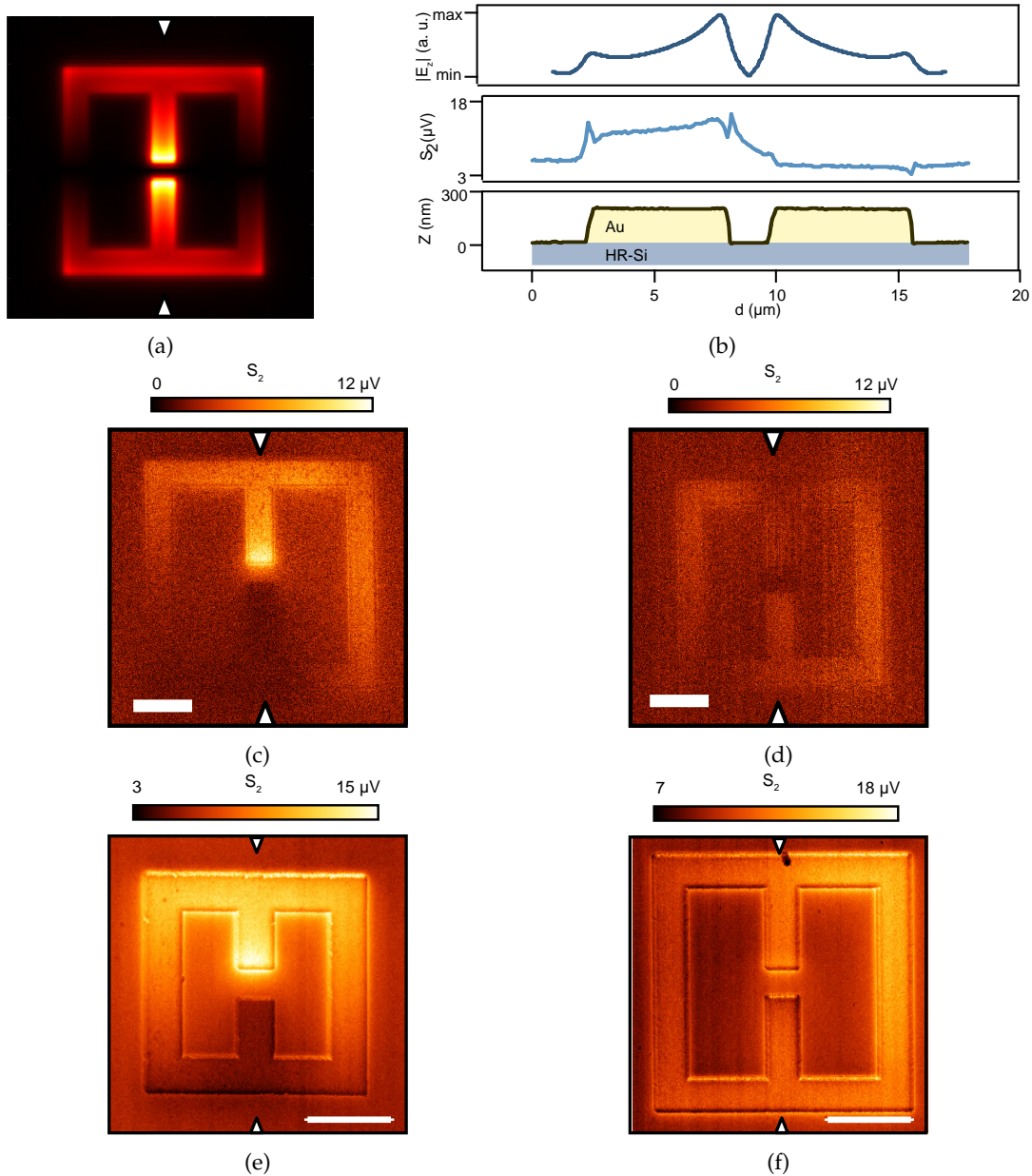


Figure 3.4: **(a)**: Simulated vertical component of the electric field on a plane above an excited SRR ($a = 19 \mu\text{m}$). **(b)**: Simulated, experimental and topographic cross section for a tuned SRR on Si. The sharp spikes in the experimental S_2 signal are artifacts from the topographic edge (see figure 3.6). **(c,d,e,f)**: Experimental s-SNOM images of 4 SRRs excited at 2.5 THz. **(c)**: Tuned SRR on quartz ($a = 19 \mu\text{m}$). **(d)**: detuned SRR on quartz ($a = 17 \mu\text{m}$). **(e)**: tuned SRR on silicon ($a = 13 \mu\text{m}$). **(f)** detuned SRR on silicon ($a = 17 \mu\text{m}$). Scale bars are $5 \mu\text{m}$.

expect the scattered field to scale with the z component of the electric field at the sample surface. Figure 3.4a shows the simulated vertical component of the electric field on a plane right above a SRR, simulated with FDTD. We can see that there is not much signal expected directly inside the gap, since the electric field is mostly orthogonal to the probe in this area. The maximum of signal is expected *on* the metal, at the edge of the gap.

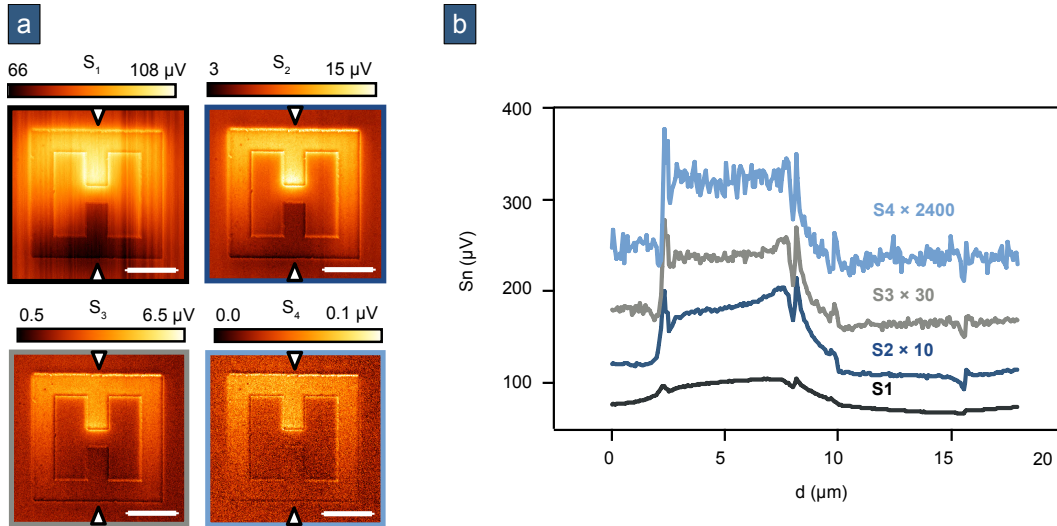


Figure 3.5: **(a)** s-SNOM images of a SRR demodulated at harmonic 1 to 4. **(b)**: Signal cross section along the axis indicated by white triangles in (a), with a 60 μV offset. Scale bars are 5 μm

Figure 3.4c and 3.4e respectively show the measured images of a resonating SRR on quartz and on silicon. For comparison, figure 3.4d and 3.4f show the measured image on detuned SRRs on both substrates.

s-SNOM images of the SRRs showed a bright and dark pattern on the arms of the structure: A bright region is imaged on the N arm of the resonator (as labeled on Figure 3.2a) with a local maxima located on the arm 500 nm away from the gap edge. As soon as the tip scans the S arm, the signal vanishes and gold appears darker than the substrate. This feature is observed on images from the 1st to the 4th harmonics of Ω (Figure 3.5). Note that typical dark fringe artifacts are also visible on the images when the probe encounters the edges of the SRR [26], but are distinct from the described features. Figure 3.6 highlights the edge artifacts on a signal cross section along the N-S axis.

The AFM topography did not show any contrast between the dark and bright areas of the device (Figure 3.6). This pattern was found to be identical on every tuned SRR we scanned, independently of its location in the array (Figure 3.7a).

When comparing the experimental images (Figure 3.4b,d) with the computed near-field distribution of the tuned SRR (Figure 3.4a), the upper half of the image is in good agreement with the FDTD simulation regarding the following features:

- There is a maximum at the edge of the N branch for both tuned SRRs.
- The contrast is higher for the SRR on the quartz substrate (+244% on quartz, against +111% on Si).
- The images of the detuned SRRs feature only material contrast and edge artifact, with no bright spot close to the gap.

In contrast, the lower part of the image strongly deviates from the predicted profile, with very low signal intensity close to the gap where the maximum is expected. The intensity at the edge of the S branch is even lower than on the substrate, both for quartz and silicon, which also differs with the images of the detuned SRRs, where the signal on gold is always slightly higher than the signal on the substrate.

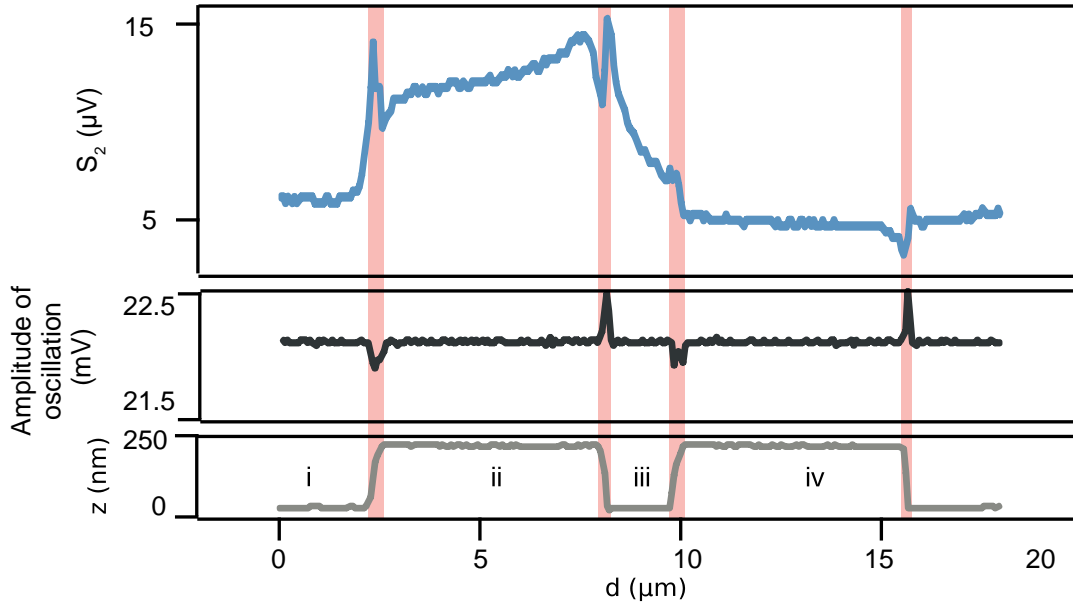


Figure 3.6: 2nd harmonic signal, probe oscillation amplitude, and topography measurement on a cross section of a SRR on silicon. The S_2 signal on the N branch (zone ii) matches the expected near-field, with a maximum close to the gap. In contrast, almost no signal is detected on the S branch (zone iv). The topography does not show any significant differences between the branches. The steep edges in the topography create artifacts[26] as they disturb the oscillation of the probe. The signal in the area highlighted in pink should not be taken into account in the image interpretation.

Similar designs of SRRs have been already studied by other THz microscopy techniques at larger scale[27–33] and do not exhibit N-S asymmetry. At smaller scale, in the work of Acuna et al.[34], authors used a technique similar to s-SNOM on SRRs but did not report this effect. However, in this study, a broadband THz source was used and authors attributed the image contrast to both the fundamental mode and surface plasmon polaritons.

To the best of our knowledge, the asymmetric feature was never reported in any THz s-SNOM previous to our work[1, 24, 35]. It was then reproduced in the recent work of Sulollari et al.[36, 37] and remains to be fully elucidated. It is worth mentioning that the observed asymmetries are similar to the patterns recently observed by Büchner et al. on IR plasmonic antennas [38]. In this work, authors attribute the asymmetry to the modification of the resonance of the antenna when strong coupling occurs between the probe and the antenna.

To help identify the origin of the asymmetry, we isolated a few hypothesis by performing a set of control experiments:

Multi-resonator effect: Since the measurements were performed in a resonator array, we suspected that the asymmetry may arise from interference with the field scattered by the surrounding SRRs. We restarted the experiment on an isolated SRR and obtained the same result with the same contrast and amplitude (figure 3.7b). This led us to conclude that the surrounding SRRs in an periodic array with a period of 50 μm do not disturb the s-SNOM experiment in any way.

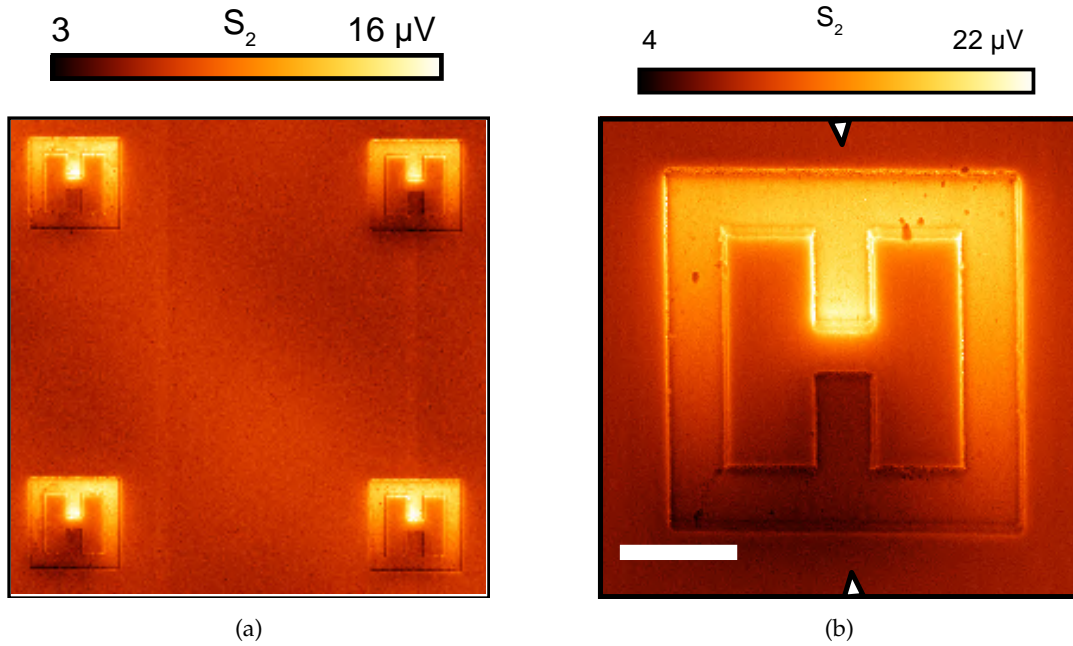


Figure 3.7: **(a)**: s-SNOM scan on 4 SRRs in a matrix. **(b)**: s-SNOM images of an isolated SRR. All SRRs give identical result. $a = 13 \mu\text{m}$ in both cases.

Phase contrast effect: If the asymmetry originated from an incidental phase contrast between the branches, we should expect to observe a reversed asymmetry for different positions of the reference mirror. We performed the experiment multiple times with different reference positions, and were never able to produce an image with a bright S arm and dark N arm. In addition, the measurement performed in pseudo-heterodyne detection instead of homodyne detection shows the same feature with a similar contrast (figure 3.8a). This observation excludes contrast with homodyne detection resulting from a phase shift between the N and S arms.

Effect linked to the probe: Since we performed the experiment with a custom made probe, we need to check that the probe is not responsible for the unexpected features of our measurements. We performed the experiment with a standard, shorter AFM probe (Arrow NCpt from NanoWorld, 10 – 15 μm pyramidal tip). Although this measurement does not accurately capture the field enhancement at the edge of the N branch, it does feature the same asymmetry as the measurement with the long Lprobe (figure 3.8b).

Effect specific to the SRR design: To get more insight regarding the nature of the phenomenon, we imaged another metallic structure able to couple with a THz field: the Log Spiral Antenna (LSA). The image of the LSA also features an asymmetry at the center, where the brightest field is expected (figure 3.9). In the case of the LSA, the asymmetry is inverted, as it is the N branch that is darker than the substrate close to the center. In the SRR images, the entire south half of the picture is darker than the north half. In contrast, with the LSA, the dark area follows the north branch along the spiral. This result confirms that N-S asymmetry is not limited to THz SRRs, and its reversal on the LSA excludes that it is simply caused by a shadowing effect of the cantilever.

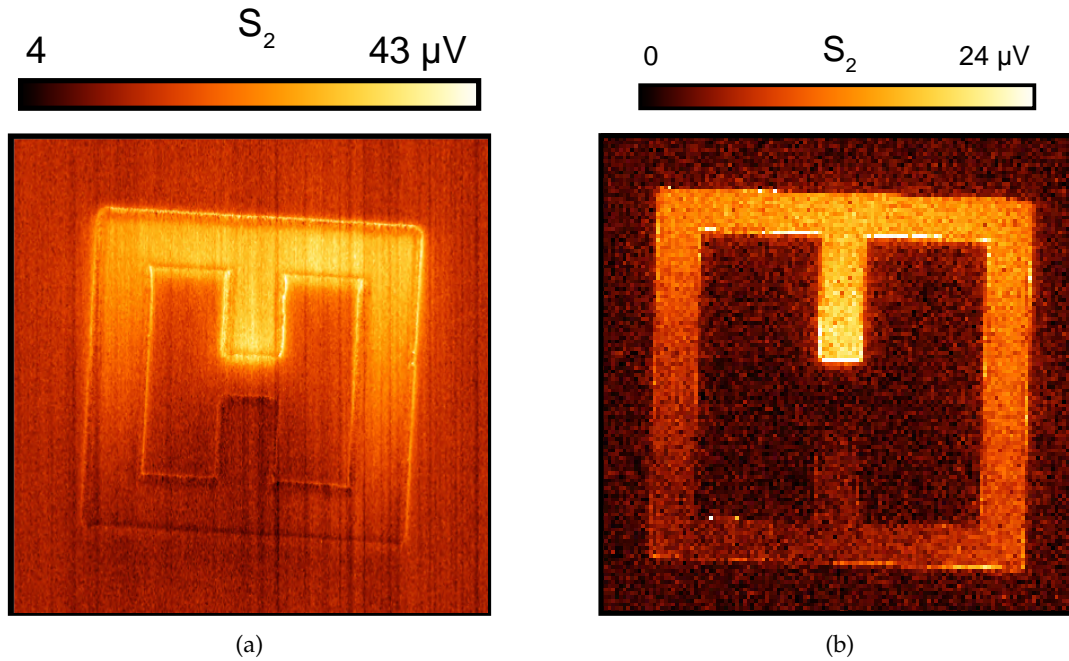


Figure 3.8: **(a)**: SRR on Si measured with PHD ($a = 13 \mu\text{m}$). **(b)**: SRR on quartz measured with a shorter AFM probe ($a = 19 \mu\text{m}$).

This series of experiments further confirms that N-S contrast is a general feature when confined near-fields of THz micro-resonators are scattered during s-SNOM imaging. In the following, we discuss the origin of this effect that we need to identify for future studies.

3.4 Discussion

We demonstrated the capability of the s-SNOM to recover information on the near-field distribution of the mode of a THz resonator. This is highlighted by the clear difference between the images of tuned and detuned SRRs, as it proves that the contrast in the picture does not originate only from the material contrast.

However, the image cannot be a direct representation of the field distribution, for such a distribution would break the Curie's symmetry principle[39]. An additional N-S contrast is also present on the images. At this point of our investigations, we cannot attribute the N-S contrast to any controllable parameter of the experiment. Indeed, we determined that N-S asymmetry is not specific to SRRs, does not originate from background, multi-resonators effect or phase-induced contrast. The asymmetry is also clearly observed on SRRs when we replaced the quartz substrate with high-resistivity silicon and changed the shape of the probe. Therefore, to elucidate the discrepancy between experimental data and calculations, we focused on the explanation of this contrast considering the origin of the measured s-SNOM signal.

The idea of imaging a photonic mode is based on the fact that the AFM probe acts as an antenna and scatters the field at its apex. Therefore we assumed that the measured scattered field directly scales with the local electric field. However, this relies on the implicit assumption that the emission pattern of the probe is unaffected by the SRR. Indeed the symmetry of the system is intrinsically broken by the fact that we excite the system at an angle, and we do not measure the total scattered field, but only the radiation emitted in a solid angle defined by the parabolic mirror.

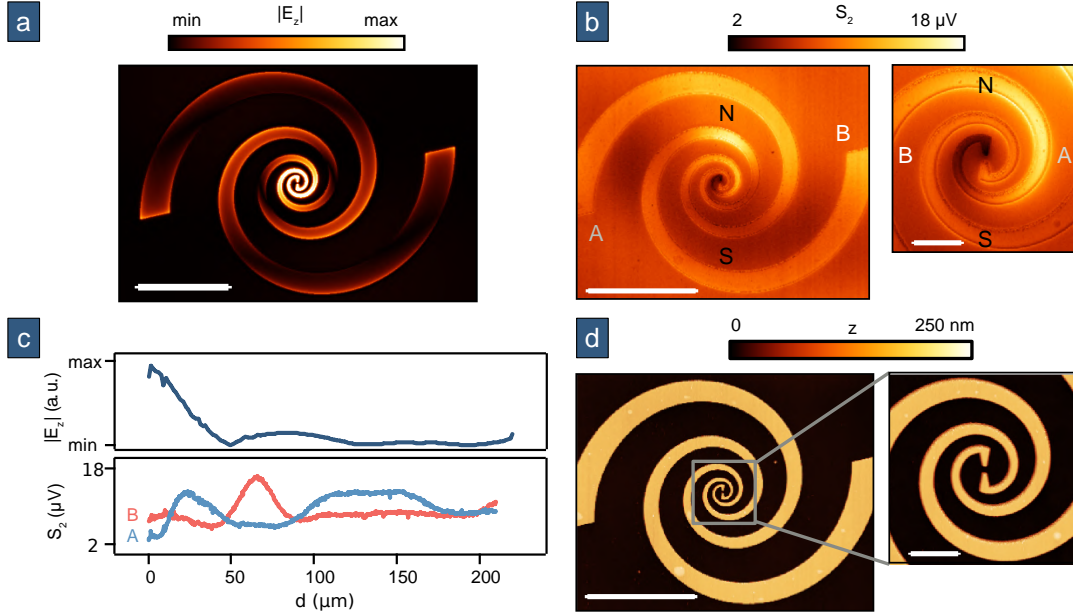


Figure 3.9: **(a)**: Computed near-field ($|E_z|^2$) on a LSA, scale bar length is 30 μm . **(b)**: s-SNOM images of an LSA: Left panel: large scale scan, scale bar length is 30 μm . Right panel: detail of the center, scale bar length is 5 μm . **(c)**: Top panel: Section along an arm of LSA in (a) (both arms give the same curve). Bottom panel: Mean sections along the arms of the LSA on (b). Blue line: arm A, red line: arm B. Origin is the center of the spiral. **(d)**: Respective topographies measured simultaneously with (b).

In figure 3.1 and equation (3.3), E_s accounts for the illumination, concentration, scattering, collection and detection of THz radiation in the probe / resonator system. Due to optical reciprocity, any requirement to illuminate the system also applies to collect the outgoing radiation. From this point of view, the bright (respectively dark) regions on our images would correspond to efficient (respectively poor) illumination and collection of light into the probe / SRR ensemble when the tip is on the N (resp. S) arm of the capacitor. Thus the measurements suggest that when the probe is above the N arm, the scattered field is mostly radiated toward the south, and inversely (figure 3.10d).

Two antennas with symmetrical radiation pattern forming an asymmetric pattern when combined is quite common in antenna theory, it is for example the mechanism used for phased array antennas[40]. However, in contrast with a phased array, the s-SNOM probe is located in the *reactive* near-field region[41] of the SRR, and even possibly in direct contact at the lowest point of the probe oscillation. Thus we cannot assume that the total radiation pattern is the interference from the sum of the radiation patterns of the probe and the SRR considered separately. We extended our calculations to reach a more realistic description of the system, now treated as a complex antenna problem.

3.4.1 FDTD simulation including the probe

We performed broadband FDTD simulations with a conductive tip placed on several spots along the arms of a SRR. Those simulations were conducted without substrate, to simplify as much as possible the problem, and to avoid artifact from truncated data in the far-field projections. Just like the SRR far-fields presented in chapter 2

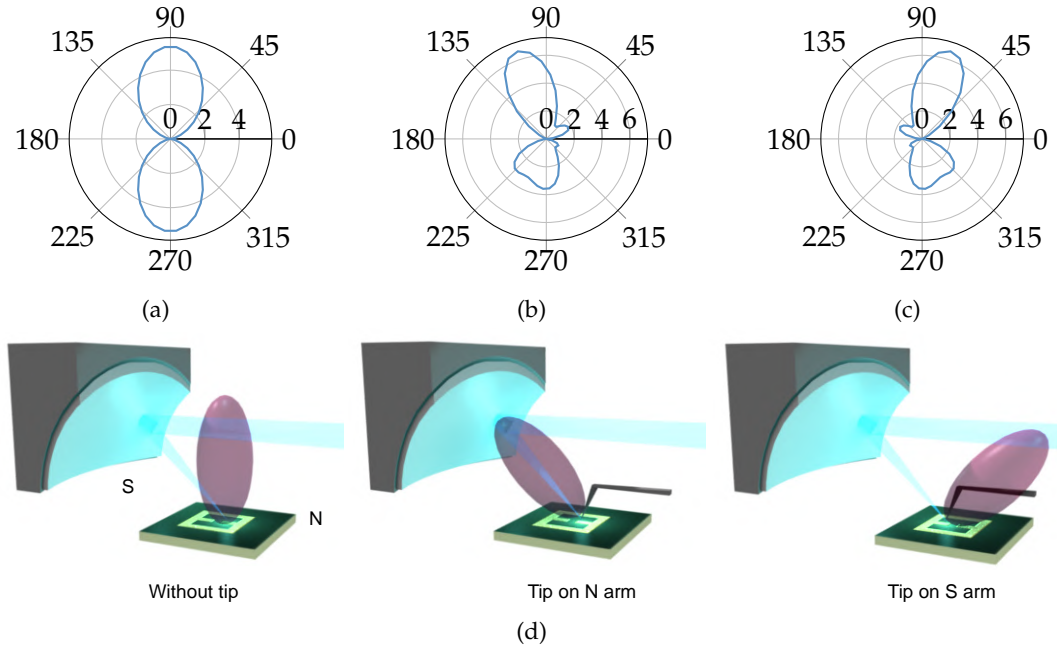


Figure 3.10: **(a,b,c)**: Far-field projection in the YZ plane of a SRR **(a)**: without probe, **(b)**: with a probe on the N arm, **(c)**: with a probe on the S arm. All far-fields are in linear scale. **(d)**: Schematic of the interpretation of the asymmetry. The coupling with the incident beam is better when the probe is on the N arm than when it is on the S arm[1].

(Figure 2.4 on page 35)), the SRR is excited with a Total-Field Scattered-Field (TFSF) source surrounding the SRR *and* the probe, and the far-field is projected from the field recorded on a closed surface surrounding the source volume. The probe was modeled as a truncated square-base pyramid (69.7 μm long and respectively 10.5 and 0.2 μm for the base and the apex side lengths).

We observed a critical influence of the position of the probe on the illumination / collection pattern of the system (Figure 3.10). If placed on the N (resp. S) arm of the capacitor, a lobe oriented S (resp. N) is generated in the far-field.

Although looking at the field scattered at a specific angle brings us closer to the real s-SNOM experiment, the simulated signal is not directly comparable to the experimental s-SNOM signal. To construct a comparable signal, we have to take into account the additional modulation from the interferometer, and the second harmonic demodulation used to remove the background signal. The additional modulation from the interferometer is calculated with equation (3.3) with a reference phase ϕ_{ref} chosen to maximize the contrast.

To simulate the second harmonic demodulation of the signal, let us assume that the probe is vertically oscillating in a sinusoidal motion. The vertical position of the probe as a function of time is

$$z(t) = A \cos(\Omega t), \quad (3.4)$$

where A is the oscillation amplitude, and Ω is the oscillation frequency. For a given horizontal probe position, the detected signal is a function of the probe position z . Using a second order Taylor expansion around $z = 0$, we approximate the signal as

a second order polynomial function of z . Hence we define a , b and c such that

$$I(z) \simeq az^2 + bz + c. \quad (3.5)$$

Combining (3.4) and (3.5), we get

$$I(t) = a\frac{A^2}{2} \cos(2\Omega t) + bA \cos(\Omega t) + ca\frac{A^2}{2}. \quad (3.6)$$

Therefore after demodulation at the frequency 2Ω , the measured signal is

$$S_2 = \left| a\frac{A^2}{2} \right|. \quad (3.7)$$

Assuming the oscillation amplitude A stays constant during the measurement (see figure 3.6 on page 59), we extract the signal by estimating the coefficient a . The estimation of a is done with a polynomial regression based on multiple simulations with different vertical probe positions. Since the actual measurement of S_2 in a s-SNOM experiment is always in arbitrary unit, we can ignore the multiplicative constant $\frac{A^2}{2}$.

To sum up the complete process to simulate the second harmonic signal measured on one horizontal position:

1. We repeat the simulation for 4 vertical probe positions.
2. We extract the amplitude and phase of the radiation emitted toward the mirror.
3. We apply the modulation from the interferometer (equation (3.3)).
4. We apply a second order polynomial regression on $I(z)$
5. The signal S_2 is the second order coefficient of the regression.

To produce a scan line to compare with the experimental data, we repeated this process for 20 positions along the y axis. The resulting scan line is plotted on figure 3.11, compared to the experimental data extracted from figure 3.4c.

The simulated cross section is in good agreement with the experiment, as it reproduces the main observation of the experimental cross sections: A maximum when the probe is at the edge of the N branch, and close to no signal when the branch is on the S branch.

To summarize, we conducted an extremely simplified numerical experiment with only a SRR and a pyramidal probe, excluding the substrate, the probe cantilever, and all other components of the s-SNOM that could induce shadowing effect or parasitic signal. Even in this minimalist (yet computationally demanding) scenario, selecting a direction of observation is enough to reproduce the strong asymmetry of the measurement.

This further confirms that the strong discrepancy between the measured image and the near-field profile is intrinsic to the s-SNOM technique, and cannot be avoided without major modification on the detection and excitation methods.

3.4.2 Interpretation

We consider the interplay between the confined near-field, its combination with the far-field illumination / collection pattern, and the aperture-limited focusing optics as a strong additional contribution to the recorded images (Numerical aperture is 0.39 in our case, according to the manufacturer information). It is known that the

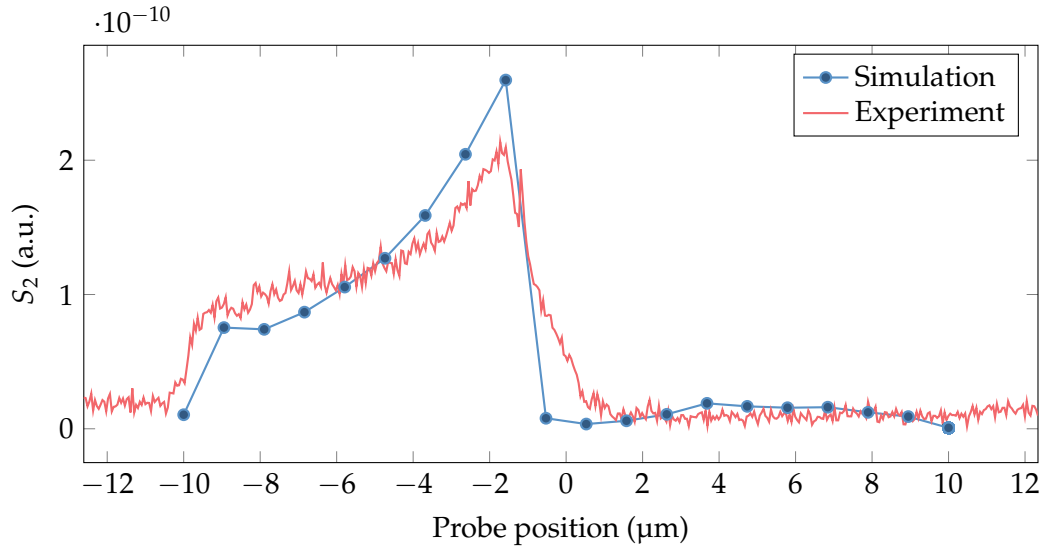


Figure 3.11: Simulated S_2 signal, extracted from the far-field scattering pattern of a SRR coupled with a $70\ \mu\text{m}$ long metallic probe, compared with the experimental S_2 profile measured on a SRR on a quartz substrate.

probe shape and oscillations contribute to the contrast of THz s-SNOM images [20]. Our results indicate that the collection mirror also participates in the contrast if the tip-sample ensemble has an anisotropic far-field pattern. Therefore, within most s-SNOM apparatuses with a mirror in front of the probe, the lobe pointing North would not be accessible. We demonstrated that the presence of the tip perturbs the photonic mode in a way that the symmetry of the device is broken.

In this framework, for a photonic resonator located at a position (x, y, z) with respect to the tip and the mirror, the scattered near-field contains information on both the spatial distribution of the photonic mode, labeled here as $\text{NF}(x, y, z)$ and the far-field pattern that is modified by the tip, labeled here as $\text{FF}(x, y, z, \theta, \varphi)$, where θ and φ describe a direction of observation. The accessible directions of observation are limited by the portion of solid angle where the FF pattern is collected. In our case, the latter is defined by the numerical aperture of the mirror. For a monochromatic incident wave with a given linear polarization, one can then write the problem as:

$$E_s(x, y, z) \propto \iint_{\text{mirror}} \text{NF}^2(x, y, z) \text{FF}^2(x, y, z, \theta, \varphi) d\theta d\varphi. \quad (3.8)$$

Note that the near-field and far-field terms in equation (3.8) are squared since they intervene both in illumination and collection. It is also worth mentioning that a more sophisticated description should integrate the scattering efficiency of the probe and the dielectric properties of the material beneath that still account for s-SNOM signal.

The far-field contribution was identified through the modeling of a scan over a SRR. Hence, the underlying phenomena is likely to occur with any antenna-like structure, including the LSA in this study (Figure 3.9). In this case, the situation is reversed compared to the SRRs, i.e. when the probe is over the N tip, the far-field pattern is not oriented towards the collecting mirror and gold appears darker than HR-Si while over the S tip, the mirror captures the far-field pattern and near-field concentration is detected.

So far, we cannot overcome this issue with current microscope designs that

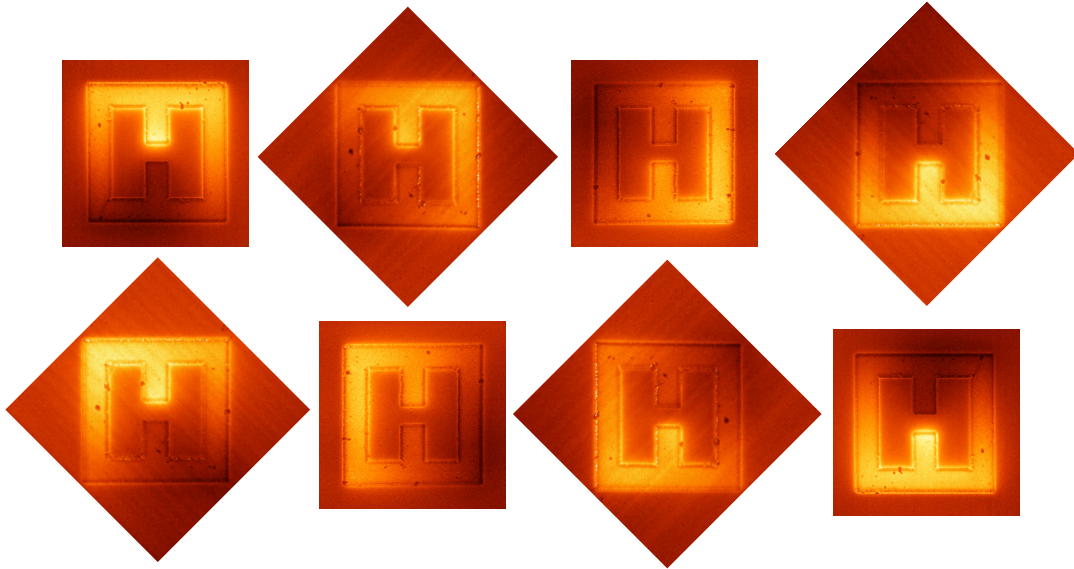


Figure 3.12: s-SNOM images of SRR differently oriented. The images are rotated to simulate illumination from 8 angles. The four images on the right are rotated versions of the images on the left.

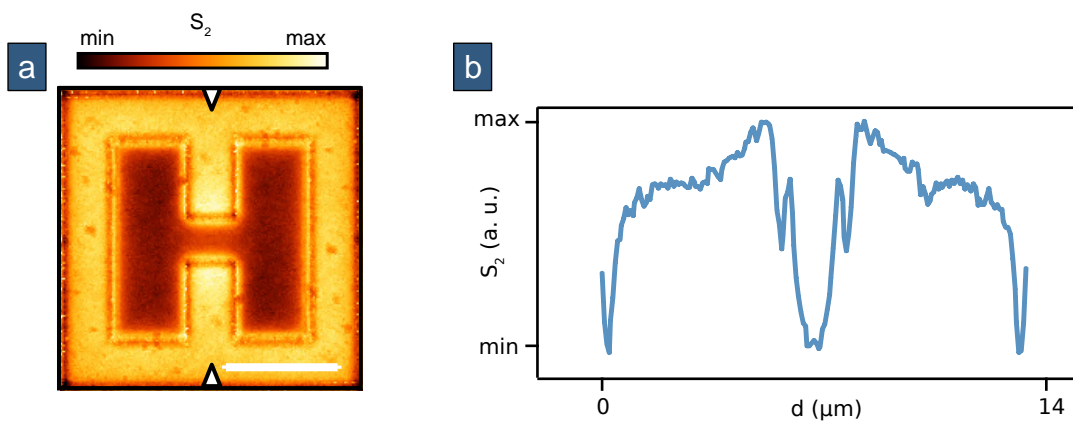


Figure 3.13: (a) Reconstructed image from the 8 orientations (b): Cross section along the branch axis.

would require to replace the parabolic mirror by a Cassegrain reflector or to rotate the mirror during the scan. However, if the mirror cannot rotate, it is possible in some particular cases to rotate the sample.

We scanned an isolated tuned SRR oriented with an angle ψ of $-45, 0, 45$ and 90° with respect to the N-S axis. Thanks to the SRR symmetry, the 4 opposed angles are obtained with a simple image rotation. Afterward, we rotated the images to orient all the SRR in the same direction. The resulting images correspond to the measurement we would get for 8 positions of the parabolic mirror (figure 3.12). We reconstruct a full image by summing all 8 images.

The reconstructed image for a SRR on silicon is shown in figure 3.13. It shows the local maxima close to the gap at the edges of both branches, in good agreement with the simulated near-field profile.

This reconstruction method is equivalent to a measurement with excitation and detection from 8 directions symmetrically distributed around the sample. Although this is better than a single angle of observation, it still does not cover the entire sphere, and there is no guarantee that information is not lost at an uncovered angle.

3.4.3 s-SNOM with attenuated total internal reflection

Simultaneous detection of the scattered field in every direction, and omnidirectional excitation is materially impossible. Yet it is still possible to make the excitation and detection independent from the far-field emission pattern of the system, making the imaging system isotropic. This can be achieved with a technique called Attenuated Total Internal Reflection (ATIR).

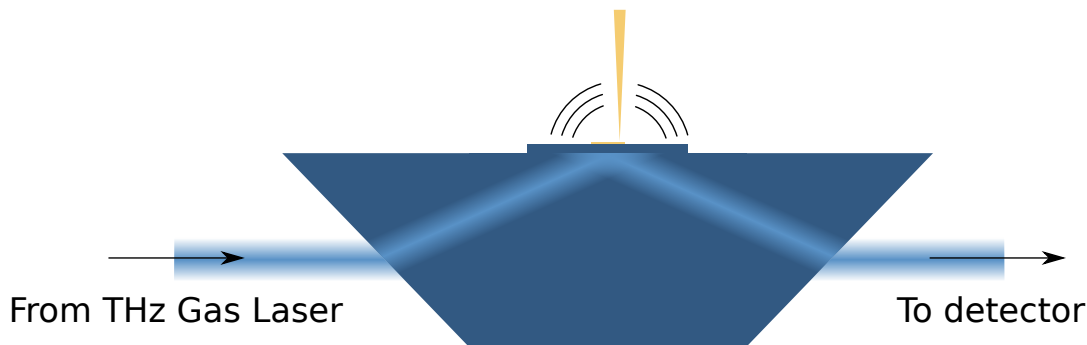


Figure 3.14: Schematic of a s-SNOM using attenuated total internal reflection. The THz beam passes through a silicon prism, where it undergoes total internal reflection. The sample is excited through the evanescent field at the surface of the prism. The energy scattered by the probe is subtracted from the reflected beam, which translates by an attenuation at the output of the prism.

In ATIR (figure 3.14), a light beam undergoes total internal reflection inside a material with high refractive index, which creates an evanescent field at the surface of the material. The sample is excited through this evanescent field. Since an evanescent wave is non propagative and has a purely imaginary wave vector, this excitation method does not depend on the radiation pattern of the sample and probe. The energy scattered by the probe is subtracted from the reflected beam. Therefore we can detect the total scattered intensity from the attenuation of the beam at the output of the material, regardless of the radiation pattern. With this method, the measured value is the additional loss introduced by the presence of the probe in the reactive near-field of our sample. Images acquired with this method are much more meaningful than images from a regular s-SNOM system.

We tried this strategy using a high resistivity silicon prism, cut and polished from a 5 mm thick wafer. The prism is mounted in the neaSNOM platform along with two parabolic mirrors for the injection and collection of the THz beam, as shown in figure 3.15a. The position of the total internal reflection is located by putting droplets of isopropanol on the prism surface and looking for an attenuation in the output beam. The experiment is only possible with silicon substrates, because of the large difference between the quartz and silicon refractive index, the beam is totally reflected at the interface and never reaches the SRR.

Figure 3.15b shows an image recorded with excitation from the prism, and regular detection of the scattered field as illustrated in figure 3.1a on page 52. As expected, the image stays asymmetric since we used the same detection scheme. The image shows a poor signal to noise ratio, but proves that we were able to excite the SRR through TIR.

As of today, we were not able to significantly improve the quality of the images recorded from the scattered signal and TIR excitation, and could not produce any conclusive image from the signal measured at the output of the prism. This is likely

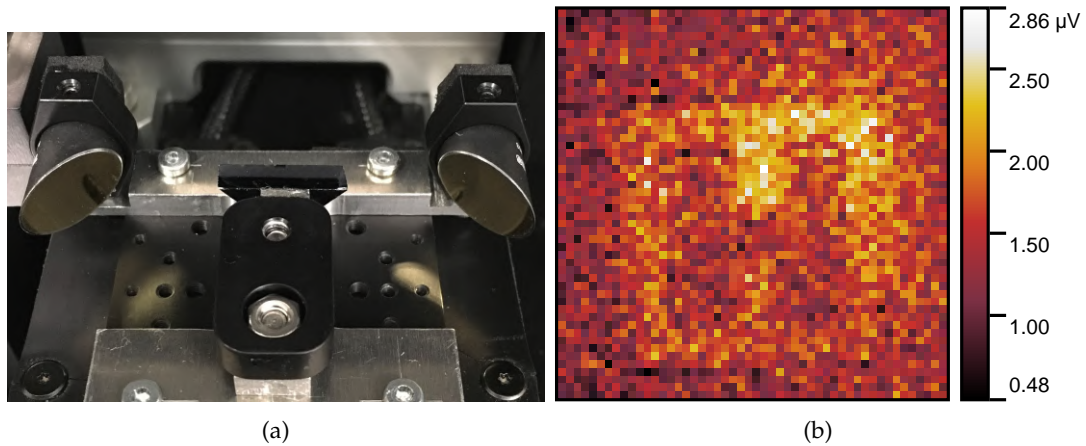


Figure 3.15: **(a)**: High resistivity silicon prism mounted in the NeaS-NOM microscope. The THz beam is focused in the prism with the parabolic mirror on the left, and collected with the parabolic mirror on the right. **(b)**: First s-SNOM image of a SRR excited through Total Internal Reflection (TIR). Only the excitation is done through the prism, the image is still constructed from the scattered field above, hence the remaining asymmetry ($a = 13 \mu\text{m}$).

due to an imperfect contact between the prism and the sample. Indeed, any surface defect or dust on one of the two surfaces can introduce a small air gap, which drastically reduces the amount of light that reaches the top surface of the substrate. Further investigation and setup improvement are still required to progress on this path.

3.5 Conclusion

We investigated the near-field characterization of SRRs using s-SNOM imaging. We were able to experimentally demonstrate the electric field confinement in the gap of the resonator. Indeed, although the measurement only gives information on the vertical component of the electric field, this is enough information to detect a localized charge accumulation. The charge distribution, along with a priori information on the material and the shape of the resonator allows for the reconstruction of the full field distribution. The s-SNOM experiment was our first measurement on single resonators when our THz-TDS could only measure large arrays of SRRs. It confirmed that with our fabrication process, there is no significant difference in the behavior of each individual SRR. We also confirmed the validity of FDTD simulations on the near-field distribution of the SRR mode, which is highly encouraging for spectroscopy and optical trapping applications.

Nonetheless, our experiments showed that the link between a s-SNOM image and the vertical electric field distribution is far from straightforward. In particular, we demonstrated that a standard s-SNOM apparatus is intrinsically asymmetric and cannot provide viable measurement of the near-field profile of any sample that could disturb the far-field radiation pattern of the s-SNOM probe.

We proposed a way to adapt the s-SNOM method in order to make it isotropic, using ATIR. The isotropy of the measurement is a necessary condition to make s-SNOM imaging of resonator a measurement tool, rather than a validation tool. This method still needs further improvement, which will be the object of future work.

References

- [1] Théo Hannotte et al. “Imaging of THz Photonic Modes by Scattering Scanning Near-Field Optical Microscopy”. In: *ACS Applied Materials & Interfaces* 14.28 (July 2022), pp. 32608–32617. DOI: [10.1021/acsami.2c01871](https://doi.org/10.1021/acsami.2c01871) (cit. on pp. 51, 52, 59, 63).
- [2] E.H. Syngé. “XXXVIII. A suggested method for extending microscopic resolution into the ultra-microscopic region”. In: *The London, Edinburgh, and Dublin Philosophical Magazine and Journal of Science* 6.35 (Aug. 1928), pp. 356–362. DOI: [10.1080/14786440808564615](https://doi.org/10.1080/14786440808564615) (cit. on p. 51).
- [3] Daniel Courjon. *Near-Field Microscopy and Near-Field Optics*. IMPERIAL COLLEGE PR, Mar. 2003. 340 pp. ISBN: 186094258X. URL: https://www.ebook.de/de/product/4350534/daniel_courjon_near_field_microscopy_and_near_field_optics.html (cit. on pp. 51, 52).
- [4] E.A. Ash and Nicholls G. “Super-resolution Aperture Scanning Microscope”. In: *Nature* 237.5357 (June 1972), pp. 510–512. DOI: [10.1038/237510a0](https://doi.org/10.1038/237510a0) (cit. on p. 51).
- [5] D. W. Pohl, W. Denk, and M. Lanz. “Optical stethoscopy: Image recording with resolution $\lambda/20$ ”. In: *Applied Physics Letters* 44.7 (Apr. 1984), pp. 651–653. DOI: [10.1063/1.94865](https://doi.org/10.1063/1.94865) (cit. on p. 51).
- [6] A. Lewis et al. “Development of a 500 Å spatial resolution light microscope”. In: *Ultramicroscopy* 13.3 (1984), pp. 227–231. ISSN: 0304-3991. DOI: [10.1016/0304-3991\(84\)90201-8](https://doi.org/10.1016/0304-3991(84)90201-8) (cit. on p. 51).
- [7] G. A. Massey. “Microscopy and pattern generation with scanned evanescent waves”. In: *Applied Optics* 23.5 (Mar. 1984), p. 658. DOI: [10.1364/ao.23.000658](https://doi.org/10.1364/ao.23.000658) (cit. on p. 51).
- [8] George Keiser and Pernille Klarskov. “Terahertz Field Confinement in Nonlinear Metamaterials and Near-Field Imaging”. In: *Photonics* 6.1 (Feb. 2019), p. 22. DOI: [10.3390/photonics6010022](https://doi.org/10.3390/photonics6010022) (cit. on p. 51).
- [9] Hironaru Murakami et al. “Laser Terahertz Emission Microscope”. In: *Proceedings of the IEEE* 95.8 (Aug. 2007), pp. 1646–1657. DOI: [10.1109/jproc.2007.898829](https://doi.org/10.1109/jproc.2007.898829) (cit. on p. 51).
- [10] Romain Lecaque et al. “THz near-field optical imaging by a local source”. In: *Optics Communications* 262.1 (June 2006), pp. 125–128. DOI: [10.1016/j.optcom.2005.12.054](https://doi.org/10.1016/j.optcom.2005.12.054) (cit. on p. 51).
- [11] O. Mitrofanov et al. “Collection-mode near-field imaging with 0.5-THz pulses”. In: *IEEE Journal of Selected Topics in Quantum Electronics* 7.4 (2001), pp. 600–607. DOI: [10.1109/2944.974231](https://doi.org/10.1109/2944.974231) (cit. on p. 51).
- [12] Markus Wächter, Michael Nagel, and Heinrich Kurz. “Tapered photoconductive terahertz field probe tip with subwavelength spatial resolution”. In: *Applied Physics Letters* 95.4 (July 2009), p. 041112. DOI: [10.1063/1.3189702](https://doi.org/10.1063/1.3189702) (cit. on p. 51).
- [13] Andreas Bitzer, Alex Ortner, and Markus Walther. “Terahertz near-field microscopy with subwavelength spatial resolution based on photoconductive antennas”. In: *Applied Optics* 49.19 (Mar. 2010), E1. DOI: [10.1364/ao.49.0000e1](https://doi.org/10.1364/ao.49.0000e1) (cit. on p. 51).

- [14] M. A. Seo et al. "Fourier-transform terahertz near-field imaging of one-dimensional slit arrays: mapping of electric-field-, magnetic-field-, and Poynting vectors". In: *Optics Express* 15.19 (Aug. 2007), p. 11781. DOI: [10.1364/oe.15.011781](https://doi.org/10.1364/oe.15.011781) (cit. on p. 51).
- [15] N. Klein et al. "A metal-dielectric antenna for terahertz near-field imaging". In: *Journal of Applied Physics* 98.1 (July 2005), p. 014910. DOI: [10.1063/1.1978972](https://doi.org/10.1063/1.1978972) (cit. on p. 51).
- [16] S Hunsche et al. "THz near-field imaging". In: *Optics Communications* 150.1-6 (May 1998), pp. 22–26. DOI: [10.1016/s0030-4018\(98\)00044-3](https://doi.org/10.1016/s0030-4018(98)00044-3) (cit. on p. 51).
- [17] Hou-Tong Chen, Roland Kersting, and Gyu Cheon Cho. "Terahertz imaging with nanometer resolution". In: *Applied Physics Letters* 83.15 (Oct. 2003), pp. 3009–3011. DOI: [10.1063/1.1616668](https://doi.org/10.1063/1.1616668) (cit. on p. 51).
- [18] F. Blanchard et al. "Real-time terahertz near-field microscope". In: *Optics Express* 19.9 (Apr. 2011), p. 8277. DOI: [10.1364/oe.19.008277](https://doi.org/10.1364/oe.19.008277) (cit. on p. 51).
- [19] J.W. Strutt. "LVIII. On the scattering of light by small particles". In: *The London, Edinburgh, and Dublin Philosophical Magazine and Journal of Science* 41.275 (June 1871), pp. 447–454. DOI: [10.1080/14786447108640507](https://doi.org/10.1080/14786447108640507) (cit. on p. 52).
- [20] Curdin Maissen et al. "Probes for Ultrasensitive THz Nanoscopy". In: *ACS Photonics* 6.5 (Apr. 2019), pp. 1279–1288. DOI: [10.1021/acsp Photonics.9b00324](https://doi.org/10.1021/acsp Photonics.9b00324) (cit. on pp. 52, 55, 56, 65).
- [21] Xinzhong Chen et al. "Modern Scattering-Type Scanning Near-Field Optical Microscopy for Advanced Material Research". In: *Advanced Materials* (Apr. 2019), p. 1804774. DOI: [10.1002/adma.201804774](https://doi.org/10.1002/adma.201804774) (cit. on p. 53).
- [22] Nenad Ocelic, Andreas Huber, and Rainer Hillenbrand. "Pseudoheterodyne detection for background-free near-field spectroscopy". In: *Applied Physics Letters* 89.10 (Sept. 2006). Number: 10, p. 101124. ISSN: 0003-6951, 1077-3118. DOI: [10.1063/1.2348781](https://doi.org/10.1063/1.2348781). URL: <http://aip.scitation.org/doi/10.1063/1.2348781> (visited on 02/07/2019) (cit. on p. 54).
- [23] P. McArdle et al. "Near-field infrared nanospectroscopy of surface phonon-polariton resonances". In: *Physical Review Research* 2.2 (June 2020), p. 023272. DOI: [10.1103/physrevresearch.2.023272](https://doi.org/10.1103/physrevresearch.2.023272) (cit. on p. 56).
- [24] T. Hannotte et al. "s-SNOM imaging of a THz photonic mode". In: *2020 45th International Conference on Infrared, Millimeter, and Terahertz Waves (IRMMW-THz)*. IEEE, Nov. 2020. DOI: [10.1109/irmmw-thz46771.2020.9370928](https://doi.org/10.1109/irmmw-thz46771.2020.9370928) (cit. on pp. 56, 59).
- [25] B. Walter et al. "Terahertz near-field imaging using batch-fabricated cantilevers with 70 μm long tips". In: *2019 44th International Conference on Infrared, Millimeter, and Terahertz Waves (IRMMW-THz)*. IEEE, Sept. 2019. DOI: [10.1109/irmmw-thz.2019.8874242](https://doi.org/10.1109/irmmw-thz.2019.8874242) (cit. on p. 55).
- [26] V. E. Babicheva et al. "Near-field edge fringes at sharp material boundaries". In: *Optics Express* 25.20 (Sept. 2017), p. 23935. DOI: [10.1364/oe.25.023935](https://doi.org/10.1364/oe.25.023935) (cit. on pp. 58, 59).
- [27] Andreas Bitzer et al. "Terahertz near-field imaging of electric and magnetic resonances of a planar metamaterial". In: *Optics Express* 17.5 (Feb. 2009), p. 3826. DOI: [10.1364/oe.17.003826](https://doi.org/10.1364/oe.17.003826) (cit. on p. 59).

- [28] Andreas Bitzer et al. "Terahertz near-field microscopy of complementary planar metamaterials: Babinet's principle". In: *Optics Express* 19.3 (Jan. 2011), p. 2537. DOI: [10.1364/oe.19.002537](https://doi.org/10.1364/oe.19.002537) (cit. on p. 59).
- [29] Hannes Merbold, Andreas Bitzer, and Thomas Feurer. "Near-field investigation of induced transparency in similarly oriented double split-ring resonators". In: *Optics Letters* 36.9 (Apr. 2011), p. 1683. DOI: [10.1364/ol.36.001683](https://doi.org/10.1364/ol.36.001683) (cit. on p. 59).
- [30] Jan Wallauer et al. "Near-field signature of electromagnetic coupling in metamaterial arrays: a terahertz microscopy study". In: *Optics Express* 19.18 (Aug. 2011), p. 17283. DOI: [10.1364/oe.19.017283](https://doi.org/10.1364/oe.19.017283) (cit. on p. 59).
- [31] Jan Wallauer, Christian Grumber, and Markus Walther. "Mapping the coupling between a photo-induced local dipole and the eigenmodes of a terahertz metamaterial". In: *Optics Letters* 39.21 (Oct. 2014), p. 6138. DOI: [10.1364/ol.39.006138](https://doi.org/10.1364/ol.39.006138) (cit. on p. 59).
- [32] Lucy L. Hale et al. "Noninvasive Near-Field Spectroscopy of Single Subwavelength Complementary Resonators". In: *Laser & Photonics Reviews* 14.4 (Mar. 2020), p. 1900254. DOI: [10.1002/lpor.201900254](https://doi.org/10.1002/lpor.201900254) (cit. on p. 59).
- [33] F. Blanchard et al. "Terahertz spectroscopy of the reactive and radiative near-field zones of split ring resonator". In: *Optics Express* 20.17 (Aug. 2012), p. 19395. DOI: [10.1364/oe.20.019395](https://doi.org/10.1364/oe.20.019395) (cit. on p. 59).
- [34] G. Acuna et al. "Surface plasmons in terahertz metamaterials". In: *Optics Express* 16.23 (Oct. 2008), p. 18745. DOI: [10.1364/oe.16.018745](https://doi.org/10.1364/oe.16.018745) (cit. on p. 59).
- [35] T. Hannotte et al. "Consequences of antenna effects on s-SNOM imaging of a photonic mode". In: *Conference on Lasers and Electro-Optics*. OSA, 2021. DOI: [10.1364/cleo_si.2021.sw2k.5](https://doi.org/10.1364/cleo_si.2021.sw2k.5) (cit. on p. 59).
- [36] Nikollao Sulollari et al. "Coherent terahertz microscopy of modal field distributions in micro-resonators". In: *APL Photonics* 6.6 (June 2021), p. 066104. DOI: [10.1063/5.0046186](https://doi.org/10.1063/5.0046186) (cit. on p. 59).
- [37] N. Sulollari et al. "Terahertz Near-Field Microscopy of Metamaterials". In: *2022 47th International Conference on Infrared, Millimeter and Terahertz Waves (IRMMW-THz)*. IEEE, Aug. 2022. DOI: [10.1109/irmmw-thz50927.2022.9895544](https://doi.org/10.1109/irmmw-thz50927.2022.9895544) (cit. on p. 59).
- [38] Rebecca Büchner et al. "Tip Coupling and Array Effects of Gold Nanoantennas in Near-Field Microscopy". In: *ACS Photonics* 8.12 (Oct. 2021), pp. 3486–3494. DOI: [10.1021/acsp Photonics.1c00744](https://doi.org/10.1021/acsp Photonics.1c00744) (cit. on p. 59).
- [39] P. Curie. "Sur la symétrie dans les phénomènes physiques, symétrie d'un champ électrique et d'un champ magnétique". In: *Journal de Physique Théorique et Appliquée* 3.1 (1894), pp. 393–415. DOI: [10.1051/jphystap:018940030039300](https://doi.org/10.1051/jphystap:018940030039300) (cit. on p. 61).
- [40] Warren L. Stutzman and Gary A. Thiele. *Antenna Theory and Design*. WILEY, May 2012. 848 pp. ISBN: 0470576642. URL: https://www.ebook.de/de/product/16212802/warren_l_stutzman_gary_a_thiele_antenna_theory_and_design.html (cit. on p. 62).
- [41] Constantine A. Balanis. *Antenna Theory*. Wiley John + Sons, Apr. 2016. ISBN: 1118642066. URL: https://www.ebook.de/de/product/24340252/constantine_a_balanis_antenna_theory.html (cit. on p. 62).

Chapter 4

Time domain spectroscopy on single SRRs

In the previous chapters, we modeled, designed and fabricated SRRs to take advantage of the field enhancement they provide in their gap. We will use the field enhancement to perform spectroscopy on nanometric samples. We used s-SNOM to experimentally validate the electric field distribution.

Using SRRs for the characterization of a low volume sample makes sense when performing spectroscopy on a single SRR. Since it is often impossible to get an identical coupling with the sample for each SRRs in a large array[1].

In this chapter, we will study how to take advantage of the high dynamic range of THz-TDS to detect the small signal from a single SRR. This requires noise analysis and error corrections that are valid and useful outside of the application presented here. Finally, we will experimentally study the behavior of a single SRR coupled to glutamic acid crystals.

4.1 Time domain spectroscopy

THz-TDS is a spectroscopy method based on the measurement of the temporal response of a system to a short THz impulsion. The amplitude and phase of the spectrum are constructed with a Fourier transform. It provides a high dynamic range (up to 100 dB), and covers more than a decade of frequency (from 0.2 THz to 6 THz, varies from one system to another).

THz-TDS (figure 4.1) uses ultrafast pulses from a femtosecond laser to generate and detect a THz pulse with a precisely controlled timing. On the emission side, the femtosecond pulse is converted into a THz pulse with devices such as photo-conductive antennas[2, 3], non-linear electro-optics crystals[4] or plasma oscillation[5]. On the detection side, the most commonly used techniques are photo-conductive or electro-optic sampling. Both techniques allow measuring the instantaneous value of the electric field during femtosecond pulse illumination.

In the case of a photo-conductive antenna, which is the method we are using, the intense femtosecond laser pulse generates pairs of electron-holes in a semiconductor, which makes the antenna conductive for about 1 ps (carrier lifetime in the semiconductor). On the emitter side, the antenna is biased with a DC voltage, thus the laser pulse triggers a short pulse of current in the antenna, which generates the broadband THz wave[6]. On the detector side, no bias is applied, but the charge carriers are accelerated by the incoming THz wave and we measure the resulting current.

Most THz-TDS systems use a beam-splitter to divide a single pulse in two parts, one going straight to the emitter, while the other goes to the detector through a delay

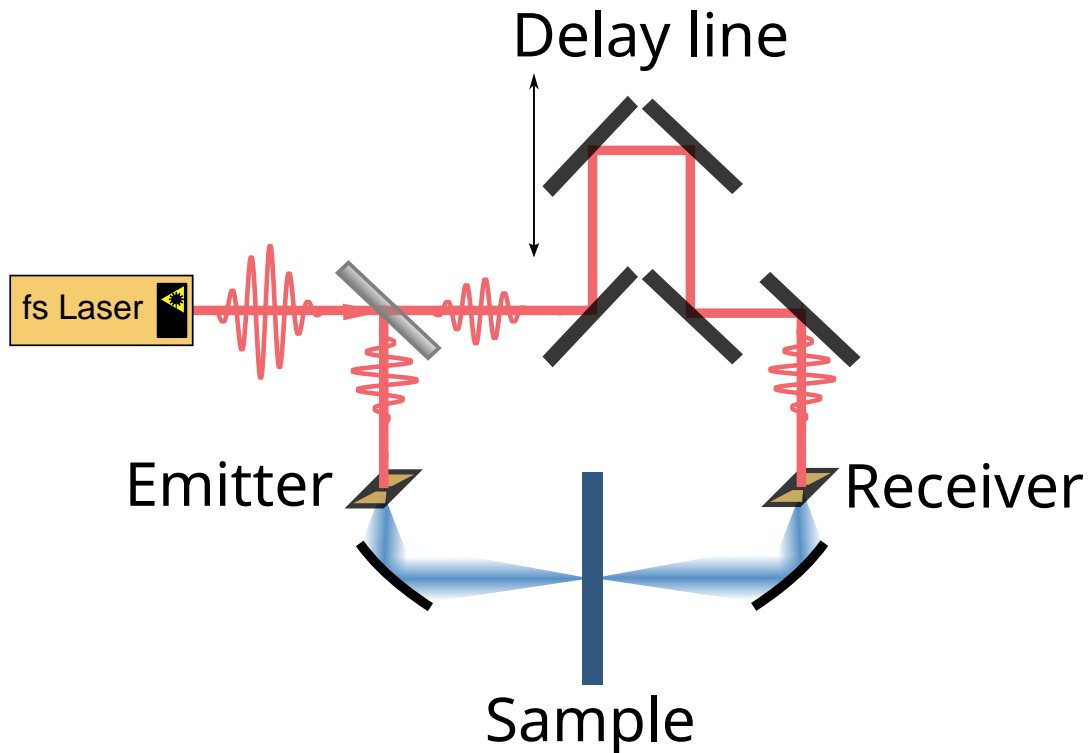


Figure 4.1: General schematic of a THz Time Domain Spectroscopy system. The red line represents the infrared path while the blue beam represents the THz pulse path.

line. The delay-line precisely controls the time delay between the emission and the detection. The transmitted pulse is reconstructed in the time domain by scanning the delay line. Other THz-TDS systems use two separate femtosecond lasers with slightly different repetition rates to scan the delay between the emission and detection without a physical delay line. This technique is much faster, but suffers from lower precision in the estimation of the delay.

In all our experiments, we use the TeraSmart THz-TDS setup by Menlo Systems GmbH. The excitation laser is a fibered Erbium doped laser with a 100 MHz repetition rate. The emitter and receiver are both indium gallium arsenide (InGaAs) based photo-conductive antennas coupled to hemispherical silicon lenses.

To direct and focus the THz beam on the sample, most THz-TDS systems use either off-axis parabolic mirror, or TPX lenses. Parabolic mirrors offer low losses and aberration-free focusing when perfectly aligned. However, even small deviations from perfect alignment leads to strong aberrations, which make the alignment process tedious, especially in the THz where there is no easy way to visualize low intensity beam. In contrast, TPX lenses have higher losses, but offer much more flexibility. Indeed, lenses are less affected by slight imperfection in the alignment, and since they do not have to be off-axis, all the components in a system with lenses can be attached to a single rail, which makes the alignment easier to begin with.

To get as much signal as possible while keeping the flexibility where we need it, we use a hybrid optical path featuring both parabolic mirrors and TPX lenses as illustrated in figure 4.2. In all our experiments, the THz beam needs to be collimated from the emitter and focused on the receiver in the same way. We use parabolic mirrors for this task that we rigidly attached to the antenna once aligned. In contrast, the way we focus (or not) the beam on the sample depends on the nature of the

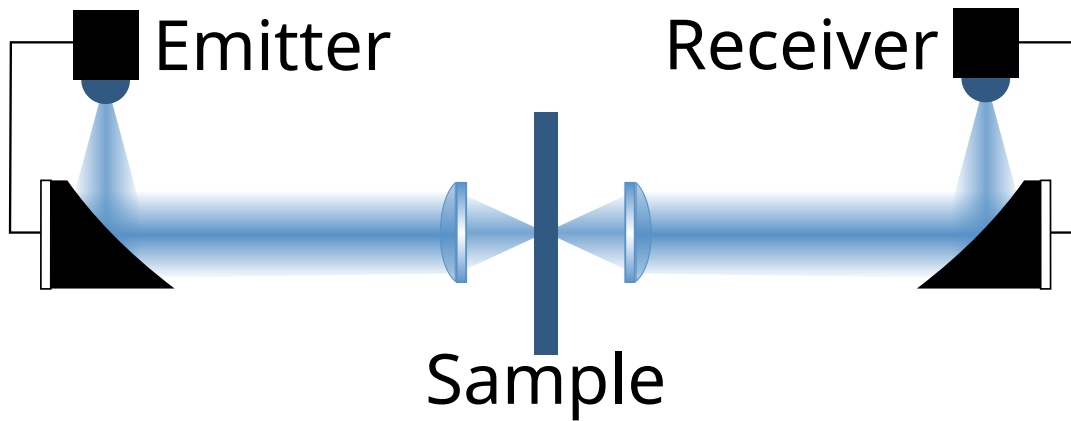


Figure 4.2: THz beam path in our THz-TDS system. Once aligned, the antenna and the parabolic mirror on each side are rigidly attached together to be used as single components. All the components are aligned on a rail.

sample and of the experiment. By using TPX lenses attached on a rail along with the two parabolic mirrors, we can easily change the focal length of the lenses or even remove them to adapt the system to the specificity of each experiment.

The whole THz optical path is enclosed in a box purged with dry nitrogen to avoid the strong absorption lines of water vapor.

To improve the signal-to-noise ratio, we average a large amount of successive traces. Figure 4.3 shows an example of pulses and its Fourier transform, averaged over 10 000 time traces.

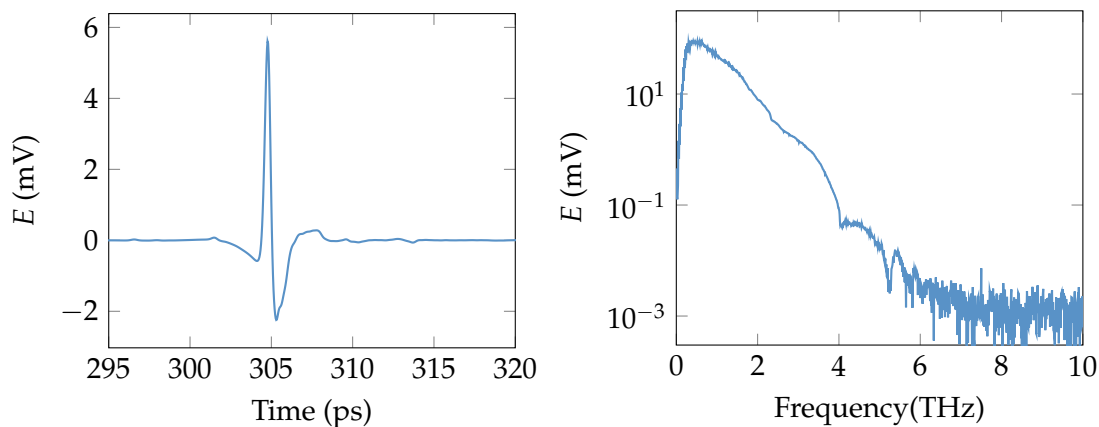


Figure 4.3: Example of signal measured in our system without sample, averaged over 10 000 traces.

4.2 Fitting procedure

To extract data from a sample with THz-TDS in transmission, we measure two pulses, one without sample for reference, and one with sample. By taking the ratio of the Fourier transform of the two traces, we get the transfer function of the sample, or transmission coefficient. This transfer function can be compared to the ones predicted by a theoretical model to extract diverse parameters such as refractive indices or absorption coefficient.

A common way to extract the parameters is to fit the theoretical transfer function to the measured one. This is done by finding the set of parameters p that minimize the error function usually defined as:

$$Err(p)(\omega) = (|\tilde{T}_{\text{exp}}| - |\tilde{T}_{\text{model}}(p)|^2) + \psi(\arg(|\tilde{T}_{\text{exp}}|) - \arg(|\tilde{T}_{\text{model}}(p)|))^2, \quad (4.1)$$

where \tilde{T}_{exp} and \tilde{T}_{model} are respectively the experimental and theoretical transfer function, and ψ is a weighting coefficient, usually set to 1 amplitude unit/rad. Combining the error on the module and on the phase as in equation (4.1) poses several issues.

In the particular case of refractive index extraction, if no importance is accorded to the physical phenomenon causing at the origin of the index, equation (4.1) can be used independently for each frequency. This is the simplest way to get an estimation of the refractive index as a function of the frequency. However, this method is only usable when the thickness of the sample is accurately known, and there is no guarantee that the resulting dispersion curve respects the Kramers-Kroenig relations, and therefore causality[7, 8]. Hence why we will avoid using this method, and rather only use integrated error and causal theoretical models.

However, even if additional precautions are taken to respect causality, this error function still carries major disadvantages. First, the efficiency and precision of the fit relies on the arbitrary value ψ . Furthermore, the precision on the estimation of the phase decreases drastically for a signal with low amplitude, yet the phase error keeps a constant weight in (4.1) regardless of the signal amplitude. This last point makes the technique unreliable for strongly absorbing samples, and forces one to arbitrarily limit the bandwidth of analysis to avoid the range of low dynamic range at high frequency.

To avoid all the aforementioned drawbacks coming from the error definition (4.1), we decided to use an alternative error function that does not rely on separate estimation of the phase and amplitude error. To keep the analysis as close as possible to the experimental data, we define this error function in the time domain[9].

We use the theoretical model to calculate the expected pulse $E_{\text{model}}(p)(t)$ from the reference pulse $E_{\text{ref}}(t)$. The theoretical pulse is given by:

$$E_{\text{model}}(p)(t) = E_{\text{ref}}(t) * T_{\text{model}}(p)(t) \quad (4.2)$$

$$= \text{FT}^{-1}[\text{FT}[E_{\text{ref}}(t)](\omega) \times \tilde{T}_{\text{model}}(p)(\omega)](t), \quad (4.3)$$

where “*” designate the convolution product, $\text{FT}[X]$ is the Fourier transform of the function X , and $T_{\text{model}}(p) = \text{FT}^{-1}[\tilde{T}_{\text{model}}(p)(\omega)]$ is the impulse response of the theoretical model.

We define the error function as:

$$Err(p) = \sum_{t=0}^{t=t_{\text{max}}} (E_{\text{model}}(p)(t) - E_{\text{sample}}(t))^2 \Delta t. \quad (4.4)$$

With this method, we compare the expected pulse with the experimental one, instead of comparing the theoretical and measured transfer function. Hence the error function is automatically weighted with the intensity of the measured signal, and there is no need to artificially remove the points at the limit of the dynamic range.

Note that according to Parseval's theorem, the norm a function is equal to the norm of its Fourier transform, therefore, the error function can also be written as:

$$Err(p) = \sum_{\omega=\omega_{\min}}^{\omega=\omega_{\max}} |\tilde{E}_{\text{model}}(p)(\omega) - \tilde{E}_{\text{sample}}(\omega)|^2 \Delta\omega. \quad (4.5)$$

This means that the same error function can also be calculated from the frequency domain, which is useful to save a few Fourier transform computations in the optimization process.

This fitting method makes the link with the analytical model developed in chapter 1, which we can now use and evaluate with the experimental THz-TDS measurement on our SRRs.

4.3 Single resonator spectroscopy

THz spectroscopy on single SRR was only recently demonstrated by Rajabali et al., who used a pair of high numerical aperture silicon lenses in direct contact with the sample to focus and collect a THz pulse through a single complementary SRR[10]. In contrast with a regular SRR, a complementary SRR is a sub-wavelength aperture in a continuous metal plane. Such a structure reflects close to 100% of the light that does not interact with the mode of the resonator. Hence the measured pulse is free from any background signal that would not have interacted with the SRR.

In an experiment on *regular* SRRs, we remove the background signal by comparing it to a reference signal measured on the same substrate, but far from any resonators. Therefore, when looking for the very weak response of a single SRR, any accidental discrepancy between the reference signal and the sample signal is likely to significantly alter the result. Such alterations can originate from multiple sources, such as non-uniform substrate thickness, surface defect or fluctuation in the THz-TDS system itself.

In our setup, we will not use lenses in direct contact with our sample, as we want to keep an easy access to the SRR. The THz pulse is only focused and collected with 5 cm focal length lenses (NA=0.356). Consequently, we expect a significantly lower signal level than in the experiment from Rajabali et al. This is why we need to check that the dynamic range of our system is high enough to detect such a small signal.

4.3.1 Single SRR signal compared to the dynamic range

To isolate the dynamic range from all the experimental parameters linked to the reference signal, we first fabricated complementary SRRs on a quartz substrate (figure 4.4). According to Babinet's principle, the field diffracted from a planar structure is identical to the field diffracted from its complementary. Hence measuring the signal through a complementary SRR is a good way to test if dynamic range is high enough to detect a single SRR.

Each SRR is placed several millimeters away from the others, such that our THz beam only interacts with a single one. Figure 4.5 shows the transmitted pulse and its spectrum, averaged over 10 000 traces. One can easily identify the resonance at 2.2 THz from the resonator. The maximum of transmission is about 0.02% (or -37 dB) compared to the transmission of a quartz substrate, which is strong enough for the dynamic range of our THz-TDS system (~ 70 dB at 2.2 THz).

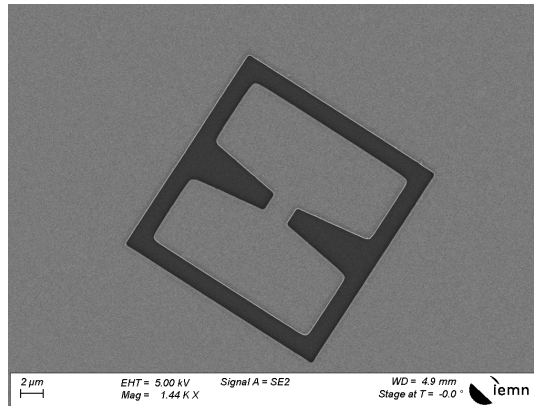


Figure 4.4: SEM picture of a complementary SRR. The darker area is an aperture through a gold plane.

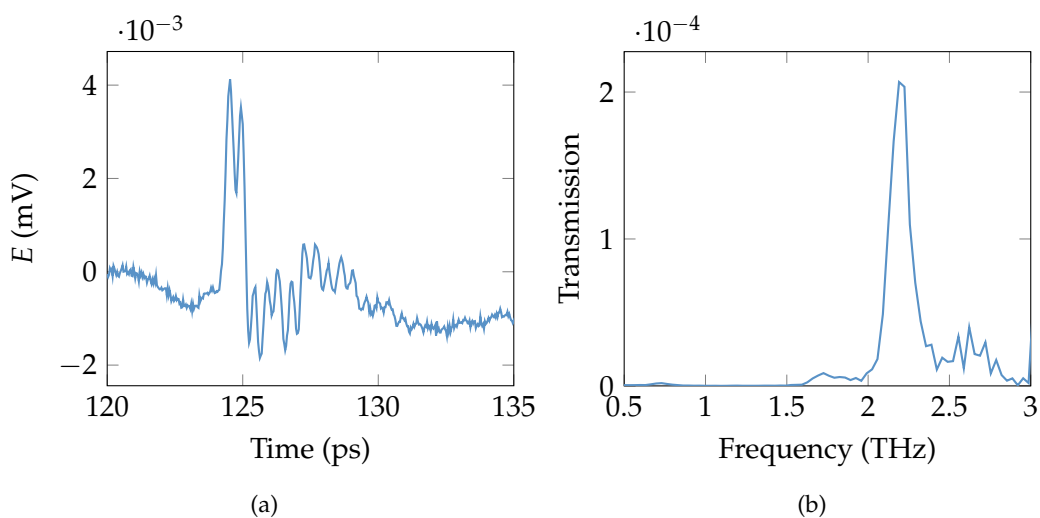


Figure 4.5: **(a)**: Time domain signal detected from a single complementary SRR. **(b)**: Transmission spectrum normalized with the transmission through quartz.

We experimentally demonstrated that we have the dynamic range necessary to detect the signal from a single complementary SRR. By comparing the complementary SRR to the dynamic range, we effectively compare our signal to the noise measured on a sample with 0% transmission, i.e. the dark noise. However, dark noise is not the only type of noise in a THz-TDS system[11]. For example, a multiplicative noise term coming from laser power fluctuation[12] could strongly affect the measurements on regular SRRs, even though we did not see it in the measurement of the complementary shape. A more complete noise analysis is necessary to correctly interpret a small signal variation extracted from a large background[13].

4.3.2 Noise analysis and error correction

The notion of “noise” in a measurement is difficult to define. In its broadest definition, it designates any deviation from the “true” signal[14]. Of course the notion of “true” signal is just as hard to define and is by definition impossible to measure. Here, we define the amplitude of the noise in a THz-TDS measurement as the statistical standard deviation of the signal. This definition correctly encapsulate the amplitude of the noise is based on two hypothesis: The “true” signal does not

change from one measurement to another. The noise has a zero mean value. We will consider this first hypothesis true for the rest of the rest of the chapter. Nonetheless, we will see later that some phenomenons also induce biases, which invalidate the second hypothesis. Hence, although the standard deviation always carries useful information on the nature of the noise, it does not represent the full picture.

Since our measurements consists of thousands of traces averaged together, the estimation of a single trace standard deviation is given by

$$\sigma_{\text{single}}(t) = \sqrt{\frac{1}{N} \sum_{i=1}^N (E_i(t) - \bar{E}(t))^2}, \quad (4.6)$$

where N is the number of traces, $E_i(t)$ is the i -th trace, and $\bar{E}(t)$ is the averaged time trace. The standard deviation of the averaged signal is

$$\sigma_{\text{avg}}(t) = \frac{\sigma_{\text{single}}(t)}{\sqrt{N}} = \frac{1}{N} \sqrt{\sum_{i=1}^N (E_i(t) - \bar{E}(t))^2}. \quad (4.7)$$

We use the same estimator to calculate the standard deviation in the frequency domain¹.

Figure 4.6 shows a measured time signal, averaged over 10 000 traces, and its spectrum, superimposed with the estimated standard deviations. As expected, the standard deviation matches the noise floor at high frequency where the signal is dominated by the dark noise. However, we also see that the standard deviation is not constant across the time trace and across the spectrum. This mean we the noise is a correlated non-white noise. To be more specific, taking a closer look at the standard deviation of the time trace, the standard deviation appears to be proportional to the derivative of the signal.

Looking back at the individual traces, we notice that there is a slight delay between the traces, typically around 10 fs, smaller than the 30 fs time step of our THz-TDS system. The origin of this delay is mostly due to thermal fluctuation of the optical fibers during the long acquisition (10 000 time traces takes about 25 minutes).

Having identified the origin of the strong correlation in the noise, we implemented a correction algorithm to remove the delay in the individual traces before averaging them together[13]. First, we select the time trace that is closest to the average, to use as a reference. Then, for each trace, we apply a delay δ_i in the frequency domain using the following formula

$$\tilde{E}_{i,\delta_i}(\omega) = \tilde{E}_i(\omega)e^{j\omega\delta_i}. \quad (4.8)$$

We use an optimization algorithm to find the delay δ_i that minimizes the difference between E_{i,δ_i} and the reference trace.

The averaged signal and standard variation after correction are plotted on figure 4.7. The correction removes most of the correlation between the standard deviation and the signal intensity. The remaining noise is now much closer to a white noise, with a signal-to-noise ratio improved by almost 20 dB between 0.5 THz and 2 THz. The amplitude of the improvement widely depends on the severity of the delay drift during the acquisition. The example illustrated in figure 4.7 is representative of a majority of our measurement, but we regularly observe much larger

¹Due to the non-linearity of equation (4.7), the standard deviation of the spectrum is *not* the Fourier transform of the standard deviation of the time traces.

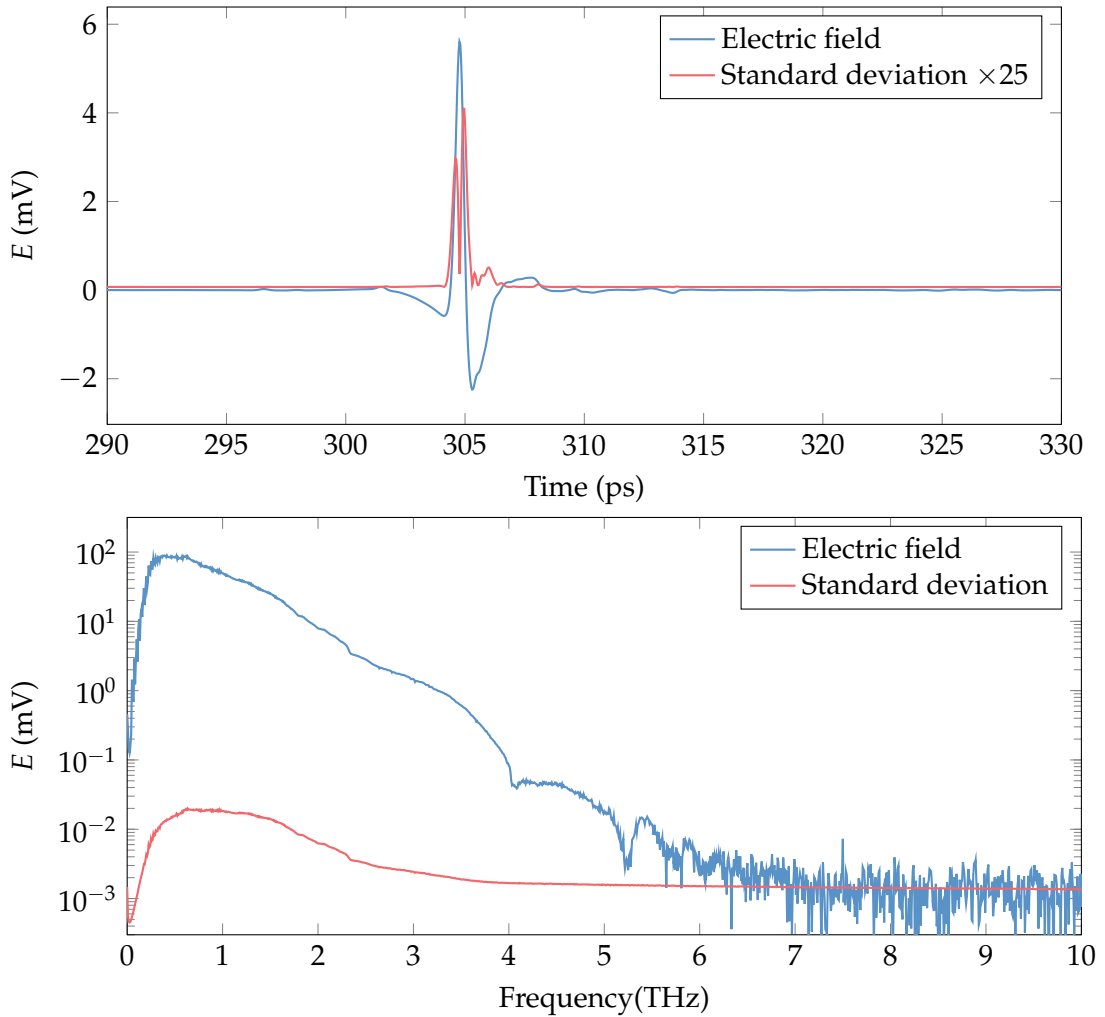


Figure 4.6: (a): Time domain signal and its standard deviation, measured on 10 000 time traces without sample. (b): Same signal in the frequency domain, and its standard deviation. Note that the signal below 180 GHz is filtered out as it is mostly unreliable[11].

delay drifts, leading to a signal-to-noise ratio improved by up to 30 dB after correction (figure 4.8). To take into account the slight fluctuations of the laser intensity during the acquisition, we also implemented an amplitude correction based on the same principle, which brings us even slightly closer to a white noise[13].

On top of adding to the standard deviation and reducing the signal to noise ratio, averaging shifted signals effectively acts as a convolution filter, reducing the signal at high frequency. Since this effect always *reduces* the signal, it is a bias and is consequently invisible in the standard deviation. We can see this filtering effect by looking at the ratio between the signal before and after correction (figure 4.9). As expected, the non-corrected signal is attenuated at high frequency by several percent, which is more than the amplitude of the signal from a single SRR (figure 4.5). Furthermore, the amplitude of the attenuation depends on the delay variation during the experiment, which we observed to be different between the reference signal and the sample signal. Assuming the delay increases linearly during the acquisition for an overall drift Δ , for an average over a large number of traces, the attenuation factor

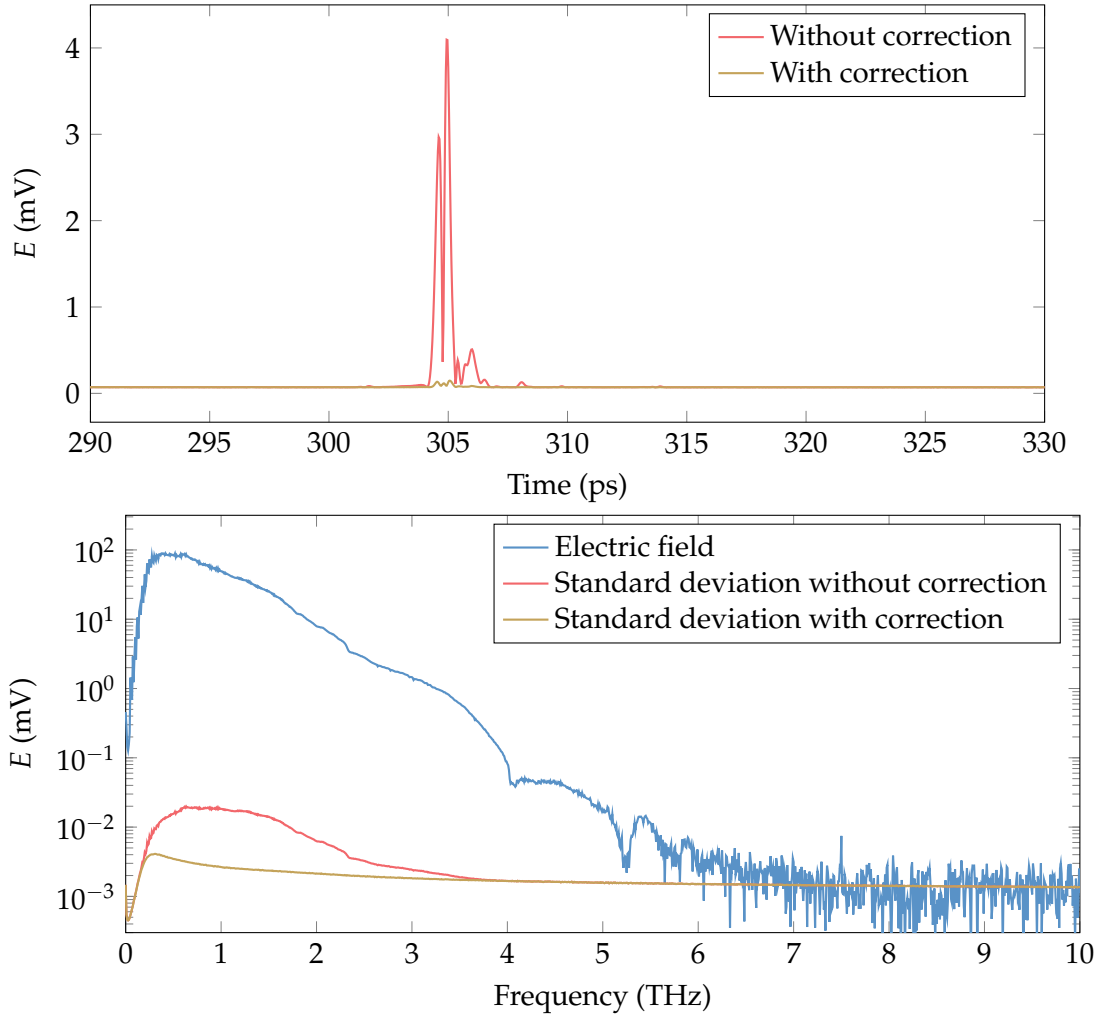


Figure 4.7: Effect of the correction in the time domain (**top**) and frequency domain (**bottom**). The correction removed most of the correlation between the standard deviation and the signal amplitude. Consequently, the signal to noise ratio between 0.5 THz and 2 THz is improved by almost 20 dB.

in *amplitude* caused by the drift can be approximated in the frequency domain as

$$A_{\Delta}(\omega) = \frac{1}{\Delta} \int_{-\frac{\Delta}{2}}^{\frac{\Delta}{2}} e^{j\omega\delta} d\delta = \text{sinc}\left(\frac{\omega\Delta}{2}\right). \quad (4.9)$$

More generally, the attenuation is the Fourier transform of the delay distribution among all the time traces. Equation (4.9) corresponds to the special case of uniform distribution. Although the delay distribution is not really uniform (see figure 4.10), the shape of the attenuation predicted by equation (4.9) is in very good agreement with the experimentally measured attenuation plotted in figure 4.9.

Figure 4.10 shows the delays δ_i estimated for each trace. Here we see that the variation of the delay is the sum of random fluctuation attributed to jitters in the delay line initial position, and a slow drift that we attribute to thermal drift in the optical fibers. On long acquisition (~ 25 minutes), we have observed drifts up to 70 fs (figure 4.10), which is more than 2 time steps, leading to signal attenuation of 15% at 3 THz (figure 4.9). Hence why the delay correction is essential for long acquisition

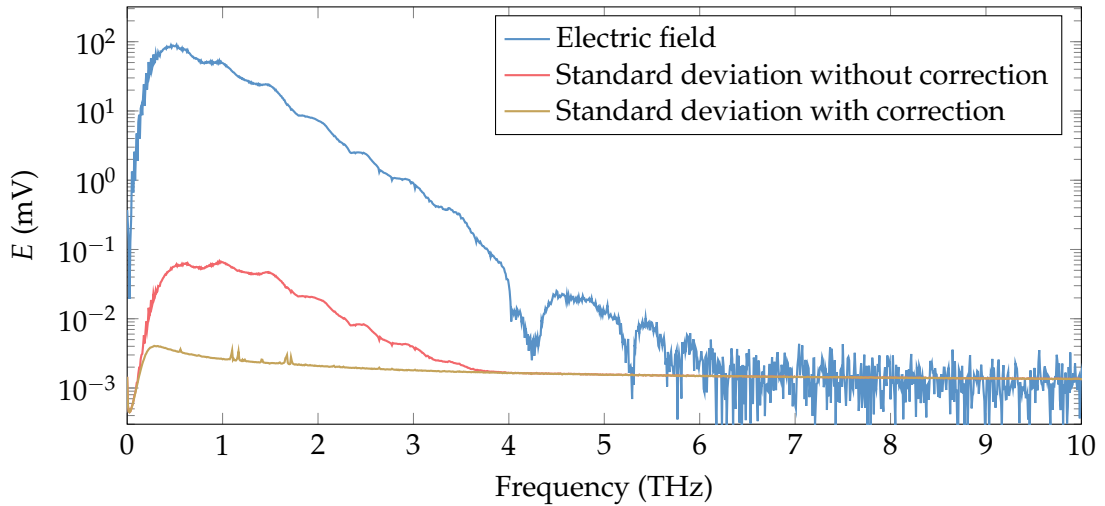


Figure 4.8: Correction effect on the standard deviation for a remarkably large delay drift. The standard deviation is reduced by 28 dB at 1 THz. The spikes in the standard deviation after correction indicate a variation in the water vapor concentration during the acquisition.

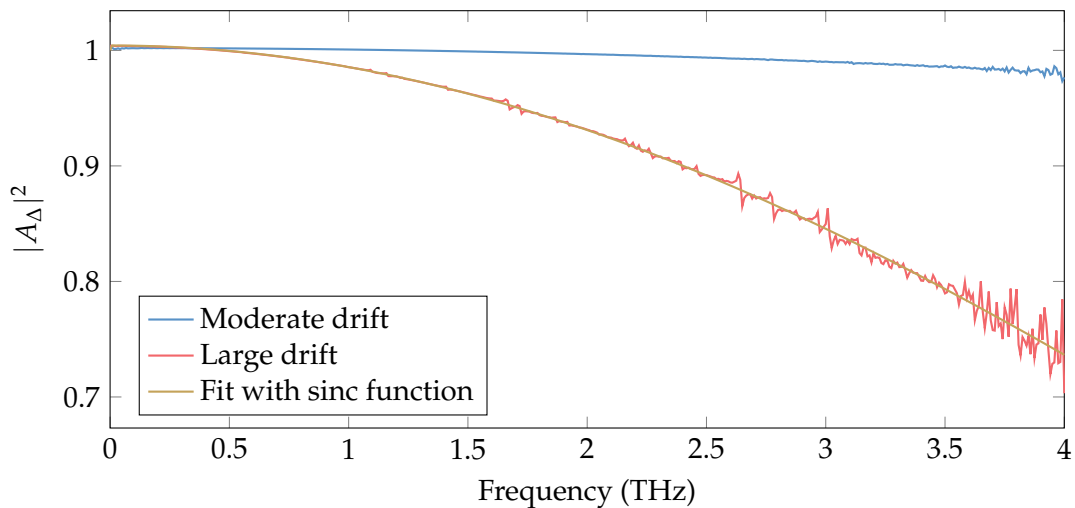


Figure 4.9: Non corrected signal divided by the corrected signal in the frequency domain for the measurement shown in figure 4.7 (blue) and figure 4.8 (red). The strength of the filtering is different for each measurement as it depends on the delay drift during the acquisition. The spikes in the red curve come from variations of water vapor concentration during the acquisition. The fit of the strongest attenuation with equation (4.9) gives $\Delta = 75$ fs. This value gives only an order of magnitude since the delay distribution is not actually uniform (see figure 4.10).

and measurement of small signal variations.

Another case where long acquisition is required is the study of strongly absorbing samples. The delay drift could be one of the cause for the lack of reproducibility in the measurements of liquid water in the THz range[11, 15–18]

We corrected the strong correlation between the standard deviation and the signal amplitude. Yet, one can note that the standard deviation still significantly goes up at low frequency such that the best signal-to-noise ratio is reached around 1 THz

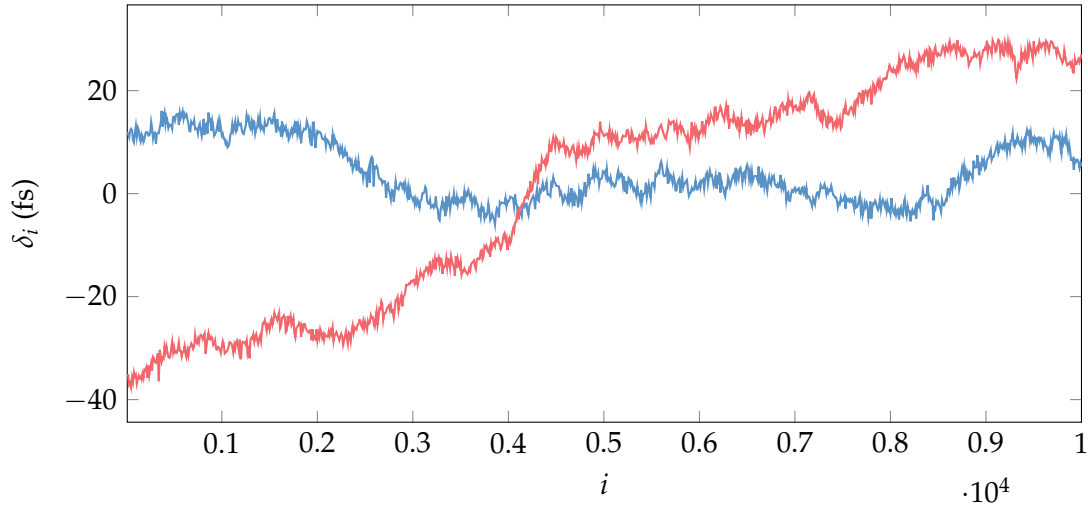


Figure 4.10: Estimated delay drift during the same two measurements as in figure 4.9. The red curve shows a drift of over 67 fs, which is more than 2 time steps of the THz-TDS.

despite the maximum of the pulse spectrum being around 0.5 THz.

4.3.3 Experimental result on single resonators

In order to test the limit of our measurement method, we fabricated resonators on a quartz substrate with a wide range of targeted resonant frequency, from 300 GHz to 3 THz. We also fabricated SRRs with different gap shapes, which should affect the quality factors, as seen in chapter 2. Each resonator is isolated and at least 2 mm away from any other structure. Wide areas without any structure were left on the substrate to be used as reference. For each resonator and the substrate reference, we take 10 000 time traces and apply the correction described in 4.3.2 before averaging. Note that the alignment of the THz path has been significantly improved between the next sets of measurements and the measurement on the complementary SRR.

Figure 4.11 shows a few examples of the resulting spectra, normalized with the reference spectrum taken on the bare substrate. We observe that the resonances of the resonator are clearly visible, with an amplitude of transmission modulation of up to 5%, which is actually much higher than the transmission through the complementary SRR. We attribute this difference to the improved alignment. We were able to measure the resonances of single SRRs with frequency ranging from 275 GHz to 3 THz.

As predicted from the FDTD simulations, the SRRs with larger capacitance have a significantly higher quality factor (see section 2.1.1). The best quality factor measured is $Q = 29.65$, corresponding to a bandwidth of 30 GHz at 1 THz (figure 4.12). The design of this SRR is the one illustrated in figure 2.7b on page 38, with a gap ratio $\frac{A}{G} = 30$, a size $a = 33 \mu\text{m}$ and 500 nm thick gold. Most metallic resonator designs featuring similar or higher quality factors in the literature relies on destructive interference from several resonators to cancel radiative losses[19, 20], or on supra-conductor material to remove the ohmic losses at cryogenic temperature[21, 22]. This is to our knowledge one of the highest quality factors achieved with individual SRRs in this frequency range at room temperature.

Although the shape of the transmission is consistent with the model developed in chapter 1, we notice significant deviation from the model at higher frequency. This

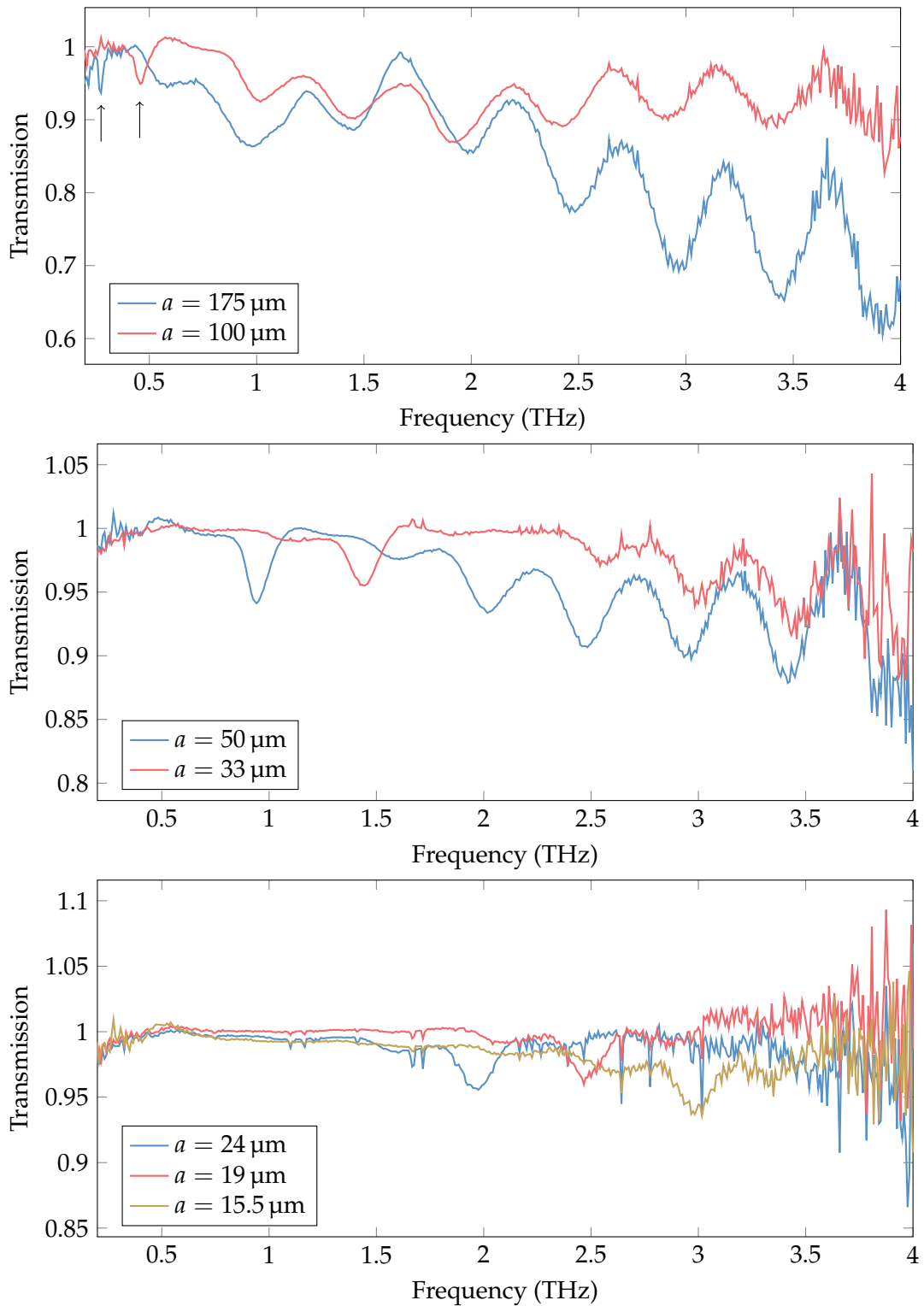


Figure 4.11: Transmission spectra of 7 individual SRRs, with sizes ranging from $15.5 \mu\text{m}$ to $175 \mu\text{m}$ normalized with the quartz transmission. The lowest resonance is measured at 275 GHz, and the highest at 3 THz. In each spectra from $33 \mu\text{m}$ to $175 \mu\text{m}$, we see a broadband modification of the reflectivity starting at roughly twice the resonance frequency.

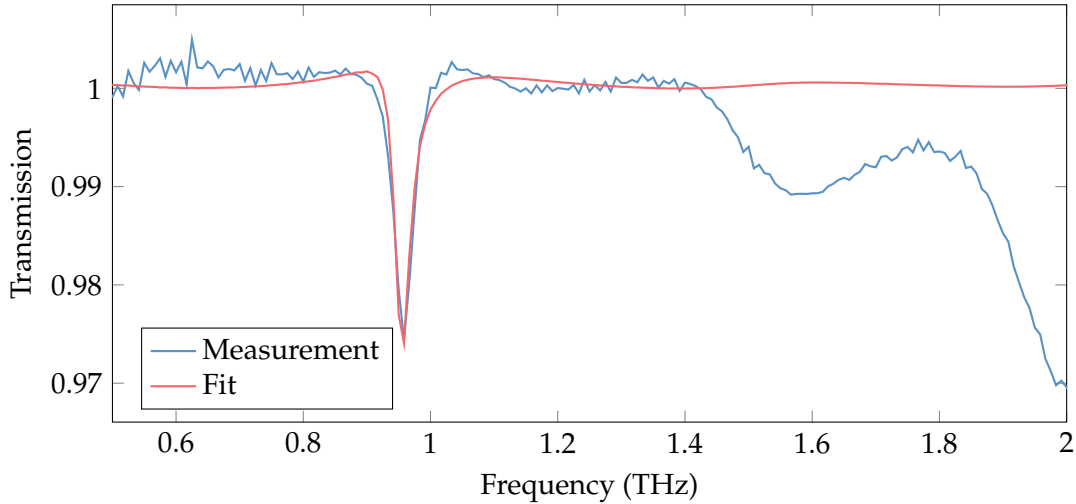


Figure 4.12: Transmission spectrum of a SRR with high quality factor. The decay rates extracted from the fit with the model from chapter 1 give $Q = 29.65$, which is consistent with the ~ 30 GHz bandwidth observed in the spectrum.

deviation is consistently seen on each SRR. It appears as several transmission minimum and maximum, but this appearance is only a consequence of the Fabry-Pérot effect in the substrate. Indeed the Fabry-Pérot is mostly canceled by the normalization with the reference, but a modification in the reflections coefficient or in the path length makes it reappear. Hence, we interpret the features at high frequency as a broadband increase in the reflection. As explained in chapter 1, our model relies on the quasi-static approximation, which is only valid when the loops of current are much smaller than the wavelength. Therefore, it is not surprising to see a deviation from the model at high frequency, where this approximation does not hold. This broadband reflection is likely due to one or a combination of the following facts:

- SRRs with similar shapes are known to have higher order resonance mode[23]. Such a mode with a low quality factor could be responsible for the reflectivity at high frequency.
- Since the THz beam is focused, the spatial distribution is frequency dependent. Specifically, the beam size is smaller at high frequency. This is usually not an issue for spectroscopy of homogeneous mediums, but when looking at a single object, the tighter focus at high frequency implies more reflection and absorption, even with a constant extinction cross section.

Nonetheless, we are able to accurately measure the resonance of single resonators in a full decade of frequency. This opens the way to experimentally study the behavior of a SRR coupled with a dispersive material.

4.4 Coupling with Glutamic Acid

The material chosen for the coupling experiment is Glutamic Acid (GA). Crystalline β -GA has a strong absorption line at 1.2 THz[24], which is in the frequency range where we have the best signal-to-noise ratio. Furthermore, our analytical model predicts a strong coupling behavior if the GA is correctly coupled (see 1.3). Therefore,

GA is a perfect material to test the validity of our model and our ability to couple a material to a single SRR.

4.4.1 Preliminary characterization of Glutamic Acid

The GA used in our experiment was purchased from TCI². We start by measuring the transmission spectrum of GA in pellet form. To reduce absorption and provide a reliable physical structure, powders are usually highly diluted (5% concentration) in a polymer such as polyethylene to form a pellet. To interpret the measurements, one has to rely on effective medium models (see 1.3.4) and potentially take into account the scattering from the particles dispersed in the matrix. Thanks to the high dynamic range of our THz-TDS system, reducing the absorption is actually unnecessary for this material. We use a press to form a ~ 0.5 mm thick pellet from *pure* GA. The high pressure from the press leads to flats and homogeneous surfaces at both sides of the pellet, which make the Fabry-Pérot effect predictable and useful to extract the permittivity and thickness of the pellet. The transmission spectrum of the pellet is shown on figure 4.13. As expected, we see a strong absorption line at 1.2 THz, and a cluster of at least 2 lines[24] around 2 THz and above.

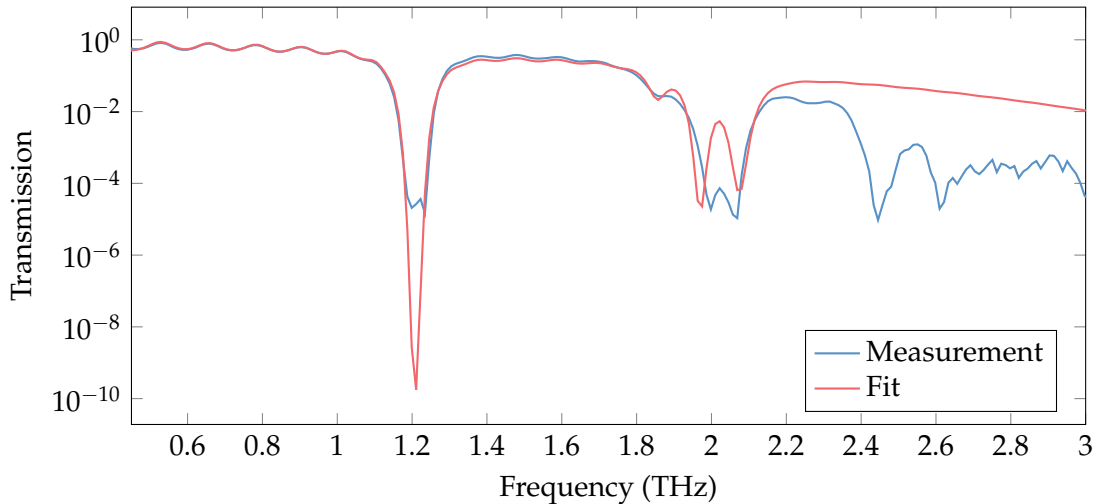


Figure 4.13: Transmission spectrum of a ~ 0.5 mm thick pellet of pure GA normalized with the transmission through the empty holder.

Taking into account the Fabry-Pérot effect, we used a Lorentzian permittivity model and the fitting method described in 4.2 to extract the parameters of the first Lorentzian mode. As mentioned in chapter 1, the Lorentz model describes the permittivity of a material whose charges act as damped harmonic oscillators[11]. The permittivity of a Lorentzian material is given by:

$$\varepsilon_l = \varepsilon_\infty + \frac{\Delta\varepsilon\omega_l^2}{\omega_l^2 + j\gamma\omega - \omega^2} \quad (4.10)$$

where ε_∞ is the permittivity at high frequency, $\Delta\varepsilon$ is the oscillator strength, γ is the linewidth of the mode (in rad/s), and ω_l is the resonance angular frequency of the mode.

The fit presented in figure 4.13 uses 5 Lorentz terms. The first one matches the main line at 1.2 THz, the next 3 model the line cluster around 2 THz, and the 5 at

²Product number: G0059

higher frequency is a purely phenomenological term that models the broadband absorption of the sample. A finer model could be used to better describe the spectrum around 2 THz and to take into account the lines at 2.45 THz and 2.6 THz. We decide to focus on the first line at 1.2 THz, around which this model is in good agreement with the measurement. The extracted parameters for this line are:

- $\varepsilon_\infty = 4.2$,³
- $\Delta\varepsilon = 0.12$,
- $2\pi\gamma = 41$ GHz,
- $2\pi\omega_l = 1.2$ THz.

Note that the thickness of the pellet is also a parameter of the fit, which converged to 0.54 mm.

4.4.2 Deposition procedure

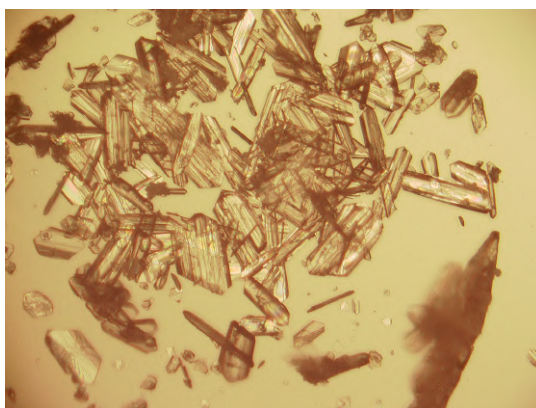


Figure 4.14: Optical microscope image formed after evaporation of 10 μ L of a saturated GA solution.

The GA solubility in water allows us to easily form GA from a saturated solution. A small drop of the saturated solution is deposited on the quartz substrate and left to dry at room temperature. Figure 4.14 shows the solid formed from the evaporation of a large (~ 10 μ L), where we can see large crystalline formation. We mentioned in section 2.2.2 that the surface state of the sample has a significant influence on the evaporation speed of small droplets and consequently on the quality of the crystals. Indeed, a droplet of water on a hydrophobic surface will take an almost spherical shape, resulting in a smaller surface area than the same droplet on a hydrophilic surface. Hence evaporation on a hydrophobic surface is slower and results in better crystals.

Figure 4.15a shows optical images of a deposition attempt on a hydrophilic surface, and figure 4.15b shows a similar attempt on a surface treated with Octadecyltrichlorosilane (OTS) (see 2.2.2). We see that the GA without OTS is at best *very* poly-crystalline, and at worst amorphous. In contrast, the GA on the hydrophobic surface is made of much larger mono-crystals.

³Here, ε_∞ describes the permittivity after the first line.

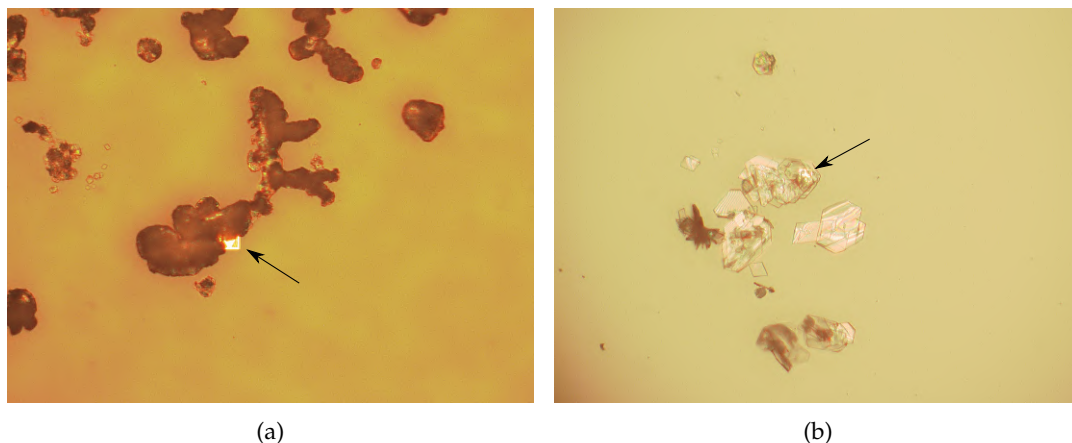


Figure 4.15: **(a)**: Deposition attempt of GA on a SRR with hydrophilic quartz surface. **(b)**: Deposition with OTS treatment making the quartz hydrophobic. The SRRs are $21\ \mu\text{m}$ large and indicated by arrows. Both attempts were done with approximately $30\ \text{nL}$ of saturated solution. Yet, the droplet on the hydrophilic surface evaporated in a few seconds, while the droplet on the hydrophobic surface lasted several minutes resulting in much better crystals.

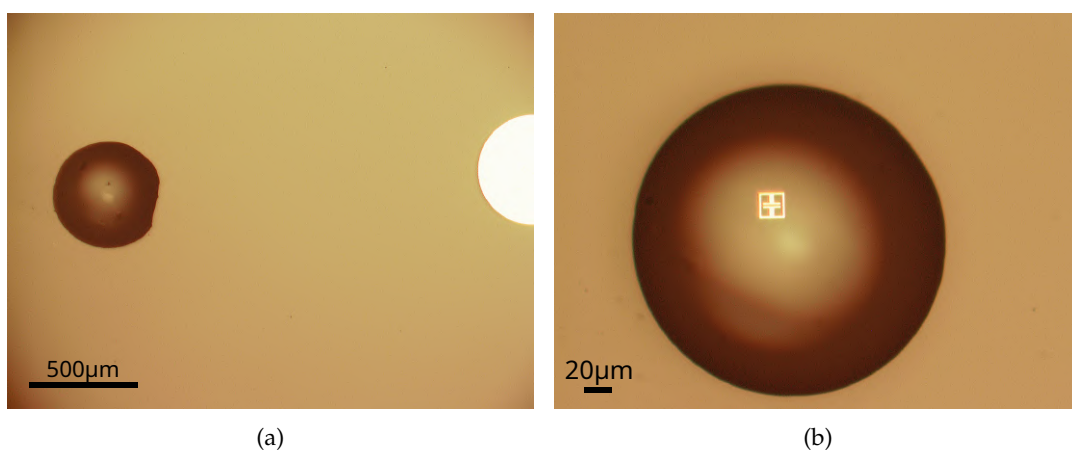


Figure 4.16: **(a)**: Drop with a diameter $< 500\ \mu\text{m}$ **(b)**: Drop with a diameter $< 250\ \mu\text{m}$.

For the deposition on the SRR, the drop of saturated GA solution should be as small as possible to limit the amount of GA around the SRR that could interact directly with the THz beam. We are able to produce droplets with a diameter on substrate less than $500\ \mu\text{m}$, and even down to $240\ \mu\text{m}$ (figure 4.16) i.e. a volume close to $30\ \text{nL}$ assuming the drop is hemispherical, and less than $5\ \text{nL}$ for the smallest ones. Figure 4.17a shows a SRR covered with GA crystals. Although the total amount of GA in the picture is less than $0.25\ \mu\text{g}$, it still covers a significant area around the SRR.

We first measured the spectrum of a similar amount of GA without SRR (figure 4.17b). We see on figure 4.18 that the low amount of GA does have a measurable impact on the transmission spectrum. Surprisingly, we see a clear minimum in the transmission at $2\ \text{THz}$, but no feature is visible at $1.2\ \text{THz}$, which is in contradiction with the measurement taken through the pellet where the absorption at $1.2\ \text{THz}$ was at least as strong as at $2\ \text{THz}$. The reason of this discrepancy is still an open question, but is likely to come from one or a combination of the following factors:

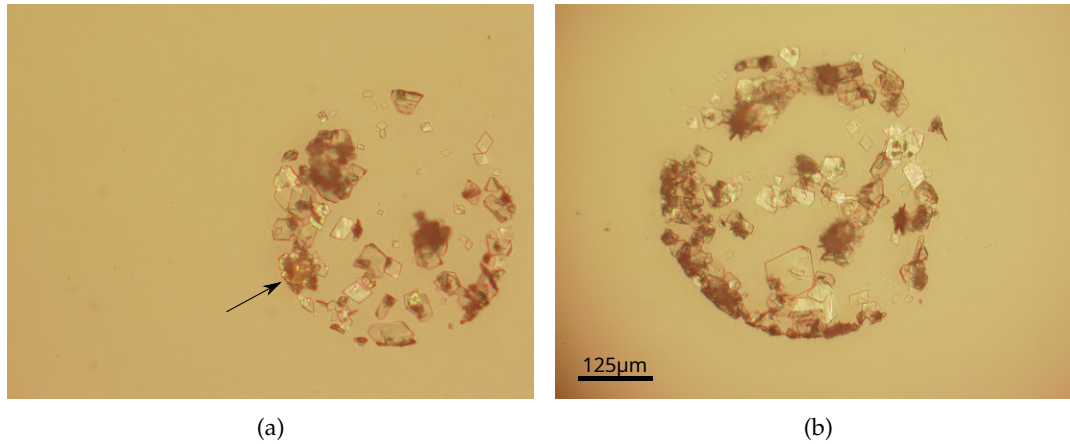


Figure 4.17: **(a)**: SRR (indicated by the arrow) covered and surrounded by GA crystals. **(b)**: GA crystals far from any structure, in a quantity similar to the one surrounding the SRRs.

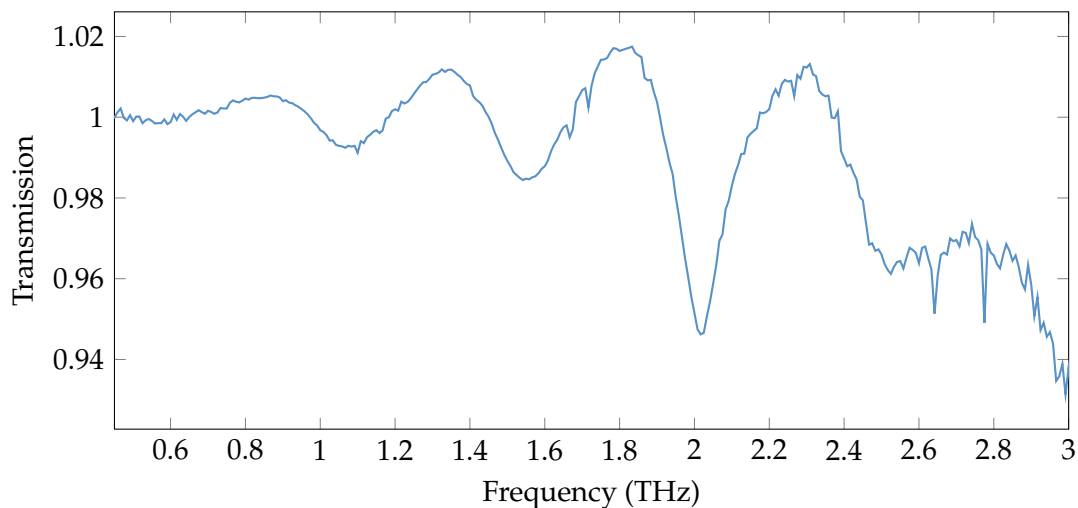


Figure 4.18: Transmission spectrum of less than $0.25 \mu\text{g}$ of GA (figure 4.17b) normalized with the substrate transmission. The reflection is broadly modified, with a clear absorption at 2 THz, and no clear feature at 1.2 THz. The sharp spikes are from residual water vapor.

Wrong crystalline structure: There exists two polymorphs of GA called α -GA and β -GA. The resonance mode at 1.2 THz only exists in β -GA[24]. Crystallization in the α form would explain the spectrum. However, β -GA is more stable at room temperature than α -GA[24], and we know from the pellet measurement that the β form was present before dissolution in water. Therefore, the crystals are expected to be in the β form.

Crystal orientation: The pellet is made of a large amount of crystals *randomly* oriented. In contrast, the vast majority of the crystals are mostly flat and oriented along the substrate. The absence of absorption could be due to a poor coupling with the 1.2 THz resonance mode in this orientation. However, this should prevent the near-field coupling with the SRR.

Destructive interference from the substrate: We performed the experiment on a $150 \mu\text{m}$ thick quartz substrate. Due to the Fabry-Pérot effect, 1.2 THz is near

a minimum in the substrate transmission whereas 2 THz is at a maximum. This means that light matter interactions are slightly enhanced at 2 THz and hindered at 1.2 THz.

Outside the absorption line at 2 THz, we see from the reappearance of the Fabry-Pérot that the reflection at the interface is modified in a broadband way, including around 1.2 THz. This is likely to affect the parameter extraction in the coupling experiment. But we should still be able to distinguish a sharp resonance in the broad Fabry-Pérot. Using micro manipulators to place a single GA crystal on the gap of the resonator would be a massive improvement in the coupling experiment.

4.4.3 Measurement result

We fabricated a second sample specifically designed to target the 1.2 THz resonance of GA. Regardless of the resonance, adding GA to a SRR will shift its resonance toward a lower frequency; we estimate that the resonance frequency should be around 1.3 THz to be correctly tuned. Following strong coupling theory (see 1.3.3), we also try to make the quality factor of the SRR match the quality factor of the GA resonance ($Q_{\text{GA}} = \frac{\omega_l}{\gamma} = 29.3$). Therefore we use the same gap geometry as the SRR from figure 4.12, i.e. a gap ratio $\frac{A}{G} = 30$. However, we achieve this gap ratio with a narrow gap $G = 500$ nm. Since the GA crystals are mostly flat, we expect them to end up *on* the gap rather than *in* the gap, this is fine as long as the gap is wider than the gold thickness. Considering the narrow gap, we reduce the gold thickness to 200 nm for this sample. This increases the radiative losses, hence we expect a quality factor lower than 29.65.

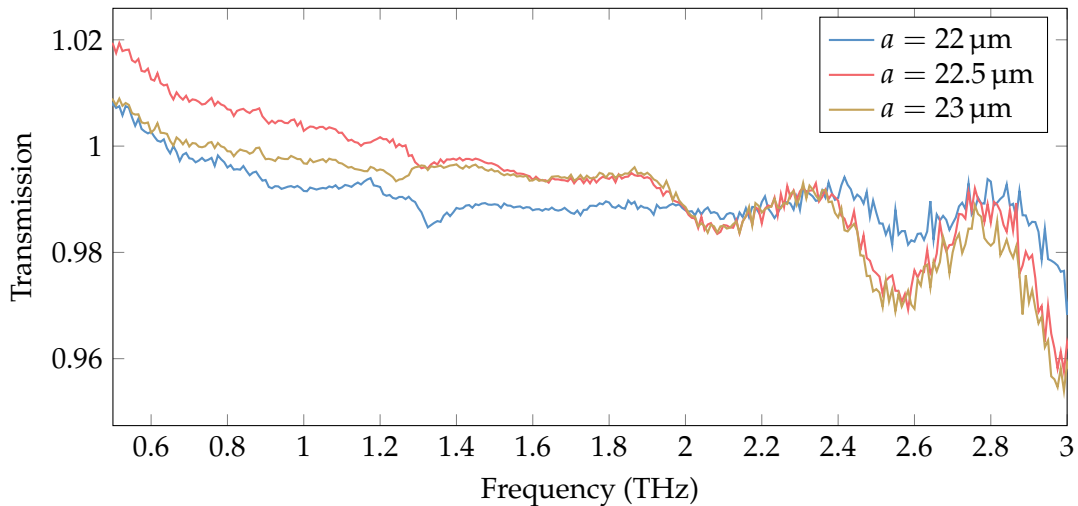


Figure 4.19: Transmission spectrum without GA, measured on the SRRs specifically designed for coupling with GA. Resonance are distinguishable around 1.3 THz, but the depth of the lines are less than 0.5%, against several percent for the previously measured SRRs (figure 4.11).

Figure 4.19 shows the measured spectrum for the SRR without GA. Unfortunately, we can already see a significant decrease in spectrum quality compared to the previous spectra (Figure 4.11, 4.12) with an extinction smaller than 0.5% against 5% for the previous measurement. This variation in the coupling is discussed in section 4.4.4.

Note that 0.5% is still much higher than 0.02% that we were able to detect with the complementary SRR. Yet we can see from figure 4.19 that we would have a hard time identifying a resonance with only 0.02% of maximum extinction. This illustrates that in this experiment, we are limited by the quality of our reference signal rather than by the dynamic range of the system.

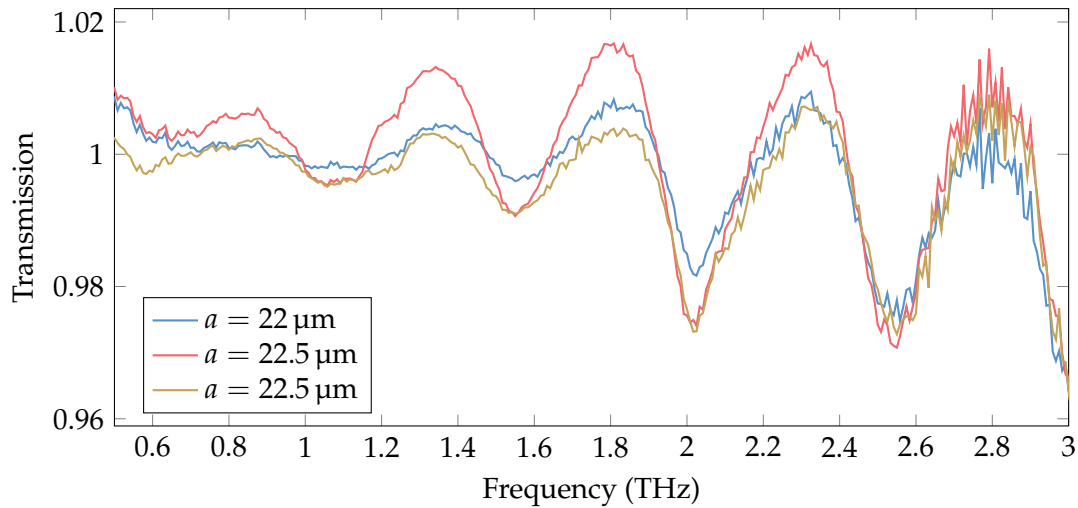


Figure 4.20: Transmission spectrum of SRRs covered with GA, where the resonances either disappeared or are reduced to a small indent in a strong Fabry-Pérot shape.

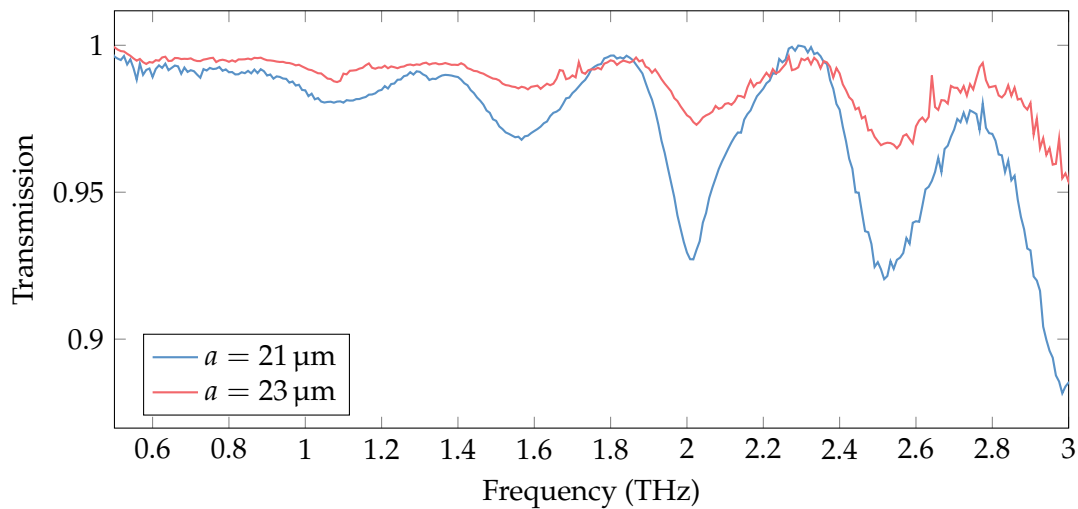


Figure 4.21: Transmission spectrum of SRRs slightly out of tune for coupling with the GA resonance. The resonances did shift toward lower frequency, which confirms the presence of a form of coupling with the GA.

Figure 4.20,4.21 shows examples of the spectrum measured on the SRRs covered in GA. As expected from the measurement on the GA droplet residue (figure 4.17b), we see a broadband modification of the reflectivity, with a minimum of transmission at 2 THz. As for the resonance of the SRR, it almost completely disappeared for most of the SRRs (figure 4.20). The features at 1.2 THz in these spectra are too small to be clearly distinguished from the Fabry-Pérot. The only SRRs whose resonances are still measurable with GA are the ones that are out of tune (figure 4.21).

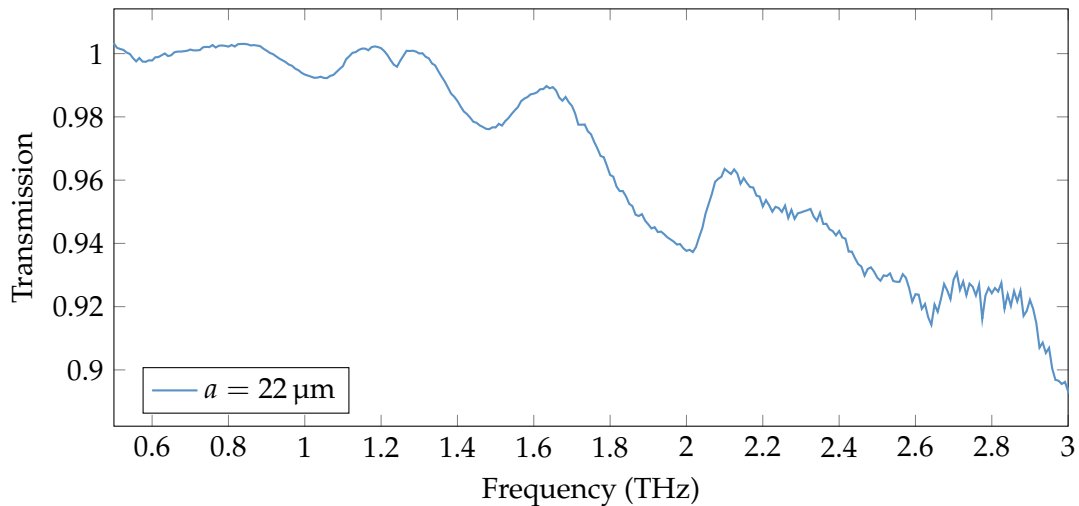


Figure 4.22: Transmission spectrum from one of the SRRs covered with GA. The resonance shift from 1.33 THz (figure 4.19), to 1.24 THz suggests that the coupled with the GA and correctly tuned to interact with its main resonance. Yet the singular and unexplained shape of the spectrum does not allow us to extract information. We were not able to reproduce a similar result.

Note that the resonance of the detuned SRR did shift toward lower frequency after being coated with GA. This confirms that there is indeed a form of coupling between the GA and the SRR, yet the behavior of the coupled system when the SRR is tuned does not match our prediction from the RLC model, nor from coupled oscillator theory i.e. a splitting of the resonance for strong coupling, or a distortion of the line shape for weak coupling.

One SRR spectrum clearly stands out from the other, plotted in figure 4.22. We see a resonance at 1.24 THz which seems to overlap the expected resonance of GA and an unusual shape in the Fabry-Pérot around it. We can affirm that it is coupled to the GA since its original resonance was measured at 1.33 THz (figure 4.19). However, the overall shape of the spectrum does not resemble any of the other spectra, with a rapidly decreasing transmission toward high frequency. The lack of understanding of the general shape of this spectra prevents us from extracting information from the spectrum shape around 1.2 THz. We were not able to reproduce a similar result.

4.4.4 About the spectra quality

To correctly interpret the measurement, we need to address the decrease in signal quality between the measurement in figure 4.11 and the ones in figure 4.19. Indeed, considering the appearance of the spectra in figure 4.19, 4.20 and 4.21, it would be fair to conclude that our signal-to-noise ratio is not good enough to extract any valuable information. Nonetheless, we previously demonstrated that we could detect a clear signal from single SRRs in a wide range of frequency and quality factors. There are a few differences in the design of the SRRs fabricated for coupling with GA (figure 4.19), compared to the one fabricated to cover a large range of frequency (figure 4.11), the most significant of which being the gold thickness. However, even on the sample made for GA, out of tune SRRs with a resonance close to 1 THz give us a much cleaner spectrum, as plotted in figure 4.23.

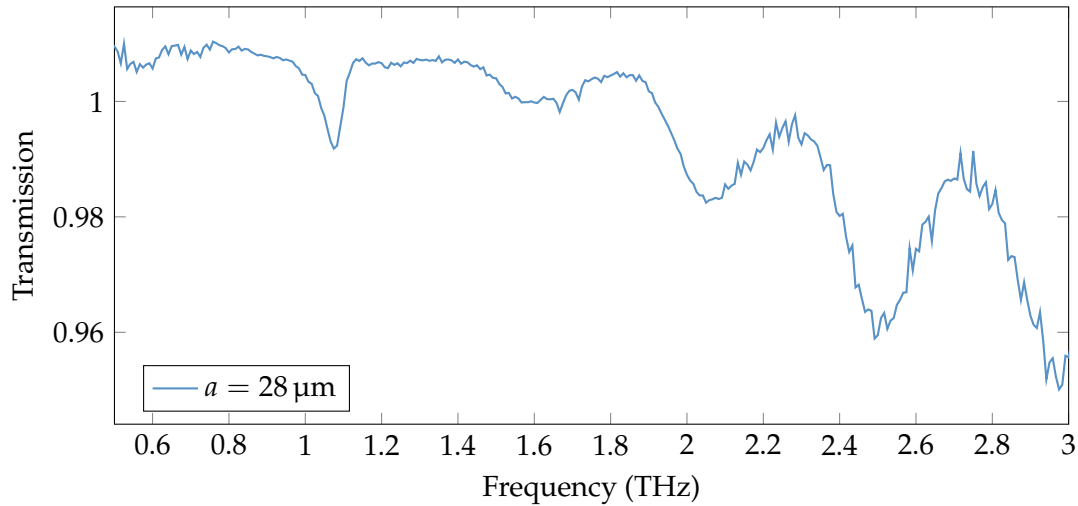


Figure 4.23: Transmission spectrum of SRR with the same design and on the same sample, but with a resonance at 1 THz. The resonance is much clearer than for any of the resonances around 1.3 THz (figure 4.19).

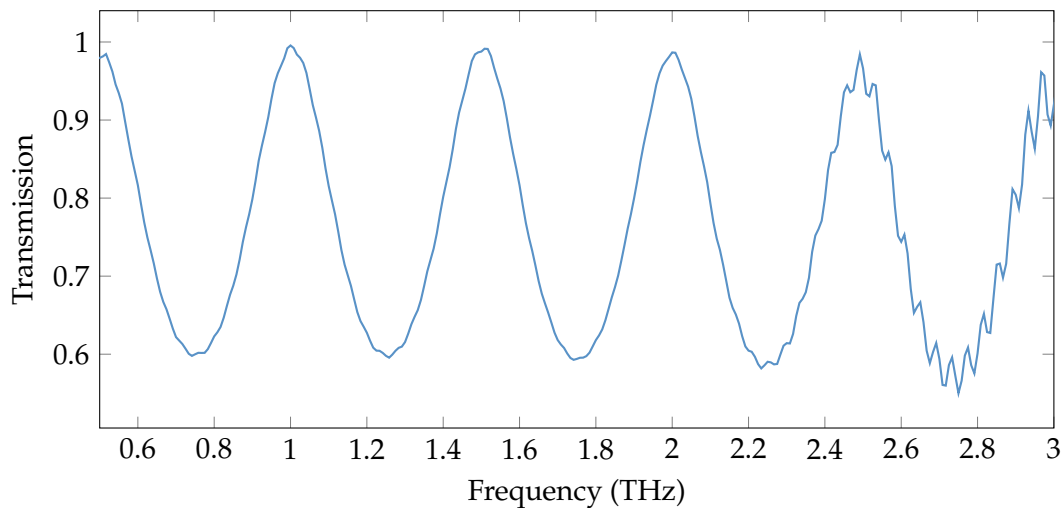


Figure 4.24: Transmission spectrum of the quartz substrate normalized with the transmission in air. The transmission maxima correspond to constructive interference at the interfaces. Oscillations at high frequency are artifacts from the temporal rectangular window.

We suggested in section 4.4.2 that the destructive interference from the multiple reflection in the substrate could be a potential explanation for the absence of absorption at 1.2 THz in the spectrum of GA crystals on quartz (figure 4.18). We were able to properly measure single SRR with resonance at 0.5, 1, 1.5, 2, 2.5, and 3 THz. Comparing those frequencies to the transmission of the quartz substrate (figure 4.24), all of them turn out to be coincident with transmission maxima in the quartz substrate. The transmission maxima correspond to the frequencies where the multiple reflections inside the substrate interfere constructively at the surface, leading to enhanced light matter interaction. This effect is purely linear and is taken into account in the transmission formula developed in chapter 1 (equation (1.50) on page 14). Indeed the change in contrast depending on the coupling with the Fabry-Pérot cavity is

clearly visible in figure 4.25b. Nonetheless, we underestimated the experimental impact on the signal-to-noise ratio. Because the SRR are fabricated on a thin substrate (150 μm), the signals from the internal reflections overlap each other, thus we cannot avoid interference with a temporal window to isolate the first pulse.

4.4.5 Coupling estimation

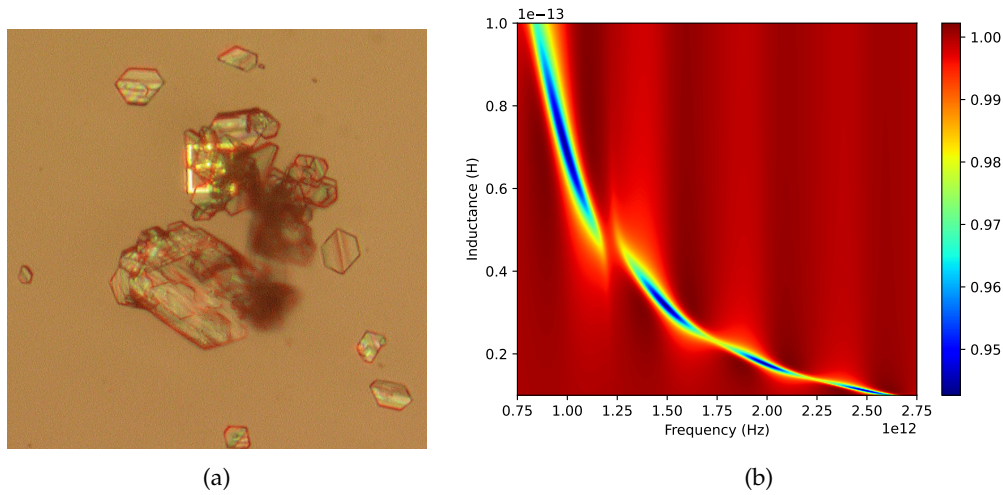


Figure 4.25: **(a)**: Optical microscope image of the SRR with a size $a = 23 \mu\text{m}$, taken as an example for coupling estimation. All the GA in the vicinity of SRR is included in the picture. **(b)**: Predicted transmission spectrum for a coupled SRRs with different inductance and with the coupling parameters estimated for the SRR shown in (a). Spectra are normalized with the transmission of the substrate. The RLC model predicts a splitting of the modes with this coupling. Outside of the GA resonance, we see a contrast modulation in the SRR resonance, explaining why the resonances measured at 1 and 1.5 THz are much more distinguishable than the one measured around 1.25 THz.

Despite the poor quality of the spectra, we can estimate the quality of the coupling between the GA and the SRRs by looking at the frequency shift after GA application. We model the capacitor of the SRR with the equivalent circuit proposed in section 1.3.4 (figure 1.10c on page 23), where a capacitor filled with GA is in series with a capacitor filled with air, and in parallel with a capacitor filled with the substrate material. Assuming that the substrate fill half of the total capacitance ($F_p = 0.5$), and with the approximation $\omega_n = \omega_0$, we can express the resonance frequencies of the resonator without and with GA as

$$\omega_0^2 = \frac{2}{L\alpha(\epsilon_{\text{sub}} + 1)}, \quad (4.11)$$

$$\text{and } \omega_c^2 = \frac{2}{L\alpha(\epsilon_{\text{sub}} + \epsilon_{\text{eff}})}, \quad (4.12)$$

where ϵ_{eff} is the effective permittivity of the medium in the *other half* of the capacitance, L is the inductance of the circuit, and α is the form factor of the capacitor such that $C = \alpha\epsilon$. Combining (4.11) and (4.12), we express the effective permittivity of the

medium above the substrate as

$$\varepsilon_{\text{eff}} = \frac{\omega_0^2}{\omega_c^2}(1 + \varepsilon_{\text{sub}}) - \varepsilon_{\text{sub}}. \quad (4.13)$$

Taking as an example the resonator with a size $a = 23 \mu\text{m}$ (figure 4.25a). We measured its original resonance $\frac{\omega_0}{2\pi} = 1.24 \text{ THz}$ (figure 4.19) and its coupled resonance $\frac{\omega_c}{2\pi} = 1.08 \text{ THz}$ (figure 4.21). With equation (4.13), we get $\varepsilon_{\text{eff}} = 2.74$. According to the measurement on the GA pellet (section 4.4.1), the permittivity of GA at low frequency is $\varepsilon_{\text{GA}} = \varepsilon_{\infty} + \Delta\varepsilon = 4.32$. Following the model from section 1.3.4, we deduce the filling factor

$$F_s = \left(\frac{1}{\varepsilon_{\text{eff}}} - 1 \right) \frac{\varepsilon_{\text{GA}}}{1 - \varepsilon_{\text{GA}}} = 0.83. \quad (4.14)$$

With this value of F_s , the Lorentz parameters measured on the pellet, and the decay rates measured on the SRR without GA, we use the coupled RLC model developed in chapter 1 to predict the behavior of SRRs with different resonance frequencies, identically coupled to GA. The resulting transmission (figure 4.25b) features the anti-crossing pattern characteristic of the strong coupling regime, with a Raby frequency $\frac{\Omega}{2\pi} = 114 \text{ GHz}$. This confirms that the resonance of GA is fully suitable to induce a splitting of the SRR mode, even with our imperfect coupling.

Nonetheless, as mentioned in section 4.4.2, we have no reason to assume that the electromagnetic properties of a GA crystal are isotropic. The anisotropy of the crystal has an influence on the coupling with the SRR that our models do not take into account. Even if the resonance at 1.2 THz happens to couple only with out of planes electric field, it does not necessarily mean that coupling in the near field is impossible. As illustrated in figure 4.26, and experimentally verified in chapter 3, the electric field from the SRR has an out of plane component. However, the *average* value of this component is zero. Evaluating the coupling with such a resonance mode for different gap sizes will give us insight about the locality of GA mode. Indeed, such a field profile should not couple with a mode delocalized over a distance larger than the gap, but should couple with a localized mode.

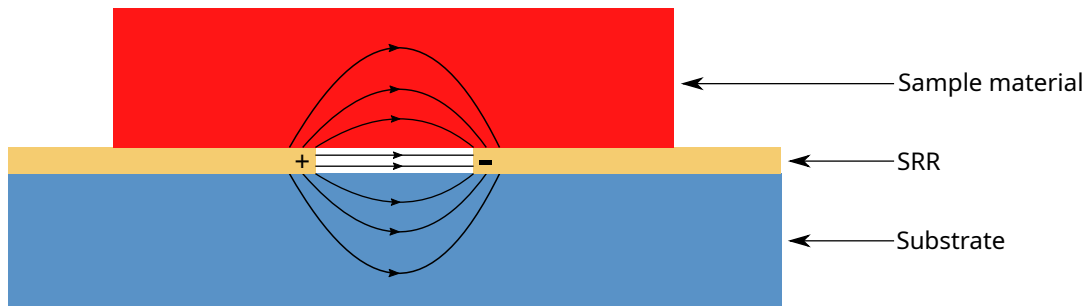


Figure 4.26: Schematic cross section of a SRR gap and its field line coupled with a crystal. The electric field is polarized out of plane above the metal, but the vertical component is anti-symmetric and has a zero mean value. A mode that couples with a vertically polarized electric field should couple to the SRR, unless the mode is delocalized over a distance larger than the gap.

4.5 Next steps

With the help of noise analysis and an error correction algorithm, we demonstrated spectroscopy on single SRRs in THz-TDS from 275 GHz to 3 THz. With a relatively low numerical aperture ($NA=0.356$), we measured up to 5% of extinction at resonance from single SRRs. Even though we are not currently able to extract information from SRRs with less than 1% of extinction, we showed with the measurement on the complementary SRR that signals down to 0.002% of the pulse intensity are well within the reach of our dynamic range. We identified and characterized the resonance of GA at 1.2 THz as a candidate for coupling with the SRR. We were able to detect the absorption of GA at 2 THz from less than $0.25 \mu\text{g}$ even without any field enhancement technique, other than the constructive interference in the substrate.

There are evidently a few obstacles left to be overcome to extract quantitative information on a nanometric amount of material from a measurement on a single SRR. But we experimentally confirmed that our SRRs are suitable for probing the permittivity of such amounts of material.

As we focused our attention on the coupling of the SRR with the GA, it appears that we underestimated the influence of the coupling of the SRR with the Fabry-Pérot cavity formed by the substrate. Using a thicker substrate will allow us to perform the experiment in a much more favorable configuration in two ways: First, we will make sure that the interference is constructive at the frequency of interest. Secondly, we will be able to separate the first transmitted impulsion, and analyze a signal free from any interference. We will also reduce the reflection from the back side of the sample with an anti-reflective coating.

Another point we will improve is the method of deposition of the GA on the SRRs. Our measurements showed that even less than $0.25 \mu\text{g}$ of GA around the SRR is enough to significantly alter the transmission spectrum and make the interpretation of the result much more difficult. In fact, the SRR we used for the coupling estimation (figure 4.25a) is the only one which was surrounded by a quantity of GA small enough to provide a relatively clean spectrum around 1.2 THz (figure 4.21). We need to improve the reliability of the deposition method to get this result on every SRRs. We identified the water evaporation speed as one of the most significant variables for the quality of the crystals. We used a hydrophobic surface treatment to change the surface area of the droplets and slow down the evaporation. This method greatly improved the quality of the crystals, but still does not allow a full control of the evaporation speed, which tends to stay too fast for very small drops. In the longer term, we will perform the deposition under a humidity controlled atmosphere. This will give us complete control over the evaporation speed and allow us to obtain good quality crystals even from droplets small enough to barely cover the SRR.

To better control the size of the drop, we will add a lithography step in our fabrication process to cover the SRR and its immediate surrounding during the surface functionalization. Hence the vicinity of the SRR will stay hydrophilic while the rest of the sample will be hydrophobic. This process will greatly facilitate the deposition of drops on the hydrophilic area.

Although a lot of improvements are still possible in our experiment, we believe that we are very close to demonstrate material parameter extraction from a measurement on a single SRR, after which we will extend our experiments to other materials, in particular to materials that are not available in large enough quantities to be measured as pellets.

References

- [1] S. J. Park et al. "Detection of microorganisms using terahertz metamaterials". In: *Scientific Reports* 4.1 (May 2014). DOI: [10.1038/srep04988](https://doi.org/10.1038/srep04988) (cit. on p. 73).
- [2] R. J. B. Dietz et al. "Low Temperature Grown Be-doped InGaAs/InAlAs Photoconductive Antennas Excited at 1030 nm". In: *Journal of Infrared, Millimeter, and Terahertz Waves* 34.3-4 (Mar. 2013), pp. 231–237. DOI: [10.1007/s10762-013-9968-4](https://doi.org/10.1007/s10762-013-9968-4) (cit. on p. 73).
- [3] Ying Zhang et al. "A Broadband THz-TDS System Based on DSTMS Emitter and LTG InGaAs/InAlAs Photoconductive Antenna Detector". In: *Scientific Reports* 6.1 (May 2016). DOI: [10.1038/srep26949](https://doi.org/10.1038/srep26949) (cit. on p. 73).
- [4] S A Bereznyaya et al. "Broadband and narrowband terahertz generation and detection in GaSe_{1-x}S_x crystals". In: *Journal of Optics* 19.11 (Oct. 2017), p. 115503. DOI: [10.1088/2040-8986/aa8e5a](https://doi.org/10.1088/2040-8986/aa8e5a) (cit. on p. 73).
- [5] R. Kersting et al. "Few-Cycle THz Emission from Cold Plasma Oscillations". In: *Physical Review Letters* 79.16 (Oct. 1997), pp. 3038–3041. DOI: [10.1103/physrevlett.79.3038](https://doi.org/10.1103/physrevlett.79.3038) (cit. on p. 73).
- [6] Yun-Shik Lee. *Principles of Terahertz Science and Technology*. Springer-Verlag GmbH, Mar. 2009. 340 pp. ISBN: 9780387095400. URL: https://www.ebook.de/de/product/12469854/yun_shik_lee_principles_of_terahertz_science_and_technology.html (cit. on p. 73).
- [7] R. de L. Kronig. "On the Theory of Dispersion of X-Rays". In: *Journal of the Optical Society of America* 12.6 (June 1926), p. 547. DOI: [10.1364/josa.12.000547](https://doi.org/10.1364/josa.12.000547) (cit. on p. 76).
- [8] H. A. Kramers. "La diffusion de la lumiere par les atomes". In: *Atti Cong. Intern. Fisica (Transactions of Volta Centenary Congress) Como 2* (1927), pp. 545–557 (cit. on p. 76).
- [9] Romain Peretti et al. "THz-TDS Time-Trace Analysis for the Extraction of Material and Metamaterial Parameters". In: *IEEE Transactions on Terahertz Science and Technology* 9.2 (Mar. 2019), pp. 136–149. DOI: [10.1109/tthz.2018.2889227](https://doi.org/10.1109/tthz.2018.2889227) (cit. on p. 76).
- [10] Shima Rajabali et al. "An ultrastrongly coupled single terahertz meta-atom". In: *Nature Communications* 13.1 (May 2022). DOI: [10.1038/s41467-022-29974-2](https://doi.org/10.1038/s41467-022-29974-2) (cit. on p. 77).
- [11] Melanie Lavancier. "Heuristic approach to take up the challenge of terahertz time-domain spectroscopy for biology". Theses. Université de Lille, Oct. 2021. URL: <https://tel.archives-ouvertes.fr/tel-03539445> (cit. on pp. 78, 80, 82, 86).
- [12] Laleh Mohtashemi et al. "Maximum-likelihood parameter estimation in terahertz time-domain spectroscopy". In: 29 (2021), p. 4912. ISSN: 1094-4087. DOI: [10.1364/oe.417724](https://doi.org/10.1364/oe.417724) (cit. on p. 78).
- [13] Elsa Denakpo et al. "Noise analysis, noise reduction and covariance estimation for Time domain Spectroscopy". In: *2022 47th International Conference on Infrared, Millimeter and Terahertz Waves (IRMMW-THz)*. IEEE, Aug. 2022. DOI: [10.1109/irmmw-thz50927.2022.9895812](https://doi.org/10.1109/irmmw-thz50927.2022.9895812) (cit. on pp. 78–80).

- [14] Vyacheslav Tuzlukov. *Signal Processing Noise*. Taylor & Francis Ltd., Oct. 2018. 688 pp. ISBN: 1420041118. URL: https://www.ebook.de/de/product/22913272/vyacheslav_tuzlukov_signal_processing_noise.html (cit. on p. 78).
- [15] Udo Kaatz. "Complex permittivity of water as a function of frequency and temperature". In: *Journal of Chemical & Engineering Data* 34.4 (Oct. 1989), pp. 371–374. DOI: [10.1021/je00058a001](https://doi.org/10.1021/je00058a001) (cit. on p. 82).
- [16] Hans J. Liebe, George A. Hufford, and Takeshi Manabe. "A model for the complex permittivity of water at frequencies below 1 THz". In: *International Journal of Infrared and Millimeter Waves* 12.7 (July 1991), pp. 659–675. DOI: [10.1007/bf01008897](https://doi.org/10.1007/bf01008897) (cit. on p. 82).
- [17] W. J. Ellison. "Permittivity of Pure Water, at Standard Atmospheric Pressure, over the Frequency Range 0-25THz and the Temperature Range 0-100°C". In: *Journal of Physical and Chemical Reference Data* 36.1 (Mar. 2007), pp. 1–18. DOI: [10.1063/1.2360986](https://doi.org/10.1063/1.2360986) (cit. on p. 82).
- [18] R. Buchner, J. Barthel, and J. Stauber. "The dielectric relaxation of water between 0°C and 35°C". In: *Chemical Physics Letters* 306.1-2 (June 1999), pp. 57–63. DOI: [10.1016/s0009-2614\(99\)00455-8](https://doi.org/10.1016/s0009-2614(99)00455-8) (cit. on p. 82).
- [19] I. Al-Naib et al. "Enhanced Q-factor in Optimally Coupled Macrocell THz Metamaterials: Effect of Spatial Arrangement". In: *IEEE Journal of Selected Topics in Quantum Electronics* 19.1 (Jan. 2013), pp. 8400807–8400807. DOI: [10.1109/jstqe.2012.2202639](https://doi.org/10.1109/jstqe.2012.2202639) (cit. on p. 83).
- [20] Ibraheem Al-Naib et al. "Conductive Coupling of Split Ring Resonators: A Path to THz Metamaterials with Ultrasharp Resonances". In: *Physical Review Letters* 112.18 (May 2014), p. 183903. DOI: [10.1103/physrevlett.112.183903](https://doi.org/10.1103/physrevlett.112.183903) (cit. on p. 83).
- [21] G. Scalari et al. "High quality factor, fully switchable terahertz superconducting metasurface". In: *Applied Physics Letters* 105.26 (Dec. 2014), p. 261104. DOI: [10.1063/1.4905199](https://doi.org/10.1063/1.4905199) (cit. on p. 83).
- [22] Janine Keller et al. "High T_c Superconducting THz Metamaterial for Ultra-strong Coupling in a Magnetic Field". In: *ACS Photonics* 5.10 (Oct. 2018), pp. 3977–3983. DOI: [10.1021/acsphotonics.8b01025](https://doi.org/10.1021/acsphotonics.8b01025) (cit. on p. 83).
- [23] Keller, Janine. "Ultra-Strong Light-Matter Coupling of 2D Electron and Hole Gases with Metallic and Superconducting Metamaterials". en. PhD thesis. 2019. DOI: [10.3929/ETHZ-B-000334147](https://doi.org/10.3929/ETHZ-B-000334147) (cit. on p. 85).
- [24] Michael T. Ruggiero et al. "Examination of L-Glutamic Acid Polymorphs by Solid-State Density Functional Theory and Terahertz Spectroscopy". In: *The Journal of Physical Chemistry A* 120.38 (Sept. 2016), pp. 7490–7495. DOI: [10.1021/acs.jpca.6b05702](https://doi.org/10.1021/acs.jpca.6b05702) (cit. on pp. 85, 86, 89).

Chapter 5

Optical trapping from the confined field of SRRs and graphene plasmonic resonances.

In the previous chapters, we demonstrated how a resonator like a Split Ring Resonator (SRR) can be used to provide large field confinement. We characterized and took advantage of this property to enhance light matter interaction and perform THz spectroscopy experiment on samples much smaller than the diffraction limit.

However, spectroscopy is not the only possible application of field confinement. In particular, a strong electric field gradient generates a force on dielectric or metallic objects, called optical force. In this chapter, we will see how the field confinement provided by a SRR can be used to create a THz optical trap.

As part of a collaboration with P.Q. Liu from the State University of New York at Buffalo (UB), made possible by the Fulbright Program, we will then see how the same principles are applicable in the mid-IR with an optical trap based on graphene plasmonic resonance.

5.1 The Optical Tweezer

Optical traps have revolutionized, from fundamental physics to investigation tools in biology with optical tweezers, and is going towards “lab-on-chip” with Optical Trapping (OT) based on metallic nanostructures. These traps combined with microfluidics show particularly high performances allowing trapping of yeast cells, and living bacteria. However, plasmonic trap suffer from absorption in the metal of the nano-resonator. This local heat source induces convection in the fluid, leading to weaker trapping or even preventing trapping of the smallest particles. Hence, there is not today, any demonstration of on-chip OT of most viruses of interest that is with dimension smaller than 50 nm.

Since the 70's, with theoretical work [1] and the following experimental demonstration [2], optical traps have revolutionized many fields of science, from fundamental physics to novel investigation tools in biology such as optical tweezers. These tweezers use free space optics to trap particles in a 3D “potential” leading to a *force proportional to the input optical power*. Optical tweezers have become an indispensable component in the biophysicists' toolkit, leading to breakthroughs in understanding DNA structure [3], RNA transcription [4], protein folding [5], cell motility [6], and single-molecule biophysics [7]. The Practical extension of optical tweezing below the range of about 100 nm for visible wavelength for a dielectric target is extremely difficult since *the OT force is proportional to the 3rd power of radius* [8].

Therefore, investigation of systems at smaller scales is hindered by optical diffraction, which limits the maximum optical forces that can be reached in optical tweezers for a given input power [9]. This is particularly detrimental for biological systems, where, to compensate for the weak gradient leading to weak forces, one needs to use high levels of optical power, which eventually will damage the specimen [10, 11]. Therefore, if large nanoparticles (NP), such as large virus or bacteria (size > 50 nm), can be trapped [12], the direct manipulation of many biological and non-biological targets (e.g. most of viruses, proteins, and small NP's) with sizes ranging from 50 nm to 5 nm, during a reasonable time (several seconds), is out of reach with reasonable power [13]. Because OT force on these objects cannot compensate for the fluidic ones. To overcome this, "lab-on-chip" techniques based near field photonic structures were developed. If some optical traps have been built from dielectric, most of them are based on metallic (plasmonic) nanostructures. This architecture employs metallic nano-structures to concentrate and enhance incident optical fields in deep-subwavelength gaps (e.g. [14–17]). *These structures yields to photonic modes with large near-field intensity gradients that greatly amplify optical forces for a given input power, enabling strong OT.* Zhang et al. were able to enhance the light field enough with dipole antennas to trap 10 nm gold particles [15] or 20 nm polystyrene beads [18]. In fact, the performances of these 3D traps are higher than the free space ones because the particle experiences the full field strength rather than an evanescent one and then requires input-power densities 2–3 orders of magnitude lower than the biological damage threshold [8].

Following the blossoming of the field of optofluidics, these plasmonic optical traps were combined with μ fluidics stage in a so-called optofluidics lab-on-chip optical tweezers [9, 19]. Several studies employed plasmonic nanostructures to trap biological objects. For instance, Miao et al. and Huang et al. used Au nano-spheres [20], or Au nano-disks [19] to trap yeast cells (spherical shape of several μ m of radius) in plasmonic OT. Going to smaller size, Righini et al. showed that living *Escherichia coli* bacteria (cylindrical shape ~ 2 μ m length 300 nm radius) can be stably trapped in a plasmonic nano-tweezer comprised of dipole nano-antennas for more than two hours without visible damage [10]. Going smaller Kang et al. [21] claimed that they managed to trap a large virus (100 nm) in dielectric traps but did not prove that the trapping was done on single particles and not an agglomeration and results have not yet been reproduced to our knowledge.

Progress in the field is fast, but there is not today any demonstration of on-chip OT of most viruses (< 50 nm) because OT suffers from limitations [8]. Indeed, the easiest way to increase OT forces is to increase the optical power. However, the amount of power that can be applied is limited by heating induced by absorption of the light in either the surrounding fluid, the target itself or the resonator. This heating will eventually boil the liquid or at least increase the temperature and therefore induces additional thermal flux around the trap. The drag forces resulting from this flux competes with the optical forces. Finally, this could simply release the trapped particle.

If nanophotonics structure allows to tackle part of the problems, heating remains a limitation for visible or NIR plasmonic OT systems because metal structures are high absorbers in this spectral range and therefore are very efficient at converting electromagnetic energy to heat. Because of its importance, this effect in metallic structure in the visible or NIR has been widely studied by the OT group of R. Quidant [22–25]. At the end, they showed so much significance that they finally decided to use it to make nano thermal sources inside a μ fluidic circuitry [26]. As a result, *the demonstration of on-chip OT of viruses sizing ~ 50 nm has never been achieved.*

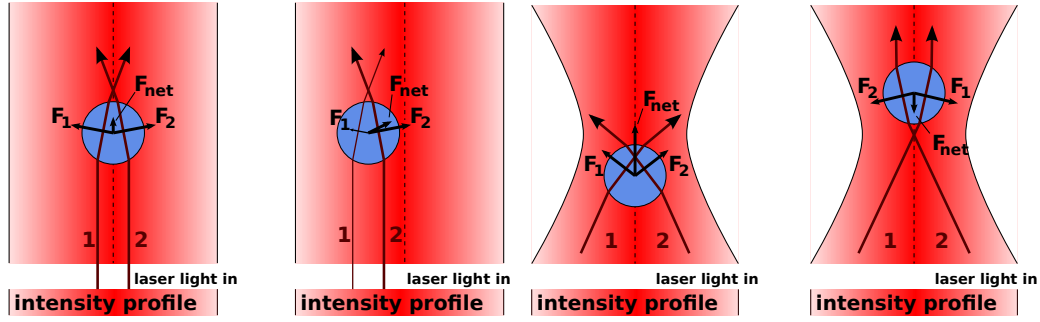


Figure 5.1: Ray optics interpretation of optical forces, case of a collimated and focused beam.

5.2 Optical forces

Optical forces can be intuitively explained by considering the momentum carried by light and its conservation. When a beam is deflected or absorbed by an object, the momentum of the beam is changed, and the difference is transferred to the object by means of an optical force (see figure 5.1). This interpretation is good enough to understand the general principle of a regular optical tweezer, but is not sufficient to give quantitative results as it uses ray optic approximation, which does not apply when studying phenomenon at scales close to the wavelength. For a general and accurate description of optical forces, one has to use Maxwell's equations to derive Lorentz's forces. This section is about the analytical calculation of optical forces from Maxwell's equation and Lorentz's formula. In addition to the forces, light can also apply a torque on a particle. Analysis and discussion about optical torque is available in appendix A on page 141.

5.2.1 General case

The only hypothesis used is the classical physic hypothesis[27]. Lorentz's forces can be obtained from Maxwell's equation in this general case.

$$\vec{\nabla} \cdot \vec{E} = \frac{\rho}{\epsilon}, \quad (5.1)$$

$$\vec{\nabla} \cdot \vec{B} = 0, \quad (5.2)$$

$$\vec{\nabla} \wedge \vec{E} = -\frac{\partial \vec{B}}{\partial t}, \quad (5.3)$$

$$\vec{\nabla} \wedge \vec{B} = \mu \vec{j} + \mu \epsilon \frac{\partial \vec{E}}{\partial t}, \quad (5.4)$$

Where \vec{E} is the electric field, \vec{B} is the magnetic field, ρ is the charge density, \vec{j} is the current density, ϵ is the vacuum dielectric permittivity and μ is the vacuum magnetic permeability. The Lorentz's force on a particle with a charge q and a speed vector \vec{v} is given by:

$$\vec{F} = q\vec{E} + q\vec{v} \wedge \vec{B}. \quad (5.5)$$

This formula can be written for an infinitesimal volume:

$$\frac{\vec{F}}{dV} = \rho \vec{E} + \vec{j} \wedge \vec{B}, \quad (5.6)$$

using (5.1) and (5.3)

$$\frac{\vec{F}}{dV} = \varepsilon(\vec{\nabla} \cdot \vec{E}) \vec{E} + \frac{1}{\mu}(\vec{\nabla} \wedge \vec{B}) \wedge \vec{B} - \varepsilon \frac{\partial \vec{E}}{\partial t} \wedge \vec{B}, \quad (5.7)$$

furthermore, the Poynting vector derivative is

$$\frac{\partial \vec{S}}{\partial t} = \frac{1}{\mu} \frac{\partial(\vec{E} \wedge \vec{B})}{\partial t} = \frac{1}{\mu} \frac{\partial \vec{E}}{\partial t} \wedge \vec{B} + \frac{1}{\mu} \vec{E} \wedge \frac{\partial \vec{B}}{\partial t} \quad (5.8)$$

$$\frac{\partial \vec{E}}{\partial t} \wedge \vec{B} = \mu \frac{\partial \vec{S}}{\partial t} + \vec{E} \wedge (\vec{\nabla} \wedge \vec{E}), \quad (5.9)$$

thus, (5.7) can be expressed as

$$\frac{\vec{F}}{dV} = \varepsilon(\vec{\nabla} \cdot \vec{E}) \vec{E} + \frac{1}{\mu}(\vec{\nabla} \wedge \vec{B}) \wedge \vec{B} - \varepsilon \mu \frac{\partial \vec{S}}{\partial t} + \varepsilon \vec{E} \wedge (\vec{\nabla} \wedge \vec{E}). \quad (5.10)$$

We add the term $(\vec{\nabla} \cdot \vec{B}) \vec{B} = 0$ to get a symmetrical expression between \vec{E} and \vec{B}

$$\frac{\vec{F}}{dV} = \varepsilon \left[(\vec{\nabla} \cdot \vec{E}) \vec{E} - \vec{E} \wedge (\vec{\nabla} \wedge \vec{E}) \right] + \frac{1}{\mu} \left[(\vec{\nabla} \cdot \vec{B}) \vec{B} - \vec{B} \wedge (\vec{\nabla} \wedge \vec{B}) \right] - \varepsilon \mu \frac{\partial \vec{S}}{\partial t}. \quad (5.11)$$

We remove the cross products from the expression using the following identity

$$\frac{1}{2} \vec{\nabla}(\vec{A} \cdot \vec{A}) = \vec{A} \wedge (\vec{\nabla} \wedge \vec{A}) + (\vec{A} \cdot \vec{\nabla}) \vec{A}, \quad (5.12)$$

thus

$$\frac{\vec{F}}{dV} = \varepsilon \left[(\vec{\nabla} \cdot \vec{E} + \vec{E} \cdot \vec{\nabla}) \vec{E} - \frac{1}{2} \vec{\nabla} E^2 \right] + \frac{1}{\mu} \left[(\vec{\nabla} \cdot \vec{B} + \vec{B} \cdot \vec{\nabla}) \vec{B} - \frac{1}{2} \vec{\nabla} B^2 \right] - \varepsilon \mu \frac{\partial \vec{S}}{\partial t}. \quad (5.13)$$

The Maxwell's Stress Tensor (MST) is defined as

$$T_{ij} = \varepsilon \left(E_i E_j - \frac{\delta_{ij}}{2} E^2 \right) + \frac{1}{\mu} \left(B_i B_j - \frac{\delta_{ij}}{2} B^2 \right), \quad (5.14)$$

which leads to this much shorter expression of the optical force

$$\frac{\vec{F}}{dV} = \vec{\nabla} \cdot T - \varepsilon \mu \frac{\partial \vec{S}}{\partial t}. \quad (5.15)$$

For forces applied on relatively massive objects (i.e. not single atoms), the inertia of the object prevents it from being affected by forces oscillating at the THz time scale and above. If the electromagnetic source is a continuous monochromatic beam, the second term of (5.15) is oscillating at twice the frequency of the light source, and has a zero mean value. Hence why we neglect it in the rest of the calculation.

Using the divergence theorem, the integrated optical force over a volume V is expressed as:

$$\vec{F}_{\text{tot}} = \iiint_V \vec{\nabla} \cdot T dV = \oint_{\partial V} T \cdot d\vec{S}, \quad (5.16)$$

Where ∂V is the surface enclosing the volume V .

This formulation is very useful in numerical computation, since it allows one to get the force on a particle knowing only the MST on a closed surface around the particle, and does not require to evaluating the tensor on every point inside the volume, which considerably reduces the memory requirement.

In that last formula, it seems like the optical force on a particle is independent of the optical index of the surrounding medium, however this formula gives the optical force as a function of the total electromagnetic field, which itself depends on the different material indices as well as the particle geometry. All this information can indirectly be found in the Maxwell stress tensor. Therefore this formula cannot be used alone, and the electromagnetic field needs to be computed with another method such as Finite Difference Time Domain (FDTD) for numerical computation.

5.2.2 Force on a neutral dielectric Rayleigh particle

We take as a definition of a Rayleigh particle, a particle whose size is negligible in regard to the spatial variation of the electromagnetic field. A dielectric sphere with a radius a in an electromagnetic field with $a \ll \lambda$ can be modeled as an electric dipole [28]. We assume the particle is electrically neutral, immobile, and does not have nonlinear properties. The electromagnetic field induced by the sphere is neglected here, the force caused by it shall be discussed later. We define the polarizability of the sphere α (in SI units) as $\vec{p} = \alpha \vec{E}$, where \vec{p} is the dipole moment. Since $a \ll \lambda$, the electric field is developed at first order, and the magnetic field is considered constant through the dipole.

The Lorentz force on the dipole is then written

$$\vec{F} = q(\vec{E}(\vec{r}_1) - \vec{E}(\vec{r}_2)) + q \frac{d(\vec{r}_1 - \vec{r}_2)}{dt} \wedge \vec{B}, \quad (5.17)$$

where \vec{r}_1 (\vec{r}_2) is the barycentre of the positive (negative) electric charge q ($-q$). The first order approximation of \vec{E} is

$$\vec{E}(\vec{r}_1) = \vec{E}(\vec{r}_2) + \begin{pmatrix} r_x \frac{\partial E_x}{\partial x} + r_y \frac{\partial E_x}{\partial y} + r_z \frac{\partial E_x}{\partial z} \\ r_x \frac{\partial E_y}{\partial x} + r_y \frac{\partial E_y}{\partial y} + r_z \frac{\partial E_y}{\partial z} \\ r_x \frac{\partial E_z}{\partial x} + r_y \frac{\partial E_z}{\partial y} + r_z \frac{\partial E_z}{\partial z} \end{pmatrix}, \quad (5.18)$$

where $\vec{r} = \vec{r}_1 - \vec{r}_2$ is the displacement vector. Therefore

$$\vec{E}(\vec{r}_1) - \vec{E}(\vec{r}_2) = \begin{pmatrix} r_x \frac{\partial E_x}{\partial x} + r_y \frac{\partial E_x}{\partial y} + r_z \frac{\partial E_x}{\partial z} \\ r_x \frac{\partial E_y}{\partial x} + r_y \frac{\partial E_y}{\partial y} + r_z \frac{\partial E_y}{\partial z} \\ r_x \frac{\partial E_z}{\partial x} + r_y \frac{\partial E_z}{\partial y} + r_z \frac{\partial E_z}{\partial z} \end{pmatrix} = (\vec{r} \cdot \vec{\nabla}) \cdot \vec{E}, \quad (5.19)$$

and

$$\vec{F} = q(\vec{r} \cdot \vec{\nabla}) \cdot \vec{E} + q \frac{d\vec{r}}{dt} \wedge \vec{B}, \quad (5.20)$$

$$\vec{F} = (\vec{p} \cdot \vec{\nabla}) \cdot \vec{E} + \frac{d\vec{p}}{dt} \wedge \vec{B}, \quad (5.21)$$

with $\vec{p} = \alpha \vec{E}$, where α is the polarizability tensor of the particle, that is a scalar value in the case of a homogeneous isotropic sphere. If the electric field is oscillating, the polarizability is described with complex values. Since we are working with the real values of the electric field and of the polarization vector, the expression becomes $\vec{p} = \Re(\alpha) \vec{E}$. Thus

$$\vec{F} = \Re(\alpha) \left[(\vec{E} \cdot \vec{\nabla}) \cdot \vec{E} + \frac{d\vec{E}}{dt} \wedge \vec{B} \right], \quad (5.22)$$

which can be rewritten using (5.12) and (5.3)

$$\vec{F} = \Re(\alpha) \left[\frac{1}{2} \vec{\nabla} E^2 + \mu \frac{d\vec{S}}{dt} \right]. \quad (5.23)$$

As in the general case, the force is divided in two parts, the first one being associated with spatial variation of intensity while the second is associated with temporal variation of intensity. If we assume that the particle is massive enough to be unaffected by forces variation at twice the light frequency and is exposed to a beam with constant intensity, then

$$\vec{F} = \frac{1}{2} \Re(\alpha) \vec{\nabla} E^2. \quad (5.24)$$

Optical forces are in general not conservative, because the particle affects the electric field distribution. Nonetheless, if the field scattered by the particle is neglected, the optical force is expressed as a gradient, therefore we can define the *pseudo*-potential:

$$U = -\frac{\Re(\alpha) E^2}{2}. \quad (5.25)$$

The polarizability of a dielectric sphere with an electric permittivity ϵ in a medium with an electric permittivity ϵ_{out} is given by [29]

$$\alpha = 4\pi a^3 \epsilon_0 \epsilon_{\text{out}} \frac{\epsilon - \epsilon_{\text{out}}}{\epsilon + 2\epsilon_{\text{out}}}. \quad (5.26)$$

Finally,

$$\vec{F} = \epsilon_0 4\pi a^3 \Re \left(\epsilon_{\text{out}} \frac{\epsilon - \epsilon_{\text{out}}}{\epsilon + 2\epsilon_{\text{out}}} \right) \vec{\nabla} E^2. \quad (5.27)$$

In the case of a particle much smaller than the field variation, the electromagnetic wave emitted from the dipole is known as Rayleigh scattering and cannot really be ignored. Indeed, the Rayleigh scattering induces a change in the momentum of light and therefore a force on the particle, which has to be taken into account. This force is along the direction of wave propagation and is given by $F_{\text{scat}} = n_{\text{out}} I C_{\text{scat}} / c$

where C_{scat} is the scattering cross section, and n_{out} is the index of the surrounding medium [2]. If the sphere is not absolutely transparent, another optical force results from the absorption, also along the direction of wave propagation and given by $F_{\text{abs}} = n_{\text{out}} I C_{\text{abs}} / c$ where C_{abs} is the absorption cross section of the particles. Both the scattering and the absorption cross section can be expressed as a function of the complex polarizability [30]

$$C_{\text{scat}} = \frac{k^4 |\alpha|^2}{6\pi\epsilon^2}, \quad (5.28)$$

$$C_{\text{abs}} = \frac{n_{\text{out}} k \Im(\alpha)}{\epsilon_{\text{out}} \epsilon_0}. \quad (5.29)$$

5.2.3 Optical forces in a Gaussian beam

The intensity of a Gaussian beam is given by

$$I(r, z) = I_0 \left(\frac{w_0}{w(z)} \right)^2 \exp \left(\frac{-2r^2}{w(z)^2} \right), \quad (5.30)$$

where r is the radial distance from the center axis of the beam, z is the axial distance from the beam's focus, I_0 is the intensity in the beam center, w_0 is the waist radius and $w(z)$ is defined as the radius where the intensity values is $1/e^2$ of their axial value in the plane z along the beam. Therefore

$$E^2(r, z) = 2\eta I(r, z) = 2\eta I_0 \left(\frac{w_0}{w(z)} \right)^2 \exp \left(\frac{-2r^2}{w(z)^2} \right), \quad (5.31)$$

where η is the characteristic impedance of the medium. Considering $w(z)$ is given by

$$w(z) = w_0 \sqrt{1 + \left(\frac{z}{z_r} \right)^2}, \quad (5.32)$$

where $z_r = \frac{\pi w_0^2}{\lambda}$ is the Rayleigh range of the beam, the spatial derivatives of E^2 can be expressed as follow

$$\frac{\partial E^2}{\partial r} = -8\eta I_0 \frac{w_0^2}{w(z)^4} r \exp \left(\frac{-2r^2}{w(z)^2} \right), \quad (5.33)$$

$$\frac{\partial E^2}{\partial z} = 4\eta I_0 \left(\frac{\lambda}{\pi} \right)^2 \frac{1}{w(z)^4} \left(\frac{2r^2}{w(z)^2} - 1 \right) z \exp \left(\frac{-2r^2}{w(z)^2} \right). \quad (5.34)$$

Thus in cylindrical coordinates

$$\vec{F}_{\text{grad}} = 2\alpha\eta I_0 \frac{1}{w(z)^4} \exp \left(\frac{-2r^2}{w(z)^2} \right) \left[\left(\frac{\lambda}{\pi} \right)^2 \left(\frac{2r^2}{w(z)^2} - 1 \right) z \vec{u}_z - 2w_0^2 r \vec{u}_r \right], \quad (5.35)$$

and

$$\vec{F}_{\text{scat/abs}} = \frac{c}{n_{\text{out}}} (C_{\text{scat}} + C_{\text{abs}}) I_0 \left(\frac{w_0}{w(z)} \right)^2 \exp \left(\frac{-2r^2}{w(z)^2} \right) \vec{u}_z. \quad (5.36)$$

5.3 Terahertz optical tweezer

5.3.1 Trapping smaller particle with terahertz radiation

As it has been shown in the previous section, the gradient force on a particle is proportional to its volume and to the intensity gradient of the beam. Therefore, in order to trap smaller particles, one must increase the power of the laser source, or decrease the volume where light is focused. Using THz waves instead of visible, near infrared or ultraviolet light is consequently counter-intuitive since the Abbe diffraction limit in this range of frequency is even more limiting. Nonetheless, the goal being to trap small particles like viruses or large proteins, increasing the intensity gradient by increasing the laser power and reducing the wavelength would work as far as trapping is concerned, but the high intensity is likely to destroy or alter the big organic molecules such as DNA [11]. Another possibility to create a strong gradient force is to avoid the diffraction limit with near-field optics, by using a metallic resonator to confine an electric field in a volume way smaller than the diffraction limit. Yet trapping particle near a metallic metasurface brings up another issue. Indeed, the laser light will heat the metal through absorption, causing convection movement that will expel the particle from the trap. This is the reason why the terahertz range is of particular interest for near field optical trapping, metals being very close to perfect electrical conductors at these frequencies, generating 100 to 1000 times less heat than in the visible or infra-red range [31].

5.3.2 Tweezer design

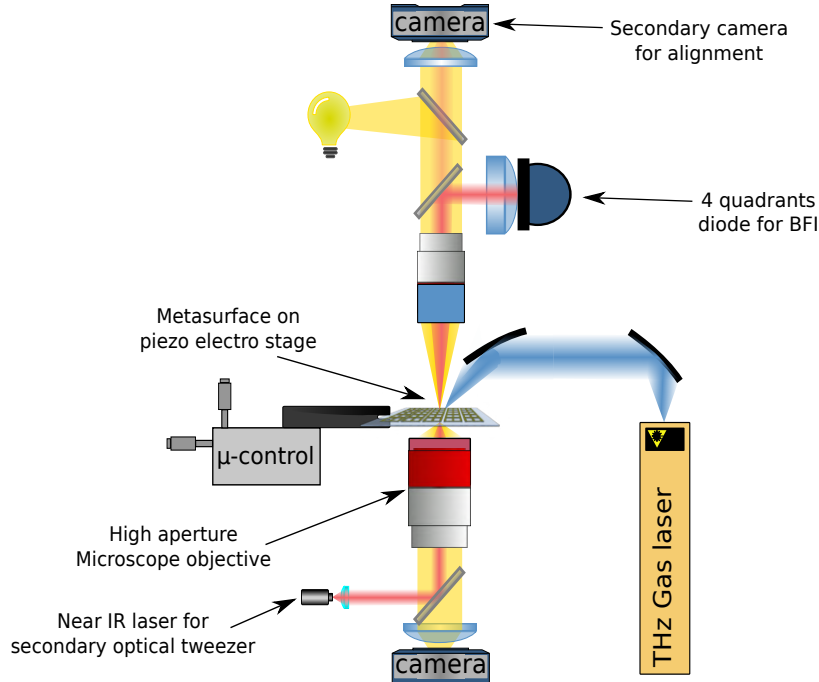


Figure 5.2: General schematic of the tweezers setup.

The terahertz optical tweezer in itself consists of a THz laser (gas or Quantum Cascade Laser), a set of parabolic mirrors to focus the beam on the sample, and the micro-resonators described in section 5.3.4 on page 114. As seen in the theoretical section, the only requirement for strong optical forces is a strong gradient in the

magnitude of the electric field. Hence the resonators described later are designed to confine an electric field in a chosen volume. Furthermore, an optical microscope is needed to observe and demonstrate trapping, and a secondary optical tweezer is used to compare and measure the stiffness of the THz trap. The secondary tweezers is a standard near infrared optical tweezers, using a microscope objective both to focus the infrared laser beam and to observe the sample. The main components of the infrared optical tweezers are:

- A 976 nm, 300 mW laser diode, which generates the secondary trapping beam
- A high aperture oil immersion microscope objective lens (NA=1.2), used to make an image of the sample, and to focus the secondary laser beam on the same plane
- A condenser lens, used to illuminate the sample for the observation, and to collimate the infrared light from the secondary laser beam gone through the sample. This light is used by the force detection module described later.
- A camera, to record the image of the sample through the objective lens.

In addition, a force measurement system designed to be used with the infrared tweezer is used to evaluate the infrared trap stiffness, and to obtain an estimation of the THz trap stiffness by comparison. A secondary camera is added for alignment. A schematic of the whole device is shown on figure 5.2.



Figure 5.3: Example of electric split ring resonator designs with three different gap sizes ($0.5\ \mu\text{m}$, $4\ \mu\text{m}$ and $6\ \mu\text{m}$), the trapezoidal shape makes the capacitance independent of the gap size.

5.3.3 Simulation

In contrast with a Gaussian beam, the field distribution in the near-field of a SRR does not take an analytical form. We have seen in chapter 3 that this field distribution is also very difficult to measure experimentally. Hence numerical simulation is the most efficient way to estimate the stability of the THz OT.

Numerical force calculation

The Lumerical software provides two ways for the calculation of the optical forces from the electromagnetic field data, described hereinafter. Those computation methods can be adapted for torque computation (see appendix A.3 on page 143).

Volumetric method The volumetric method evaluates the optical forces in every mesh of a cuboid aligned with the coordinate system. For each of these mesh, the force density is calculated directly from the Lorentz formula on an infinitesimal volume (5.6) on page 102, with a charge and current density evaluated from Maxwell's equation and numerical value of the electromagnetic field obtained with the FDTD method. The total force is then calculated by integrating the force density over the whole volume. The main advantage of this method is that it allows one to get a map of the force density at every point of the volume, and to get the total force on a more specific volume inside the cuboid by using custom a window before the integration. Recording the electromagnetic field in every mesh of the volume is however very heavy in terms of memory requirement

MST method The MST method evaluates Maxwell's Stress Tensor on the surface defining the volume, and uses the formula (5.16) on page 103 to compute the force. Like the volumetric method, the volume can only be a cuboid aligned with the coordinate system. But in this case, there is no integration technique that can be used to get the force on a sub-volume. As it had been shown in section 5.2.1, this method allows one to get the force on the volume knowing only the electromagnetic field on the surface of the cuboid without additional approximation, making it very efficient in terms of memory and time requirement. It can however be subject to numerical noise making it less reliable when the force is small [32].

Comparison of both methods To summarize the theoretical strengths and weaknesses of each technique:

- The MST technique has much lower memory requirements.
- The MST technique is sensitive to numerical noise when the force is small.
- The volumetric method does not work for special material such as Perfect Electrical Conductor (PEC), where the optical force is applied on an infinitesimal volume.
- The volumetric technique is less reliable when the mesh is coarse.
- The volumetric technique allows for more possibility about the shape of the volume where the force needs to be calculated.

To simulate the optical forces on a sphere above a SRR, we are always able to find a cube of homogeneous media surrounding the particle. We use the MST method in our simulations.

Simulation result

The most common criteria to estimate the stability of an optical trap is to compare the pseudo-potential (see (5.25) on page 104) with $k_B T$, where k_B is the Boltzmann constant, and T is the temperature. A trap is considered stable when the potential well is deeper than $10k_B T$. Note that this approach only takes into account the depth of the well, and not its width, which plays a significant role in the probability of a particle being ejected from a potential well by Brownian motion (see 5.3.4 on page 110 for a more detailed description of Brownian motion).

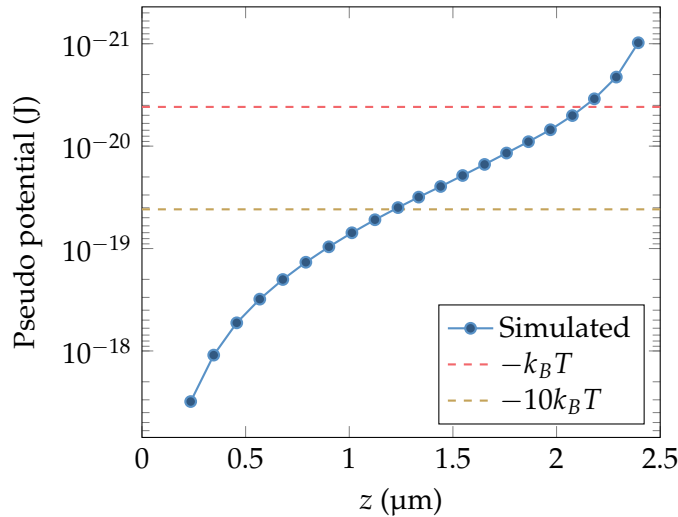


Figure 5.4: Pseudo-potential of a diamond particle above a SRR. Value extracted from FDTD simulation with 1 mW input power. The potential well is compared to thermal energy $k_B T$ at $T = 300$ K to estimate the stability of the trap.

To estimate the viability of the SRR as a trapping device, we use the MST method to compute the force on a dielectric sphere with a radius $r = 500$ nm and a refractive index $n = 2.4$, which is the refractive index of diamond. The sphere is placed above one of the arms of a gold SRR, and the simulation is repeated for multiple positions of the bead along the vertical axis. The force is then integrated to estimate the pseudo-potential. Figure 5.4 shows the calculated potential assuming a THz input power of 1 mW, compared to $k_B T$ and $10k_B T$ with $T = 300$ K. We see that the calculated pseudo-potential is indeed deeper than $10k_B T$. Furthermore, we have access to sources more powerful than 1 mW, and the temperature can be lowered if needed. Hence SRR are fully suitable for optical trapping of diamond micro-particles.

5.3.4 Experiment

Secondary infrared optical tweezers

The final objective of this experimental setup is to demonstrate optical trapping in the terahertz range. It includes a classical infrared secondary optical tweezers, which will be useful to set the particle around the trap and measure the force from the main terahertz tweezer.

The setup used for the infrared optical tweezer is based on the commercially available “Modular Tweezers OTKB/M” from THORLABS along with the Force measurement module and the fluorescence module. It includes a 300 mW fibred infrared laser diode at 976 nm (BL976-SAG300), a trapping objective (100X oil immersion Nikon objective lens with 0.23 mm working distance, 1.25 numerical aperture), a condenser lens (10X Nikon objective lens with 7 mm working distance and 0.25 numerical aperture), a quadrant position detector, a camera and all the optomechanical and optic components needed for alignment (see figure 5.5). A few elements have been changed in the setup in order to allow the addition of the THz setup. The purpose of the condenser lens is both to illuminate the sample, and to collect the laser light used for the force measurement. The objective lens sold by THORLABS is perfectly suitable for this. However the 7mm working distance is too small to

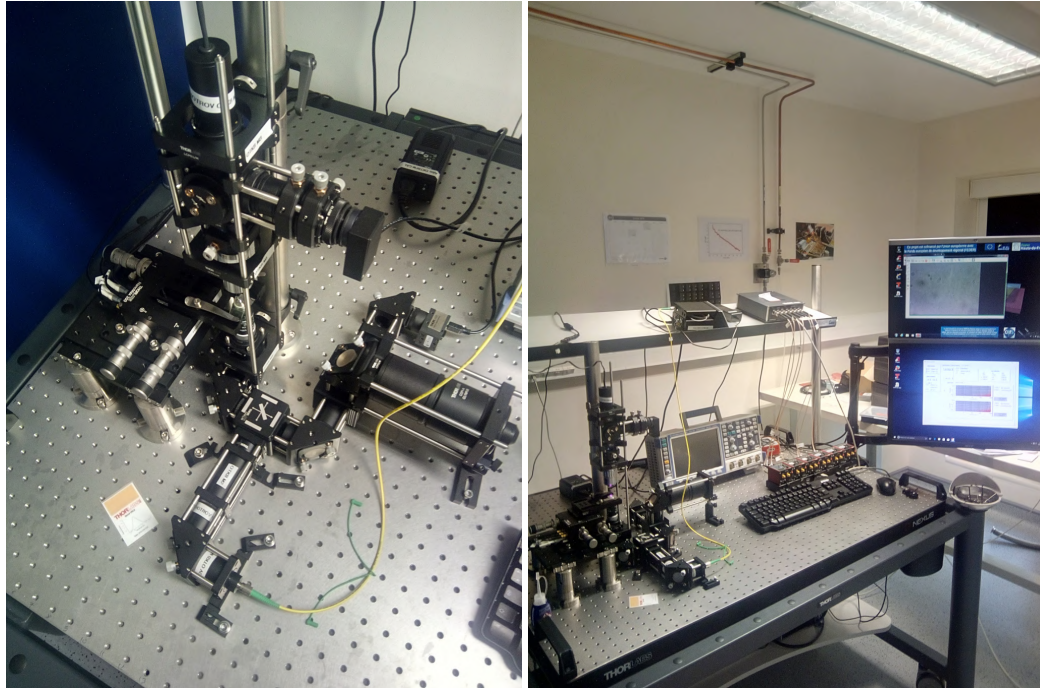


Figure 5.5: Infrared optical tweezer.

allow the future implementation of the terahertz tweezer in the experiment. This objective lens is therefore replaced with the MY10X-803 from Mitutoyo which has the same numerical aperture with a 34 mm working distance which should leave enough space for future additional components interacting with the sample. In addition, a secondary camera is used to observe the sample from the condenser lens, giving a convenient view point to align the THz focal point with the infrared focal spot. The illumination system has been improved with an additional lens, a diffuser and a more powerful LED source. The illumination setup realized with these elements is a Köhler illumination setup [33], where the light from the source is focused on the back focal plane of the condenser lens, in order to get a uniform illumination on the sample, and avoiding to get an image of the source in the imaged plane. The setup with the additional elements is represented with annotation in figure 5.6.

Force measurement

Our experimental setup offers two ways to measure the forces applied by the THz trap on a particle. The first one is based on the measurement of the equilibrium position when the particle is trapped by the secondary tweezer. The second is based on direct measurement of the particles speed and acceleration

Infrared trap stiffness measurement The force measurement module from THORLABS is designed to evaluate the stiffness of the infrared optical tweezer, and will not be able to directly detect the terahertz trap stiffness. However, it is possible to compare the infrared trap stiffness with the terahertz trap stiffness with the deviation of the equilibrium point of a trapped particle in presence of the terahertz field. Indeed, at equilibrium, the force from the infrared field and the force from the terahertz field cancel each other, since the force from the infrared tweezer can be deduced at every point of space from the measurement and the analytical optical force formulas, the terahertz trap stiffness is accessible. However, this technique

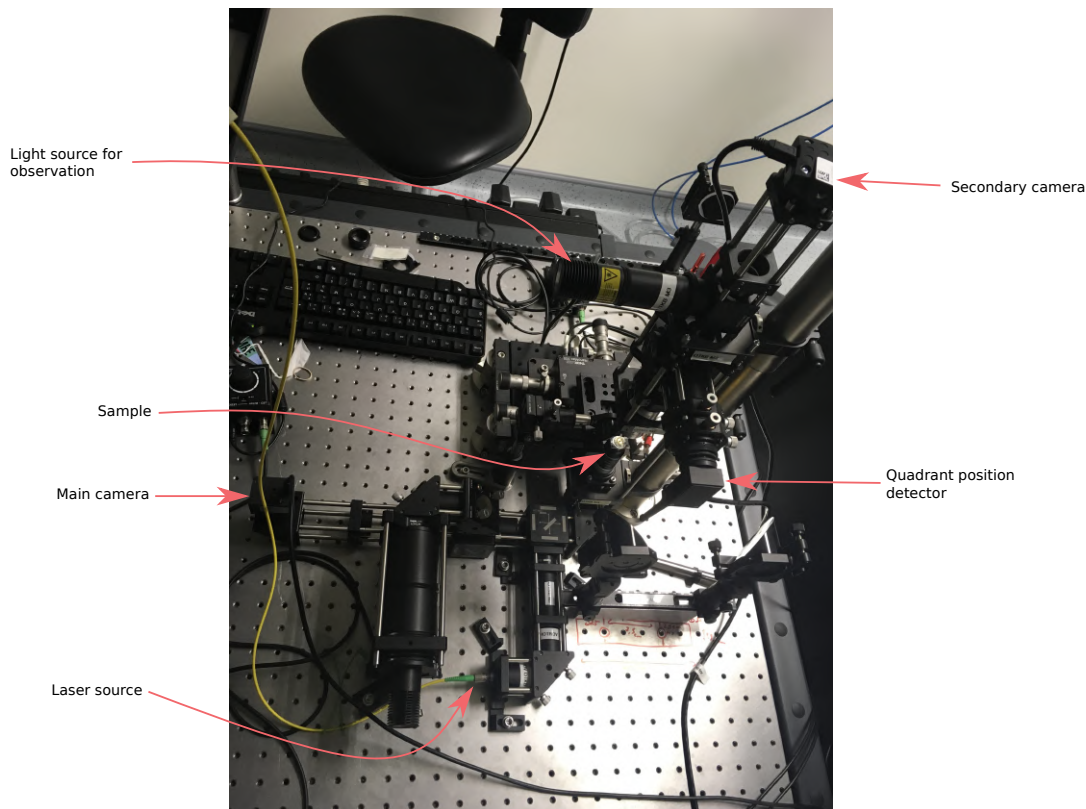


Figure 5.6: Annotated photograph of the modified setup

is not perfect considering the presence of gold metasurface that can also interact with infrared light, causing heat, convection movement, and reflection. These phenomena will disturb the force field created by the infrared light alone, and therefore decrease the accuracy of the comparative measurement.

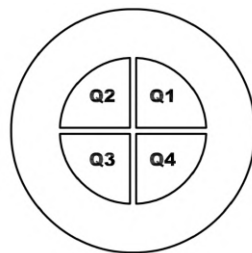


Figure 5.7: Shape and positioning of the diode in the quadrant position detector PDQ80A

In the complete infrared optical tweezer (figure 5.2 on page 106), a condenser lens is used both to illuminate the sample with white light, and to receive the laser light coming from the sample. The sample is located on the front focal plane of this lens. The force measurement module is based on Back Focal plane Interference (BFI), it uses a lens to conjugate the back focal plane of the condenser lens with a quadrant position detector. The quadrant position detector is made out of four photodiodes, positioned as shown in figure 5.7 and delivers three signals corresponding respectively to the differential signal along the X axis $((Q2 + Q3) - (Q1 + Q4))$, the differential signal along the Y axis $((Q1 + Q2) - (Q3 + Q4))$, and the sum signal $(Q1 + Q2 + Q3 + Q4)$. Those signals allow to evaluate the position of a light spot

on the detector. A dichroic mirror is used to retrieve only the laser light beyond the sample without affecting the illumination system. Since the plane of the detector is conjugated with the back focal plane of the condenser lens, the optical field detected is the Fourier transform of the optical field on the sample plane. In the case where a particle is trapped near the focal point of the laser, the light spot position on the back focal plane is proportional to the relative position of the particle in respect to the focal point, regardless of the focal point position itself.

The OTKBFM-CAL module (from Thorlabs) provides an analysis software that uses two methods to compute the stiffness of the infrared optical trap based on the quadrant detector signal. The first one is based on the equipartition theorem, stating that the average energy associated with each degree of freedom of a system is given by

$$\langle E_i \rangle = \frac{1}{2} k_b T, \quad (5.37)$$

where k_b is the Boltzmann constant and T is the temperature. Furthermore, when the particle is trapped with the infrared optical tweezer, the particle is close to the center of the trap, and the potential of the trap can be approximated as a quadratic function. Therefore, the average energy of each translational degree of freedom is given by

$$\langle E_i \rangle = \frac{1}{2} k_i \langle x_i^2 \rangle, \quad (5.38)$$

where k_i is the stiffness of the trap in the direction of the degree of freedom i . Thus

$$k_i = \frac{k_b T}{\langle x_i^2 \rangle}. \quad (5.39)$$

The second method is based on the Power Spectrum Density (PSD) of position fluctuations. Without turbulence in the fluid surrounding the particle and considering the particle is light enough that the inertia term $m\ddot{x}(t)$ is negligible in regard to the forces involved, its position is described as a damped oscillator following the Langevin equation

$$\beta \dot{x}_i(t) + k_i x_i(t) = F(t), \quad (5.40)$$

where $\beta = 6\pi\eta a$ is the drag coefficient, η is the fluid viscosity, a is the radius of the particle and $F(t)$ is thermal fluctuation induced force. The PSD is therefore in the form

$$S(f) = \frac{k_b T}{\pi^2 \beta (f^2 + f_c^2)}, \quad (5.41)$$

where the roll-off frequency is given by

$$f_c = \frac{k_i}{2\pi\beta}. \quad (5.42)$$

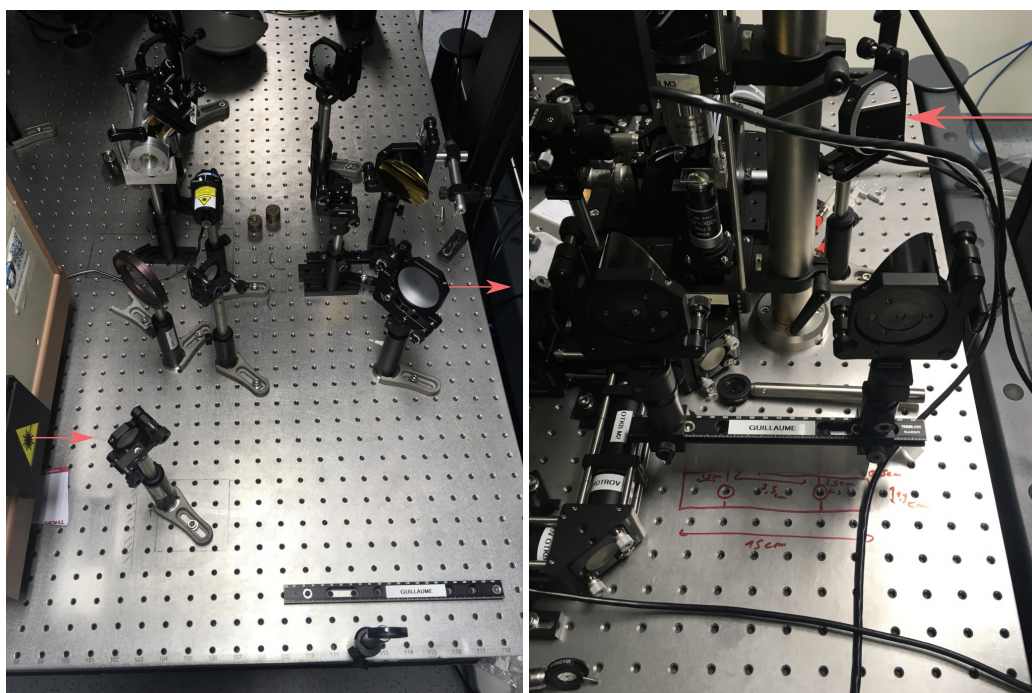
The measured PSD can be fitted to evaluate f_c and the trap stiffness k_i .

Forces from speed and acceleration The video recording of the optical trapping allows one to track precisely the position of a given particles in time, considering there

is no large variation of speed between two images, the speed and acceleration of the particles can be measured. Assuming optical force and viscous drag are the only forces applied to the particle, the sum of the forces applied to the particle is obtained with Newton's second law as in equation (5.40). However as the particle size and mass decrease, random movements due to brownian motion start to become significant, and the data need to be filtered in order to get an accurate estimation of the optical force. Furthermore, it is difficult to access information about the position and movement along the axis orthogonal to the observation plan from images obtained from an optical microscope.

Each of them having their own significant default, both methods need to be used in complementarity.

Terahertz beam path



(a) Laser side.

(b) Tweezer side.

Figure 5.8: THz optical setup. **(a)**: The beam goes through a polarization rotator made of three planar mirrors. It is then enlarged with two confocal parabolic mirrors and directed toward the tweezer optical table. **(b)**: The beam diameter is reduced with two confocal parabolic mirrors and focused on the sample with another parabolic mirror.

The terahertz source used in this experiment is the FIRL-100 far infrared continuous laser from Edinburgh Instrument. Its output is a gaussian beam of frequency 2.5 THz ($\lambda = 118.8$ nm). This beam is guided and focused toward the sample with plane and parabolic mirrors. Because the THz laser is used for other experiments, the laser and the optical tweezer are on two different optical tables. the optical setup is divided in two part:

The laser side, where the beam is polarized and widened to reduce diffraction through the path toward the second table. (see figure 5.8a)

The tweezer side, where the beam is reduced to its original size and focused on the sample. (see figure 5.8b on the preceding page)

At the laser output, the beam has a horizontal polarization; a set of three mirrors is used to rotate this polarization in order to match the orientation of the sample. The beam is widened with two confocal parabolic mirrors with respective focal lengths 25.4 mm and 50.8 mm which has the effect of doubling its width while keeping (or correcting if needed) the collimation. On the other table, the beam size is reduced back to its original size with another couple of confocal parabolic mirrors with respective focal lengths 101.6 mm and 50.8 mm. The reduced collimated beam is finally focused on the sample with a last parabolic mirror with a 25.4 mm focal length. The resulting beam is focused with up to 0.45 numerical aperture, which means a focus spot radius down to $\sim 80 \mu\text{m}$. The measured THz power after the last parabolic mirror is about 30 mW, which is more than enough according to the simulations.

Microfluidics cell

In order to demonstrate optical trapping with terahertz waves, the liquid medium in which particles will be suspended must be transparent in the terahertz range, which is not the case of a polar liquid like water. The medium chosen for the demonstration is hexane, a non-polar liquid transparent in terahertz, less dense and less viscous than water. In a classic optical trapping experiment, a drop of water with a microparticle is putted between two glass slides in the same way as in a regular optical transmission microscope. However, if the same protocol is applied with hexane instead of water, the hexane evaporates completely within a few seconds. This is why a microfluidic cell has to be designed in order to isolate the hexane from the atmosphere.



Figure 5.9: Component used to fill the microfluidics cell.

Cell design The microfluidic cell is designed to work with the component shown on the figure 5.9. The upper part of the cell is a quartz slab with two holes where hexane is injected, the bottom part is a 150 microns quartz slide with metasurfaces on it. Between these two quartz layers, the shape of the microfluidic channel is delimited with a solid resist. The choice of the resist is leaded by two criteria: it

must be able to hold hexane during an extended period of time, and must be in solid state so it can be shaped before being polymerized. In order to test the fabrication process, the first shape of the channel is a simple rectangle. This shape is good enough to demonstrate optical trapping in hexane. It could later be replaced by a more complex channel shape allowing control over the fluid movement inside the cell.

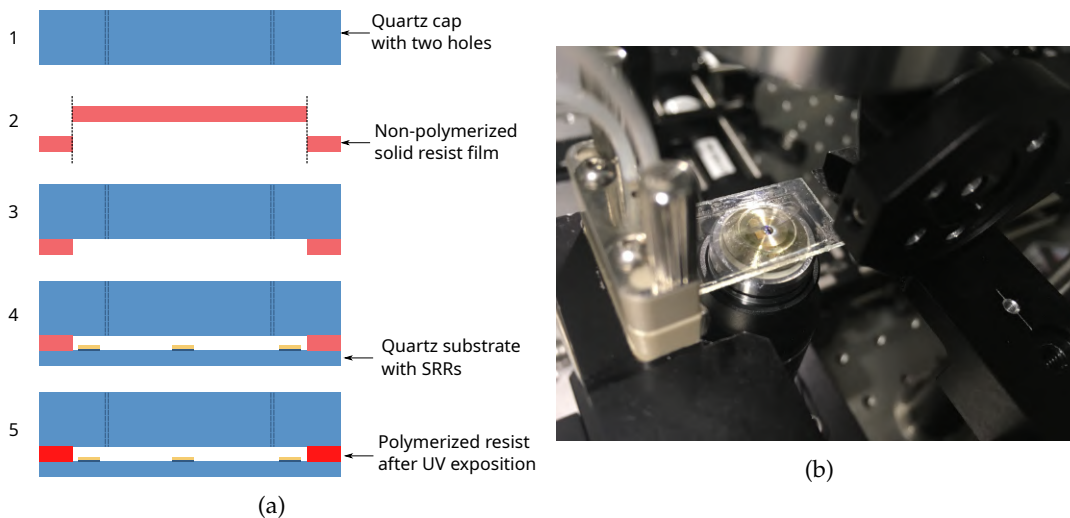


Figure 5.10: **(a)**: Step by step illustration of the microfluidics cell fabrication process. **(b)**: Complete microfluidic cell mounted in the optical tweezer setup.

Cell fabrication The microfluidics cell is fabricated according to the following steps (figure 5.10a):

1. Using laser ablation, a 1.5×3 mm rectangle is cut from a 1 mm thick quartz substrate, and two holes are pierced for the microfluidic access. The sides are polished to relieve stress caused by laser cutting.
2. The shape of the microfluidic channel is cut from the resist film with a punch.
3. The shaped resist film is applied on the quartz top with a heating laminator.
4. The quartz top with the resist is put on the $150 \mu\text{m}$ thick quartz sample with the previously fabricated SRRs.
5. The cell is heated and exposed to UV light to polymerize the resist.

The advantage of the solid resist in this process is that it can be shaped without being polymerized, thus the cell can be sealed by heating it while the resist is not polymerized, but in contact with both quartz slides.

Figure 5.10b shows a fully assembled microfluidic cell mounted in the OT experiment. The process is reliable and the resulting cells are easily filled with hexane using syringes. No sign of degradation is visible on the resist, and infrared optical trapping of micro-particles inside the cell is possible.

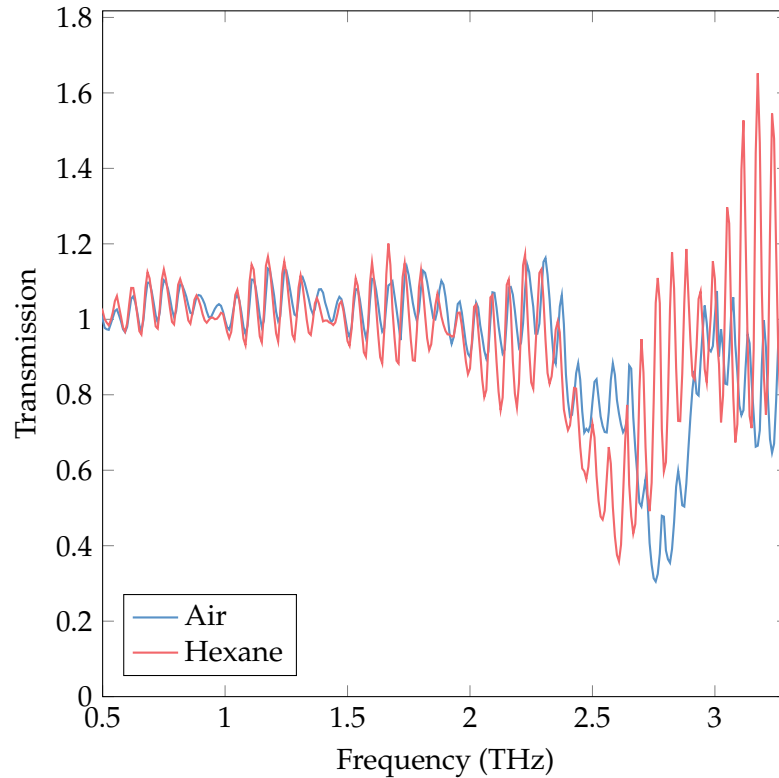


Figure 5.11: THz Time Domain Spectroscopy (THz-TDS) transmission spectrum of the same SRR array in a microfluidic cell. As expected, the resonance shifts toward lower frequency when hexane is injected in the cell. The spectra are normalized with the transmission of the cell far from the SRRs (without and with hexane). The large fluctuations are due to the multiple reflection inside the three layers of the microfluidic cell.

THz-TDS characterization of the SRR submerged in hexane

Since hexane has a higher refractive index than air, we expect the resonance frequency of the SRR to be shifted toward lower frequency when hexane is injected in the microfluidic cell. Since the SRR must be in resonance with the THz laser at 2.52 THz *with* hexane in the cell, we measure the transmission spectrum of SRR arrays inside the cell. Figure 5.11 shows the measured transmission spectra through the same SRR array, with the cell empty, and with the cell filled with hexane. Due to the multiple reflections in the cell's three layers, the spectra are strongly affected by the Fabry-Pérot effect even after normalization. Yet the resonance from the SRR array is still clearly visible, and the spectra confirms that the resonance is shifted to lower frequency with hexane. Hence we can accurately select the SRR that resonates with our THz laser.

Particle sample

To test the performance of our optical tweezer, we will start by using dielectric particles that are large enough to be easily observable and trapped with the secondary optical near-IR optical tweezer, so we can apply the method presented in 5.3.4.

We selected two kinds of particles for the proof of concept: Silica beads and diamond particles.

Silica beads are calibrated spheres of SiO_2 , with sizes ranging from a few hundreds of nanometers to a few micrometers. Their spherical shape and size precision make them ideal for trapping with a gaussian beam OT. As such they are commonly used in optical trapping experiment biology research[34]. This make this particle ideal for precise characterization of the optical forces generated by the THz OT. Another common particle used in OT application is polystyrene[3, 4, 7], but this material is not compatible with non-polar solvent.

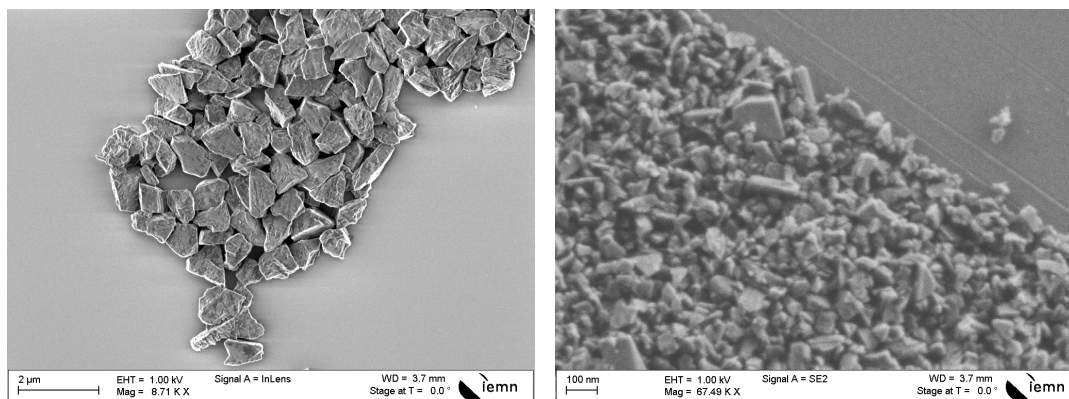


Figure 5.12: SEM images of the diamond particles with two different size distributions. The shapes are far from spherical, which can be an issue for the gaussian beam OT, but does not matter as much for the near-field OT.

The diamond particles are monocrystalline synthetic diamond formed by high-pressure/high-temperature synthesis. They are initially made for polishing application and bought from the Diprotex company¹. They are low cost and available in large quantity in a wide range of sizes (from 50 nm to 80 μm). Their shape are much more random than the silica particles (figure 5.12), which make them harder to trap and measure with the gaussian beam OT. However, the high refractive index and low absorption of diamond in the THz range theoretically leads to greater optical forces from the SRR near-field trap.

Both types of particles are highly hydrophilic, thus easy to disperse in water, which suggests a large density of hydroxyl groups at their surface. However, they do not form stable suspension in non-polar solvent, and instead tend to immediately cluster in large lumps that fall to the bottom of the solution. To facilitate the bounding between the particle and the non-polar solvent, we use surface functionalization with Octadecyltrichlorosilane (OTS), which replaces the polar hydroxyl termination with non-polar carbon chain (see 2.2.2 on page 46 for more detail on OTS treatment).

Figure 5.13 shows a picture of diamond particles in hexane a few seconds after agitation, before and after treatment with OTS. We successfully managed to create stable suspensions of diamond and silica micro-particles in hexane. The suspensions can be injected in the microfluidic device for trapping experiments.

5.3.5 Protocol and result

All the necessary elements are now gathered to proceed to the proof of concept experiment. Once our test particle is suspended in hexane and injected in the microfluidic cell,

¹“MSY type micron diamond”, <https://www.diprotex.com/-Diamond-types-68->



Figure 5.13: Photograph of diamond microparticles (sizes ranging from $0.5\ \mu\text{m}$ to $1\ \mu\text{m}$) in hexane. **Left:** Without surface treatment. **Right:** With OTS surface treatment. Both solutions were agitated a few seconds before the photograph was taken.

- A particle is trapped with the secondary optical tweezer and brought close to the gap of a SRR
- The power of the infrared laser is lowered down to the limit of stability of the trap
- The THz beam is turned on

When the THz beam is turned on, the particle should be attracted toward the gap, causing at least a displacement of the equilibrium point. When the THz beam is turned off, the particle should either go back to the center of the secondary trap, or be set free if the THz trap had completely drawn the particle away from the infrared trap.

Unfortunately, all the numerous attempts were unsuccessful, and we were not able to experimentally demonstrate the existence of any force correlated with the THz input (outside of quite visible thermal effects). The reason for this failure is still to be found, and will be the object of further investigation. In order to minimize the number of unknown parameter in the experiment, the following adjustment will be implemented in the experiment:

Loss reduction in the THz beam path: Since the optical forces are harder to detect or generate than initially expected, increasing the THz excitation power will increase our chances of success. We can reduce the power loss by removing the water vapor along the beam path, using dry air purged pipes around the beam. This would increase the beam intensity and optical forces by up to 20%.

Advanced microfluidics: A more advanced microfluidic design will allow us to gain better control over the fluid dynamics occurring in the trapping experiment.

Static charge suppression: Since hexane and quartz are both good electrical insulators, static charges build up in the liquid and particles when they move through channels[35–39]. Those static charges creates additional forces that prevent the

OT experiment to be performed. We will limit the charges accumulation by using conducting tubes and channels to bring the suspension to the OT area.

To conclude, we fabricated SRRs that create an electric field gradient when excited at resonance. We predicted from simulation that this electric field gradient is strong enough to generate a stable trap with only 1 mW of incident power. We build a THz optical path to focus up to 30 mW of THz power on the experiment. We assembled a microfluidic platform compatible with non-polar solvent. We checked that our SRRs were correctly tuned with our excitation laser when submerged in hexane. We selected and treated micro-particles compatible with THz optical forces. We use a secondary optical near-field optical tweezer to realize the experiment in a controlled way. Yet we could not generate or detect any appreciable force on our particles. Nonetheless, it is highly improbable that THz optical trapping is fundamentally impossible. Indeed optical trap based on metallic structure are known to work both at higher frequency, in the near-IR[17, 19, 40], and at much lower frequencies, down to the kHz range, where the gradient force is more commonly called dielectrophoresis force[41–43]. Hence we will pursue the investigation in order to understand why the experiment was unsuccessful so far.

5.4 Graphene plasmonic tweezer

In this thesis, we focused almost exclusively on SRR for field confinement in the THz domain. Nonetheless, a large part of the concepts developed here, including optical forces, are applicable to other kinds of structure and frequency range. In this section, we will focus on the work done at the University at Buffalo on the conception of an optical tweezer based on graphene plasmonic resonances. This work was done under the supervision of Pr. Liu. This collaboration was made possible by the Fulbright grant that I got for the year 2021.

Knowing that graphene exhibits surface plasmons featuring even greater field confinement than metallic structures [44], we consider graphene structures to reach the macromolecule scale. Graphene, being a monoatomic layer, is moreover intrinsically suitable to fabricate nano-structure. Plasmonic tweezers based on graphene structures have several appealing advantages over metallic plasmonic tweezers :

Flexibility: Optical trap based on plasmonic or LC resonance with metallic structure severely lacks flexibility. The operation frequency and the trap location are fixed during fabrication. Therefore if those traps allow one to catch and release a particle, they cannot move a trapped particle to a desired location. The carrier density in graphene varies with the electrostatic gating, which in turn determines the frequency and strength of the plasmonic resonances of a graphene structure. Therefore, graphene plasmonic tweezers allow for convenient electrical switching on/off, modulation and continuous tuning of the trapping force and position.

Greater field confinement: Graphene surface plasmons feature exceedingly large field confinement and enhancement compared to metal plasmon in the visible range (confinement factor in the range of ~ 100 can be readily achieved in the mid-IR spectral region). Therefore, graphene plasmonic tweezers may be able to trap small nano-objects (tens of nm diameter).

In addition, working with graphene in the mid infrared range implies a few beneficial side effects:

- The mid-IR trapping light does not produce photoluminescence or fluorescence which may otherwise interfere with various optical characterizations of the trapped objects.
- Graphene has a relatively high thermal conductivity, which facilitates removal of the heat due to absorption of trapping light.
- Graphene is transparent in visible light thanks to its extremely small thickness, which makes it more convenient to image trapped objects.

However, using graphene in a liquid environment is significantly more challenging than using metal. Indeed molecules of the liquid can be adsorbed by the graphene, effectively doping it and altering its electrical and optical properties. Furthermore, to avoid local heating in the confined electric field and allow a large quality factor, the liquid must have low absorption at the chosen mid-IR wavelength. A suitable liquid must therefore be transparent at this wavelength (e.g. 10 μm) and not interact with graphene. None of the mentioned conditions are respected for water, as it is known to lead to doping of graphene [45], and have strong absorption in the mid-infrared range [46].

The design of a graphene plasmonic tweezer consist of four main parts:

The graphene structure has to support plasmonic resonance mode featuring a highly confined electric field. The position and frequency of the mode must be tunable with an appropriate gate structure.

The gate structure has to provide electronic control over the position and strength of the plasmonic trap. It should not alter the mid-IR excitation, nor the visible observation.

The microfluidic platform must bring NPs close to the trapping position and be compatible with non-polar solvent such as hexane and decane (transparent in the mid-IR range)

The microscopic observation should provide real time visualization of the trap and NPs.

5.4.1 Graphene structure

A large variety of graphene structures support tunable plasmonics resonances providing large field confinement. Such structures include ribbons[47, 48], disks[49, 50] and antidots[51, 52]. Among those type of structure, the Graphene Nano-ribbon (GNR) is the most suitable for a conveyor belt type application. Indeed the plasmonic resonance frequency of a graphene structure depends on the graphene carrier density. The carrier density can be changed through electrostatic gating. Therefore, if the structure is illuminated with a constant narrow band source, one can turn on an off the resonance by changing the gate voltage. The specificity of the GNR in this regard is that it can be locally gated to support a resonance only on a finite section. This section defines the trap position, and can be continuously moved along the GNR without modification of the excitation light.

We simulated the electric field distribution for a GNR with a non uniform carrier density. The GNR is excited with a perpendicularly polarized plane wave. A 500 nm long section has a Fermi energy $E_{fg} = 0.4$ eV, representing the gated section, while the rest has a Fermi energy $E_{f0} = 0.1$ eV. The width and excitation wavelength are chosen such that the GNR is resonant with a 0.4 eV energy level. Figure 5.14 shows

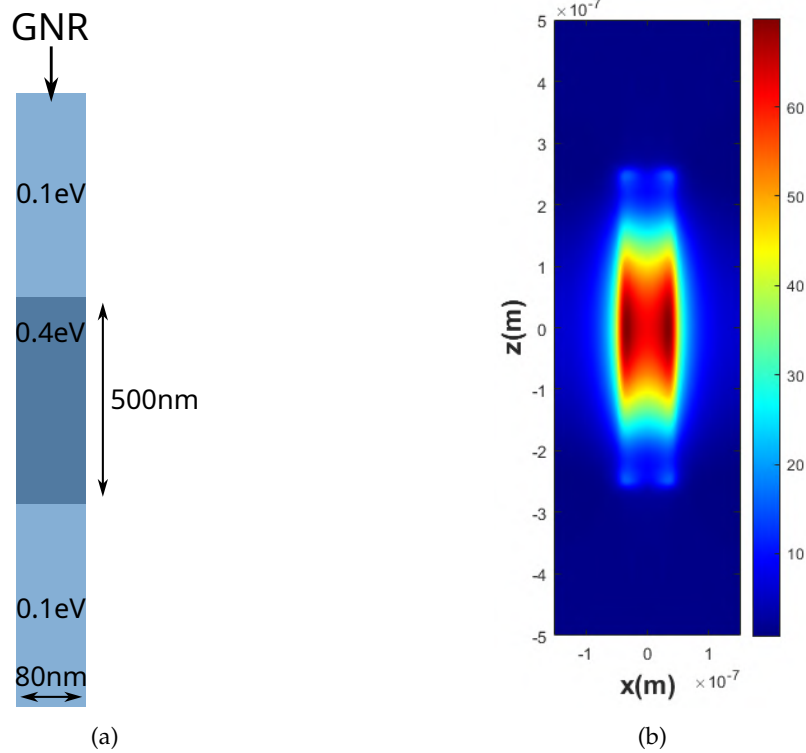


Figure 5.14: **(a)**: Schematic of the simulated structure. The GNR is excited with a plane wave horizontally polarized. We use periodic boundary condition in the plane of the GNR. **(b)**: Field profile above a GNR with a non-uniform Fermi energy as represented in (a).

the simulated field in a plane above the GNR. We see that this structure provide a strong field confinement localized on the gated section.

The confinement provided from the GNR structure was shown to be sufficient for stable trapping of a 50 nm dielectric particle with a refractive index $n = 2.5$ [53, 54].

5.4.2 Gate structure

The carrier density of the graphene is tunable with electrostatic gating. Experimentally, this is done by applying a voltage between the graphene and a conductor placed ~ 100 nm above or below the graphene. The graphene and the gate are separated by an insulator. The gating only affects the graphene area close to the conductor. Since the sample will be observed with a high numerical aperture objective, the observation and the mid-IR excitation cannot be on the same side of the substrate. The mid-IR excitation is applied *through* the gate structure.

To create a conveyor belt structure where we can control the position of the gated area, we will divide the gate in multiple insulated sections as illustrated in figure 5.15. However, this gate structure is made of conductive wires oriented along the polarization of the excitation beam. Thus such a structure would completely block the mid-IR beam and prevent optical excitation of the GNR. On the other hand, a completely transparent gate structure would not be ideal either since it would allow the potentially powerful mid-IR to propagate beyond the graphene structure and in the liquid cell where it would heat up the liquid and create unwanted convection movement.

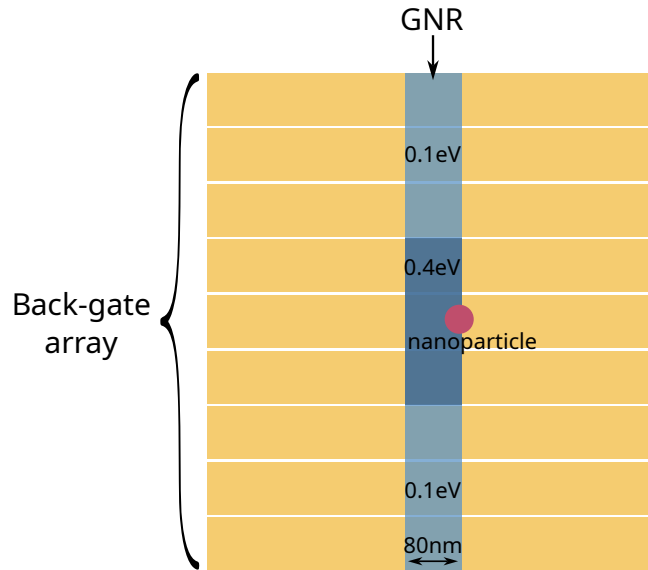


Figure 5.15: Gate structure subdivided to provide movable trapping position. In this picture, the polarization of the mid-IR beam must be horizontal to excite the GNR, hence this gate structure is opaque to the excitation beam.

To provide efficient excitation from the mid-IR beam while preventing the beam to propagate in the cell, we design a gate structure with sub-wavelength slots along the GNR. Since the apertures are sub-wavelength, the structure has close to 100% reflectivity. However, the GNR is excited by the evanescent field close to the aperture. Figure 5.16 shows the simulated field profile of a GNR excited through a sub-wavelength slot compared to a GNR directly excited by a plane wave. The FDTD simulation shows that the local field enhancement provided by the slot actually enhances the coupling with the mid-IR beam compared to a gate structure with close to 100% transmission, made of a gold rod aligned along the GNR.

Finally, the conveyor belt gate structure is illustrated in figure 5.17a. Before building a fully functional optical conveyor belt, we first have to experimentally demonstrate graphene optical trapping. For the first proof of concept, the gate subdivision in individually controllable sections is unnecessary. Hence the gate structure for the proof of concept experiment is a gold plane with slots aligned with the GNRs, as shown on figure 5.17b.

5.4.3 Device fabrication

To sum up the main characteristic of our device design:

- The substrate is CaF_2 as it is highly transparent in the mid-IR.
- The graphene structure is made of 80 nm wide GNRs.
- The gate is a full gold plane with slots running along the GNRs.
- The gate is isolated from the graphene and contacts with a HfO_2 layer.
- The GNRs are connected to a source and a drain for conductivity measurement.

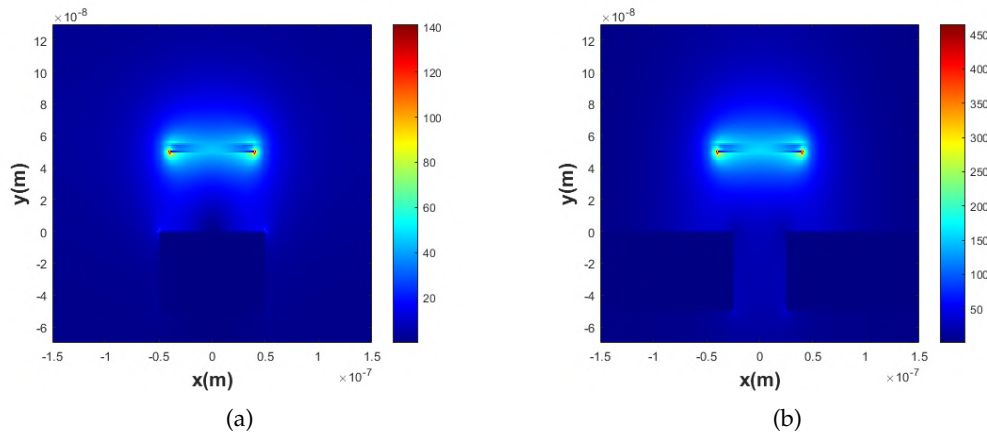


Figure 5.16: **(a)**: Field profile of a GNR above a gold wire with close to 100% transmission. **(b)**: Field profile of a GNR above a nano-slot in a gold layer. The field confinement above the nano-slot is more than three times stronger.

A schematic of the device with all aforementioned components is represented in figure 5.18a. The gate slots, GNRs, sources and drains are patterned with e-beam lithography (see 2.2 on page 44 for detail on the lithography process).

The device is fabricated according to the following steps (figure 5.18b):

1. The process starts with a 0.5 mm thick CaF_2 substrate.
2. Gold gate structure deposition, patterned with e-beam lithography.
3. HfO_2 layer deposition.
4. Chemical Vapor Deposition (CVD) grown graphene transfer from a copper foil substrate
5. GNR patterning with e-beam lithography and oxygen plasma etching
6. Gold contact structure deposition, patterned with e-beam lithography.

5.4.4 Graphene characterization

To proceed to the trapping experiment, we first need to characterize the conductivity of the GNRs, and their optical resonance, depending on the gate voltage, and on the surrounding medium.

Conductivity

For the conductivity measurement, we use a three probe station to connect the gate, the source and the drain, we apply a constant source-drain voltage $V_{sd} = 0.1 \text{ V}$, and measure the source-drain current as a function of the source-gate voltage. The measurement is done with increasing and decreasing gate voltage to take into account any hysteresis effect. We also measure the source-gate current to monitor the possible leakage current.

Since the graphene is not under a protective layer, its conductivity is likely to be affected by the surrounding medium. In the trapping experiment, the surrounding medium will not be air, but a non-polar liquid such as hexane or decane. Since hexane is non conductive and does not damage metallic probes, we simply repeat

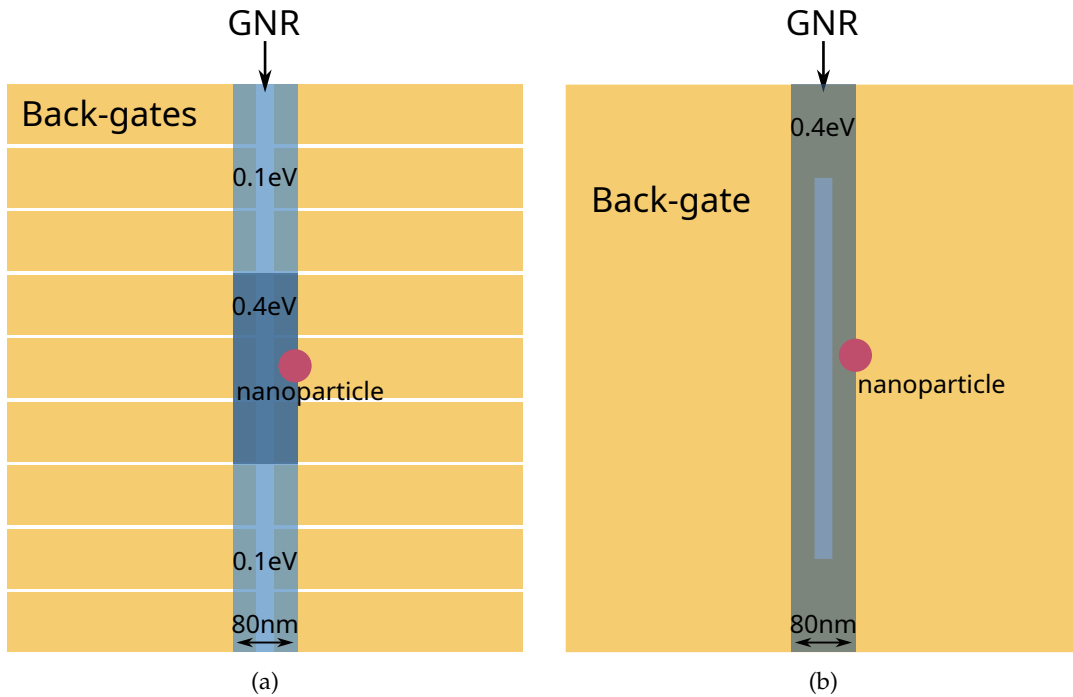


Figure 5.17: **(a)**: Schematic of a gate structure compatible with the optical conveyor belt. In addition to the gating purpose, this structure protects the sample from the excitation source, and enhances the coupling between the GNR and the excitation beam. **(b)**: Schematic of the gate structure used for the proof of concept experiment. The coupling is further enhanced by taking advantage of the slots aperture resonance.

the same measurement with a few drops of hexane covering the device. Neither the probes nor the device are moved between the two measurements.

The measured currents are plotted in figure 5.19. Based on this measurement, we conducted the following observations:

1. We are able to tune the graphene conductivity with the gate voltage.
2. The tunability is not disturbed by the presence of hexane.
3. There is a measurable hysteresis likely due to the charge trapping effect in the imperfect CVD graphene[55].
4. Hexane increases the conductivity of the GNRs by about 10%, but slightly increases the hysteresis.

To deduce the fermi energy level of the graphene from the conductivity measurement, we need to compare its minimum at the charge neutrality point (CNP). Unfortunately, we were not able to reach a minimum of conductivity to measure the CNP, as doing so would require applying gate voltages above 40 V, which is likely to break the HfO_2 insulating layer.

Mid-IR spectrum

Since the exact value of the Fermi energy is unknown, it is difficult to accurately predict the resonance frequency of the GNR at a given voltage. Ideally, we need to

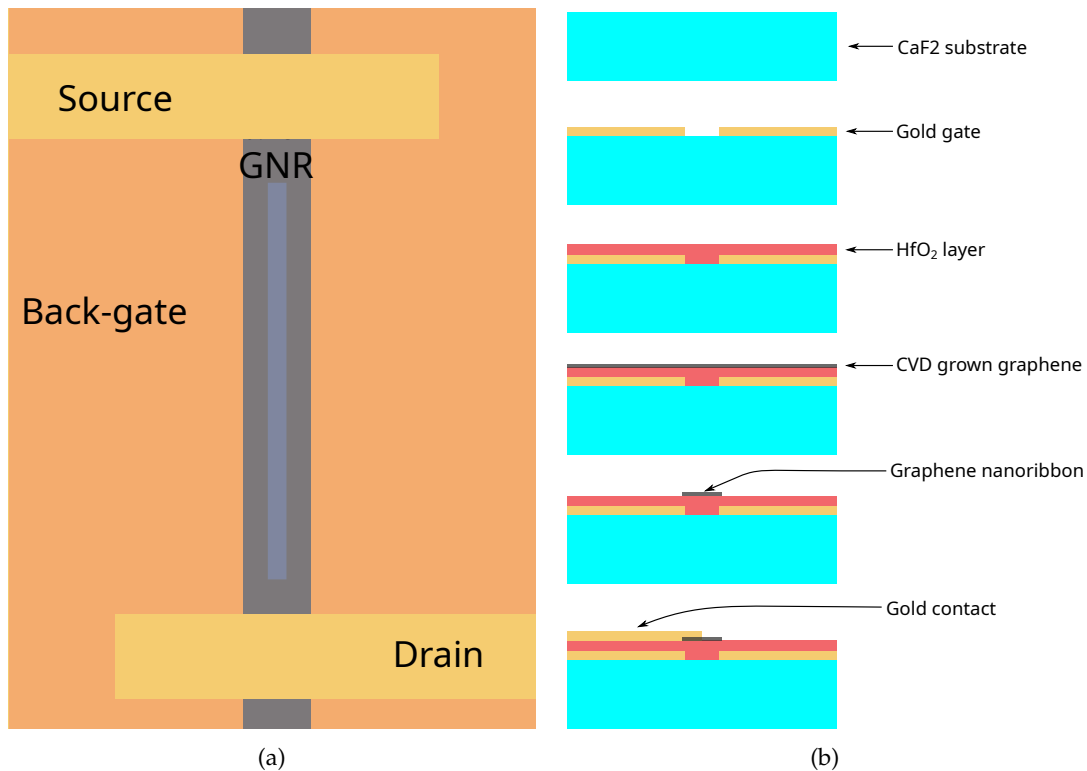


Figure 5.18: **(a)**: Top view schematic of the fabricated device. The gate is isolated from the other component with a HfO_2 layer. The drain and source contact serves for graphene characterization. **(b)**: Step by step schematic of the fabrication process.

know the value of the gate voltage V_{sg} such that the plasmonic resonance of the GNR is at the frequency of the CO_2 laser ($\lambda = 9.32 \mu\text{m}$).

We characterize the sample optical properties with a FTIR spectrometer (Bruker Vertex 70v²) coupled with a microscope in reflection. The microscope uses a Cassegrain type reflective objective, which allows for simultaneous FTIR measurement and visible observation. Figure 5.20a shows a view of the sample from the microscope, the white vertical rectangle represents the aperture used to limit the area of measurement. This area covers 4 slots along one GNR. To get a reflection coefficient, the reference is taken by shifting the sample horizontally, in such a way that the aperture does not cover any slot, but still covers the contact structure.

To our knowledge, farfield measurements of the resonance of a single GNR in the mid-IR do not exist in the literature. However, we used FDTD simulation to calculate the reflection spectrum of the device for different graphene chemical potential. Figure 5.20b shows the simulated transmission. We see a clear anti-crossing behavior characteristic of the strong coupling regime[56–58]. We see in the reflection spectra that when the resonance of the slot and of the GNR are far from each other, the resonance of the slot is much more visible than the resonance of the GNR. In contrast when the frequencies are close, we have two lines with intensity similar to the slot alone. Therefore, if we can detect the resonance of the 4 slots, we should detect the splitting when the GNR resonance frequency is close to the slot resonance.

²<https://www.bruker.com/fr/products-and-solutions/infrared-and-raman/ft-ir-research-spectrometers/vertex-research-ft-ir-spectrometer/vertex-70v-ft-ir-spectrometer.html>

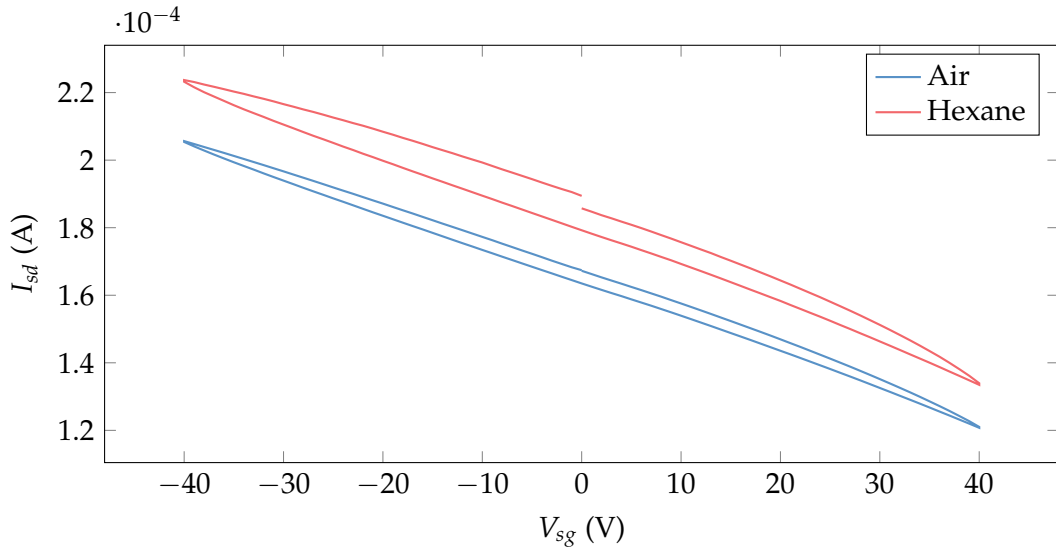


Figure 5.19: Source-Drain current as a function of the gate voltage with a constant source-drain voltage $V_{sd} = 0.1$ V, measured in air and in hexane. The presence of hexane increases the graphene conductivity but does not disturb its tunability.

Figure 5.21 shows the measured reflection coefficient on an area covering 4 slots (figure 5.20a). We see a clear resonance in the spectra around 850 cm^{-1} . However, we were not able to see any change in this spectrum when applying a gate voltage. This is likely due to one of the following reasons:

- We were not able to bring the GNR resonance close enough to 850 cm^{-1} .
- Alignment and slot shape imperfection, causing the coupling between the slots and GNR to be weaker than expected.
- Imperfection in the GNR, resulting in a broader resonance.

5.4.5 Microfluidic sample holder

The sample holder is made of two copper slabs separated by a flexible ring, forming a closed cell with optical, fluidic and electronic access (Figure 5.22). The bottom slab features a 2" wide and $200\text{ }\mu\text{m}$ thick sapphire window, glued with epoxy. We chose sapphire because of its solidity and high transparency in the visible range. This allows us to have a window thin enough to be compatible with an oil immersion high numerical aperture microscope objective. Additionally, sapphire is also mostly opaque to mid-IR radiation, which protects the microscope objective from the CO_2 laser beam. The top slab features (Figure 5.22c):

- A 0.5 mm thick CaF_2 window, transparent in both the mid-IR and the visible range, glued with epoxy.
- 2 fluidic accesses.
- Copper clips with Teflon screws to clamp the sample on the windows, electrically connected to the main body of the sample holder.
- A connector for electrical connection between the sample and the outside of the cell. The internal connections are soldered to gold coated glass slides glued to the slab. The sample is connected to the slides with wire bonding.

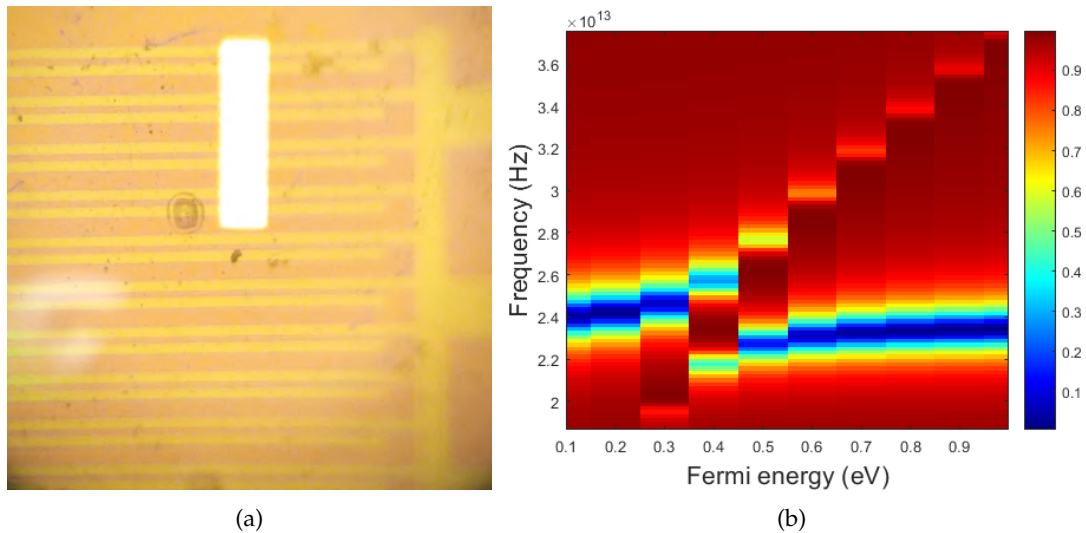


Figure 5.20: **(a)**: Photograph of the fabricated device through the optical microscope. The clear rectangle is an image of the aperture through which the Fourier-Transform Infrared (FTIR) spectrum is measured. The aperture covers 4 slots aligned along 1 GNR. **(b)**: Simulated reflection spectrum of the device for different graphene chemical potential. The simulation predicts a strong coupling regime between the slot and GNR resonances.

5.4.6 Optical setup

Just like the THz tweezer, we build the mid-IR optical tweezer starting from the OTKB modular optical tweezer from Thorlabs to take advantage of the provided tool for observation and force measurement. However, in the case of the mid-IR tweezer, the gate structure prevents transmission illumination. The schematic of the complete optical setup is illustrated in figure 5.23.

Illumination: We implemented a reflective Köhler[33] illumination scheme. In a reflective illumination, the objective lens also acts as a condenser lens. We use a white LED coupled to a ground glass plate as a light source and a 50 mm focal length lens to image the light source on the back focal plane of the objective lens. The white light is injected in the main path with a 50% transmission beamsplitter.

Mid-IR beam path: The excitation light source for the trapping experiment is a continuous wave CO₂ laser emitting at a wavelength $\lambda = 9.32 \mu\text{m}$, with a power up to 17W. Due to the very large available optical power provided by the laser, the focusing on the sample do not need to be extremely tight. The mid-IR beam is brought to the tweezer with plane mirror and directly focused on the sample with a 45° off-axis parabolic mirror with an effective focal length EFL=50.8 mm.

Secondary optical tweezer: A near infrared laser beam ($\lambda = 978 \text{ nm}$) is expanded and injected in the main path with a dichroic mirror. It is tightly focused with the high numerical aperture objective lens to create a Gaussian optical trap[2]. This secondary optical tweezer is identical to the one used for the THz optical tweezer (see 5.3.4 on page 109).

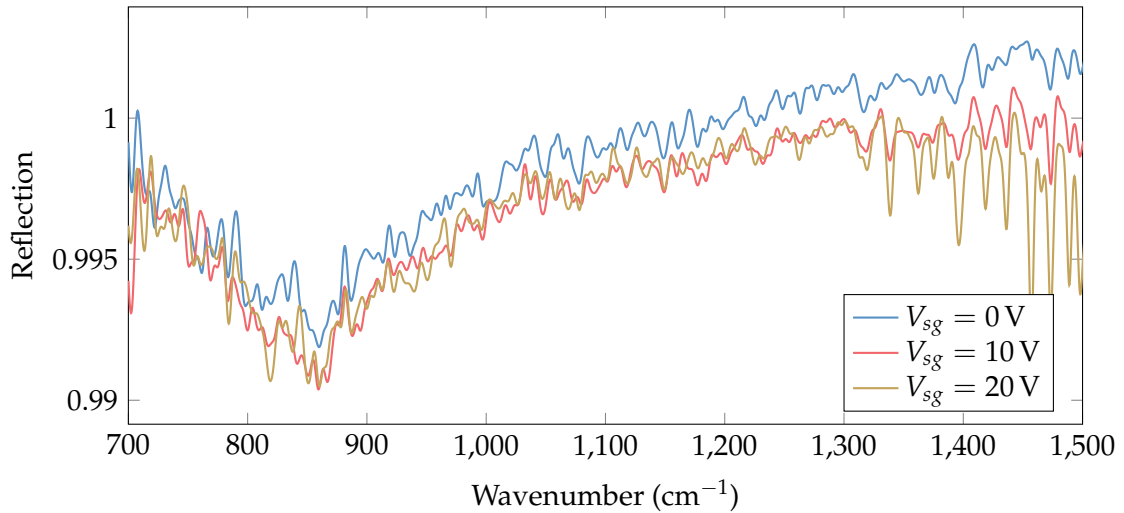


Figure 5.21: FTIR reflection spectrum of the area represented in figure 5.20a. The area covers 4 slots along a graphene ribbon. We were not able to detect any change in the spectrum when applying a gate voltage.

Fluorescence: We use fluorescence to help imaging small particles. We use a UV (365 nm) LED source as excitation. This wavelength is compatible with dye such as DAPI[59] and Marina Blue[60]. It is also ideal for the excitation of fluorescent quantum dots (e.g. CdSe)[61]. The UV light is injected in the main path with a dichroic mirror.

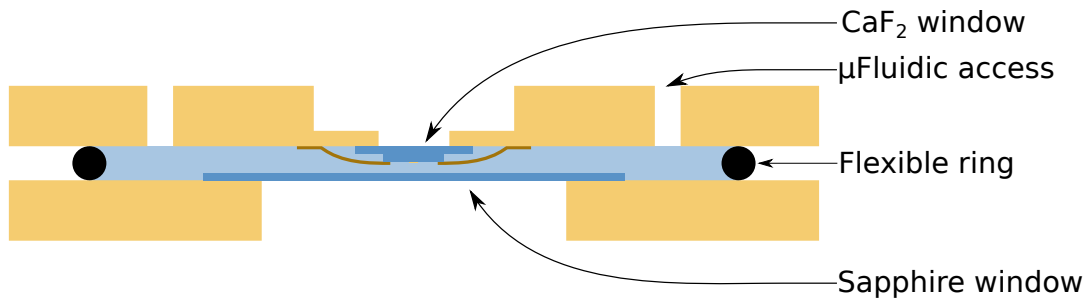
Observation: The experiment is imaged on a camera with a high numerical aperture (NA=1.2) microscope lens and a 200 mm focal length lens. Near-IR and UV filters are placed before the camera to remove residual light from the secondary OT and the fluorescence excitation. We use a camera with a better sensitivity compared to the one provided in the OTKB package.

5.4.7 Experimental results and next steps

The protocol for the trapping experiment is the same as for the THz optical tweezer described in 5.3.5 on page 117. We use the same diamond particles treated with OTS. We did not reach the demonstration of optical forces from the GNR, but we identified several elements that needs to be improved to properly conduct the OT experiment:

GNR characterization: As explained in 5.4.4, we did not succeed in measuring the resonance frequency of the GNRs, which means we have no way to ensure the existence of field confinement during the OT experiment. This point will be addressed with one of the following method:

- Increasing the coupling between the slots and GNR to improve the FTIR measurement. We will do so by using more slots and decreasing the HfO₂ thickness.
- Mid-IR scattering Scanning Near-field Optical Microscopy (s-SNOM) imaging of the GNR. s-SNOM imaging will be performed using a CO₂ laser as an excitation source, in order to precisely localize the graphene plasmon at the OT excitation wavelength[62–64].



(a)



(b)

(c)

Figure 5.22: **(a)**: Schematic cross section of the sample holder. The sample is held in place against the CaF_2 window with metal clips. The top copper plate is shaped to facilitate mid-IR access at 45° . Electrical connections are not represented in this schematic. **(b)**: Assembled sample holder. **(c)**: Inside view of the top plate with a mounted test sample. The electrical connection is done with wire bonding with the gold coated glass slides glued to the copper and soldered to the external electrical connection.

Imaging and fluorescence: The visualization of small transparent particles like diamond is more difficult with reflection illumination than transmission. This is why the fluorescence technique is particularly useful in this configuration. However, if our system is capable of performing fluorescence imaging on particles without a device (figure 5.24), the photo-luminescence from the gold gate structure makes the fluorescence unusable during the OT experiment. We will adjust the excitation wavelength to avoid this issue.

Device material: The choice of CaF_2 for the substrate material was in large part motivated by its transparency in the visible range. However, since we decided on using a completely opaque gate structure, this criteria is no longer relevant. Hence why the future device will be fabricated on high resistivity silicon, which is also transparent in the mid-IR range. This change will make the fabrication process much more reliable. Additionally, we noticed that CaF_2 tends to break easily under mechanical and thermal constraints compared to a silicon substrate.

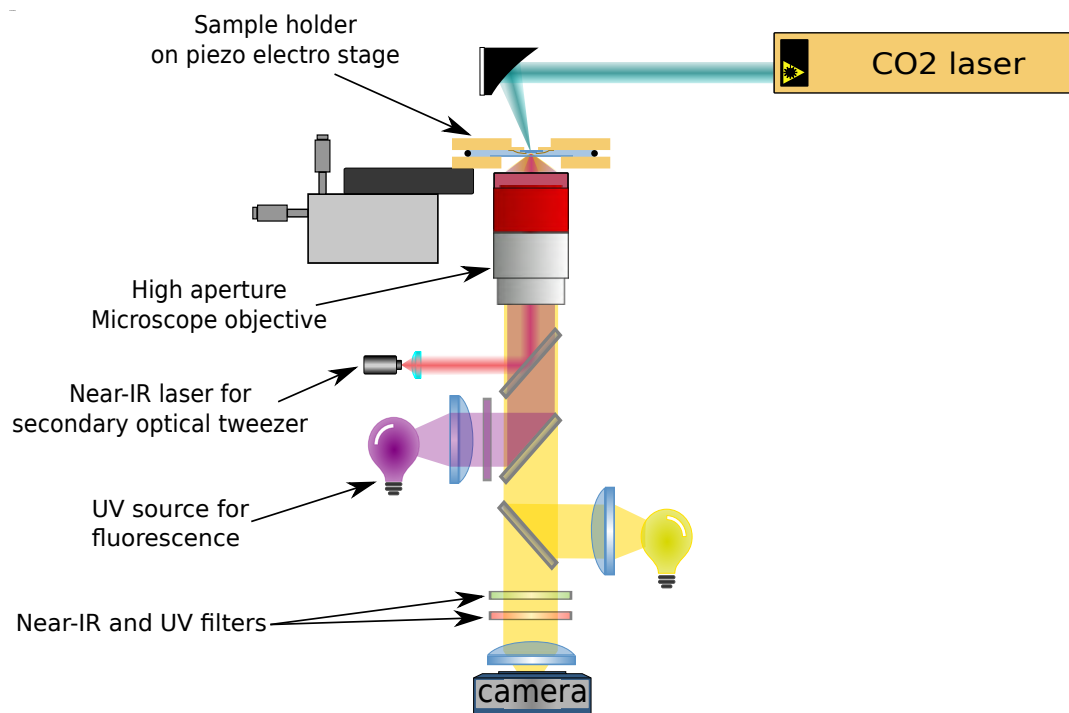


Figure 5.23: Schematic of the optical setup, including the illumination, observation, mid-IR excitation, and fluorescence excitation.

Dispersion of the particle in hexane: Although the OTS surface treatment of the diamond particle gets us a suspension of diamond hexane, this suspension is still not nearly as stable as a suspension of untreated diamond in water. As a result, the vast majority of particles in the cell get quickly stuck to surfaces, and it particles rarely reach the trapping zone. Improving suspension stability will greatly enhance the feasibility of the experiment. This remark is also valid for the THz trap.

To conclude, we designed a graphene based optical conveyor belt for manipulation of NP. We accomplished most of the preliminary work necessary for the project, including the design and fabrication of a prototype device for the proof of concept, assembly of the optical setup providing visualization, mid-IR excitation and a near-IR secondary OT, and the design and fabrication of a fluidic platform to perform the experiment. This project is still actively ongoing, and we have clearly defined the next elements to work on to achieve the first proof of concept.

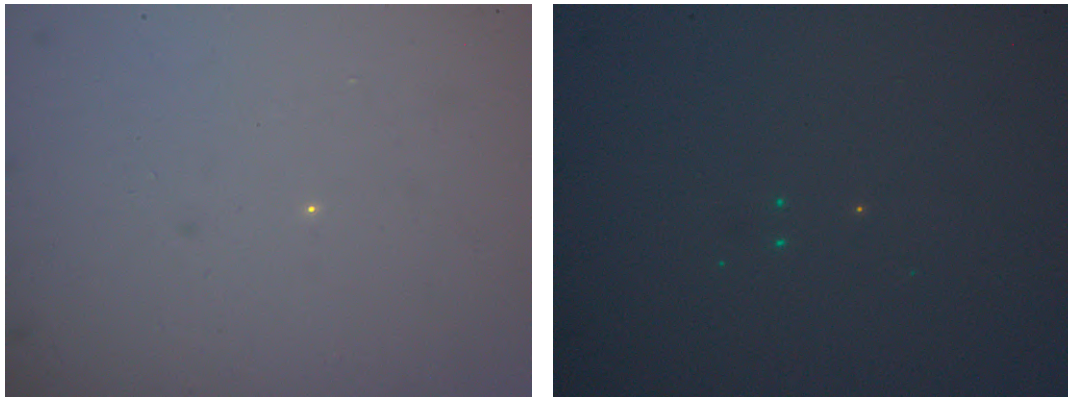


Figure 5.24: Two optical images of the same spot in a cell without reflective device. **(a)**: With only white light illumination. Only a reflective gold particle is visible. **(b)**: With white light and UV illumination. We see the fluorescence from CdSe quantum dots.

References

- [1] A. Ashkin. “Acceleration and Trapping of Particles by Radiation Pressure”. In: *Physical Review Letters* 24.4 (Jan. 1970), pp. 156–159. DOI: [10 . 1103 / physrevlett. 24. 156](https://doi.org/10.1103/physrevlett.24.156) (cit. on p. 99).
- [2] A. Ashkin et al. “Observation of a single-beam gradient force optical trap for dielectric particles”. In: *OPTICS LETTERS / Vol. 11, No. 5* (1986). DOI: [10 . 1364 / OL. 11. 000288](https://doi.org/10.1364/OL.11.000288) (cit. on pp. 99, 105, 127).
- [3] S. B. Smith, Y. Cui, and C. Bustamante. “Overstretching B-DNA: The Elastic Response of Individual Double-Stranded and Single-Stranded DNA Molecules”. In: *Science* 271.5250 (Feb. 1996), pp. 795–799. DOI: [10 . 1126 / science. 271. 5250. 795](https://doi.org/10.1126/science.271.5250.795) (cit. on pp. 99, 117).
- [4] Elio A. Abbondanzieri et al. “Direct observation of base-pair stepping by RNA polymerase”. In: *Nature* 438.7067 (Nov. 2005), pp. 460–465. DOI: [10 . 1038 / nature04268](https://doi.org/10.1038/nature04268) (cit. on pp. 99, 117).
- [5] Elizabeth A. Shank et al. “The folding cooperativity of a protein is controlled by its chain topology”. In: *Nature* 465.7298 (May 2010), pp. 637–640. DOI: [10 . 1038 / nature09021](https://doi.org/10.1038/nature09021) (cit. on p. 99).
- [6] Steven M. Block, David F. Blair, and Howard C. Berg. “Compliance of bacterial flagella measured with optical tweezers”. In: *Nature* 338.6215 (Apr. 1989), pp. 514–518. DOI: [10 . 1038 / 338514a0](https://doi.org/10.1038/338514a0) (cit. on p. 99).
- [7] Claudia Veigel et al. “The motor protein myosin-I produces its working stroke in two steps”. In: *Nature* 398.6727 (Apr. 1999), pp. 530–533. DOI: [10 . 1038 / 19104](https://doi.org/10.1038/19104) (cit. on pp. 99, 117).
- [8] David Erickson et al. “Nanomanipulation using near field photonics”. In: *Lab on a Chip* 11.6 (2011), p. 995. DOI: [10 . 1039 / c01c00482k](https://doi.org/10.1039/c01c00482k) (cit. on pp. 99, 100).
- [9] Mathieu L. Juan, Maurizio Righini, and Romain Quidant. “Plasmon nano-optical tweezers”. In: *Nature Photonics* 5.6 (May 2011), pp. 349–356. DOI: [10 . 1038 / nphoton. 2011. 56](https://doi.org/10.1038/nphoton.2011.56) (cit. on p. 100).
- [10] M. Righini et al. “Nano-optical Trapping of Rayleigh Particles and Escherichia coli Bacteria with Resonant Optical Antennas”. In: *Nano Letters* 9.10 (Oct. 2009), pp. 3387–3391. DOI: [10 . 1021 / nl803677x](https://doi.org/10.1021/nl803677x) (cit. on p. 100).

- [11] C Kielbassa. “Wavelength dependence of oxidative DNA damage induced by UV and visible light”. In: *Carcinogenesis* 18.4 (Apr. 1997), pp. 811–816. DOI: [10.1093/carcin/18.4.811](https://doi.org/10.1093/carcin/18.4.811) (cit. on pp. 100, 106).
- [12] A Ashkin and J. Dziedzic. “Optical trapping and manipulation of viruses and bacteria”. In: *Science* 235.4795 (Mar. 1987), pp. 1517–1520. DOI: [10.1126/science.3547653](https://doi.org/10.1126/science.3547653) (cit. on p. 100).
- [13] Yuanjie Pang et al. “Optical trapping of individual human immunodeficiency viruses in culture fluid reveals heterogeneity with single-molecule resolution”. In: *Nature Nanotechnology* 9.8 (July 2014), pp. 624–630. DOI: [10.1038/nnano.2014.140](https://doi.org/10.1038/nnano.2014.140) (cit. on p. 100).
- [14] A. N. Grigorenko et al. “Nanometric optical tweezers based on nanostructured substrates”. In: *Nature Photonics* 2.6 (May 2008), pp. 365–370. DOI: [10.1038/nphoton.2008.78](https://doi.org/10.1038/nphoton.2008.78) (cit. on p. 100).
- [15] Weihua Zhang et al. “Trapping and Sensing 10 nm Metal Nanoparticles Using Plasmonic Dipole Antennas”. In: *Nano Letters* 10.3 (Mar. 2010), pp. 1006–1011. DOI: [10.1021/nl904168f](https://doi.org/10.1021/nl904168f) (cit. on p. 100).
- [16] Ju-Hyung Kang et al. “Low-power nano-optical vortex trapping via plasmonic diabolo nanoantennas”. In: *Nature Communications* 2.1 (Sept. 2011). DOI: [10.1038/ncomms1592](https://doi.org/10.1038/ncomms1592) (cit. on p. 100).
- [17] Brian J. Roxworthy et al. “Application of Plasmonic Bowtie Nanoantenna Arrays for Optical Trapping, Stacking, and Sorting”. In: *Nano Letters* 12.2 (Jan. 2012), pp. 796–801. DOI: [10.1021/nl203811q](https://doi.org/10.1021/nl203811q) (cit. on pp. 100, 119).
- [18] Abhay Kotnala and Reuven Gordon. “Quantification of High-Efficiency Trapping of Nanoparticles in a Double Nanohole Optical Tweezer”. In: *Nano Letters* 14.2 (Jan. 2014), pp. 853–856. DOI: [10.1021/nl404233z](https://doi.org/10.1021/nl404233z) (cit. on p. 100).
- [19] Lina Huang, Sebastian J. Maerkl, and Olivier J. F. Martin. “Integration of plasmonic trapping in a microfluidic environment”. In: *Optics Express* 17.8 (Mar. 2009), p. 6018. DOI: [10.1364/oe.17.006018](https://doi.org/10.1364/oe.17.006018) (cit. on pp. 100, 119).
- [20] Xiaoyu Miao and Lih Y. Lin. “Trapping and Manipulation of Biological Particles Through a Plasmonic Platform”. In: *IEEE Journal of Selected Topics in Quantum Electronics* 13.6 (2007), pp. 1655–1662. DOI: [10.1109/jstqe.2007.910996](https://doi.org/10.1109/jstqe.2007.910996) (cit. on p. 100).
- [21] Pilgyu Kang et al. “Nanophotonic detection of freely interacting molecules on a single influenza virus”. In: *Scientific Reports* 5.1 (July 2015). DOI: [10.1038/srep12087](https://doi.org/10.1038/srep12087) (cit. on p. 100).
- [22] V. Garcés-Chávez et al. “Extended organization of colloidal microparticles by surface plasmon polariton excitation”. In: *Physical Review B* 73.8 (Feb. 2006). DOI: [10.1103/physrevb.73.085417](https://doi.org/10.1103/physrevb.73.085417) (cit. on p. 100).
- [23] Maurizio Righini et al. “Parallel and selective trapping in a patterned plasmonic landscape”. In: *Nature Physics* 3.7 (May 2007), pp. 477–480. DOI: [10.1038/nphys624](https://doi.org/10.1038/nphys624) (cit. on p. 100).
- [24] G. Baffou, R. Quidant, and C. Girard. “Heat generation in plasmonic nanostructures: Influence of morphology”. In: *Applied Physics Letters* 94.15 (Apr. 2009), p. 153109. DOI: [10.1063/1.3116645](https://doi.org/10.1063/1.3116645) (cit. on p. 100).
- [25] Guillaume Baffou, Christian Girard, and Romain Quidant. “Mapping Heat Origin in Plasmonic Structures”. In: *Physical Review Letters* 104.13 (Apr. 2010). DOI: [10.1103/physrevlett.104.136805](https://doi.org/10.1103/physrevlett.104.136805) (cit. on p. 100).

- [26] Guillaume Baffou and Romain Quidant. “Thermo-plasmonics: using metallic nanostructures as nano-sources of heat”. In: *Laser & Photonics Reviews* 7.2 (Apr. 2012), pp. 171–187. DOI: [10.1002/lpor.201200003](https://doi.org/10.1002/lpor.201200003) (cit. on p. 100).
- [27] Yefeng Yu. “Theoretical analysis, design and fabrication of nano-optomechanical systems (NOMS)”. Theses. Université Paris-Est, Nov. 2011. URL: <https://tel.archives-ouvertes.fr/tel-00675279> (cit. on p. 101).
- [28] P.W. Smith, A. Ashkin, and W. J. Tomlinson. “Four-wave mixing in an artificial Kerr medium”. In: *OPTICS LETTERS / Vol. 6, No. 6* (1981). DOI: [10.1364/OL.6.0002844](https://doi.org/10.1364/OL.6.0002844) (cit. on p. 103).
- [29] Ari Sihvola. “Dielectric Polarization and Particle Shape Effects”. In: *Journal of Nanomaterials* 2007 (2007), pp. 1–9. DOI: [10.1155/2007/45090](https://doi.org/10.1155/2007/45090) (cit. on p. 104).
- [30] Qiwen Zhan. “Trapping metallic Rayleigh particles with radial polarization”. In: *OPTICS EXPRESS* 3382 (2004). DOI: [10.1364/opex.12.003377](https://doi.org/10.1364/opex.12.003377) (cit. on p. 105).
- [31] Mark A. Ordal et al. “Optical properties of Au, Ni, and Pb at submillimeter wavelengths”. In: *Applied Optics* 26.4 (Feb. 1987), p. 744. DOI: [10.1364/ao.26.000744](https://doi.org/10.1364/ao.26.000744) (cit. on p. 106).
- [32] Olav Gaute Hellesø. “Optical pressure and numerical simulation of optical forces”. In: *Applied Optics* 56.12 (Apr. 2017), p. 3354. DOI: [10.1364/ao.56.003354](https://doi.org/10.1364/ao.56.003354) (cit. on p. 108).
- [33] August Köhler. “Ein neues Beleuchtungsverfahren für mikrophotographische Zwecke”. In: *Zeitschrift für wissenschaftliche Mikroskopie und für mikroskopische Technik* 10.4 (1893), pp. 433–440 (cit. on pp. 110, 127).
- [34] Robert M. Simmons et al. “Quantitative Measurements of Force and Displacement Using an Optical Trap”. In: *Biophysical Journal* 70 (1996). DOI: [10.1016/s0006-3495\(96\)79746-1](https://doi.org/10.1016/s0006-3495(96)79746-1) (cit. on p. 117).
- [35] B. Ravelo et al. “Demonstration of the triboelectricity effect by the flow of liquid water in the insulating pipe”. In: *Journal of Electrostatics* 69.6 (Dec. 2011), pp. 473–478. DOI: [10.1016/j.elstat.2011.06.004](https://doi.org/10.1016/j.elstat.2011.06.004) (cit. on p. 118).
- [36] M. Zdanowski. “Static electrification properties of hexane and cyclohexane mixtures”. In: *2008 IEEE International Conference on Dielectric Liquids*. IEEE, June 2008. DOI: [10.1109/icdl.2008.4622521](https://doi.org/10.1109/icdl.2008.4622521) (cit. on p. 118).
- [37] V. A. Tolpekin et al. “Flow Electrification in Nonaqueous Colloidal Suspensions, Studied with Video Microscopy”. In: *Langmuir* 20.20 (Sept. 2004), pp. 8460–8467. DOI: [10.1021/la0496587](https://doi.org/10.1021/la0496587) (cit. on p. 118).
- [38] Gérard Touchard. “Flow electrification of liquids”. In: *Journal of Electrostatics* 51-52 (May 2001), pp. 440–447. DOI: [10.1016/s0304-3886\(01\)00081-x](https://doi.org/10.1016/s0304-3886(01)00081-x) (cit. on p. 118).
- [39] V. N. Egorov. “Electrification of petroleum fuels”. In: *Chemistry and Technology of Fuels and Oils* 6.4 (Apr. 1970), pp. 260–266. DOI: [10.1007/bf00723571](https://doi.org/10.1007/bf00723571) (cit. on p. 118).
- [40] J. Berthelot et al. “Three-dimensional manipulation with scanning near-field optical nanotweezers”. In: *Nature Nanotechnology* 9.4 (Mar. 2014), pp. 295–299. DOI: [10.1038/nnano.2014.24](https://doi.org/10.1038/nnano.2014.24) (cit. on p. 119).
- [41] Ronald Pethig. “Review—Where Is Dielectrophoresis (DEP) Going?” In: *Journal of The Electrochemical Society* 164.5 (Dec. 2017), B3049–B3055. DOI: [10.1149/2.0071705jes](https://doi.org/10.1149/2.0071705jes) (cit. on p. 119).

- [42] N.G Green, H Morgan, and Joel J Milner. “Manipulation and trapping of sub-micron bioparticles using dielectrophoresis”. In: *Journal of Biochemical and Biophysical Methods* 35.2 (Sept. 1997), pp. 89–102. DOI: [10.1016/s0165-022x\(97\)00033-x](https://doi.org/10.1016/s0165-022x(97)00033-x) (cit. on p. 119).
- [43] Meike Beer et al. “A novel microfluidic 3D platform for culturing pancreatic ductal adenocarcinoma cells: comparison with in vitro cultures and in vivo xenografts”. In: *Scientific Reports* 7.1 (Apr. 2017). DOI: [10.1038/s41598-017-01256-8](https://doi.org/10.1038/s41598-017-01256-8) (cit. on p. 119).
- [44] Sukosin Thongrattanasiri and F. Javier Garcia de Abajo. “Optical Field Enhancement by Strong Plasmon Interaction in Graphene Nanostructures”. In: *Physical Review Letters* 110.18 (Apr. 2013). DOI: [10.1103/physrevlett.110.187401](https://doi.org/10.1103/physrevlett.110.187401) (cit. on p. 119).
- [45] Tim O. Wehling, Alexander I. Lichtenstein, and Mikhail I. Katsnelson. “First-principles studies of water adsorption on graphene: The role of the substrate”. In: *Applied Physics Letters* 93.20 (Nov. 2008), p. 202110. DOI: [10.1063/1.3033202](https://doi.org/10.1063/1.3033202) (cit. on p. 120).
- [46] John E. Bertie and Zhida Lan. “Infrared Intensities of Liquids XX: The Intensity of the OH Stretching Band of Liquid Water Revisited, and the Best Current Values of the Optical Constants of H₂O(l) at 25 °C between 15,000 and 1 cm⁻¹”. In: *Applied Spectroscopy* 50.8 (Aug. 1996), pp. 1047–1057. DOI: [10.1366/0003702963905385](https://doi.org/10.1366/0003702963905385) (cit. on p. 120).
- [47] Long Ju et al. “Graphene plasmonics for tunable terahertz metamaterials”. In: *Nature Nanotechnology* 6.10 (Sept. 2011), pp. 630–634. DOI: [10.1038/nnano.2011.146](https://doi.org/10.1038/nnano.2011.146) (cit. on p. 120).
- [48] Victor W. Brar et al. “Highly Confined Tunable Mid-Infrared Plasmonics in Graphene Nanoresonators”. In: *Nano Letters* 13.6 (May 2013), pp. 2541–2547. DOI: [10.1021/nl400601c](https://doi.org/10.1021/nl400601c) (cit. on p. 120).
- [49] Hugen Yan et al. “Tunable infrared plasmonic devices using graphene/insulator stacks”. In: *Nature Nanotechnology* 7.5 (Apr. 2012), pp. 330–334. DOI: [10.1038/nnano.2012.59](https://doi.org/10.1038/nnano.2012.59) (cit. on p. 120).
- [50] Zheyu Fang et al. “Active Tunable Absorption Enhancement with Graphene Nanodisk Arrays”. In: *Nano Letters* 14.1 (Dec. 2013), pp. 299–304. DOI: [10.1021/nl404042h](https://doi.org/10.1021/nl404042h) (cit. on p. 120).
- [51] Xiaolong Zhu et al. “Plasmon–Phonon Coupling in Large-Area Graphene Dot and Antidot Arrays Fabricated by Nanosphere Lithography”. In: *Nano Letters* 14.5 (Apr. 2014), pp. 2907–2913. DOI: [10.1021/nl500948p](https://doi.org/10.1021/nl500948p) (cit. on p. 120).
- [52] Peter Q. Liu et al. “Electrically tunable graphene anti-dot array terahertz plasmonic crystals exhibiting multi-band resonances”. In: *Optica* 2.2 (Feb. 2015), p. 135. DOI: [10.1364/optica.2.000135](https://doi.org/10.1364/optica.2.000135) (cit. on p. 120).
- [53] Peter Qiang Liu and Puspita Paul. “Graphene Nanoribbon Plasmonic Conveyor Belt Network for Optical Trapping and Transportation of Nanoparticles”. In: *ACS Photonics* 7.12 (Nov. 2020), pp. 3456–3466. DOI: [10.1021/acsp Photonics.0c01353](https://doi.org/10.1021/acsp Photonics.0c01353) (cit. on p. 121).
- [54] Puspita Paul and Peter Q. Liu. “Dynamically Reconfigurable Bipolar Optical Gradient Force Induced by Mid-Infrared Graphene Plasmonic Tweezers for Sorting Dispersive Nanoscale Objects”. In: *Advanced Optical Materials* 10.3 (Dec. 2021), p. 2101744. DOI: [10.1002/adom.202101744](https://doi.org/10.1002/adom.202101744) (cit. on p. 121).

- [55] Xieyu Chen et al. "Hysteretic behavior in ion gel-graphene hybrid terahertz modulator". In: *Carbon* 155 (Dec. 2019), pp. 514–520. DOI: [10.1016/j.carbon.2019.09.007](https://doi.org/10.1016/j.carbon.2019.09.007) (cit. on p. 124).
- [56] G. S. Agarwal. "Vacuum-Field Rabi Splittings in Microwave Absorption by Rydberg Atoms in a Cavity". In: *Physical Review Letters* 53.18 (Oct. 1984), pp. 1732–1734. DOI: [10.1103/physrevlett.53.1732](https://doi.org/10.1103/physrevlett.53.1732) (cit. on p. 125).
- [57] Yifu Zhu et al. "Vacuum Rabi splitting as a feature of linear-dispersion theory: Analysis and experimental observations". In: *Physical Review Letters* 64.21 (May 1990), pp. 2499–2502. DOI: [10.1103/physrevlett.64.2499](https://doi.org/10.1103/physrevlett.64.2499) (cit. on p. 125).
- [58] Peter Q. Liu et al. "Highly tunable hybrid metamaterials employing split-ring resonators strongly coupled to graphene surface plasmons". In: *Nature Communications* 6.1 (Nov. 2015). DOI: [10.1038/ncomms9969](https://doi.org/10.1038/ncomms9969) (cit. on p. 125).
- [59] Jan Kapuscinski. "DAPI: a DNA-Specific Fluorescent Probe". In: *Biotechnic & Histochemistry* 70.5 (Jan. 1995), pp. 220–233. DOI: [10.3109/10520299509108199](https://doi.org/10.3109/10520299509108199) (cit. on p. 128).
- [60] Wei-Chuan Sun, Kyle R Gee, and Richard P Haugland. "Synthesis of novel fluorinated coumarins: Excellent UV-light excitable fluorescent dyes". In: *Bioorganic & Medicinal Chemistry Letters* 8.22 (Nov. 1998), pp. 3107–3110. DOI: [10.1016/s0960-894x\(98\)00578-2](https://doi.org/10.1016/s0960-894x(98)00578-2) (cit. on p. 128).
- [61] Li-Jiao Tian et al. "Fluorescence dynamics of the biosynthesized CdSe quantum dots in *Candida utilis*". In: *Scientific Reports* 7.1 (May 2017). DOI: [10.1038/s41598-017-02221-1](https://doi.org/10.1038/s41598-017-02221-1) (cit. on p. 128).
- [62] Jianing Chen et al. "Optical nano-imaging of gate-tunable graphene plasmons". In: *Nature* 487.7405 (June 2012), pp. 77–81. DOI: [10.1038/nature11254](https://doi.org/10.1038/nature11254) (cit. on p. 128).
- [63] A. Pagies et al. "THz near-field nanoscopy of graphene layers". In: *2015 40th International Conference on Infrared, Millimeter, and Terahertz waves (IRMMW-THz)*. IEEE, Aug. 2015. DOI: [10.1109/irmmw-thz.2015.7327531](https://doi.org/10.1109/irmmw-thz.2015.7327531) (cit. on p. 128).
- [64] Jiawei Zhang et al. "Terahertz Nanoimaging of Graphene". In: *ACS Photonics* 5.7 (June 2018), pp. 2645–2651. DOI: [10.1021/acsp Photonics.8b00190](https://doi.org/10.1021/acsp Photonics.8b00190) (cit. on p. 128).

Conclusion and perspectives

Overcoming the diffraction limit to enhance and investigate the interactions of light with objects far smaller than the light wavelength brings up a lot of challenges, from the visible to the Terahertz range. In particular, biological objects such as viruses or large proteins are expected to have vibration mode in the THz range, but are orders of magnitude smaller than THz wavelengths. In this thesis, we focused on a resonant approach to confine a THz field in an arbitrary small volume. First we worked on the single resonator itself, in order to understand its interactions with a propagative THz wave, its near-field properties and most importantly, how it behaves when coupled to a subwavelength object. Then, we tackled the application of field confinement to THz-TDS of nano-objects through a single resonator, and optical trapping.

A SRR essentially behaves as a RLC circuit, and is therefore affected by the dielectric permittivity of the material in its capacitor. Experimentally, the behavior of the SRR is studied with a THz-TDS transmission or reflection measurement. To keep a solid link between the measurement and the physical properties of the SRR and its surrounding, we developed a model to describe the reflection and transmission coefficient of a single SRR on a substrate. This model is constructed under the quasi-static approximation, which is valid for wavelengths much larger than the SRR size. This model expresses the transmission and reflection coefficients from the basic properties of a RLC circuit, as well as the complex permittivity of the material to which it is coupled, and *how* it is coupled. Taking a closer look at the particular case of a SRR coupled to a material with its own resonance, we showed that our model renders strong coupling. Taking the example of Glutamic Acid (GA), an amino acid with a resonance at 1.2 THz in its crystal forms, we expect the strong coupling regime to be within reach of our experiments.

Using the model as a guideline, we designed and fabricated SRRs specifically thought to be used individually. We settled for a symmetric design with a single gap in the center, and a loop on each side. We used FDTD simulations to study how the different shape parameters affect the resonance frequency, the quality factor and the far-field coupling directivity. Although we were not able to understand the exact relationship between the shape of the SRR and its radiative losses, the simulated far-field emission patterns show that the SRR mostly couples to the far-field through the two continuous metal lines essentially acting as linear antennas. It gives us a knob to adjust the directivity of the SRR by changing the distance between the antennas, and adjust the quality factor by changing their lengths relative to the resonance wavelength. About the fabrication, the e-beam lithography process is reliable and we were able to fabricate SRRs with gaps smaller than 30 nm. Working with single SRRs allows us to push our fabrication process to its limit and to use more advanced fabrication processes such as Focused Ion Beam (FIB) ablation to create even smaller gaps. Hence gap sizes down to the scale of single proteins are feasible.

We experimentally validated the electric field distribution provided by the SRR with s-SNOM. We showed that most s-SNOM systems are fundamentally unadapted to image objects that act as antennas. Indeed, the excitation and detection in a

s-SNOM system is directional. Consequently, the system is strongly affected by changes in the directivity of the s-SNOM probe and sample. We proposed an alternative configuration to make s-SNOM compliant with samples affecting the directivity of the probe. Nonetheless, we were able to produce an image of the resonant mode for the first time in this frequency range. We confirmed the electric field concentration in the SRR capacitor.

We experimentally showed that spectroscopy on a single SRR is well within reach of commercial THz-TDS systems, even in configurations allowing direct access to the gap. We identified the delay drift during long acquisition to be a major source of error in THz-TDS. We implemented a correction algorithm that proved to be *essential* to take advantage of the full dynamic range of a THz-TDS system. We performed spectroscopy on single SRRs from 275 GHz to 3 THz. Putting our SRR design to the test, we reached exceptionally high quality factors up to 29.65. Although we have not demonstrated strong coupling with GA resonance, we detected its presence in the gap of a single resonator. Once we get rid of the destructive interference in the substrate, improve the GA deposition technique, and identify the sources of unwanted difference between a SRR measurement and a reference measurement, we will be able to demonstrate strong coupling with a single GA crystal.

Finally, we investigated the possibility of using the field confinement provided by SRRs to generate optical forces. According to our FDTD simulations, the electric field gradient induced by the resonance of a SRR is strong enough to generate a stable optical trap, even with excitation power an order of magnitude lower than the power of our THz laser source. We reached the same conclusion for the field enhancement provided by GNR in the mid-infrared. For the experimental demonstration, we constructed an optical platform providing up to 30 mW of excitation power, microscopic imaging, and force measurement. We developed a microfluidic platform compatible with non-polar solvent, external THz excitation and observation with a short working distance objective. The behavior of micro-particles in a non-polar solvent turned out to be much more challenging than we anticipated, as they tend to stick to each other and to the container surface. We managed to substantially hinder this behavior with surface functionalization, but further investigation in surface chemistry is necessary to improve our microfluidic tools. Additionally, We will make sure that the multiple reflections in the microfluidic cells interfere constructively, and make most of the cell surface conductive to avoid build up of electrostatic charge. Then, we will be able to properly measure the optical forces from the THz optical trap.

To conclude, this work provided useful tools for the modelisation of resonators, allowing the extraction of physical properties of material from a transmission experiment. It also led us to practical guidelines to adjust the quality factor and directivity of such resonators. We measured the first images of a THz photonic mode with s-SNOM and introduced a new interpretation for near-field imaging of micro-antenna. We developed an algorithmic tool to eliminate a major source of error in THz-TDS, which allowed us to demonstrate THz spectroscopy on single SRRs on more than a decade of frequency range, and detected record breaking amounts of material in their gap. We explored the subject of non-polar microfluidic to take advantage of micro-resonator field confinement to bring optical trapping toward the mid-infrared and THz range.

I believe that the demonstration of the strong coupling regime is within very close reach. Then, the future of this work will be multidisciplinary, as it will open the way to spectroscopy on samples that were previously impossible to measure individually in this frequency range, such as viruses, proteins or single 2D material

structures such as graphene nano-ribbons. In addition to the tools developed here for field confinement and spectroscopy, this requires physically manipulating objects at the nanoscale and to understanding their surface chemistry. Nonetheless, THz spectroscopy on a single protein is conceivable. Combining spectroscopy and optical trapping, the hope is to observe the changes in the spectral properties of a biological object while it is trapped with radiation close to its own resonance frequency.

Appendix A

Optical torque

A.1 Torque calculation in the static approximation

In this part, the time derivative of the intensity is neglected. Let us \vec{T}_x , \vec{T}_y and \vec{T}_z be the three column vectors of the MST. The torque applied to the origin on an infinitesimal volume is given by

$$\frac{\vec{\tau}}{dV} = \vec{r} \wedge \frac{\vec{F}}{dV}, \quad (\text{A.1})$$

where $\vec{r} = x\vec{u}_x + y\vec{u}_y + z\vec{u}_z$ is the position vector, therefore

$$\vec{\tau}_{tot} = \iiint_V \vec{r} \wedge \vec{F}, \quad (\text{A.2})$$

in particular if $\vec{\tau}_{tot} = \mathcal{T}_x\vec{u}_x + \mathcal{T}_y\vec{u}_y + \mathcal{T}_z\vec{u}_z$

$$\mathcal{T}_x = \iiint_V (yF_z - zF_y), \quad (\text{A.3})$$

$$\mathcal{T}_x = \iiint_V (y\vec{\nabla} \cdot \vec{T}_z - z\vec{\nabla} \cdot \vec{T}_y) dV. \quad (\text{A.4})$$

Using the following identity

$$\vec{\nabla}(\phi\vec{A}) = (\vec{\nabla}\phi) \cdot \vec{A} + \phi \cdot (\vec{\nabla} \cdot \vec{A}), \quad (\text{A.5})$$

where \vec{A} is a vector field and ϕ is a scalar field, one gets

$$y\vec{\nabla} \cdot \vec{T}_z = \vec{\nabla}(y\vec{T}_z) - \vec{u}_y \cdot \vec{T}_z, \quad (\text{A.6})$$

thus (A.4) becomes

$$\mathcal{T}_x = \iiint_V \left(\vec{\nabla}(y\vec{T}_z - z\vec{T}_y) - \vec{u}_y \cdot \vec{T}_z + \vec{u}_z \cdot \vec{T}_y \right) dV. \quad (\text{A.7})$$

One can see from its definition (5.14) on page 102 that the MST is a symmetric tensor, implying $\vec{u}_y \cdot \vec{T}_z = \vec{u}_z \cdot \vec{T}_y$. Finally, with the divergence theorem

$$\mathcal{T}_x = \oint_{\partial V} (y\vec{T}_z - z\vec{T}_y) \cdot \vec{dS}. \quad (\text{A.8})$$

And with the same reasoning

$$\mathcal{T}_y = \iint_{\partial V} (z\vec{T}_x - x\vec{T}_z) d\vec{S}, \quad (\text{A.9})$$

$$\mathcal{T}_z = \iint_{\partial V} (x\vec{T}_y - y\vec{T}_x) d\vec{S}. \quad (\text{A.10})$$

Which can also be written as

$$\vec{\mathcal{T}} = \iint_{\partial V} (\vec{r} \wedge T) d\vec{S}. \quad (\text{A.11})$$

Therefore the optical torque on a particle can also be numerically computed with the Maxwell's Stress Tensor (MST) known on a closed surface around it.

A.2 Torque calculation on an ellipsoidal particle

An ellipsoid in an electromagnetic field can also be modelled as an electric dipole, but because of its anisotropic shape, the polarizability has to be expressed as a tensor. Therefore the electromagnetically induced dipole $\vec{p} = \alpha \vec{E}$ and \vec{E} are no longer necessarily collinear, and therefore a torque is apply on the particle, unless \vec{E} is an eigenvector of α which is the equilibrium condition.

In the rest of this section, $(\vec{u}_x, \vec{u}_y, \vec{u}_z)$ is an orthonormal basis align with the main axis of the ellipsoidal particle, since the material itself is isotropic, those axis are also eigenvectors of the polarizability tensor [1]. This last is therefore a diagonal tensor in this basis.

Let us consider an electric field

$$\vec{E} = E_0 \frac{\sqrt{2}}{2} \cos(\omega t) \vec{u}_x + E_0 \frac{\sqrt{2}}{2} \cos(\omega t + \varphi) \vec{u}_y, \quad (\text{A.12})$$

and a polarizability tensor

$$\alpha = \begin{pmatrix} \alpha_x & 0 & 0 \\ 0 & \alpha_y & 0 \\ 0 & 0 & \alpha_z \end{pmatrix}. \quad (\text{A.13})$$

This electric field is linearly polarized if $\varphi = 0$, and circularly polarized if $\varphi = \pm \frac{\pi}{2}$, the polarization is otherwise elliptic. Assuming the particle is immobile, the torque is given by

$$\vec{\mathcal{T}} = \left[\begin{pmatrix} \alpha_x & 0 & 0 \\ 0 & \alpha_y & 0 \\ 0 & 0 & \alpha_z \end{pmatrix} \begin{pmatrix} E_0 \frac{\sqrt{2}}{2} \cos(\omega t) \\ E_0 \frac{\sqrt{2}}{2} \cos(\omega t + \varphi) \\ 0 \end{pmatrix} \right] \wedge \begin{pmatrix} E_0 \frac{\sqrt{2}}{2} \cos(\omega t) \\ E_0 \frac{\sqrt{2}}{2} \cos(\omega t + \varphi) \\ 0 \end{pmatrix}, \quad (\text{A.14})$$

thus

$$\vec{\mathcal{T}} = \begin{pmatrix} \alpha_x E_0 \frac{\sqrt{2}}{2} \cos(\omega t) \\ \alpha_y E_0 \frac{\sqrt{2}}{2} \cos(\omega t + \varphi) \\ 0 \end{pmatrix} \wedge \begin{pmatrix} E_0 \frac{\sqrt{2}}{2} \cos(\omega t) \\ E_0 \frac{\sqrt{2}}{2} \cos(\omega t + \varphi) \\ 0 \end{pmatrix}, \quad (\text{A.15})$$

$$\vec{\mathcal{T}} = (\alpha_x - \alpha_y) \frac{E_0^2}{4} [\cos(2\omega t + \varphi) + \cos(\varphi)] \vec{u}_z. \quad (\text{A.16})$$

Assuming that the period of oscillation is much shorter than the reaction time of the system, the torque can be averaged in time

$$\langle \vec{\mathcal{T}} \rangle = (\alpha_x - \alpha_y) \frac{E_0^2}{4} \cos(\varphi) \vec{u}_z. \quad (\text{A.17})$$

According to this formula, the average torque on the particle with a circular polarization ($\varphi = \pm \frac{\pi}{2}$) is zero. Nevertheless analytical and numerical works on the subject[2] as well as recent experimental results [3] suggest that the torque should be non-zero in this case, this could be due to an angular momentum transfer between the light and the particle, which is not taken into account here since the modification of the electric field from the particle is neglected.

A.3 Numerical torque computation

The FDTD software does not natively provide tools to compute the torque applied on a particle. The tools can however be written with the force calculation tool as a basis since the data used to get the force and the torque are essentially the same, and the function can therefore be adapted quite easily.

A.3.1 Volumetric technique adaptation

Since the volumetric technique compute the force $\vec{F}(\vec{r})$ on every mesh of the volume, the torque applied to the origin on this mesh is $\vec{\mathcal{T}}(\vec{r}) = \vec{r} \wedge \vec{F}(\vec{r})$. This result is then integrated on the whole volume to get the total torque.

A.3.2 MST technique adaptation

In the MST computation analysis group, the Maxwell Stress tensor is evaluated on every cell of the cuboid surrounding the volume. The formula (A.11) on the preceding page can therefore be used to integrate the total torque.

A.3.3 Test of the torque calculation

The torque calculation is tested with a prolate spheroid in a focused gaussian beam. In that case the particle should be subject to a torque that leads it to align with the polarization of the light if the particle is small in respect to the beam waist, or with the propagation direction of the beam otherwise [2]. Thus a torque should be observed with the main axis of the spheroid oriented with a 45° angle in respect to the polarization axis. In this configuration, the torque given by both technique is nearly identical and consistent with the expectation. The torque is directed such that the particle would align with the polarization of the beam.

References

- [1] Ari Sihvola. "Dielectric Polarization and Particle Shape Effects". In: *Journal of Nanomaterials* 2007 (2007), pp. 1–9. DOI: [10.1155/2007/45090](https://doi.org/10.1155/2007/45090) (cit. on p. 142).

-
- [2] Stephen H. Simpson and Simon Hanna. “Optical trapping of spheroidal particles in Gaussian beams”. In: *J. Opt. Soc. Am. A* 24, 430-443 (2007). DOI: [10.1364/josaa.24.000430](https://doi.org/10.1364/josaa.24.000430) (cit. on p. 143).
- [3] René Reimann et al. “GHz Rotation of an Optically Trapped Nanoparticle in Vacuum”. In: *Physical Review Letters* 121.3 (July 2018). DOI: [10.1103/physrevlett.121.033602](https://doi.org/10.1103/physrevlett.121.033602) (cit. on p. 143).